Universität Hamburg
DER FORSCHUNG | DER LEHRE | DER BILDUNG

Dynamical mean-field theory for solids with strong coupling to the electromagnetic field

Dissertation
zur Erlangung des Doktorgrades
an der Fakultät für Mathematik, Informatik und Naturwissenschaften

Fachbereich Physik
der Universität Hamburg

vorgelegt von
Katharina Lenk

Hamburg
2024

Gutachter der Dissertation:	Prof. Dr. Martin Eckstein Prof. Dr. Tim Wehling
Zusammensetzung der Prüfungskommission:	Prof. Dr. Ludwig Mathey Prof. Dr. Martin Eckstein Prof. Dr. Tim Wehling Prof. Dr. Daniela Pfannkuche Prof. Dr. Henning Moritz
Vorsitzender der Prüfungskommission:	Prof. Dr. Ludwig Mathey
Datum der Disputation:	20. August 2024
Vorsitzender des Fach-Promotionsausschusses PHYSIK:	Prof. Dr. Markus Drescher
Leiter des Fachbereichs PHYSIK:	Prof. Dr. Wolfgang J. Parak
Dekan der Fakultät MIN:	Prof. Dr.-Ing. Norbert Ritter

Abstract

Recent advances in the study of quantum cooperative effects in coupled light-matter systems open up unprecedented pathways to manipulate the properties of materials without external drive. This is due to vacuum fluctuations of the electromagnetic field, which hybridize with matter degrees of freedom even in thermal equilibrium and thereby influence the behavior of the system. In this thesis, we focus on the theoretical study of such photon-induced effects. We first present a collective theory for single-mode models and then apply dynamical mean-field theory (DMFT) to macroscopic solids interacting with a continuum of electromagnetic modes.

The collective theory is based on diagrammatic techniques and assumes a linear dipolar coupling to one single cavity mode. It allows expressing the electric susceptibility of the system inside the cavity in terms of the bare matter response. We find that the radiative corrections of the static susceptibility vanish in the thermodynamic limit if the single-particle coupling is finite. Moreover, the formalism proves that nonlinearities in the matter response play a crucial role in affecting the equilibrium state of finite-size systems. As an example, we apply the theory to a simple model of a quantum paraelectric with dipole-dipole interactions and demonstrate that the cavity mode leads to an enhancement of the static electric response in small clusters of material.

DMFT, however, is most appropriate for extended solids consisting of a macroscopic number of atoms or molecules. Therefore, we consider a setting, where a continuum of electromagnetic modes gives rise to a non-vanishing total effect even in the thermodynamic limit. The modes correspond to surface plasmon polaritons (SPPs) at a dielectric-metal interface. We study two different model systems: In the first case, we consider a two-dimensional solid that couples to the vacuum fluctuations of the SPPs via a linear dipolar interaction. Within static mean-field approximation, the material exhibits a ferroelectric phase transition that is not affected by the electromagnetic radiation field. Bosonic DMFT provides a more accurate description and reveals that the light-matter interaction enhances the ferroelectric order and stabilizes the ferroelectric phase. In the second case, we study a two-dimensional Hubbard model, which couples to the electromagnetic modes via Peierls phase factors. Even without light-matter interaction, the system may undergo a Mott metal-isulator transition. We follow a diagrammatic approach to incorporate photon-induced effects into the DMFT formalism. Our results suggest that the coupling to the electromagnetic field favors the metallic state over the Mott insulating phase.

In summary, this thesis demonstrates that the interplay of light and matter opens up new possibilities to modify the static response of microscopic systems and to control phase transitions in macroscopic solids, even in thermal equilibrium. Moreover, it highlights that DMFT can serve as a valuable theoretical tool to study quantum cooperative effects in systems with strong light-matter interactions.

Zusammenfassung

Jüngste Fortschritte in der Erforschung quantenkooperativer Effekte in gekoppelten Licht-Materie-Systemen eröffnen nie dagewesene Möglichkeiten, die Eigenschaften von Materialien ohne externe Stimulation zu manipulieren. Grund dafür sind Vakuumfluktuationen des elektromagnetischen Feldes, die selbst im thermischen Gleichgewicht mit den Freiheitsgraden der Materie hybridisieren und dadurch das Verhalten des Systems beeinflussen. In dieser Arbeit befassen wir uns mit der theoretischen Untersuchung solcher photoneninduzierter Effekte. Wir stellen zunächst eine kollektive Theorie für Singlemode-Modelle vor und wenden dann dynamische Molekularfeldtheorie (DMFT) auf makroskopische Festkörper an, die mit einem Kontinuum elektromagnetischer Moden wechselwirken.

Die kollektive Theorie basiert auf diagrammatischen Methoden und setzt eine lineare, dipolare Kopplung an eine einzelne Cavitymode voraus. Sie erlaubt es, die elektrische Suszeptibilität des Systems in der Cavity durch die Antwort der ungekoppelten Materie auszudrücken. Wir stellen fest, dass die Strahlungskorrekturen zur statischen Suszeptibilität im thermodynamischen Limes verschwinden, sofern die Einteilchen-Kopplung endlich ist. Des Weiteren beweist der Formalismus, dass Nichtlinearitäten in der Materialantwort eine bedeutende Rolle bei der Beeinflussung des Gleichgewichtszustands von Systemen endlicher Größe spielen. Als Beispiel wenden wir die Theorie auf ein einfaches Modell eines Quantenparaelektrikums mit Dipol-Dipol-Wechselwirkungen an und zeigen, dass die Cavitymode in kleinen Materialclustern zu einer Verstärkung der statischen elektrischen Antwort führt.

DMFT eignet sich dagegen vor allem für ausgedehnte Festkörper, die aus einer makroskopischen Anzahl von Atomen oder Molekülen bestehen. Daher betrachten wir ein Setting, in dem ein Kontinuum elektromagnetischer Moden selbst im thermodynamischen Limes einen nicht verschwindenden Gesamteffekt hervorruft. Die Moden gehören zu Oberflächenplasmonen-Polaritonen (OPP) einer Grenzfläche zwischen einem Metall und einem Dielektrikum. Wir untersuchen zwei verschiedene Modelle: Im ersten Fall betrachten wir einen zweidimensionalen Festkörper, der über eine dipolare Wechselwirkung an die Vakuumfluktuationen der OPP koppelt. Innerhalb der statischen Molekularfeldnäherung weist das Material einen ferroelektrischen Phasenübergang auf, der nicht durch das elektromagnetische Strahlungsfeld beeinflusst wird. Bosonische DMFT liefert eine genauere Beschreibung und offenbart, dass die Licht-Materie-Wechselwirkung die ferroelektrische Ordnung verstärkt und die ferroelektrische Phase stabilisiert. Im zweiten Fall untersuchen wir ein zweidimensionales Hubbard-Modell, das über Peierls-Faktoren an die elektromagnetischen Moden koppelt. Auch ohne Licht-Materie-Wechselwirkung kann das System einen Mott Metall-Isolator-Übergang durchlaufen. Wir nutzen diagrammatische Methoden, um photoneninduzierte Effekte in den DMFT Formalismus zu integrieren. Unsere Ergebnisse weisen darauf hin, dass die Kopplung an das elektromagnetische Feld die metallische Phase gegenüber der Mott-isolierenden Phase begünstigt.

Insgesamt verdeutlicht diese Arbeit, dass das Zusammenspiel von Licht und Materie sogar im thermischen Gleichgewicht neue Möglichkeiten eröffnet, die statische Suszeptibilität mikroskopischer Systeme zu modifizieren und Phasenübergänge in makroskopi-

schen Festkörpern zu kontrollieren. Außerdem zeigt sie auf, dass DMFT als wertvolles theoretisches Werkzeug zur Untersuchung quantenkooperativer Effekte in Systemen mit starker Licht-Materie-Wechselwirkung dienen kann.

Eidesstattliche Versicherung / Declaration on oath

Hiermit versichere ich an Eides statt, die vorliegende Dissertationsschrift selbst verfasst und keine anderen als die angegebenen Hilfsmittel und Quellen benutzt zu haben.

Sofern im Zuge der Erstellung der vorliegenden Dissertationsschrift generative Künstliche Intelligenz (gKI) basierte elektronische Hilfsmittel verwendet wurden, versichere ich, dass meine eigene Leistung im Vordergrund stand und dass eine vollständige Dokumentation aller verwendeten Hilfsmittel gemäß der Guten wissenschaftlichen Praxis vorliegt. Ich trage die Verantwortung für eventuell durch die gKI generierte fehlerhafte oder verzerrte Inhalte, fehlerhafte Referenzen, Verstöße gegen das Datenschutz- und Urheberrecht oder Plagiate.

Hamburg, den _____ _____

Contents

1. Introduction

1.1. Manipulating matter with quantum light

In recent years, the study of quantum cooperative effects in coupled light-matter systems has become a rapidly evolving field of research that merges two complementary disciplines of physics. On the one hand, it integrates quantum optics, which mostly focuses on the study of photons and their interaction with single or small ensembles of emitters. On the other hand, it intersects with condensed matter physics, which investigates collective phenomena in solids composed of a macroscopic number of atoms or molecules. But unlike quantum optics, condensed matter physics often either does not account for light-matter interactions or relies on a classical description of the electromagnetic field.

Indeed, the optical control of quantum many-body systems with intense classical laser fields can lead to a plethora of fascinating effects and even create novel phases [9]. However, harnessing the true quantum nature of light and matter opens entirely new avenues to manipulate the properties of macroscopic systems without external drive. This is due to the fact that even in vacuum, charges and magnetic degrees of freedom couple to the quantum fluctuations of the electromagnetic field and thus interact with virtual photons in their environment.

A well-known consequence of this behavior is the so-called Lamb shift, i.e., the radiative correction of energy levels in an atom caused by the vacuum fluctuations of the electromagnetic field. For the hydrogen atom, the Lamb shift lifts the degeneracy between the $2s_{1/2}$ and $2p_{1/2}$ states resulting from the Dirac equation. This was first observed experimentally in 1947 by Willis E. Lamb and Robert C. Retherford [53]. Moreover, the Dutch physicist Hendrik Casimir predicted in 1948 that the radiation pressure of virtual photons gives rise to an effective attractive force between two perfectly conducting uncharged plates [55]. This is due to a modification of the zero-point fluctuations between the plates, leading to a radiation pressure that is weaker inside the plates than outside. And indeed, in 1997, this so-called Casimir force was demonstrated experimentally with a degree of accuracy of five percent [54].

Another textbook example where the interaction of matter with the electromagnetic vacuum plays an important role is the Purcell effect. This effect manifests when an atom is placed inside an optical resonator. It refers to the suppression or enhancement of the atom's spontaneous emission rate depending on the fundamental cavity frequency [73]. The Purcell effect can be attributed to the boundary conditions imposed by the cavity mirrors, which modify the local density of states of the radiation field at the position of the atom. This modification affects the atom's coupling to the vacuum fluctuations of light and thus alters its spontaneous emission rate. Importantly, the Purcell effect demonstrates that the behavior of a quantum system can be controlled by changing its

electromagnetic environment.

However, the Lamb shift, the Casimir force and the Purcell effect correspond to a regime, where the interaction between light and matter is weak. In free space, the strength of the coupling is determined by the small value of the fine structure constant $\alpha \approx 1/137$. As a result, the effect of the electromagnetic vacuum fluctuations is negligibly weak and experimentally hard to observe. The strength of the interaction increases if the electromagnetic field is restricted to a finite volume, e.g., inside a cavity. But also in Purcell's experiment, the cavity losses dominated over the coupling between light and matter. In order to achieve more striking effects, it is therefore desirable to strongly enhance the interaction with the photon field.

Today, this can be accomplished on various platforms through a strong spatial confinement of the electromagnetic field. In particular, nanoplasmonic cavities allow for an extreme compression of the electromagnetic field even below the diffraction limit [51], and high-finesse optical cavities exhibit very low loss rates, enabling the light-matter coupling to become the dominant energy scale in the system [85]. This strategy is applicable to both microscopic and macroscopic systems, as it influences the single-particle coupling strength, i.e., the interaction of the radiation field with each individual emitter.

Another quantity only relevant to systems composed of multiple particles is the collective light-matter coupling, which determines how strongly the entire system and its collective modes interact with the electromagnetic field. The collective coupling is proportional to the single-particle coupling and therefore is influenced by the (effective) cavity volume. Moreover, increasing the number of emitters N enhances the collective interaction with the electromagnetic field, which scales as $\sqrt{N}$. Consequently, the limiting factor for the collective light-matter coupling is the number of particles per volume. In dense solids, it is common to transition into a regime where the collective coupling is the dominant energy scale in the system, while the single-particle coupling remains weak.

These technological and scientific developments have paved the way for new fields of research, such as "Polaronic chemistry", where the strong hybridization of light and matter inside a dark cavity is used to modify chemical reaction rates, charge transfer, or excitation transfer. This has been demonstrated in theory and experiments and mostly involves molecular systems [23, 76, 25, 83]. Most notably, many of these observations have been made at strong collective but weak single-particle coupling. This implies that cooperative effects have a significant impact on the system's behavior. However, achieving a comprehensive theoretical description of these phenomena is still a matter of ongoing research [83].

Moreover, in solid state physics, there are many promising proposals to engineer the properties of macroscopic materials through the vacuum fluctuations of light inside a cavity. This is particularly interesting for so-called quantum materials, as they already exhibit collective quantum many-body phenomena that are often sensitive to small external stimuli like pressure or temperature [78]. For instance, multiple theoretical studies predict the possibility of cavity-mediated superconductivity [79, 26], and it has been shown that the coupling to a cavity mode may modify the effective spin-exchange interactions [46, 81] and lead to the creation of Mott polaritons [47] in strongly correlated

electron systems. Another example is the superradiant excitonic insulator phase reported in Ref. [66] or the possibility of cavity-enhanced magnetism with a simultaneous condensation of photons discussed in Ref. [75]. Apart from these theoretical findings, a recent experiment demonstrates the cavity-mediated control of the metal-to-insulator transition in 1T-TaS_2 [42].

Furthermore, there have been interesting theoretical works on photon-induced ferroelectricity, which also plays an important role in this thesis. For example, in Ref. [58], a "ferroelectric photo ground state" has been predicted for the perovskite $SrTiO_3$ (STO). In this material, the displacement of titanium and oxygen atoms in the unit cell gives rise to a finite electric polarization of the solid, turning it into a ferroelectric. Without external stimuli, this phase transition never occurs, even down to zero temperature, due to nuclear quantum fluctuations. However, as shown in Ref. [58], this effect can be suppressed by the vacuum fluctuations of a single cavity mode if a photon-phonon coupling is introduced. As a result, the material may undergo a transition to the ferroelectric state, which is accompanied by a finite photon occupation in the cavity.

Moreover, Ref. [6] reports on a cavity-enhanced ferroelectric phase transition in a dipolar material between two metallic mirrors. The material couples to light via infrared-active phonons. In contrast to [58], the model includes multiple modes of the electromagnetic field and also takes into account plasmons in the metal mirrors. It is shown that the interplay of photons, phonons, and plasmons strongly modifies the excitation spectrum of the system. In addition, the description contains phonon nonlinearities, which are essential to cavity-induced ferroelectricity, as they lead to a coupling between the individual modes. Ultimately, this causes a softening of a dipolar phonon mode, such that the ferroelectric state is stabilized.

1.2. Purpose of the thesis

The examples mentioned above are only a tiny fraction of the innumerable scientific advances in this vivid and fascinating area of research. But the vision of steering and engineering material properties on demand by manipulating the quantum fluctuations of the electromagnetic field also comes with challenges. In particular, it requires suitable theoretical methods to predict the behavior of these highly complex quantum many-body systems. For most settings, an exact simulation of all degrees of freedom is computationally unfeasible. Therefore, it is vital to find appropriate approximate schemes that still allow for an accurate description of these systems.

A computationally tractable framework commonly used in condensed matter physics is dynamical mean-field theory (DMFT). This method has proven to be particularly useful for strongly correlated electron systems [29], and has also been extended to bosonic models [3, 4, 1]. DMFT is an embedding approach that maps a macroscopic lattice model to an impurity problem coupled to an effective environment. In order to solve the problem self-consistently, the self-energy for the lattice Green's function is assumed to be purely local. This approximation becomes exact if the coordination number of the lattice approaches infinity [68, 70]. In this thesis, we extend the DMFT frame-

work to solids with strong coupling to the electromagnetic field. A major advantage of this method is its ability to incorporate a continuum of electromagnetic modes without further simplifications such as a Markov or rotating wave approximation.

Before we proceed, however, let us comment on the meaning of "strong coupling" in the tiltle of this thesis. In general, there is no unique definition of this term. In condensed matter physics, the expression is usually used if the magnitude of the interaction with one degree of freedom greatly exceeds all other relevant energy scales in the system, such that a perturbative treatment in this parameter is no longer valid. For instance, the strong coupling regime of the Hubbard model is reached if the local electron-electron interaction is much larger than the hopping matrix element [19]. Similarly, the electron-phonon coupling in the Holstein model is called strong if the bipolaron binding energy (i.e., the energy scale of the phonon-mediated electron-electron interaction) widely surpasses the hopping amplitude [24].

In quantum optics, this term is understood differently. Typically, it refers to open systems, such as a cavity with imperfect mirrors, and is only well-defined for single-mode models. In that case, the coupling to the electromagnetic mode is considered strong if it exceeds the loss rate of the cavity. Moreover, there are other expressions to quantify the light-matter interaction strength that are also applicable to closed systems. For example, the "ultrastrong coupling regime", denotes the range of parameters, where the ratio η between the coupling to the cavity mode and the energy of the bare matter excitations is larger than ≈ 0.1. In this regime, higher-order processes become significant, leading to a hybridization of states with different photon numbers. In the "deep-strong coupling regime", where $\eta \gtrsim 1$, these processes even dominate [50].

However, this classification cannot be directly extended to systems involving multiple electromagnetic modes. This is particularly relevant to this thesis since we consider solids interacting with a continuum of modes. In some cases, it is possible to relate a system to a generic one-mode model. For instance, in Ref. [49], an emitter that interacts with a continuum of modes inside a rectangular waveguide has been compared to an effective Rabi model. Alternatively, it has been suggested in Ref. [50] that the coupling strength between an atom and a mode continuum should be quantified by comparing its relaxation rate Γ to the atomic transition frequency.

These examples illustrate that there is no universal strategy to categorize the strength of light-matter interactions in arbitrary systems. Moreover, these concepts cannot be directly applied to collections of interacting emitters or macroscopic solids. In these systems, it is not even clear whether the decisive factor is the single-particle coupling or the collective interaction, which can differ by many orders of magnitude. Due to this ambiguity, we refrain from providing a strict definition of the term "strong coupling" within this thesis. Instead, we use this expression in a broader context to indicate that the interaction with the electromagnetic field is strongly enhanced as compared to free space and thus affects the equilibrium state of the solid in a non-trivial way.

1.3. Thesis outline

The remainder of this thesis consists of an introductory chapter (Ch. 2), three main chapters (Ch. 3 - Ch. 5), and a brief conclusion (Ch. 6). Additionally, App. A and B contain supplementary information and detailed derivations related to Ch. 4 and 5.

In Ch. 2, we begin with some basic concepts and methods. We introduce the standard DMFT formalism for fermionic and bosonic systems and discuss the quantum description of light-matter interactions. In particular, we focus on the dipole gauge representation of the light-matter Hamiltonian and elucidate why a static mean-field approximation fails to capture any photon-induced effects in a large class of systems. Moreover, we introduce a minimal model of a ferroelectric material that plays an important role in the subsequent chapters and explore its mean-field phase diagram.

Next, we delve into the main part, where the three major projects of this thesis are presented. In Ch. 3, we introduce a collective theory for general matter Hamiltonians that couple linearly to a single cavity mode (also see [60]). Later, this helps us conceptualize an interesting setting for the DMFT formalism. The diagrammatic approach enables us to express the collective response of the total system in terms of the bare susceptibility for the matter part. Importantly, this formalism takes into account fluctuations beyond a static mean-field approximation, which often cannot capture light-induced effects on the equilibrium state of a solid [59, 60, 61].

Although the method is limited to one-mode models, it offers insights into the underlying mechanisms and allows us to identify some important factors that are required to influence a system through the vacuum fluctuations of the electromagnetic field. In particular, we find that even for strong collective coupling, the effect of the cavity mode vanishes in the thermodynamic limit (i.e., for $N \to \infty$) if the single-particle coupling is finite. Consequently, it is not possible to influence a macroscopic solid with only one electromagnetic mode. Moreover, we see that the cavity corrections for finite systems can be attributed to nonlinearities of the matter response, which is in accordance with the observations in Ref. [6] for the cavity-enhanced ferroelectricity.

We apply the theory to a simple model of a material with static dipole-dipole interactions. In the thermodynamic limit, the material may undergo a paraelectric-to-ferroelectric phase transition. Moreover, similar to the perovskite $SrTiO_3$ (STO), it exhibits a quantum-paraelectric state, where ferroelectricity is suppressed even at low temperatures due to quantum fluctuations. We focus on the paraelectric and quantum-paraelectric regime, and consider small clusters of material. Calculations of the leading-order cavity correction show that the static susceptibility is enhanced due to the light-matter interaction. Moreover, a phenomenological comparison to STO suggests that measurable effects can only be observed in small systems with large single-particle light-matter coupling, i.e., small cavity volumes.

DMFT, in contrast, is most appropriate for extended solids consisting of a macroscopic number of atoms or molecules. In the following chapters, we therefore consider a setting, where a non-trivial effect of the vacuum fluctuations of light can be expected even for a macroscopic material. According to the collective theory, this is not possible in a simple single-mode model with linear light-matter interaction. However, if multiple electromag-

netic modes couple to the matter degrees of freedom, a non-vanishing combined effect may emerge.

An example of a system supporting a continuum of electromagnetic modes is a simple dielectric-metal interface. In this setting, the surface plasmons of the metal hybridize with the free radiation field, forming surface plasmon polaritons (SPPs). The SPP dispersion and the spatial structure of the corresponding modes is strongly modified as compared to free space. This has two important consequences: First, the electromagnetic field is strongly confined to the interface, which leads to an enhancement of the light-matter interaction. And second, the light-matter coupling strength can be tuned by adjusting the distance from the interface. Therefore, we consider a hetero-structure in which a two-dimensional (2D) layer of material is positioned near a dielectric-metal interface. The 2D solid is embedded in the dielectric region and couples to the SPP mode supported by the interface.

We use this setting for two types of materials. In Ch. 4, we study a 2D solid with a ferroelectric phase transition (also see [61]). The matter Hamiltonian is similar to the one discussed in the previous chapter. The light-matter interaction is represented as a dipolar coupling to the SPP mode. This linear coupling gives rise to an effective photon-mediated dipole-dipole interaction. Due to its highly non-local nature, it cannot be directly incorporated in a standard DMFT formalism. To address this challenge, we map the system to an auxiliary spin-boson model that only contains local interactions. This approach enables us to solve the problem using bosonic DMFT (B-DMFT).

We find that the coupling to the SPP mode enhances the static electric susceptibility in the paraelectric regime and increases the order parameter in the ferroelectric phase. Both effects are most pronounced near the phase transition and lead to a stabilization of the ferroelectric phase. Even though our microscopic model differs from previous work, our results are in accordance with those presented in Ref. [6] and [58].

In Ch. 5, we extend our investigation to a 2D single-band Hubbard model to analyze the effect of the SPP mode on the Mott metal-insulator transition. The Hubbard model does not contain any dipolar transitions but features mobile electrons that can move between neighboring lattice sites. Therefore, the light-matter interaction is not described by a linear dipolar coupling. Instead, it is introduced via a Peierls substitution, which couples the photonic degrees of freedom to current-type operators. Consequently, a mapping to a bosonic auxiliary problem, as utilized in the previous chapter, is not possible. Instead, we follow a diagrammatic approach similar to the GW+DMFT formalism [7] and incorporate the coupling to the SPP mode as an additional non-local self-energy contribution.

Our results suggest that the light-matter interaction favors the metallic state. Partly, this can be attributed to a renormalization of the hopping matrix elements due to the second-order contribution of the light-matter interaction. However, our calculations thus far only include a limited number of diagrams and do not yet incorporate the feedback of the matter degrees of freedom on the SPP mode. Thus, we briefly discuss at the end of Ch. 5 how the formalism can be further refined.

We conclude the thesis in Ch. 6 with a few final remarks and possible future prospects.

2. Preliminaries

2.1. Dynamical mean-field theory for fermions

Dynamical mean-field theory (DMFT) is an important approximation scheme in condensed matter physics that is applicable to a wide range of quantum many-body problems. Originally developed for fermionic systems between 1989 and 1992 [68, 70, 27, 43], it has since become one of the most powerful and versatile techniques to study systems with strongly correlated electrons. The key idea of DMFT is to map a lattice model to an effective impurity problem. Assuming that the self-energy is purely local, the parameters of this impurity model can be related to the local lattice quantities by a set of self-consistent equations. In general, this is just an approximation, but it becomes exact if the coordination number of the lattice approaches infinity [68, 70]. Similar to a conventional mean-field approach, the DMFT approximation neglects all spatial fluctuations. However, temporal fluctuations are fully taken into account [29].

2.1.1. The Hubbard Hamiltonian

In the following, we illustrate the DMFT formalism for the Hubbard model. Despite its simplicity, the Hubbard Hamiltonian correctly reproduces many effects originating from strong electronic correlations. It was first proposed in the early 1960s as a model for transition metal oxides [32, 45, 36, 37], but has been applied to a multitude of other systems such as heavy fermions [13, 74] or high-temperature superconductors [89] in the subsequent years.

The single-band Hubbard Hamiltonian reads as

$$\hat{H} = -t \sum_{\langle ij \rangle \sigma} \left(\hat{c}^\dagger_{i\sigma} \hat{c}_{j\sigma} + \text{H.c.} \right) + U \sum_j \hat{n}_{j\uparrow} \hat{n}_{j\downarrow} - \mu \hat{N}, \tag{2.1}$$

where $\langle ... \rangle$ indicates a summation over nearest-neighbor pairs, the operator $\hat{c}_{i\sigma}$ ($\hat{c}^\dagger_{i\sigma}$) annihilates (creates) an electron of spin σ at site i, $\hat{n}_{i\sigma} = \hat{c}^\dagger_{i\sigma} \hat{c}_{i\sigma}$ corresponds to the number density of electrons with spin σ, and $\hat{N} = \sum_{i\sigma} \hat{n}_{i\sigma}$ denotes the total electron number operator. The first term in (2.1) is a kinetic contribution and enables the electrons to hop between neighboring lattice sites. It can be diagonalized by a lattice Fourier transform, i.e.,

$$\hat{H}_{\text{hop}} = \sum_{\boldsymbol{k}} \epsilon_{\boldsymbol{k}} \hat{c}^\dagger_{\boldsymbol{k}\sigma} \hat{c}_{\boldsymbol{k}\sigma}, \tag{2.2}$$

where the electronic dispersion $\epsilon_{\boldsymbol{k}}$ depends on the geometry of the system. The second term constitutes a local repulsive interaction between electrons at the same site. It may

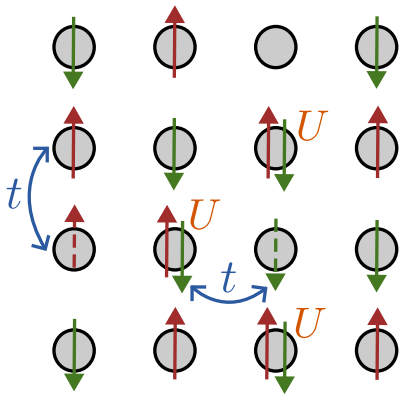

Figure 2.1.: *Illustration of the single-band Hubbard model.*

be considered as a strongly screened Coulomb interaction. Due to the Pauli exclusion principle, a single site can only be occupied by electrons in different states; therefore, the interaction only acts on electrons of opposite spin. In addition, there is a chemical potential term that allows us to fix the number of particles. A graphical representation of the Hubbard Hamiltonian is shown in Fig. 2.1.

Henceforth, we work at half filling, which means $\mu = U/2$. In this case, the Hubbard model may undergo a phase transition that is driven by the interaction U. At $U = 0$, the system is metallic since there is a single band and only half of its states are occupied. However, if U exceeds a critical value, the system becomes a so-called Mott insulator. This can be explained as follows: at low U, the kinetic term dominates, and the electrons are free to move around the lattice. For that purpose, two electrons have to occupy the same site at least temporarily. However, as U is increased the cost in energy for doubly occupied sites becomes so large that the motion of the electrons is frozen; as a result, the system becomes insulating. While normal band theory fails to predict this behavior, DMFT captures the Mott insulating phase of the Hubbard model [28].

2.1.2. The impurity model

As mentioned above, the key idea of DMFT is to map a lattice model to an effective impurity problem. For the Hubbard Hamiltonian, the impurity model can be described by an imaginary-time action of the form

$$S_{\mathrm{imp}} = -\int_0^\beta d\tau \int_0^\beta d\tau' \sum_\sigma \bar{c}_\sigma(\tau)\mathcal{G}_\sigma^{-1}(\tau,\tau')c_\sigma(\tau') + U\int_0^\beta d\tau n_\uparrow(\tau)n_\downarrow(\tau), \tag{2.3}$$

where β denotes the inverse temperature, $\bar{c}_\sigma$ and c_σ are fermionic fields, and n_σ corresponds to the number density of electrons with spin σ. There are several ways to derive this expression. A common approach is the so-called cavity method, where all sites but

one are formally integrated out from the full lattice action. The action (2.3) then results from a cumulant expansion up to second order [29]. As illustrated in Fig. 2.2, the interaction with all other sites of the lattice is included in the effective "non-interacting" Green's function $\mathcal{G}_\sigma$ for the impurity, which is also referred to as the Weiss field. It is important to note that the Weiss field depends on the imaginary-time difference $\tau - \tau'$, and thus, is retarded. This accounts for the fact that an electron may hop from the impurity to another site at time τ, move around the lattice, and return to the impurity site at some later time τ', or vice versa. For some applications, it is more convenient to write the Weiss field in terms of the hybridization function Δ. The latter only describes the dynamics of the electrons hopping in and out of the impurity, whereas the Weiss field also incorporates the local dynamics. In Matsubara representation, the two quantities are related by the following equation:

$$\mathcal{G}_\sigma^{-1}(i\omega_n) = i\omega_n + \mu - \Delta_\sigma(i\omega_n). \tag{2.4}$$

The Green's function on the impurity is defined as

$$G_\sigma^{\mathrm{imp}}(\tau) = -\langle c(\tau)\bar{c}(0)\rangle_{S_{\mathrm{imp}}}, \tag{2.5}$$

where $\langle ...\rangle_{S_{\mathrm{imp}}} = \mathcal{Z}^{-1}\int \mathcal{D}[\bar{c}, c](e^{-S_{\mathrm{imp}}}...)$ with the partition function $\mathcal{Z} = \int \mathcal{D}[\bar{c}, c]e^{-S_{\mathrm{imp}}}$ indicates that the expectation value is evaluated using the impurity action (2.3). With this, one can define an impurity Dyson equation

$$\Sigma_{\mathrm{imp}}(i\omega_n) = \mathcal{G}_\sigma^{-1}(i\omega_n) - {G_\sigma^{\mathrm{imp}}}^{-1}(i\omega_n) \tag{2.6}$$

with a local self-energy Σ_{imp}. However, the Weiss field $\mathcal{G}_\sigma$ is still unknown. In the next step, we relate the impurity Green's function and the self-energy to the corresponding lattice quantities, which enables us to determine $\mathcal{G}_\sigma$ self-consistently.

Before we move on, however, it should be mentioned that even for given $\mathcal{G}_\sigma$, solving the impurity problem is a highly non-trivial task. There are various ways to achieve this. A very simple approximation only valid in some regimes is iterated perturbation theory (IPT) [27, 29]. Other diagrammatic approaches include the non- or one-crossing approximation (NCA/OCA) [20]. Furthermore, it is possible to solve the impurity problem using the continuous-time Quantum Monte-Carlo method (CT-QMC) [87, 31] or exact diagonalization [29].

2.1.3. The self-consistent equations

To fix the Weiss field, we need to define additional relations between the quantities on the impurity and the corresponding lattice quantities. The impurity model and the lattice model are considered to be consistent if

$$G_\sigma^{\mathrm{imp}} = G_\sigma^{\mathrm{loc}}, \tag{2.7}$$

i.e., if the Green's function on the impurity is equal to the local lattice Green's function. Moreover, the self-energy for the lattice $\Sigma_{\boldsymbol{k}}$ is replaced by the $\boldsymbol{k}$-independent (local) impurity self-energy, that is,

$$\Sigma_{\boldsymbol{k}} = \Sigma_{\mathrm{imp}}. \tag{2.8}$$

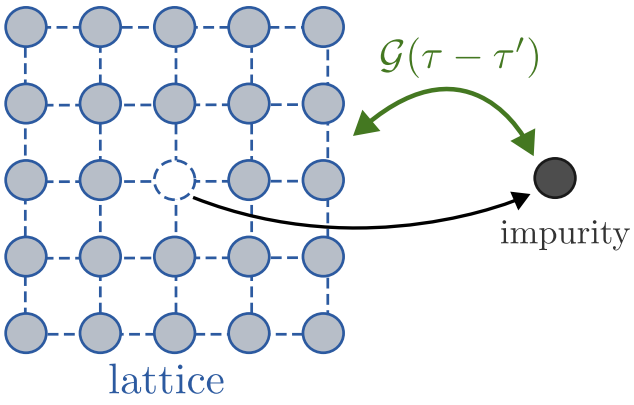

Figure 2.2.: *In the effective impurity model, the interaction with the rest of the lattice is included in the retarded Weiss field* $\mathcal{G}(\tau, \tau')$.

This is the central approximation of DMFT, and in fact it can be shown that this assumption becomes exact for systems with infinite coordination number [68, 70]. With this, the lattice Green's function is given by

$$G_{\sigma \boldsymbol{k}}(i\omega_n) = \frac{1}{i\omega_n + \mu - \epsilon_{\boldsymbol{k}} - \Sigma_{\mathrm{imp}}}, \tag{2.9}$$

(where $\Sigma_{\boldsymbol{k}}$ has already been replaced by Σ_{imp}) and thus,

$$G^{\mathrm{loc}}_{\sigma}(i\omega_n) = \frac{1}{N}\sum_{\boldsymbol{k}} G_{\sigma \boldsymbol{k}}(i\omega_n) = \frac{1}{N}\sum_{\boldsymbol{k}} \frac{1}{i\omega_n + \mu - \epsilon_{\boldsymbol{k}} - \Sigma_{\mathrm{imp}}}. \tag{2.10}$$

Together, Eq. (2.5), (2.6), (2.7) and (2.10) form a closed set of self-consistent equations, which can be solved in an iterative procedure. A possible realization of the algorithm is illustrated in Fig. 2.3. It consists of the following steps:

1. Start from an initial guess for the impurity self-energy Σ_{imp}.
2. Calculate the local Green's function $G^{\mathrm{loc}}_{\sigma}$ using Eq. (2.10).
3. Use the self-consistency condition (2.7) to determine the Weiss field $\mathcal{G}_{\sigma}$ from Eq. (2.6), and pass it to the impurity solver.
4. Solve the impurity problem to obtain a new impurity Green's function $G^{\mathrm{imp}}_{\sigma}$ and a new self-energy Σ_{imp}. (The latter can be calculated from Eq. (2.6)).
5. Compare the new outcomes to the previous values. If they coincide, the iteration is finished. Otherwise, repeat the procedure starting from step 2 until convergence is reached.

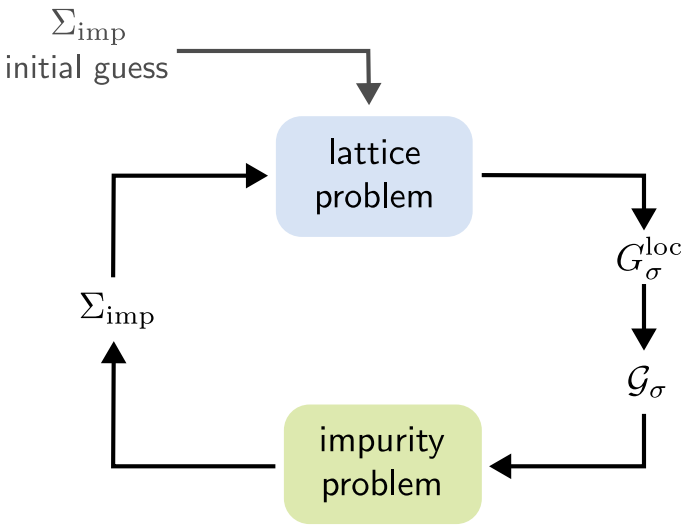

Figure 2.3.: *Illustration of the DMFT loop for the Hubbard model.*

2.1.4. DMFT formalism on the Keldysh contour

In the previous subsections, we introduced DMFT using the imaginary-time path integral formalism. The self-consistent equations were presented in $\boldsymbol{k}$-space and Matsubara representation. This approach offers the advantage that the Green's function, the Weiss field and the self-energy are diagonal in imaginary frequency. As a result, the self-consistent DMFT equations take a particularly simple form.

However, the DMFT approach can also be extended to the Keldysh contour, which includes both imaginary and real times. With this, the formalism becomes applicable to systems out of equilibrium [5]. But even in thermal equilibrium, it can be desirable to determine results on the real-time axis since they provide direct access to real-frequency spectra using a standard Fourier transform. In Matsubara representation, this requires an analytic continuation, e.g., using a Padé approxiamtion [10] or the maximum entropy method [84], which is computationally more challenging and more prone to errors.

On the other hand, the main disadvantage of non-equilibrium DMFT is that the self-consistent equations must be solved in the time domain, where the two-time correlation functions are not diagonal. Consequently, simple multiplications in frequency space turn into convolutions on the Keldysh contour, and the procedure becomes computationally more expensive. However, thanks to causality, the resulting self-consistent equations may be reduced to Volterra integral equations, which can be solved numerically using an efficient time-stepping procedure [80].

In the Keldysh formalism, the impurity action for the Hubbard model reads as

$$S_{\mathrm{imp}} = \int_{\mathcal{C}} dt dt' \sum_\sigma \bar{c}_\sigma(t) \mathcal{G}_\sigma^{-1}(t,t') c_\sigma(t') - U \int_{\mathcal{C}} dt\, n_\uparrow(t) n_\downarrow(t), \tag{2.11}$$

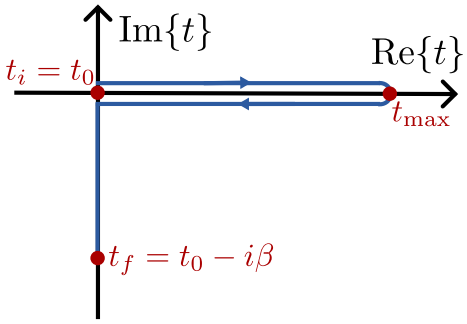

Figure 2.4.: *Graphical representation of the Keldysh contour in the complex-time plane. It consists of a forward and a backward branch on the real-time axis, as well as an imaginary (Matsubara) branch.*

where $\mathcal{C}$ denotes the full Keldysh contour with its imaginary and real time branches (see Fig. 2.4). In this representation, the Matsubara component $C^{\mathrm{M}}(\tau)$ of an arbitrary two-time correlation function $C(t,t')$ is equivalent to $-iC(-i\tau,0)$, and the path integral $\langle ... \rangle_{S_{\mathrm{imp}}} = \mathcal{Z}^{-1} \int \mathcal{D}[\bar{c},c](e^{iS_{\mathrm{imp}}}...)$ with the partition function $\mathcal{Z} = \int \mathcal{D}[\bar{c},c]e^{iS_{\mathrm{imp}}}$ corresponds to a contour-ordered expectation value. Again, the Weiss field can be written in terms of a hybridization function Δ. In the time domain, the two quantities are related by the equation

$$\mathcal{G}_\sigma^{-1}(t,t') = (i\partial_t + \mu)\delta_{\mathcal{C}}(t,t') - \Delta_\sigma(t,t'). \tag{2.12}$$

The impurity Green's function is defined as

$$G_\sigma^{\mathrm{imp}} = -i\langle c_\sigma(t)\bar{c}_\sigma(t')\rangle_{S_{\mathrm{imp}}}, \tag{2.13}$$

and enters the impurity Dyson equation

$$\mathcal{G}_\sigma + G_\sigma^{\mathrm{imp}} * \Sigma_{\mathrm{imp}} * \mathcal{G}_\sigma = G_\sigma^{\mathrm{imp}}, \tag{2.14}$$

where the operator $*$ indicates a convolution in the time domain.

In DMFT, the lattice self-energy is approximated by the local impurity self-energy Σ_{imp}, such that the lattice Dyson equation reads as

$$[(i\partial_t + \mu - \epsilon_{\boldsymbol{k}})\mathbb{I} - \Sigma_{\mathrm{imp}}] * G_{\boldsymbol{k}\sigma} = \mathbb{I}. \tag{2.15}$$

In this notation, the identity matrix $\mathbb{I}$ refers to a δ-function $\delta_{\mathcal{C}}(t,t')$ on the time contour. The local Green's function can be calculated from the lattice Green's function $G_{\boldsymbol{k}}(t,t')$ by the sum

$$G_\sigma^{\mathrm{loc}}(t,t') = \frac{1}{N}\sum_{\boldsymbol{k}} G_{\boldsymbol{k}\sigma}(t,t'). \tag{2.16}$$

As in standard DMFT, it is assumed that $G_\sigma^{\mathrm{loc}}(t,t')$ can be identified with the Green's function $G_\sigma^{\mathrm{imp}}(t,t')$ on the impurity. The formulas above constitute a set of self-consistent equations and can be solved by the same iterative procedure as illustrated in Fig. 2.3 and described in Sec. 2.1.3. However, solving the impurity and the lattice Dyson equation (2.14) and (2.15) requires more computational effort, as they include convolutions instead of simple multiplications. An efficient algorithm for this purpose is implemented, e.g., in the open-source software package NESSi (Non-Equilibrium Systems Simulation Library) [80].

However, it should be mentioned that there is more than one way to formulate the self-consistency. For instance, it is possible to eliminate the Weiss field and express the self-consistent equations only in terms of the hybridization function. In this case, the impurity Dyson equation (2.14) is replaced by the relation

$$\Delta_\sigma + G_\sigma^{(1)} * \Delta_\sigma = G_\sigma^{(2)}, \tag{2.17}$$

where

$$G_\sigma^{(1)}(t,t') = \frac{1}{N}\sum_{\boldsymbol{k}} \epsilon_{\boldsymbol{k}} G_{\boldsymbol{k}\sigma}(t,t') \tag{2.18}$$

$$G_\sigma^{(2)}(t,t') = \frac{1}{N}\sum_{\boldsymbol{k}} [\epsilon_{\boldsymbol{k}} + \epsilon_{\boldsymbol{k}} G_{\boldsymbol{k}\sigma}(t,t')\epsilon_{\boldsymbol{k}}]. \tag{2.19}$$

Just like the Dyson equation, Eq. (2.17) is a Volterra integral equation and can be solved for Δ_σ using the same techniques. The DMFT loop shown in Fig. 2.3 is modified as depicted in Fig. 2.5. The algorithm can be summarized as follows:

1. Start from an initial guess for the self-energy Σ_{imp}.
2. Solve the lattice Dyson equation (2.15) for $G_{\boldsymbol{k}\sigma}$ and calculate $G_\sigma^{(1)}$ and $G_\sigma^{(2)}$ defined in (2.18) and (2.19).
3. Determine the hybridization function Δ_σ using Eq. (2.17) .
4. Solve the impurity problem and obtain the new impurity self-energy Σ_{imp}.
5. Repeat the procedure with the new self-energy starting from the second step until convergence is reached.

Which formulation of the self-consistency scheme is most appropriate, has to be determined on a case-by-case basis. For instance, the second approach can be more convenient if the impurity solver does not take the Weiss field but the hybridization function as an input. Moreover, for some systems, the numerical solution of the impurity Dyson equation may be unstable or give rise to artifacts that are not present if the self-consistent equations are rewritten in terms of the hybridization function. This behavior can even be sensitive to seemingly small details, such as the lattice geometry.

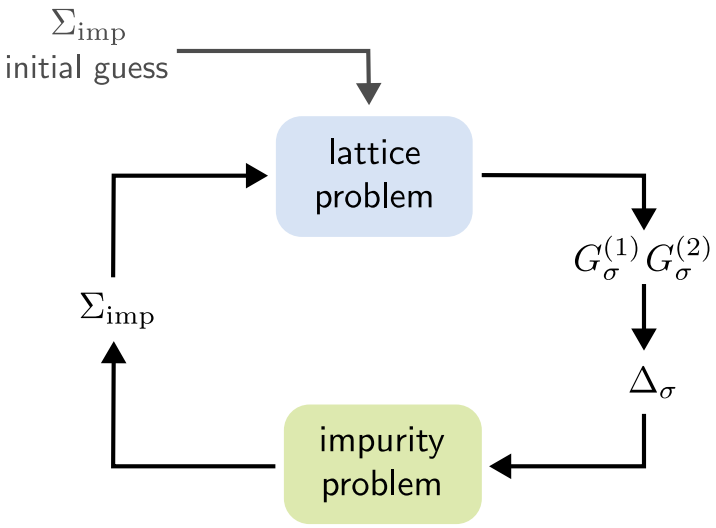

Figure 2.5.: *Alternative to the standard DMFT loop shown in Fig. 2.3, where the self-consistent equation for the Weiss field $\mathcal{G}_\sigma$ is replaced by a relation for the hybridization function Δ_σ.*

2.2. Dynamical mean-field theory for bosons

As mentioned previously, DMFT was originally developed for fermionic lattice models and offers a computationally tractable method for analyzing systems with strongly correlated electrons that becomes exact in the limit of infinite coordination numbers. However, in the subsequent years, the formalism has been extended to bosonic degrees of freedom, opening new avenues for the study of bosonic quantum many-body systems with strong correlations. The core concept of bosonic DMFT (B-DMFT) remains analogous to its fermionic counterpart: a lattice problem is mapped to an auxiliary impurity model coupled to a self-consistently determined environment, under the assumption of a purely local self-energy. However, there are some challenges specific to bosonic many-body systems. This is due to the fact that bosons are not subject to the Pauli exclusion principle and thus may form a condensate. In particular, contributions from normal and condensed particles behave differently in the limit of infinite coordination numbers. Consequently, the derivation of the DMFT equations for fermions cannot be directly translated to the bosonic version. First attempts to address these challenges by introducing a different scaling of the hopping amplitude for normal and condensed bosons [12, 35] failed to reproduce the non-interacting limit, where DMFT should be exact [4]. However, soon after, Anders et al. successfully derived a B-DMFT formalism for the Bose-Hubbard model that yields consistent results [3].

2.2.1. The Bose-Hubbard model

In the folowing, we review the main ideas of B-DMFT for the Bose-Hubbard model, which was the first system studied in this context. It is described by the Hamiltonian

$$\hat{H} = -t \sum_{\langle i,j \rangle} \hat{b}_i^\dagger \hat{b}_j + \frac{U}{2} \sum_i \hat{n}_i(\hat{n}_i - 1) - \mu \sum_i \hat{n}_i, \tag{2.20}$$

where $\langle ... \rangle$ indicates the sum over nearest neighbor pairs, $\hat{b}_i^\dagger$ and $\hat{b}_j$ are bosonic creation and annihilation operators, and $\hat{n}_i = \hat{b}_i^\dagger \hat{b}_i$ denotes the number operator for site i. Experimentally, the Bose-Hubbard model has been realized using ultra-cold atoms in an optical lattice [33, 34, 40, 39].

In thermal equilibrium, the system may exhibit three different phases: a normal phase at high temperature, a superfluid phase at low temperature, and a Mott-insulating phase at zero temperature [3]. The latter only exists for $U \gg zt$, where z denotes the coordination number of the lattice. If the hopping dominates, there is a quantum phase transition to the superfluid phase. The Mott-insulating phase is characterized by an integer number of particles per site, a gapped excitation spectrum, and a vanishing compressibility [4]. The superfluid phase breaks the global $U(1)$-symmetry of the system and is indicated by a non-zero expectation value of the bosonic operators [38]. For the two-dimensional and three-dimensional cubic lattice, all of these phases are reproduced within B-DMFT. In particular for the three-dimensional case, the results are in remarkably good agreement with lattice QMC calculations [3].

2.2.2. The impurity model

Even though the Hamiltonian (2.20) shares the same structure as the fermionic Hubbard model, it cannot be mapped to the same impurity problem. This is due to the fact that, unlike fermions, bosonic particles may form a condensate. An impurity action accommodating this behavior has been derived in [3], and reads as

$$\begin{aligned} S_{\text{imp}} = &\int_0^\beta d\tau\, \bar{b}(\tau)(\partial_\tau - \mu) b(\tau) + \frac{U}{2} \int_0^\beta d\tau n(\tau)(n(\tau) - 1) \\ &- \frac{1}{2} \int_0^\beta d\tau \int_0^\beta d\tau' \boldsymbol{b}^\dagger(\tau) \boldsymbol{\Delta}(\tau - \tau') \boldsymbol{b}(\tau') - \boldsymbol{h}^\dagger \int_0^\beta d\tau\, \boldsymbol{b}(\tau) \end{aligned} \tag{2.21}$$

with the complex fields $b(\tau)$ and $\bar{b}(\tau)$, and the spinor $\boldsymbol{b}^\dagger = (\bar{b}, b)^T$. The two effective fields $\boldsymbol{\Delta}(\tau)$ and $\boldsymbol{h}^\dagger$ include the interaction between the impurity site and the lattice and have to be determined self-consistently. Their meaning is illustrated in Fig. 2.21. As shown in the graphic, the hybridization function $\boldsymbol{\Delta}(\tau)$ describes the coupling of the impurity site to the normal ("non-condensed") bosons, while the static field $\boldsymbol{h}^\dagger$ accounts for the interaction of the impurity site with the condensed particles on the surrounding lattice.

Analogous to the fermionic case, we can introduce a Weiss field $\boldsymbol{\mathcal{G}}(\tau)$, which is related to the hybridization function by the equation

$$\boldsymbol{\Delta}(i\nu_n) = -i\nu_n \boldsymbol{\tau}_z - \mu \mathbb{I} + \boldsymbol{\mathcal{G}}^{-1}(i\nu_n), \tag{2.22}$$

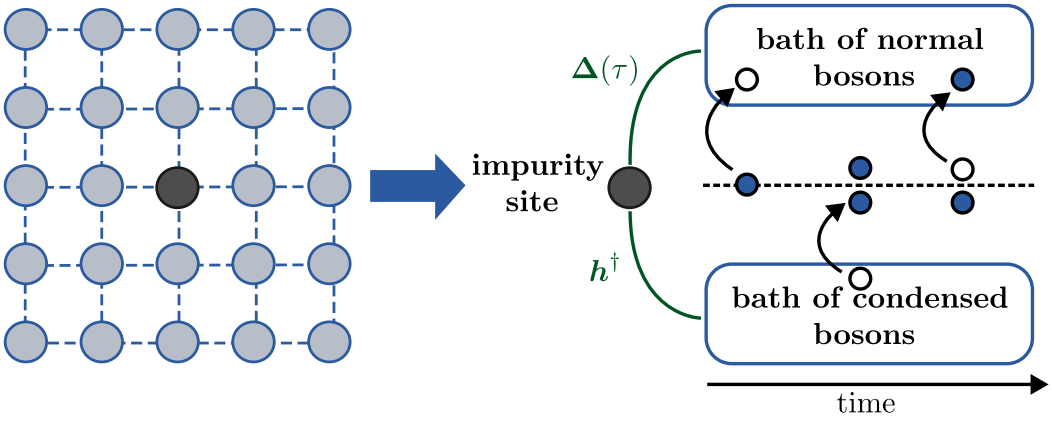

Figure 2.6.: *Illustration of the B-DMFT approximation for the Bose-Hubbard model. The full lattice problem is mapped to a single-site impurity model that couples to a bath of normal and condensed bosons. Particles can hop between these two reservoirs and the impurity site, leading to a change in the integer occupation. The coupling to the bath of normal bosons is described by the hybridization function* $\boldsymbol{\Delta}(\tau)$*, while transitions from and to the bath of condensed bosons are contained in the effective field* $\boldsymbol{h}^\dagger$*. [Graphic reproduced from [4].]*

where $\boldsymbol{\tau}_z$ denotes the z-component of the vector of Pauli matrices. However, both $\boldsymbol{\Delta}(\tau)$ and $\boldsymbol{\mathcal{G}}(\tau)$ are 2×2-matrices. The off-diagonal elements correspond to anomalous terms describing the annihilation or creation of two particles. These contributions vanish in the normal phase. The local self-energy is defined by the impurity Dyson equation

$$\begin{aligned} \boldsymbol{\Sigma}_{\mathrm{imp}}(i\nu_n) =& \boldsymbol{\mathcal{G}}^{-1}(i\nu_n) - \boldsymbol{G}_{\mathrm{con}}^{\mathrm{imp}\,-1}(i\nu_n) \\ =& i\nu_n \boldsymbol{\tau}_z + \mu\mathbb{I} + \boldsymbol{\Delta}(i\nu_n) - \boldsymbol{G}_{\mathrm{con}}^{\mathrm{imp}\,-1}(i\nu_n), \end{aligned} \tag{2.23}$$

where $\boldsymbol{G}_{\mathrm{con}}^{\mathrm{imp}}$ denotes the connected Green's function of the impurity. Introducing the order parameter

$$\boldsymbol{\Phi} = \langle \boldsymbol{b}(\tau) \rangle_{S_{\mathrm{imp}}}, \tag{2.24}$$

it is given by

$$\boldsymbol{G}_{\mathrm{con}}^{\mathrm{imp}} = -\langle \boldsymbol{b}(\tau) \boldsymbol{b}^\dagger(0) \rangle_{S_{\mathrm{imp}}} + \boldsymbol{\Phi}\boldsymbol{\Phi}^\dagger. \tag{2.25}$$

The static field $\boldsymbol{h}^\dagger$ can be calculated from the hybridization function and the order parameter and reads as

$$\boldsymbol{h}^\dagger = [zt - \Delta_{11}(i\nu_n = 0) - \Delta_{12}(i\nu_n = 0)]\boldsymbol{\Phi}^\dagger. \tag{2.26}$$

It is specific to the bosonic formalism, and does not have an analogue in fermionic DMFT.

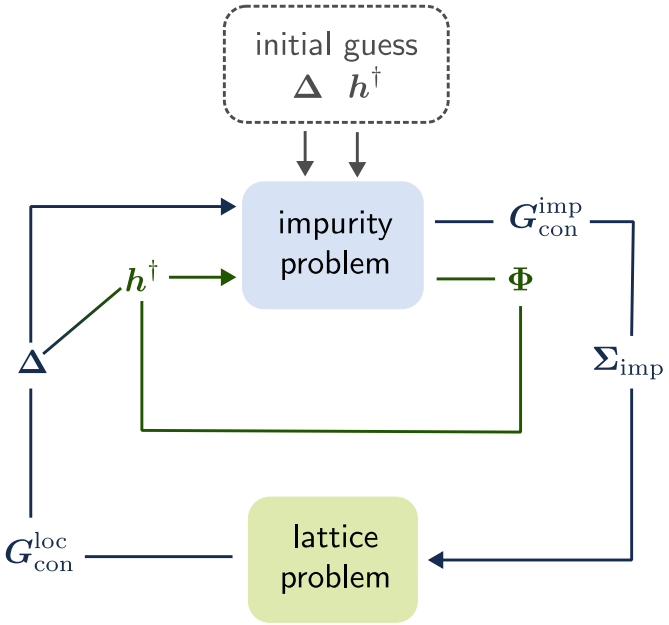

Figure 2.7.: *Graphical illustration of the B-DMFT algorithm for the Bose-Hubbard model.*

2.2.3. The self-consistent equations

To establish a direct relation between the impurity action (2.21) and the lattice model, we equate the impurity Green's function with the local lattice Green's function, i.e.,

$$\boldsymbol{G}_{\mathrm{con}}^{\mathrm{imp}} = \boldsymbol{G}_{\mathrm{con}}^{\mathrm{loc}}. \tag{2.27}$$

Moreover, we replace the $\boldsymbol{k}$-dependent self-energy by the local impurity self-energy Σ_{imp}, so that the local lattice Green's function is given by

$$\boldsymbol{G}_{\mathrm{con}}^{\mathrm{loc}} = \frac{1}{N}\sum_{\boldsymbol{k}} \left[i\nu_n \boldsymbol{\tau}_z + (\mu - \epsilon_{\boldsymbol{k}})\mathbb{I} - \boldsymbol{\Sigma}_{\mathrm{imp}}\right]^{-1}. \tag{2.28}$$

These conditions are analogous to fermionic DMFT. In addition, we assume that the order parameter $\boldsymbol{\Phi}$ computed from the impurity action matches the one for the lattice model.

In summary, we have a closed set of self-consistent equations, consisting of Eq. (2.23) to (2.28). The solution can be determined through an iterative procedure, illustrated in Fig. 2.7. The algorithm involves the following steps:

1. Start from an initial guess for the effective fields $\boldsymbol{\Delta}(\tau)$ and $\boldsymbol{h}^{\dagger}$.
2. Determine the connected impurity Green's function $\boldsymbol{G}_{\mathrm{con}}^{\mathrm{imp}}$ and the order parameter $\boldsymbol{\Phi}$ from the impurity action (2.21).
3. Calculate the impurity self-energy using the Dyson equation (2.23).
4. Obtain the local lattice Green's function from Eq. (2.28).
5. Compute a new hybridization function $\boldsymbol{\Delta}(\tau)$ using the self-consistency condition (2.27) and Eq. (2.23).
6. Use equation (2.26) to update the static field $\boldsymbol{h}^{\dagger}$.
7. Repeat this procedure from the second step until convergence is reached.

This brief overview reveals that the B-DMFT formalism for the Bose-Hubbard model and the DMFT method for the fermionic Hubbard Hamiltonian share many similarities. However, there are some key distinctions specific to B-DMFT: (i) the impurity model contains an additional static field $\boldsymbol{h}^{\dagger}$ that is determined self-consistently from the condensate order parameter and the hybridization function; (ii) the hybridization function also contains anomalous terms; and (iii) the self-consistent equations are formulated in terms of connected correlation functions. Furthermore, it should be mentioned that the B-DMFT approach developed in [3] is not restricted to complex bosonic variables. In Ref. [1] it was adapted to real bosonic fields to investigate a scalar φ^4 quantum field theory.

2.3. Quantum light-matter interactions

In this thesis, the interaction between light and matter is treated on the quantum level. This is particularly important since we consider systems in thermal equilibrium, where the average photon number is usually equal to zero. Consequently, the classical electromagnetic radiation field vanishes and does not affect the matter degrees of freedom. However, this classical description does not include quantum fluctuations, which are even present if the electromagnetic field is in a vacuum state.

The following subsections give a brief introduction to quantum light-matter interactions. We start from the description of the free electromagnetic field in Sec. 2.3.1. Then we turn to the interaction between light and matter in Sec. 2.3.2. We specifically focus on the formulation in dipole gauge, which is particularly well suited for the systems studied in this thesis. In Sec. 2.3.3, we conclude this chapter with a short discussion of the static mean-field approximation for a general Hamiltonian with dipolar light-matter coupling. We will see that fluctuations beyond mean-field must be taken into account in order to capture photon-induced effects on the equilibrium state of the system.

2.3.1. Quantum description of the free radiation field in polarizable media

In free space, the fundamental quantities of classical electrodynamics are the electric field $\boldsymbol{E}$ and the magnetic field $\boldsymbol{B}$. They satisfy Maxwell's equations, which, together with the Lorentz force law, provide a full mathematical description of the theory of electricity, magnetism, and classical optics. In this formalism, the electric field $\boldsymbol{E}$ contains both the electrostatic field created by the charge density ρ (Gauss's law), and the field induced by a temporal change in the magnetic field $\boldsymbol{B}$ (Faraday's law). These two contributions can be separated by splitting the electric field $\boldsymbol{E}$ into a longitudinal component $\boldsymbol{E}_\parallel$ with $\nabla \times \boldsymbol{E}_\parallel = 0$, and a transverse part $\boldsymbol{E}_\perp$ that is defined by the relation $\nabla \cdot \boldsymbol{E}_\perp = 0$. In this description, $\boldsymbol{E}_\parallel$ can be identified with the instantaneous field generated by the charge density ρ, while $\boldsymbol{E}_\perp$ corresponds to the free radiation field. In most cases, the transverse part is quantized, whereas the electric field energy corresponding to the longitudinal contribution $\boldsymbol{E}_\parallel$ can be rewritten as an instantaneous Coulomb interaction between the charged particles (see, e.g., [14]), and may thus be incorporated in the model for the bare matter.

Alternatively, the classical theory of electromagnetism can be formulated in terms of a vector potential $\boldsymbol{A}$ and a scalar potential ψ, where $\boldsymbol{E} = -\nabla\psi - \partial_t \boldsymbol{A}$ and $\boldsymbol{B} = \nabla \times \boldsymbol{A}$. However, this representation is not unambiguous, since the electric and magnetic field are invariant under a gauge transformation of the form $\boldsymbol{A} \to \boldsymbol{A} + \nabla f$ and $\psi \to \psi - \partial_t f$, where f denotes an arbitrary twice continuously differentiable function of position and time. A common way to fix $\boldsymbol{A}$ is the so-called Coulomb or radiation gauge, which is defined by the relation $\nabla \cdot \boldsymbol{A} = 0$. With this, the vector potential is purely transverse and therefore only enters $\boldsymbol{E}_\perp = -\partial_t \boldsymbol{A}$. On the other hand, ψ only contributes to $\boldsymbol{E}_\parallel = -\nabla\psi$, since $\nabla \times \nabla \cdot \psi = 0$.

In a polarizable medium with permittivity $\varepsilon(\boldsymbol{r})$, the electric field $\boldsymbol{E}$ can be replaced by the electric displacement field $\boldsymbol{D} = \varepsilon_0 \varepsilon \boldsymbol{E}$. The latter already incorporates the polar-

ization density of the medium that is generated by the bound charges in the presence of an external electric field $\boldsymbol{E}$. With this, Gauss's law turns into $\nabla \cdot \boldsymbol{D} = \rho_\mathrm{f}$, where ρ_f corresponds to the free charges embedded in the medium. Analogous to $\boldsymbol{E}$, the displacement field can be split into a longitudinal component $\boldsymbol{D}_\parallel$, which is related to the field created by the free charge density ρ_f, and a transverse component $\boldsymbol{D}_\perp$ that is linked to the free radiation field. The Coulomb gauge condition can be generalized to $\nabla \cdot [\varepsilon(\boldsymbol{r})\boldsymbol{A}(\boldsymbol{r})] = 0$. If this is supplemented by the relation $\nabla \times [\varepsilon(\boldsymbol{r})\nabla\psi(\boldsymbol{r})] = 0$, the transverse displacement field can be expressed only in terms of $\boldsymbol{A}$, while the longitudinal component is purely given by ψ.

In the absence of free charges or currents, $\boldsymbol{D}_\parallel$ vanishes, so that (in the generalized Coulomb gauge) $\psi = 0$, and $\boldsymbol{D} = -\varepsilon_0\varepsilon\partial_t\boldsymbol{A}$. Moreover, $\boldsymbol{D}$ and $\boldsymbol{A}$ both satisfy a homogeneous wave equation, which can be derived from macroscopic Maxwell's equations. Based on this representation Glauber and Lewenstein developed a quantization procedure, where $\boldsymbol{D}$ and $\boldsymbol{A}$ play the role of two conjugate variables [30]. The corresponding quantum fields can be described in terms of bosonic operators $\hat{a}_{\boldsymbol{q}}$ and $\hat{a}^\dagger_{\boldsymbol{q}}$ that annihilate or create a photon in mode $\boldsymbol{q}$. The electric field operator and the vector potential can be expanded in these modes and read as

$$\hat{\boldsymbol{E}}(\boldsymbol{r}) = \sum_{\boldsymbol{q}} \sqrt{\frac{\omega_{\boldsymbol{q}}}{2\varepsilon_0\varepsilon(\boldsymbol{r})V}} \left[\boldsymbol{\phi}_{\boldsymbol{q}}(\boldsymbol{r})\hat{a}_{\boldsymbol{q}} + \mathrm{H.c.}\right] \tag{2.29}$$

and

$$\hat{\boldsymbol{A}}(\boldsymbol{r}) = \sum_{\boldsymbol{q}} \frac{i}{\sqrt{2\varepsilon_0\varepsilon(\boldsymbol{r})\omega_{\boldsymbol{q}}V}} \left[\boldsymbol{\phi}_{\boldsymbol{q}}(\boldsymbol{r})\hat{a}_{\boldsymbol{q}} - \mathrm{H.c.}\right], \tag{2.30}$$

where V denotes the volume of the system, $\omega_{\boldsymbol{q}}$ represents the dispersion relation of light and the mode functions $\boldsymbol{\phi}_{\boldsymbol{q}}(\boldsymbol{r})$ define the spatial structure and the polarization direction of the corresponding mode. The particular shape of $\boldsymbol{\phi}_{\boldsymbol{q}}(\boldsymbol{r})$ depends on the electromagnetic environment. In free space, for instance, the electromagnetic field can be expanded in plane waves, i.e., $\boldsymbol{\phi}(\boldsymbol{r}) \sim e^{i\boldsymbol{q}\cdot\boldsymbol{r}}$, where $\boldsymbol{q}$ denotes the wave vector that can take any continuous value. This changes if the electromagnetic environment is modified, e.g., by a waveguide or a cavity, or in the presence of a metal surface, where the boundary conditions impose a different spatial structure on the modes and restrict the wave vectors to certain values. In general, however, the mode functions must satisfy the generalized eigenvalue equation [30, 63]

$$\omega^2_{\boldsymbol{q}}\mu_0\varepsilon_0\varepsilon(\boldsymbol{r})\boldsymbol{\phi}_{\boldsymbol{q}}(\boldsymbol{r}) = \frac{1}{\sqrt{\varepsilon(\boldsymbol{r})}}\nabla \times \nabla \times \sqrt{\varepsilon(\boldsymbol{r})}\boldsymbol{\phi}_{\boldsymbol{q}}(\boldsymbol{r}) \tag{2.31}$$

and the normalization condition

$$\frac{1}{V}\int d^3r\, \bar{\boldsymbol{\phi}}_{\boldsymbol{q}}(\boldsymbol{r}) \cdot \boldsymbol{\phi}_{\boldsymbol{q}'}(\boldsymbol{r}) = \delta_{\boldsymbol{q},\boldsymbol{q}'}. \tag{2.32}$$

With this, the Hamiltonian for the free electromagnetic radiation field

$$\hat{H}_\mathrm{field} = \frac{1}{2}\int d^3r \left[\varepsilon_0\varepsilon(\boldsymbol{r})\hat{\boldsymbol{E}}(\boldsymbol{r})^2 + \frac{1}{\mu_0}(\nabla \times \hat{\boldsymbol{A}}(\boldsymbol{r}))^2\right] \tag{2.33}$$

can be written in a diagonal form

$$\hat{H}_{\text{field}} = \sum_{\boldsymbol{q}} \omega_{\boldsymbol{q}} \hat{a}^\dagger_{\boldsymbol{q}} \hat{a}_{\boldsymbol{q}}, \tag{2.34}$$

i.e., the quantum description of the free electromagnetic field is analogous to the one for a collection of non-interacting harmonic oscillators.

2.3.2. Light-matter Hamiltonian in dipole gauge

In the previous subsection, we have discussed the quantum description of the electromagnetic radiation field in the absence of (free) matter. Now we turn to combined light-matter systems, where charged particles and photons interact with each other. In general, there is no unambiguous way to express the coupling between light and matter. This is due to the fact that the electromagnetic field is invariant under a gauge transformation. In quantum physics, gauge transformations can be expressed in terms of a unitary operator $\hat{\mathcal{W}}$ that transforms the Hamiltonian as $\hat{\mathcal{W}}\hat{H}\hat{\mathcal{W}}^\dagger$. Similar to the classical case, two Hamiltonians related by a gauge transformation correspond to the same system and, thus, give rise to the same physical predictions. The only difference between the individual descriptions is that they correspond to a different separation of light and matter degrees of freedom (i.e., only the interpretation of the corresponding operators changes) [15, 63]. However, this mixing of light and matter becomes relevant if the Hilbert space of a system is truncated. In that case, the result depends on the gauge of the original Hamiltonian, and the resulting (projected) Hamiltonians are no longer gauge equivalent. As a result, they may lead to dramatically different physical predictions [63, 16]. This raises the question of which gauge should be chosen as a starting point in order to obtain the most accurate approximation.

A common way to include the coupling between light and matter in the Hamiltonian is minimal substitution. In this scheme, the momentum operator is shifted by the term $-q\hat{\boldsymbol{A}}$, where q denotes the electric charge of the respective particle. In a dielectric medium, the resulting Hamiltonian corresponds to the generalized Coulomb gauge that is characterized by the condition $\nabla \cdot [\varepsilon(\boldsymbol{r})\boldsymbol{A}(\boldsymbol{r})] = 0$. For a solid interacting with the electromagnetic field, this yields

$$\hat{H}^C = \hat{H}_{\text{el}} + \hat{H}_{\text{field}} \tag{2.35}$$

where $\hat{H}_{\text{field}}$ denotes the Hamiltonian of the free electromagnetic field, and the electronic part in second quantization reads as

$$\hat{H}_{\text{el}} = \int d^3r \sum_\sigma \hat{\Psi}^\dagger_\sigma(\boldsymbol{r}) \frac{(-i\nabla + e\hat{\boldsymbol{A}}(\boldsymbol{r}))^2}{2m} \hat{\Psi}_\sigma(\boldsymbol{r}) + \hat{H}_{\text{latt}} + \hat{H}_{\text{int}}. \tag{2.36}$$

Here e denotes the elementary charge, the field operators $\hat{\Psi}_\sigma(\boldsymbol{r})^\dagger$ ($\hat{\Psi}_\sigma(\boldsymbol{r})$) create (annihilate) an electron at position $\boldsymbol{r}$, $\hat{H}_{\text{latt}}$ is an arbitrary periodic lattice potential due to the atomic cores, and $\hat{H}_{\text{int}}$ represents the electrostatic Coulomb interaction between different electrons.

In this thesis, we focus on materials consisting of localized dipoles or tight-binding models, where the electrons are strongly bound to individual atoms. For these kinds of systems, it can be helpful to expand the electronic field operators in Wannier orbitals $w_{\boldsymbol{R}n}(\boldsymbol{r})$, which are strongly localized around the lattice site $\boldsymbol{R}$, i.e.,

$$\hat{\Psi}_\sigma(\boldsymbol{r}) = \sum_\alpha w_\alpha(\boldsymbol{r})\hat{c}_{\alpha\sigma}, \tag{2.37}$$

where the multiindex $\alpha = (\boldsymbol{R}, n)$ includes the atomic position $\boldsymbol{R}$ and the band index n, and $\hat{c}_{\alpha\sigma}$ represents the corresponding annihilation operator for an electron with spin σ. Up to this point, the Hamiltonian is still invariant under a gauge transformation. However, this changes if we perform a projection on a subset of bands n. This brings us back to the question of whether the Coulomb gauge Hamiltonian is the best choice for a truncation of the Hilbert space. In general, the answer depends on the system and the types of states that are considered. It has been shown for similar systems that the Coulomb gauge does not necessarily yield the most accurate results. Instead, for localized dipoles or tight-binding models, the dipole gauge Hamiltonian seems particularly well suited for a projection on a subset of matter states [16, 63].

The dipole gauge version of Hamiltonian (2.35) can be obtained by performing a multicenter Power-Zienau-Woolley transformation. Details of the derivation can be taken from Ref. [63]. Here, we only highlight the most important points. The transformation leaves the vector potential $\hat{\boldsymbol{A}}$ invariant and shifts the electric field operator by a term proportional to the polarization density of the material. Moreover, the matter states are modified according to

$$\hat{\mathcal{W}}\hat{\Psi}_\sigma(\boldsymbol{r})\hat{\mathcal{W}}^\dagger \approx \sum_\alpha e^{-ie\chi(\boldsymbol{r},\boldsymbol{R}_\alpha)} w_\alpha(\boldsymbol{r})\hat{c}_{\alpha\sigma}, \tag{2.38}$$

where $\chi(\boldsymbol{r}, \boldsymbol{r}')$ denotes the line integral of the vector potential along a straight path

$$\chi(\boldsymbol{r}, \boldsymbol{r}') = \int_{\boldsymbol{r}}^{\boldsymbol{r}'} d\boldsymbol{s}\hat{A}(\boldsymbol{s}). \tag{2.39}$$

This has the following consequences: (i) up to small magnetic corrections, which will be neglected throughout this thesis, the vector potential is removed from the kinetic part of the electronic Hamiltonian (first term in Eq. (2.36)). (ii) The shift of the electric field in the free field Hamiltonian (2.33) gives rise to two additional terms: a linear coupling between the electric radiation field and the polarization density, as well as a term that is quadratic in the polarization density. (iii) Pairs of electron creation and annihilation operators at sites $\boldsymbol{R}_\alpha$ and $\boldsymbol{R}_{\alpha'}$ are dressed by a phase factor $e^{-ie\chi_{\alpha,\alpha'}}$, where

$$\chi_{\alpha,\alpha'} = \chi(\boldsymbol{R}_\alpha, \boldsymbol{R}_{\alpha'}). \tag{2.40}$$

This is analogous to the so-called Peierls substitution that is commonly used in semi-classical tight-binding models [72].

With this, the Hamiltonian in dipole gauge is given by

$$\hat{H} = \hat{H}_{\text{kin}} + \hat{H}'_{\text{latt}} + \hat{H}'_{\text{int}} + \hat{H}_{EP} + \hat{H}_{PP} + \hat{H}_{\text{field}}, \tag{2.41}$$

where the kinetic term reads as

$$\hat{H}_{\mathrm{kin}} = \sum_{\alpha,\alpha'} \sum_{\sigma} t^{\mathrm{kin}}_{\alpha,\alpha'} \hat{c}^{\dagger}_{\alpha\sigma} \hat{c}_{\alpha'\sigma} e^{-ie\chi_{\alpha,\alpha'}} \tag{2.42}$$

with

$$t^{\mathrm{kin}}_{\alpha\alpha'} = \int d^3r\, \bar{w}_{\alpha}(\boldsymbol{r}) \frac{(-i\nabla)^2}{2m} w_{\alpha'}(\boldsymbol{r}). \tag{2.43}$$

The particular shape of the transformed lattice and electron-electron interaction Hamiltonian $\hat{H}'_{\mathrm{latt}}$ and $\hat{H}'_{\mathrm{int}}$ depends on their original form. In general, matrix elements between pairs of operators $\hat{c}^{\dagger}_{\alpha\sigma}$ and $\hat{c}_{\alpha'\sigma}$ are decorated with a Peierls phase factor $e^{-ie\chi_{\alpha,\alpha'}}$. For a system consisting of N unit cells, the linear coupling between the electric field and the dipolar transitions of the solid takes the form

$$\hat{H}_{EP} = \sum_{\sigma} \sum_{\alpha,\alpha'} \sum_{\boldsymbol{q}} \sqrt{\frac{\omega_{\boldsymbol{q}}}{2}} \left[\gamma^{\alpha\alpha'}_{\boldsymbol{q}} \hat{a}_{\boldsymbol{q}} + \mathrm{H.c.} \right] \hat{c}^{\dagger}_{\alpha\sigma} \hat{c}_{\alpha'\sigma} e^{-ie\chi_{\alpha,\alpha'}} \tag{2.44}$$

with

$$\gamma^{\alpha\alpha'}_{\boldsymbol{q}} = \sqrt{\frac{e^2 D^2_{\alpha\alpha'}}{\varepsilon_0 \varepsilon V}} \boldsymbol{\phi}_{\boldsymbol{q}}(\boldsymbol{R}_{\alpha\alpha'}), \tag{2.45}$$

where

$$\boldsymbol{R}_{\alpha\alpha'} = (\boldsymbol{R}_{\alpha} + \boldsymbol{R}_{\alpha'})/2 \tag{2.46}$$

denotes the midpoint between site $\boldsymbol{R}_{\alpha}$ and $\boldsymbol{R}_{\alpha'}$, and

$$D_{\alpha\alpha'} = \int d^3r\, \bar{w}_{\alpha}(\boldsymbol{r}) \boldsymbol{r} w_{\alpha'}(\boldsymbol{r}) \tag{2.47}$$

are the dipole matrix elements for transitions between orbital α and α'. With this notation, the self-interaction term of the polarization density reads as

$$\hat{H}_{PP} = \sum_{\sigma_1} \sum_{\sigma_2} \sum_{\alpha,\alpha'} \sum_{\beta,\beta'} \sum_{\boldsymbol{q}} \frac{\bar{\gamma}^{\alpha\alpha'}_{\boldsymbol{q}} \gamma^{\beta\beta'}_{\boldsymbol{q}}}{2} \hat{c}^{\dagger}_{\alpha\sigma_1} \hat{c}_{\alpha'\sigma_1} e^{ie\chi_{\alpha,\alpha'}} \hat{c}^{\dagger}_{\beta\sigma_2} \hat{c}_{\beta'\sigma_2} e^{-ie\chi_{\beta,\beta'}}. \tag{2.48}$$

The last term in Eq. (2.41) corresponds to the free electromagnetic field and is given by Eq. (2.33) or (2.34).

In this thesis, we consider two types of systems. In Sec. 3.2 and Ch. 4, we focus on solids consisting of localized dipoles, i.e., we assume that all dipole matrix elements between different sites vanish. Moreover, the models do not contain tunneling between different sites. In this case, there are no Peierls phase factors, since the line integral $\chi_{\alpha,\alpha'} = 0$ for equal sites $\alpha = \alpha'$. The complementary case is considered in Ch. 5, where we study a single-band Hubbard model that does not feature any dipolar transitions, i.e., $D_{\alpha\alpha'} = 0$. As a result, $\hat{H}_{EP}$ and $\hat{H}_{PP}$ vanish. However, the electrons may hop between different lattice sites. With this, the light-matter interaction only enters via the Peierls phase.

2.3.3. Mean-field decoupling of light and matter

A common method to gain first insights into the equilibrium state of a system is the static mean-field approximation. In this formalism, the interaction between two operators $\hat{A}$ and $\hat{B}$ is decoupled using the substitution $\hat{A}\hat{B} \to A\hat{B} + \hat{A}B - AB$, where $A = \langle\hat{A}\rangle$ and $B = \langle\hat{B}\rangle$. This amounts to neglecting quantum fluctuations of the form $(\hat{A} - A)(\hat{B} - B)$. For a system of localized dipoles, where the Peierls phase factors are equal to one, this approximation can be used to decouple the light-matter interaction.

We consider a general Hamiltonian of the form

$$\hat{H} = \hat{H}_{\text{mat}} + \hat{H}_{EP} + \hat{H}_{PP} + \hat{H}_{\text{field}} \tag{2.49}$$

with a free field Hamiltonian $\hat{H}_{\text{field}}$ given by (2.34) and a matter Hamiltonian $\hat{H}_{\text{mat}}$ that describes the isolated dipoles as well as possible interactions between them. For the dipolar transitions, we define the local operators $\hat{p}_{\boldsymbol{R}nn'\sigma} = \hat{c}^\dagger_{\boldsymbol{R}n\sigma}\hat{c}_{\boldsymbol{R}n'\sigma}$. Introducing the multiindex $r = (\boldsymbol{R}nn'\sigma)$ that contains the lattice site, the band indices n and n', and the spin index σ, the linear light-matter coupling can be written as

$$\hat{H}_{EP} = \sum_r \sum_{\boldsymbol{q}} \sqrt{\frac{\omega_{\boldsymbol{q}}}{2}} \left(\gamma_{\boldsymbol{q}r}\hat{a}^\dagger_{\boldsymbol{q}} + \text{H.c.}\right)\hat{p}_r. \tag{2.50}$$

Using the same notation, the dipole-dipole interaction reads as

$$\hat{H}_{PP} = \sum_{r,r'} \frac{\bar{\gamma}_{\boldsymbol{q}r}\gamma_{\boldsymbol{q}r'}}{2}\hat{p}_r\hat{p}_{r'}. \tag{2.51}$$

We perform a mean-field decoupling of the photon operators $\hat{a}^{(\dagger)}_{\boldsymbol{q}}$ and the dipole operators $\hat{p}_r$. With this, $\hat{H}_{EP}$ can be split into three contributions

$$\hat{H}_{EP} \to \hat{H}^{\text{mf,mat}}_{EP}(\bar{a}_{\boldsymbol{q}}, a_{\boldsymbol{q}}) + \hat{H}^{\text{mf,field}}_{EP}(p_r) + f_{EP}(\bar{a}_{\boldsymbol{q}}, a_{\boldsymbol{q}}, p_r). \tag{2.52}$$

The first term only contains matter operators. The electromagnetic field just enters via the expectation value $a_{\boldsymbol{q}} = \langle\hat{a}_{\boldsymbol{q}}\rangle$ and its complex conjugate. It is given by

$$\hat{H}^{\text{mf,mat}}_{EP}(\bar{a}_{\boldsymbol{q}}, a_{\boldsymbol{q}}) = \sum_r \sum_{\boldsymbol{q}} \sqrt{\frac{\omega_{\boldsymbol{q}}}{2}} \left(\gamma_{\boldsymbol{q}r}\bar{a}_{\boldsymbol{q}} + \text{c.c.}\right)\hat{p}_r. \tag{2.53}$$

In the second part, the field is described by quantum mechanical operators, whereas the dipoles are replaced by their quantum average $p_r = \langle\hat{p}_r\rangle$, i.e.,

$$\hat{H}^{\text{mf,field}}_{EP}(p_r) = \sum_r \sum_{\boldsymbol{q}} \sqrt{\frac{\omega_{\boldsymbol{q}}}{2}} \left(\gamma_{\boldsymbol{q}r}\hat{a}^\dagger_{\boldsymbol{q}} + \text{H.c.}\right)p_r. \tag{2.54}$$

The last term

$$f_{EP}(\bar{a}_{\boldsymbol{q}}, a_{\boldsymbol{q}}, p_r) = -\sum_r \sum_{\boldsymbol{q}} \sqrt{\frac{\omega_{\boldsymbol{q}}}{2}} \left(\gamma_{\boldsymbol{q}r}\bar{a}_{\boldsymbol{q}} + \text{c.c.}\right)p_r \tag{2.55}$$

is a function of $\bar{a}_{\boldsymbol{q}}$, $a_{\boldsymbol{q}}$ and p_r and does not include any operators.

Similarly, the dipole-dipole interaction can be decoupled, which yields

$$\hat{H}_{PP} \to \hat{H}_{PP}^{\mathrm{mf}} + f_{PP}(p_r) \tag{2.56}$$

with the mean-field Hamiltonian

$$\hat{H}_{PP}^{\mathrm{mf}} = \sum_{r,r'} \bar{\gamma}_{\boldsymbol{q}r} \gamma_{\boldsymbol{q}r'} p_r \hat{p}_{r'} \tag{2.57}$$

and a function

$$f_{PP}(p_r) = -\sum_{r,r'} \frac{\bar{\gamma}_{\boldsymbol{q}r} \gamma_{\boldsymbol{q}r'}}{2} p_r p_{r'} \tag{2.58}$$

of the expectation value p_r.

With this, the total Hamiltonian can be replaced by

$$\hat{H} \to \hat{H}_{\mathrm{field}}^{\mathrm{mf}}(p_r) + \hat{H}_{\mathrm{mat}}^{\mathrm{mf}}(\bar{a}_{\boldsymbol{q}}, a_{\boldsymbol{q}}) + f(\bar{a}_{\boldsymbol{q}}, a_{\boldsymbol{q}}, p_r), \tag{2.59}$$

where

$$\hat{H}_{\mathrm{field}}^{\mathrm{mf}}(p_r) = \hat{H}_{\mathrm{field}} + \hat{H}_{EP}^{\mathrm{mf,field}}(p_r) \tag{2.60}$$

contains all terms depending on photon operators. On the other hand,

$$\hat{H}_{\mathrm{mat}}^{\mathrm{mf}}(\bar{a}_{\boldsymbol{q}}, a_{\boldsymbol{q}}) = \hat{H}_{\mathrm{mat}} + \hat{H}_{EP}^{\mathrm{mf,mat}}(\bar{a}_{\boldsymbol{q}}, a_{\boldsymbol{q}}) + \hat{H}_{PP}^{\mathrm{mf}} \tag{2.61}$$

only includes matter operators, whereas the field is treated semi-classically. Moreover, there is the function

$$f(\bar{a}_{\boldsymbol{q}}, a_{\boldsymbol{q}}, p_r) = f_{EP}(\bar{a}_{\boldsymbol{q}}, a_{\boldsymbol{q}}, p_r) + f_{PP}(p_r). \tag{2.62}$$

We now proceed by calculating the semi-classical equations of motion for the photon operators using the mean-field Hamiltonian (2.60) for the electromagnetic field. This yields

$$\dot{a}_{\boldsymbol{q}} = i \left\langle \left[\hat{H}_{\mathrm{field}}^{\mathrm{mf}}, \hat{a}_{\boldsymbol{q}} \right] \right\rangle = -i\omega_{\boldsymbol{q}} a_{\boldsymbol{q}} - i \sum_r \sqrt{\frac{\omega_{\boldsymbol{q}}}{2}} \gamma_{\boldsymbol{q}r} p_r. \tag{2.63}$$

In the static case, the time derivative vanishes, and the solution reads as

$$a_{\boldsymbol{q}} = -\sum_r \frac{\gamma_{\boldsymbol{q}r}}{\sqrt{2\omega_{\boldsymbol{q}}}} p_r \tag{2.64}$$

$$\bar{a}_{\boldsymbol{q}} = -\sum_r \frac{\bar{\gamma}_{\boldsymbol{q}r}}{\sqrt{2\omega_{\boldsymbol{q}}}} p_r. \tag{2.65}$$

With this, we can eliminate the expectation values $a_{\boldsymbol{q}}$ and $\bar{a}_{\boldsymbol{q}}$ in the mean-field Hamiltonian (2.61) for the matter. In particular, we find that

$$\hat{H}_{EP}^{\mathrm{mf,mat}} = -\hat{H}_{PP}^{\mathrm{mf}}, \tag{2.66}$$

i.e., the linear light-matter coupling and the self-interaction term of the polarization density exactly cancel each other. As a result, the static mean-field Hamiltonian of the material is identical to the Hamiltonian of the bare matter

$$\hat{H}_{\mathrm{mat}}^{\mathrm{mf}} = \hat{H}_{\mathrm{mat}}. \tag{2.67}$$

Similarly,

$$f_{EP}(\bar{a}_{\boldsymbol{q}}, a_{\boldsymbol{q}}, p_r) = -f_{PP}(p_r), \tag{2.68}$$

and thus

$$f(\bar{a}_{\boldsymbol{q}}, a_{\boldsymbol{q}}, p_r) = 0. \tag{2.69}$$

This is a crucial result, as it proves that the static mean-field approximation does not capture any light-induced effects on systems of the type discussed above. Instead, it predicts a complete decoupling of light and matter. Moreover, it highlights the importance of the dipolar self-interaction that leads to a perfect cancellation of the linear light-matter coupling within the static mean-field formalism. This fact has been discussed previously, e.g., in the context of the superradiant phase transition [15, 59]. However, the static mean-field theory constitutes a semi-classical approach and does not take into account quantum fluctuations. Therefore, an important goal of this thesis is to go beyond this approximation and to investigate whether it is possible to manipulate the equilibrium properties of matter by exploiting the true quantum nature of light.

2.4. Ferroelectric phase transition in a minimal model of interacting dipoles

Ferroelectricity is a state of matter characterized by a spontaneous electric polarization that can be reverted with an external electric field. The prefix "ferro" does not refer to the chemical element iron but originates from the analogous phenomenon of ferromagnetism, where the material acquires a magnetic dipole moment [52].

A minimal model of a solid that may undergo a transition to a ferroelectric state will be studied in Sec. 3.2 and Ch. 4. It consists of N two-level systems (TLS) with a single dipolar transition, and the individual atoms or molecules interact via a static dipole-dipole interaction. The energy levels of the isolated TLS are separated by a gap Δ, so that the corresponding Hamiltonian can be written as $\hat{H}_0 = \frac{\Delta}{2}\sum_r(\hat{c}_{er}^\dagger \hat{c}_{er} - \hat{c}_{gr}^\dagger \hat{c}_{gr})$, where the operator $\hat{c}_{ir}^\dagger$ ($\hat{c}_{ir}$) creates (annihilates) an electron in state $i \in \{g, e\}$ at site r. Note that we suppress the spin index, as it only gives rise to an additional sum but does not change the physics. Introducing the pseudo-spin operators

$$\hat{\sigma}_{\nu,r} = (\hat{c}_{er}^\dagger, \hat{c}_{gr}^\dagger)\boldsymbol{\tau}_\nu \begin{pmatrix} \hat{c}_{er} \\ \hat{c}_{gr} \end{pmatrix}, \tag{2.70}$$

where $\boldsymbol{\tau}_\nu$ with $\nu \in \{x, y, z\}$ denotes the ν-component of the vector of Pauli matrices, the Hamiltonian can be rewritten as

$$\hat{H}_0 = \frac{\Delta}{2}\sum_r \hat{\sigma}_{z,r}. \tag{2.71}$$

In this notation, the electric polarization operator of the TLS at site r is given by $\hat{\sigma}_{x,r} = \hat{c}_{er}^\dagger \hat{c}_{gr} + \hat{c}_{gr}^\dagger \hat{c}_{er}$. We add an attractive dipole-dipole coupling of the form

$$\hat{H}_{\text{int}} = -\frac{\alpha}{2} \sum_{r,r'} f_{r,r'} \hat{\sigma}_{x,r} \hat{\sigma}_{x,r'}, \tag{2.72}$$

where $f_{r,r'}$ defines the spatial structure of the interaction. We assume that $f_{r,r'}$ only depends on the distance between site r and r', and that it is normalized as

$$\sum_{\delta r} f_{r,r'+\delta r} = 1. \tag{2.73}$$

For instance, we consider an all-to-all interaction of the form $f_{r,r'} = \frac{1}{N}$ in Sec. 3.2, and study a two-dimensional square lattice with a nearest-neighbor interaction

$$f_{r,r'} = \begin{cases} \frac{1}{4} & , r, r' \text{ nearest neighbors} \\ 0 & , \text{otherwise} \end{cases}$$

in Ch. 4. In the latter case, the total Hamiltonian

$$\hat{H} = \hat{H}_0 + \hat{H}_{\text{int}} \tag{2.74}$$

is equivalent to a two-dimensional transverse-field Ising model, which was first introduced by De Gennes to describe potassium-dihydrogen-phosphate-type ferroelectrics [17]. It has been solved exactly by Zhang in 2021 using a mapping to a three-dimensional Ising model without transverse field [90].

Here, we briefly discuss the static mean-field approximation for the model, which already gives first insights into the equilibrium phases of the system. We start from a static mean-field decoupling of the dipole-dipole interaction using the substitution $\hat{\sigma}_{x,r}\hat{\sigma}_{x,r'} \to \hat{\sigma}_{x,r}\sigma_x + \sigma_x\hat{\sigma}_{x,r'} - \sigma_x^2$ (also see Sec. 2.3.3), where we have assumed that the electric polarization $\sigma_x = \langle \hat{\sigma}_{x,r} \rangle$ is homogenous over the entire solid. Since the last term does not contain any operators, it does not enter the equations of motion for the system; therefore, it will be omitted in the following. Using the normalization condition (2.73) for $f_{r,r'}$, the mean-field Hamiltonian reads as

$$\hat{H}^{\text{mf}} = \hat{H}_0 + \hat{H}_{\text{int}}^{\text{mf}} \tag{2.75}$$

with

$$\hat{H}_{\text{int}}^{\text{mf}} = -\alpha\sigma_x \sum_r \hat{\sigma}_{x,r}. \tag{2.76}$$

The expectation value σ_x corresponds to the electric polarization of the material. Hence, it also represents the order parameter for the ferroelectric phase transition. In the normal (disordered) phase, σ_x vanishes, and the system is paraelectric. But as soon as the system enters the ordered phase and becomes ferroelectric, the solid acquires a non-vanishing electric dipole moment, and σ_x takes a finite value different from zero. In the next step, we derive a self-consistent equation for the order parameter that allows

us to determine the phase diagram for the system. For that purpose, we introduce an additional external static field h that couples to the total polarization of the solid. With this, the mean-field Hamiltonian can be written as

$$\hat{H}^{\mathrm{mf}}[h] = \hat{H}^{\mathrm{mf}} - h\sum_r \hat{\sigma}_{x,r} = \sum_r \hat{H}_r^{\mathrm{mf}}[h] \tag{2.77}$$

with the single-site mean-field Hamiltonian

$$\hat{H}_r^{\mathrm{mf}}[h] = \frac{\Delta}{2}\hat{\sigma}_{z,r} - \alpha\sigma_x\hat{\sigma}_{x,r} - h\hat{\sigma}_{x,r}. \tag{2.78}$$

The latter can be diagonalized, and has eigenvalues

$$E_\pm[h] = \pm\sqrt{(\Delta/2)^2 + (\alpha\sigma_x + h)^2}. \tag{2.79}$$

Moreover, we define the partition function

$$\mathcal{Z}_r[h] = \mathrm{tr}\left\{e^{-\beta\hat{H}_r^{\mathrm{mf}}[h]}\right\} = e^{-\beta E_+[h]} + e^{-\beta E_-[h]}. \tag{2.80}$$

The order parameter for $h = 0$ can then be calculated by taking the derivative

$$\sigma_x = \frac{1}{\beta}\frac{\partial}{\partial h}\ln\mathcal{Z}_r[h]\bigg|_{h=0}, \tag{2.81}$$

which yields the self-consistent equation

$$\sigma_x = \tanh\left[\beta\sqrt{(\Delta/2)^2 + (\alpha\sigma_x)^2}\right]\frac{\alpha}{\sqrt{(\Delta/2)^2 + (\alpha\sigma_x)^2}}\sigma_x. \tag{2.82}$$

Independent of the parameters β, Δ and α, there is always the trivial solution $\sigma_x = 0$; however, this solution becomes unstable in the ferroelectric regime. In this case, both sides of Eq. (2.82) can be divided by σ_x, and we obtain

$$1 = \tanh\left[\beta\sqrt{(\Delta/2)^2 + (\alpha\sigma_x)^2}\right]\frac{\alpha}{\sqrt{(\Delta/2)^2 + (\alpha\sigma_x)^2}}. \tag{2.83}$$

If Eq. (2.83) is solvable, there are two solutions with opposite sign corresponding to two opposing polarization directions. As the system picks one of them in the ferroelectric state, the phase transition is accompanied by a spontaneous symmetry breaking.

Fig. 2.8(a) displays the results for the order parameter as a function of temperature ($T = 1/\beta$) at various values of α, where Δ sets the unit of energy. The curves have been determined numerically using a fixed-point iteration. Note that even in the symmetry-broken phase, we only plot one solution, as the negative solution is completely symmetrical to the positive one. At low temperatures, $\sigma_x > 0$ and the system is ferroelectric. As T is increased, the order parameter continuously drops to zero, which indicates a second-order phase transition to the paraelectric state. For increasing dipole-dipole interaction strength α, the critical point is shifted to higher temperatures, i.e.,

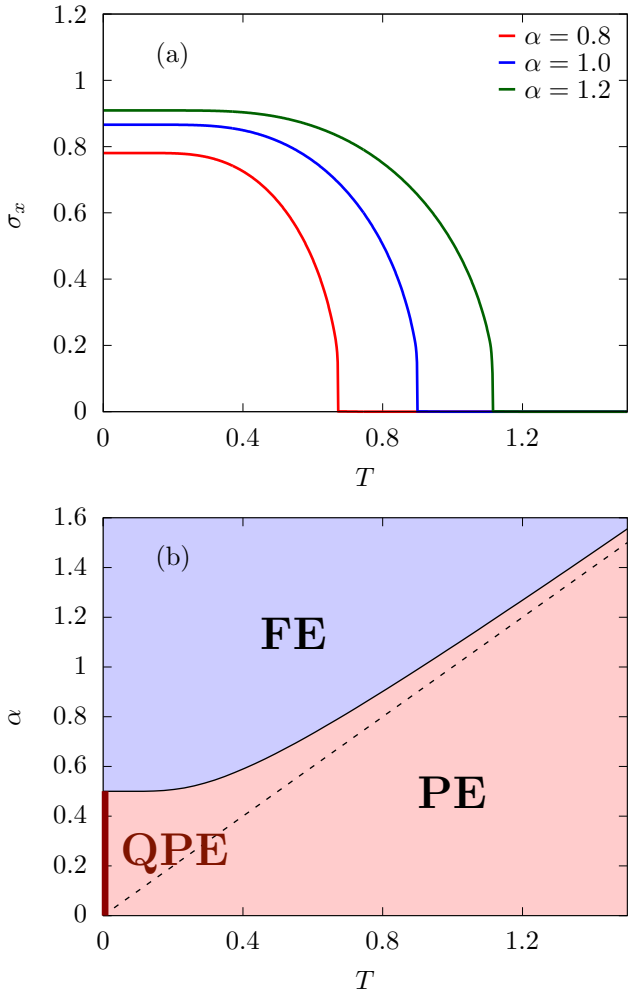

Figure 2.8.: *Mean-field results for the ferroelectric phase transition in the model described by Hamiltonian* (2.74)*. The unit of energy is given by the level splitting* Δ*. (a) Positive solution for the order parameter as a function of temperature at various values of the static dipole-dipole interaction strength* α*. (b) Phase diagram in the* α*-*T*-plane. The blue-shaded region indicates the ferroelectric (FE) regime, whereas the red-shaded area corresponds to the paraelectric (PE) state. The dark red line at zero temperature marks the quantum-paraelectric (QPE) phase. Moreover, the black dashed line indicates the boundary between the ferroelectric and paraelectric state for a system with vanishing level splitting* Δ*. In this case, there is no quantum-paraelectric regime. [Graphic adapted from Ref. [61].]*

the ferroelectric phase is stabilized. This can also be seen in Fig. 2.8(b), where the phase diagram in the T-α-plane is shown.

It is also interesting to note that, even at zero temperature, the dipole-dipole coupling α has to overcome a certain critical value to induce ferroelectricity in the system. This can also be deduced from Eq. (2.83). In the limit $\beta \to \infty$, i.e., in the zero-temperature limit, the right-hand side of (2.83) reaches its maximum with respect to β and goes to $\frac{\alpha}{\sqrt{(\Delta/2)^2+(\alpha\sigma_x)^2}}$. Consequently, a valid non-zero solution for σ_x only exists if $1 \leq \frac{\alpha}{\sqrt{(\Delta/2)^2+(\alpha\sigma_x)^2}}$. In particular, this means that the phase transition is only possible for $\alpha \geq \Delta/2$ even at $T = 0$. In this case, the ferroelectric state is not destabilized by thermal fluctuations. Instead, the transition is inhibited due to the microscopic splitting of the energy levels. Therefore, this is a quantum effect, and the corresponding regime is referred to as the quantum-paraelectric phase. For $\Delta = 0$, this phase does not exist. As indicated by the dashed line in Fig. 2.8(b), the phase boundary for vanishing Δ is given by a straight line with slope α. Again, this can be derived from Eq. (2.83): Setting Δ to zero yields $1 = \tanh\left[\beta\alpha|\sigma_x|\right]/|\sigma_x|$. Near the phase transition, the order parameter σ_x goes to zero. With this, $\tanh\left[\beta\alpha|\sigma_x|\right] \approx \beta\alpha|\sigma_x|$ and the equation can be solved for $T = 1/\beta$ and reads as $T = \alpha$. The quantum paraelectric state can also be understood from a different point of view: If the energy gap Δ vanishes, the model is equivalent to the Ising model and the phase transition is always possible for a given critical temperature $T_c > 0$. This case can be considered as a classical version of the system. For $\Delta > 0$, however, there is tunneling between the "classical" configurations, which decreases the tendency to order. If α is small, the ferroelectric state can be suppressed even down to zero temperature.

It should be mentioned, however, that the Hamiltonian considered above does not represent a microscopic model for any real material. In fact, the phenomenon of ferroelectricity is caused by the interplay of many degrees of freedom and is usually accompanied by a change in the crystal structure. In general, there are two major mechanisms that may give rise to the spontaneous electric polarization of a solid. If the transition is of the displacive type, the formation of the permanent dipole moment is due to an asymmetrical shift of the equilibrium ion positions in the crystal lattice. For instance, this is the case in barium titanate ($BaTiO_3$). In an order-disorder ferroelectric, however, each unit cell already has a non-vanishing dipole moment, even above the critical temperature. However, the dipoles point in random directions, such that the average polarization vanishes. Below the critical temperature, the dipoles are aligned, and the solid becomes ferroelectric. An example of such a system is potassium dihydrogen phosphate (KDP) [88].

Another interesting material that has been studied recently in the context of quantum light-matter interactions is $SrTiO_3$ (STO) [69, 58]. According to classical physics, it may undergo a ferroelectric phase transition if it is cooled down below a certain critical temperature. However, experiments have shown that the unperturbed material remains paraelectric even in the low-temperature regime. This behavior is caused by quantum fluctuations that freeze the ferroelectric mode and prevent it from softening to zero frequency. Nevertheless, it has been observed that at low temperatures, the material

can be easily pushed to a metastable ferroelectric state, for instance by applying strain, through isotope substitution or using classical ultrashort laser pulses [71, 64]. This confirms that the material is already at the verge of a ferroelectric phase transition and, therefore, constitutes a quantum paraelectric at $T = 0$. With this, STO exhibits the same phases as the minimal model discussed above. Therefore, we will again refer to STO in Sec. 3.2 and Ch. 4 even though the system of interacting TLS does not represent a valid microscopic description of the material.

3. Collective theory for an interacting solid in a single-mode cavity

As discussed in Sec. 2.3.3, a static mean-field description cannot capture any light-induced effects in solids with a purely linear, dipolar coupling to the electromagnetic field. Therefore, we aim to analyze fluctuations beyond the static mean-field limit. As a starting point, we consider a material that only couples to a single cavity mode. Similar single-mode settings have been studied previously in a multitude of theoretical publications and constitute a promising platform to control the properties of periodic electronic systems [58, 46, 47, 81, 62]. Experimentally, they can be realized, for instance, by a Fabry-Pérot cavity or a split-ring resonator [65]. In the latter case, it is even possible to confine the electromagnetic field to a volume much smaller than the wavelength $\lambda = \Omega/c$, where Ω denotes the resonance frequency of the cavity. This allows large light-matter coupling strengths to be achieved, but also restricts the amount of matter that fits inside the cavity. However, if the resonator is in the µm regime, it may still contain a macroscopic number of atoms $N \sim 10^{10}$.

For the single-mode setting, there are two important energy scales to quantify the coupling between light and matter. On the one hand, there is the single-particle coupling g_1, which corresponds to the interaction between each individual transition dipole and the photon mode. Since $g_1^2 \sim \frac{1}{V}$, it can be enhanced by decreasing the volume of the resonator. Small mode volumes even make it possible to enter the ultrastrong coupling regime, where g_1^2 becomes comparable to the bare energy scales in matter [50]. However, typical experimental setups only involve a small number of emitters, and, thus, are not applicable to macroscopic solids.

On the other hand, there is the collective coupling $g_n^2 = Ng_1^2$ that determines the hybridization between a collective excitation of the material and the cavity mode. It is proportional to the density $n = \frac{N}{V}$, and, therefore, remains finite even in the thermodynamic limit, where $N \to \infty$. Nevertheless, the collective coupling strength g_n^2 can easily be of the order of 1eV if the density is high, and become comparable to or larger than other fundamental energy scales in the system. Therefore, it seems reasonable to ask whether it is possible to influence the equilibrium state of a macroscopic solid even when the single-particle coupling g_1^2 is weak.

There are different ways to answer this question. One possible approach is to consider a Hamiltonian that describes the coupling of the quantized collective matter excitation to the cavity mode, and directly analyze the hybrid light-matter response. For instance, this has been done in Ref. [58], where the collective Hamiltonian for infrared-active phonons in $SrTiO_3$ has been studied. In this chapter, we follow a different route: Starting from a microscopic Hamiltonian, we derive a collective theory, and obtain the response of the

hybrid light-matter system in terms of the response for the bare matter. This allows us to analyze how the cavity mode affects the collective behavior of the material. In particular, we find that in finite systems even the static susceptibility can be modified by the light-matter interaction. However, this effect vanishes in the thermodynamic limit, which implies that it is impossible to influence the equilibrium state of a macroscopic solid with a single cavity mode.

All results and derivations presented in this chapter can also be found in Ref. [60]. In Sec. 3.1, we review the derivation of the collective theory for a general matter Hamiltonian that couples to a single cavity mode. Sec. 3.2 contains the results for a specific model of interacting dipoles.

3.1. Collective theory for a generic matter Hamiltonian

3.1.1. Model Hamiltonian

We consider a generic material that consists of N polarizable units (atoms or molecules). The Hamiltonian $\hat{H}_{\text{mat}}$ describes the isolated matter. It may also contain direct interactions between the individual units, such as electrostatic dipole-dipole interactions or electron-lattice interactions. For each unit r of the solid, we assume a dipolar transition operator $ed\hat{p}_r$ with the elementary charge e, a length scale d, and a dimensionless operator $\hat{p}_r$. The latter may either correspond to electronic transition dipoles as in Sec. 2.3.2, or to the displacement of ions within a unit cell. Moreover, we introduce the total dipole operator $\hat{P} = \sum_r \hat{p}_r$, which couples to a single cavity mode of frequency Ω. We denote the photon creation and annihilation operators by $\hat{a}$ and $\hat{a}^\dagger$ and introduce the field quadrature $\hat{X} = (\hat{a}^\dagger + \hat{a})/\sqrt{2}$. The mode is assumed to be homogenous over the entire system. With this, the electric field operator is given by $\hat{E} = \sqrt{\frac{\Omega}{V\varepsilon_0\varepsilon}}\hat{X}$, where ε is the electric permittivity of the surrounding medium and V represents the cavity volume. Hence, the total Hamiltonian of the system reads as

$$\hat{H} = \hat{H}_{\text{mat}} + \hat{H}_{Ed} + \hat{H}_{dd} + \Omega a^\dagger a, \;\; \hat{H}_{Ed} = \sqrt{\Omega} g_1 \hat{X}\hat{P}, \;\; \hat{H}_{dd} = \frac{g_1^2}{2}\hat{P}^2 \tag{3.1}$$

with the single-particle coupling $g_1 = \sqrt{d^2 e^2/\varepsilon_0 \varepsilon V}$.

3.1.2. Light-induced interaction

In the next step, we derive an effective description of the system that only depends on the matter degrees of freedom. For that purpose, we use the imaginary-time path integral formalism. We represent the cavity mode by the complex bosonic fields $a(\tau)$ and $\bar{a}(\tau)$, and introduce the Grassmann variables $c(\tau)$ and $\bar{c}(\tau)$ for the matter part. With this, the full action reads as

$$S = S_{\text{mat}}[\bar{c}, c] + S_{Ed}[\bar{c}, c; \bar{a}, a] + S_{dd}[\bar{c}, c] + S_{\text{field}}[\bar{a}, a], \tag{3.2}$$

where S_{mat} corresponds to the isolated solid and

$$S_{\mathrm{field}}[\bar{a}, a] = \int_0^\beta d\tau\, \bar{a}(\tau)(\partial_\tau + \Omega)a(\tau), \tag{3.3}$$

is the action of the free electromagnetic radiation field. The light-matter coupling terms are given by

$$S_{dd} + S_{Ed} = \frac{g_1^2}{2}\int_0^\beta d\tau P(\tau)^2 + g_1\sqrt{\frac{\Omega}{2}}\int_0^\beta d\tau \big(a(\tau) + \bar{a}(\tau)\big)P(\tau), \tag{3.4}$$

with the collective dipole moment $P(\tau) = \sum_r p_r(\tau)$.

Since (3.2) is quadratic in the photon-fields, they can be readily integrated out. This yields an effective action

$$S_{\mathrm{eff}}[\bar{c}, c] = S_{\mathrm{mat}}[\bar{c}, c] + S_{\mathrm{ind}}[\bar{c}, c] \tag{3.5}$$

that only depends on the matter degrees of freedom. The effect of the light-matter coupling is fully contained in the cavity-induced interaction S_{ind}, which is defined by the relation

$$e^{-S_{\mathrm{ind}}} = e^{-S_{dd}}\int \mathcal{D}[\bar{a}, a]e^{-(S_{\mathrm{field}}+S_{Ed})}. \tag{3.6}$$

Solving the Gaussian path integral gives

$$S_{\mathrm{ind}} = \frac{1}{2}\int_0^\beta d\tau \int_0^\beta d\tau' P(\tau)\frac{1}{N}V_{\mathrm{ind}}(\tau - \tau')P(\tau'), \tag{3.7}$$

with

$$V_{\mathrm{ind}}(\tau) = \frac{g_n^2\Omega}{2}\big[D_0(\tau) + D_0(\beta - \tau)\big] + g_n^2\delta(\tau). \tag{3.8}$$

Note that we have already symmetrized the interaction. Moreover, we have introduced the collective coupling strength $g_n^2 = Ng_1^2$. The free photon propagator is given by

$$D_0(\tau) = -\langle a(\tau)\bar{a}(0)\rangle_{S_{\mathrm{field}}} = -\frac{e^{-\tau\Omega}}{1 - e^{-\beta\Omega}}. \tag{3.9}$$

In Matsubara representation, it reads as

$$D_0(i\nu_m) = \frac{1}{i\nu_m - \Omega}. \tag{3.10}$$

and therefore,

$$V_{\mathrm{ind}}(i\nu_m) = g_n^2\frac{\nu_m^2}{\nu_m^2 + \Omega^2}. \tag{3.11}$$

As can be seen from this expression, the zero frequency component of the induced interaction vanishes. This is in accordance with the static mean-field approximation discussed in Sec. 2.3.3 that amounts to ignoring all other components. Our goal is, to take account of all these contributions and investigate their effect on the equilibrium state of the system.

3.1.3. Hubbard-Stratonovich representation

In order to derive the collective theory, we re-express the effective action (3.5) in terms of a single collective variable. For that purpose, we introduce a real bosonic Hubbard-Stratonovich field $\varphi(\tau)$ and decouple the cavity-induced interaction (3.7). The matrix V_{ind} is positive definite; therefore, we can use the identity

$$e^{-S_{\mathrm{ind}}} = \frac{1}{Z_V} \int \mathcal{D}[\varphi] e^{-\frac{1}{2}\int_0^\beta d\tau \int_0^\beta d\tau' \varphi(\tau) V_{\mathrm{ind}}^{-1}(\tau-\tau')\varphi(\tau') - i\int_0^\beta d\tau \sum_r \frac{\varphi(\tau)}{\sqrt{N}} p_r(\tau)}, \tag{3.12}$$

with an irrelevant constant Z_V that will be omitted in the following. Hence, the effective action (3.5) is equivalent to the action

$$\begin{aligned} S_{\mathrm{HS}}[\bar{c}, c; \varphi] =& S_{\mathrm{mat}} + \frac{1}{2}\int_0^\beta d\tau \int_0^\beta d\tau' \varphi(\tau) V_{\mathrm{ind}}^{-1}(\tau-\tau')\varphi(\tau') \\ &+ i\int_0^\beta d\tau \sum_r \frac{\varphi(\tau)}{\sqrt{N}} p_r(\tau). \end{aligned} \tag{3.13}$$

Based on this result, we can already derive an exact relation between the interacting φ-propagator

$$W(\tau) = \langle \varphi(\tau)\varphi(0)\rangle_S^{\mathrm{con}} \tag{3.14}$$

and the matter susceptibility. The latter can be calculated from the generating function

$$Z[\xi] = \int \mathcal{D}[\bar{c}, c] \int \mathcal{D}[\varphi] e^{-S_{\mathrm{HS}}} e^{\frac{i}{\sqrt{N}}\int_0^\beta d\tau \xi(\tau) \sum_r p_r} \tag{3.15}$$

by taking the second derivative

$$\chi(\tau-\tau') \equiv \frac{1}{N}\sum_{r,r'} \langle p_r(\tau) p_{r'}(\tau')\rangle_S^{\mathrm{con}} = -\frac{\delta}{\delta\xi(\tau)}\frac{\delta}{\delta\xi(\tau')} \log Z[\xi]\Big|_{\xi=0}. \tag{3.16}$$

On the other hand, we can substitute the integration variable φ with $\tilde{\varphi} = \varphi - \xi$ in Eq. (3.15). This removes the linear source term but shifts the variable ξ to the quadratic part of the action. The generating function then reads as

$$Z[\xi] = \int \mathcal{D}[\bar{c}, c] \int \mathcal{D}[\tilde{\varphi}] e^{-\left(S_{\mathrm{mat}} + \frac{1}{2}\int_0^\beta d\tau \int_0^\beta d\tau' (\tilde{\varphi}(\tau)+\xi(\tau)) V_{\mathrm{ind}}^{-1}(\tau-\tau')(\tilde{\varphi}(\tau')+\xi(\tau')) + \frac{i}{\sqrt{N}}\int_0^\beta d\tau \tilde{\varphi}(\tau) P(\tau)\right)}. \tag{3.17}$$

Taking the derivative of this expression now yields

$$\begin{aligned} \frac{\delta}{\delta\xi(\tau)}\frac{\delta}{\delta\xi(\tau')} \log Z[\xi]\Big|_{\xi=0} =& -V_{\mathrm{ind}}^{-1}(\tau-\tau') + \\ &+ \int_0^\beta d\tau_1 \int_0^\beta d\tau_2 V_{\mathrm{ind}}^{-1}(\tau-\tau_1) W(\tau_1-\tau_2) V_{\mathrm{ind}}^{-1}(\tau_2-\tau'). \end{aligned} \tag{3.18}$$

Thus, in Matsubara representation, we find the relation

$$\chi(i\nu_m) = V_{\text{ind}}(i\nu_m)^{-1} - V_{\text{ind}}(i\nu_m)^{-1} W(i\nu_m) V_{\text{ind}}(i\nu_m)^{-1} \tag{3.19}$$

Now we turn back to the Hubbard-Stratonovich action (3.13). We want to integrate out the matter degrees of freedom. For that purpose, we introduce the function

$$\mathcal{G}_{\text{mat}}[y] = -\frac{1}{N} \log \int \mathcal{D}[\bar{c}, c] e^{-\left(S_{\text{mat}} + i \sum_r \int_0^\beta d\tau p_r(\tau) y(\tau)\right)}, \tag{3.20}$$

such that

$$\int \mathcal{D}[\bar{c}, c] e^{-\left(S_{\text{mat}} + \frac{i}{\sqrt{N}} \sum_r \int_0^\beta d\tau p_r(\tau) \varphi(\tau)\right)} = e^{-N \mathcal{G}_{\text{mat}}[\varphi/\sqrt{N}]} \tag{3.21}$$

It also represents the generating function for the connected collective correlation functions of the bare material, i.e.,

$$\begin{aligned} \frac{\delta}{\delta y(\tau_1)} \cdots \frac{\delta}{\delta y(\tau_n)} \mathcal{G}_{\text{mat}}[y]\Big|_{y=0} &= -\frac{(-i)^n}{N} \sum_{r_1,\ldots,r_n} \langle p_{r_1}(\tau_1) \cdots p_{r_n}(\tau_n) \rangle^{\text{con}} \\ &\equiv \chi^{(n)}_{\text{mat}}(\tau_1, ..., \tau_n). \end{aligned} \tag{3.22}$$

(In the following, we use the shorthand notation $\chi^{(2)}_{\text{mat}} = \chi_{\text{mat}}$ for the second order correlation function.) Thus, we can expand the function in a Taylor series

$$\mathcal{G}_{\text{mat}}[y] = \sum_{n=2,4,\ldots} \frac{1}{n!} \int_0^\beta d\tau_1 \cdots d\tau_n \, y(\tau_1) \cdots y(\tau_n) \, \chi^{(n)}_{\text{mat}}(\tau_1, ..., \tau_n), \tag{3.23}$$

where the zeroth order term is just an irrelevant constant and, therefore, has been omitted. Furthermore, we assume that the action S_{mat} is invariant under inversions (i.e. reversing the sign of p_r); as a result, only even orders contribute. Note that this is only true if there is no spontaneous symmetry breaking. For instance, if the solid underwent a transition to a ferroelectric phase, this condition would no longer be fulfilled. Thus, in systems where inversion symmetry can be broken, the theory is only valid within the normal phase. With this, the Hubbard-Stratonovich action (3.13) is equivalent to

$$S[\varphi] = \frac{1}{2} \int_0^\beta d\tau \int_0^\beta d\tau' \varphi(\tau) V^{-1}_{\text{ind}}(\tau - \tau') \varphi(\tau') + N \mathcal{G}_{\text{mat}}[\varphi/\sqrt{N}]. \tag{3.24}$$

The first term and the quadratic term in $N\mathcal{G}_{\text{mat}}[\varphi/\sqrt{N}]$ can be combined, such that the final result is given by

$$S[\varphi] = \frac{1}{2} \int_0^\beta d\tau \int_0^\beta d\tau' \varphi(\tau) W_0^{-1}(\tau - \tau') \varphi(\tau') + \sum_{n=4,6,\ldots}^{\infty} N^{1-\frac{n}{2}} S^{(n)}, \tag{3.25}$$

$$S^{(n)} = \frac{1}{n!} \int_0^\beta d\tau_1 ... \int_0^\beta d\tau_n \, \chi^{(n)}_{\text{mat}}(\tau_1, ..., \tau_n) \varphi(\tau_1) ... \varphi(\tau_n), \tag{3.26}$$

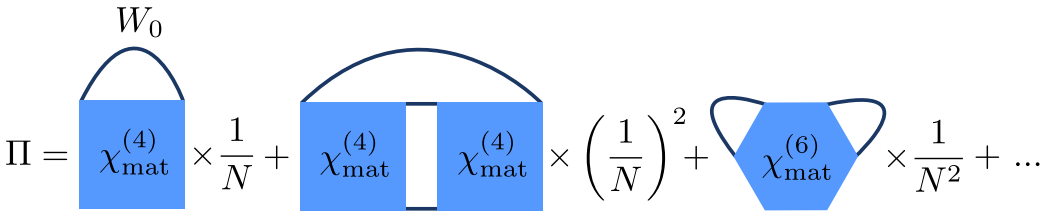

Figure 3.1.: *Diagrammatic representation of the self-energy* Π. *The lines correspond to the non-interacting* φ*-propagator, while the* n*-point interaction vertices are given by* $\chi^{(n)}_{\mathrm{mat}}/N^{\frac{n-2}{n}}$, *where* $\chi^{(n)}_{\mathrm{mat}}$ *denotes the* n*th-order connected correlation function of the matter. [Graphic reproduced from Ref. [60].]*

where

$$W_0^{-1} = V_{\mathrm{ind}}^{-1} + \chi_{\mathrm{mat}} \quad \Rightarrow \quad W_0 = \frac{V_{\mathrm{ind}}}{1 + V_{\mathrm{ind}}\chi_{\mathrm{mat}}}. \tag{3.27}$$

This action only depends on a single collective variable φ. The material specific properties are fully contained in the collective correlation functions $\chi^{(n)}_{\mathrm{mat}}$, which give rise to n-point interactions of the auxiliary Hubbard-Stratonovich field φ. The effect of the cavity mode only enters the quadratic term.

3.1.4. Perturbation series

Based on Eq. (3.25), we derive a diagrammatic expansion for the full propagator W of the Hubbard-Stratonovich field. The latter can be written in terms of the bare propagator W_0 defined in (3.27) and a self-energy Π that contains the corrections, i.e.,

$$W^{-1} = W_0^{-1} - \Pi. \tag{3.28}$$

With this, the matter susceptibility (3.19) becomes

$$\chi = V_{\mathrm{ind}}^{-1} - V_{\mathrm{ind}}^{-1}\frac{1}{V_{\mathrm{ind}}^{-1} + \chi_{\mathrm{mat}} - \Pi}V_{\mathrm{ind}}^{-1} = \frac{\chi_{\mathrm{mat}} - \Pi}{1 + (\chi_{\mathrm{mat}} - \Pi)V_{\mathrm{ind}}}. \tag{3.29}$$

Our goal is to analyze the effect of the light-matter interaction on a system in equilibrium; therefore, we consider the static response of the system, i.e., we focus on the zero frequency component. As mentioned previously, the induced interaction $V_{\mathrm{ind}}(i\nu_0) = 0$, and hence,

$$\chi(i\nu_0) = \chi_{\mathrm{mat}}(i\nu_0) - \Pi(i\nu_0). \tag{3.30}$$

We can see from this expression that the static self-energy also constitutes the correction to the static susceptibility.

To gain a better understanding of these corrections, we consider the diagrammatic expansion of Π. The lowest order diagrams are shown in Fig. 3.1. Here the lines correspond to the bare Hubbard-Stratonovich propagator W_0 and the polygons represent the nth order non-linear response functions $\chi^{(n)}_{\mathrm{mat}}$ of the matter. Moreover, as indicated in the graphic, each interaction vertex scales as $1/N^{n/2-1}$. We can distinguish two limiting cases: (i) If the number of dipoles N is small, the interaction vertices are of order one, and the series is controlled by the number of lines W_0. The latter are proportional to the collective coupling $g_n^2 = Ng_1^2$, which is of the order g_1^2 for small N. Typically, since $g_1^2 \sim 1/V$, this is a rather small quantity; therefore, the leading diagram is the Hartree diagram (first diagram in Fig. 3.1). (ii) For a large number of particles ($N \gg 1$) and fixed collective coupling g_n^2 (which can take values comparable to or greater than the energy scales of matter), the series is no longer controlled by the interaction lines W_0. However, the vertices are suppressed by the prefactor $1/N^{n/2-1}$. Again, the Hartree diagram represents the leading diagram.

Let us also briefly discuss the extreme case in which $N \to \infty$ but the density N/V (and thus g_n^2) is fixed. This is nothing but the thermodynamic limit. In this case, even the Hartree diagram vanishes, and thus $\Pi = 0$. Consequently, the static response of the material is not modified due to the light-matter interaction.The corresponding frequency dependent susceptibility (3.29) is given by

$$\chi = \frac{\chi_{\mathrm{mat}}}{1 + \chi_{\mathrm{mat}} V_{\mathrm{ind}}}. \tag{3.31}$$

This expression coincides with the standard RPA (random phase approximation) equation that can be obtained within a heuristic mean-field treatment.

3.1.5. Hartree diagram

We now proceed by analyzing the Hartree diagram (first diagram in Fig. 3.1), which represents the leading order correction to the susceptibility in most regimes. Using standard diagrammatic rules, the corresponding mathematical expression reads as

$$\Pi_H(\tau_1, \tau_2) = -\frac{1}{2N} \int_0^\beta d\tau_3 d\tau_4 \, \chi^{(4)}_{\mathrm{mat}}(\tau_1, \tau_2, \tau_3, \tau_4) W_0(\tau_3, \tau_4). \tag{3.32}$$

We are particularly interested in the static component ($i\nu_0$) of the self-energy, as it influences the equilibrium properties of the system. It is given by

$$\begin{aligned} \Pi_{\mathrm{stat}} =& \frac{1}{\beta} \int_0^\beta d\tau_1 d\tau_2 \, \Pi_H(\tau_1, \tau_2) \\ =& -\frac{1}{2N\beta} \int_0^\beta d\tau_1 d\tau_2 d\tau_3 d\tau_4 \, \chi^{(4)}_{\mathrm{mat}}(\tau_1, \tau_2, \tau_2, \tau_3) W_0(\tau_3 - \tau_4), \end{aligned} \tag{3.33}$$

where the fourth order correlation function $\chi^{(4)}_{\mathrm{mat}}$ can be calculated from the fourth derivative of the generating function $\mathcal{G}_{\mathrm{mat}}[y]$ (cf. Eq. (3.22)). It is possible to replace the

τ-integrated derivatives by derivatives with respect to a static field h using the relation

$$\begin{aligned}\int_0^\beta d\tau_1 \frac{\delta}{\delta y(\tau_1)} \log \int \mathcal{D}[\bar{c},c] e^{-\left(S_{\rm mat}+i\sum_r \int_0^\beta d\tau p_r(\tau) y(\tau)\right)} \\ = i\frac{\partial}{\partial h} \log \int \mathcal{D}[\bar{c},c] e^{-S_{\rm mat}(h)}\end{aligned} \tag{3.34}$$

with $S_{\rm mat}(h) = S_{\rm mat} + h\sum_r \int_0^\beta d\tau p_r(\tau)$. This yields the following expression

$$\begin{aligned}\Pi_{\rm stat} = -\frac{1}{2N\beta}\int_0^\beta d\tau_3 d\tau_4\, W_0(\tau_3-\tau_4)(i)^2 \times \\ \times \frac{\partial^2}{\partial h^2}\frac{\delta^2}{\delta y(\tau_3)\delta y(\tau_4)}\Big(\frac{-1}{N}\Big) \log \int \mathcal{D}[\bar{c},c] e^{-\left(S_{\rm mat}(h)+i\sum_r \int_0^\beta d\tau p_r(\tau) y(\tau)\right)}\Big|_{\substack{y=0\\h=0}}.\end{aligned} \tag{3.35}$$

The remaining derivatives with respect to the source field $y(\tau)$ then give the second order correlation function for the bare material with an additional source field h (but without cavity)

$$\begin{aligned}\frac{\delta^2}{\delta y(\tau_3)\delta y(\tau_4)}\Big(\frac{-1}{N}\Big) \log \int \mathcal{D}[\bar{c},c] e^{-\left(S_{\rm mat}(h)+i\sum_r \int_0^\beta d\tau p_r(\tau) y(\tau)\right)}\Big|_{y=0} \\ = \frac{1}{N}\sum_{r,r'} \langle p_r(\tau_3) p_{r'}(\tau_4)\rangle_h^{\rm con} \equiv \chi_h(\tau_3-\tau_4),\end{aligned} \tag{3.36}$$

where $\langle\cdots\rangle_h = \langle\cdots\rangle_{S_{\rm mat}(h)}$ denotes the expectation value in the presence of the field h. In summary, we obtain

$$\Pi_{\rm stat} = \frac{1}{2N\beta}\frac{\partial^2}{\partial h^2}\int_0^\beta d\tau_3 d\tau_4\, W_0(\tau_3-\tau_4)\chi_h(\tau_3-\tau_4)\Big|_{h=0}. \tag{3.37}$$

Using time-translation invariance and the symmetry $W_0(\tau) = W_0(\beta-\tau)$, this can be rewritten as

$$\Pi_{\rm stat} = \frac{1}{2N}\frac{\partial^2}{\partial h^2}\int_0^\beta d\tau\, W_0(\beta-\tau)\chi_h(\tau)\Big|_{h=0}. \tag{3.38}$$

Transforming the equation above to Matsubara space then yields

$$\Pi_{\rm stat} = \frac{1}{2N\beta}\sum_m\ W_0(i\nu_m)\frac{\partial^2\chi_h(i\nu_m)}{\partial h^2}\Big|_{h=0}. \tag{3.39}$$

From this expression, we can already deduce two important points: (i) In contrast to the macroscopic response (thermodynamic limit), the static correction of the susceptibility at finite N depends on all frequencies $i\nu_m$. This is due to the nonlinearities of the matter response contained in $\frac{\partial^2\chi_h(i\nu_m)}{\partial h^2}$, which mix different Matsubara components. As a result, the light-matter coupling gives rise to a non-vanishing contribution. Note that the importance of nonlinearities for cavity-induced effects has already been highlighted

for other systems, e.g., in [6]. (ii) The cavity correction becomes small if the photon frequency Ω is large compared to the energy scales of the matter and in the limit of high temperatures (i.e., $\beta \to 0$). This can be explained by the following considerations: Above some large energy scale $E_{\max}$ that is entirely set by the material, the matter response χ_h goes to zero, i.e., for $\nu_m = 2\pi m/\beta \gg E_{\max}$ $\chi_h(i\nu_m) \to 0$. Apart from that, the induced interaction V_{ind} is small for Matsubara frequencies $\nu_m \ll \Omega$. As a result, the effect of the cavity is small if $\Omega \gg E_{\max}$ and $\beta E_{\max} \ll 1$.

3.2. Minimal model with all-to-all interaction

To illustrate the collective theory, we analyze the $1/N$ correction for a simple model Hamiltonian. A similar system has also been studied in Ref. [15] in a wide range of parameters. We assume that the matter part consists of N two-level systems (TLS) with eigenstates $|g_r\rangle$ and $|e_r\rangle$ that are separated by an energy gap Δ. Analogous to Sec. 2.4, we represent the TLS by pseudo-spin operators $\hat{\sigma}_{\nu,r}$ with $\nu \in \{x, y, z\}$ (see Eq. (2.70)). With this the Hamiltonian for the non-interacting emitters is given by $\hat{H}_{\text{at}} = \frac{\Delta}{2} \sum_r \hat{\sigma}_{z,r}$. The eigenstates are of opposite parity, so that the transitions between $|g_r\rangle$ and $|e_r\rangle$ are associated with an electric dipole moment. Thus, the Pauli operator $\hat{\sigma}_{x,r}$ corresponds to the dipolar transitions, and represents the dimensionless operator $\hat{p}_r$ introduced in Sec. 3.1.1. In addition, we include a static all-to-all dipole-dipole interaction between the individual two-level systems, so that the matter Hamiltonian reads as

$$\hat{H}_{\text{mat}} = \frac{\Delta}{2} \sum_{r=1}^{N} \hat{\sigma}_{z,r} - \frac{\alpha}{2N} \sum_{r,r'} \hat{\sigma}_{x,r} \hat{\sigma}_{x,r'}. \tag{3.40}$$

The mean-field phase diagram of this model has already been discussed in Sec. 2.4 and is shown in Fig. 2.8. In the limit $N \to \infty$, the system exhibits a second-order phase transition to a ferroelectric state driven by the dipole-dipole interaction α. In this phase, the dipolar moments align, and the solid acquires a macroscopic electric polarization. For $\Delta > 0$ and small α, the system remains paraelectric even down to zero temperature. This is due to quantum fluctuations that suppress the ferroelectric ordering; therefore, the low-temperature regime is also referred to as the quantum-paraelectric phase. As mentioned previously, the collective theory is only valid in a system that is invariant under inversions (see Sec. 3.1.3). Since this symmetry is broken in the ferroelectric phase, we study the effect of the cavity mode only in the paraelectric and quantum-paraelectric regimes.

3.2.1. Imaginary-time action

In principle, we could directly apply the collective theory derived in Sec. 3.1 to the model Hamiltonian (3.40). For that purpose, we would have to determine the susceptibility of the bare material and the corresponding cavity corrections. However, we slightly adapt the approach to the present system. This allows us to carry out most calculations analytically.

As in the original formalism, the photon fields can be integrated out, which yields an effective action

$$S_{\text{eff}}[\bar{c}, c] = \sum_r S_{\text{at}}[\bar{c}, c] - S_V[\bar{c}, c]. \tag{3.41}$$

Here, we have combined the direct dipole-dipole interaction and the photon-mediated interaction in a single term

$$S_V = \frac{1}{2N} \int_0^\beta d\tau \int_0^\beta d\tau' P(\tau) V(\tau - \tau') P(\tau'), \tag{3.42}$$

with $V(\tau) = \alpha\delta(\tau) - V_{\text{ind}}(\tau)$. Note that the sign has been chosen such that V is positive if the single-particle coupling g_1^2 is small. With this the first term S_{at} corresponds to the non-interacting dipoles. We can now decouple the combined interaction S_V using a Hubbard-Stratonovich transformation

$$e^{S_V} = \frac{1}{Z_V} \int \mathcal{D}[\varphi] e^{-\frac{1}{2}\int_0^\beta d\tau \int_0^\beta d\tau' \varphi(\tau) V^{-1}(\tau-\tau')\varphi(\tau') - \int_0^\beta d\tau \sum_r \frac{\varphi(\tau)}{\sqrt{N}} p_r(\tau)}. \tag{3.43}$$

This is analogous to the approach discussed in Sec. 3.1.3 for the induced interaction. However, we do not include a factor i in the linear coupling term, because the action S_V has opposite sign to S_{ind}. Relation (3.19) changes accordingly and now reads as

$$\chi(i\nu_m) = -V(i\nu_m)^{-1} + V(i\nu_m)^{-1} W(i\nu_m) V(i\nu_m)^{-1}. \tag{3.44}$$

In the next step, we integrate out the matter degrees of freedom. Again, this is analogous to the derivation discussed in Sec. 3.1.3, apart from two modifications: (i) Since the interaction V already includes the direct dipole-dipole interactions of the matter and S_{at} only describes the non-interacting atoms, $\chi_{\text{mat}}^{(n)}$ is replaced by the atomic susceptibilities $\chi_{\text{at}}^{(n)}$, and (ii) to account for the factor i in the linear coupling term, we have to use $N\mathcal{G}_{\text{at}}[-i\varphi/\sqrt{N}]$ instead of $N\mathcal{G}_{\text{mat}}[\varphi/\sqrt{N}]$. This finally yields

$$S[\varphi] = \frac{1}{2} \int_0^\beta d\tau \int_0^\beta d\tau' \varphi(\tau) V^{-1}(\tau - \tau') \varphi(\tau') + N\mathcal{G}_{at}[-i\varphi/\sqrt{N}]. \tag{3.45}$$

Using the Taylor expansion of $\mathcal{G}_{\text{at}}$, we obtain

$$S[\varphi] = \frac{1}{2} \int_0^\beta d\tau \int_0^\beta d\tau' \varphi(\tau) W_0^{-1}(\tau - \tau') \varphi(\tau') + \sum_{n=4,6,\ldots} (-1)^{\frac{n}{2}} N^{1-\frac{n}{2}} S^{(n)}, \tag{3.46}$$

$$S^{(n)} = \frac{1}{n!} \int_0^\beta d\tau_1 \ldots \int_0^\beta d\tau_n \, \chi_{\text{at}}^{(n)}(\tau_1, \ldots \tau_n) \varphi(\tau_1) \ldots \varphi(\tau_n), \tag{3.47}$$

where

$$W_0^{-1} = V^{-1} - \chi_{\text{at}} \quad \Rightarrow \quad W_0 = \frac{V}{1 - \chi_{\text{at}} V}. \tag{3.48}$$

Note that the sign of the terms of order $n = 2, 6, 10, \ldots$ has been reversed due to the additional i factor.

3.2.2. Mean-field theory

Based on the action (3.46), we can now consider the susceptibility to different orders of approximation. The mean-field description is obtained by keeping only the leading term in $1/N$, i.e., setting $W = W_0$. Substituting this into Eq. (3.44) yields

$$\chi_{\mathrm{mf}} = \frac{1}{V}\Big[\frac{1}{1-\chi_{\mathrm{at}}V} - 1\Big] = \frac{\chi_{\mathrm{at}}}{1-\chi_{\mathrm{at}}V}. \tag{3.49}$$

Since the light-induced part of the interaction V vanishes at $i\nu_m = 0$, the static contribution is given by

$$\chi_{\mathrm{mf}}(0) = \frac{\chi_{\mathrm{at}}(0)}{1-\chi_{\mathrm{at}}(0)\alpha}. \tag{3.50}$$

This expression diverges if

$$1 - \chi_{\mathrm{at}}(0)\alpha = 0, \tag{3.51}$$

which indicates a second-order phase transition. The latter corresponds to the ferroelectric phase transition discussed earlier.

The atomic susceptibility can be calculated analytically and reads as

$$\begin{aligned}\chi_{\mathrm{at}}(\tau) =& \frac{1}{Z}\mathrm{tr}\big(e^{-(\beta-\tau)\hat{H}_{\mathrm{at}}}\hat{\sigma}_x e^{-\tau\hat{H}_{\mathrm{at}}}\hat{\sigma}_x\big) = \frac{e^{(\beta-\tau)\Delta/2}e^{-\tau\Delta/2} + e^{-(\beta-\tau)\Delta/2}e^{\tau\Delta/2}}{e^{\beta\Delta/2}+e^{-\beta\Delta/2}} \\ =& \frac{\cosh((\beta-2\tau)\Delta/2)}{\cosh(\beta\Delta/2)}.\end{aligned} \tag{3.52}$$

Transforming this into Matsubara space gives

$$\int_0^\beta d\tau e^{i\nu_m\tau}\chi_{\mathrm{at}}(\tau) = \tanh\Big(\frac{\beta\Delta}{2}\Big)\Big[\frac{1}{i\nu_m+\Delta} - \frac{1}{i\nu_m-\Delta}\Big] = \tanh\Big(\frac{\beta\Delta}{2}\Big)\frac{2\Delta}{\Delta^2+\nu_m^2}, \tag{3.53}$$

such that $\chi_{\mathrm{at}}(0) = \tanh\left(\frac{\beta\Delta}{2}\right)\frac{2}{\Delta}$. Therefore, the condition (3.51) can only be satisfied if α exceeds a critical value of at least $\Delta/2$ even at zero temperature. Otherwise, the system remains in a paraelectric or quantum-paraelectric state. This is in accordance with the results discussed in Sec. 2.4.

3.2.3. Static Hartree diagram

We now consider the leading-order correction for the static susceptibility. As in Sec. 3.1.4, we introduce a self-energy Π, such that the full Hubbard-Stratonovich propagator is given by $W^{-1} = W_0^{-1} - \Pi$. The bare propagator W_0 is defined in Eq. (3.48). Inserting this into Eq. (3.44) yields the susceptibility

$$\chi(i\nu_m) = \frac{\chi_{\mathrm{at}}(i\nu_m) + \Pi(i\nu_m)}{1-(\chi_{\mathrm{at}}(i\nu_m)+\Pi(i\nu_m))V(i\nu_m)}. \tag{3.54}$$

At zero frequency, the cavity-mediated part of the interaction vanishes; hence, the static response is given by

$$\chi(0) = \frac{\chi_{\mathrm{at}}(0) + \Pi(0)}{1 - (\chi_{\mathrm{at}}(0) + \Pi(0))\alpha}. \tag{3.55}$$

The atomic susceptibility has already been calculated in the previous section (see Eq. (3.53)). To obtain the static self-energy, we evaluate the expression for the Hartree diagram

$$\Pi_{\mathrm{stat}} = \frac{1}{2N\beta} \sum_m \; W_0(i\nu_m) \frac{\partial^2 \chi_h(i\nu_m)}{\partial h^2}\Big|_{h=0} \tag{3.56}$$

derived in Sec. 3.1.5. The bare propagator W_0 can directly be calculated from Eq. (3.48). The response function χ_h corresponds to the isolated atoms in the presence of an external static field h, i.e., we have to calculate the susceptibility $\chi_h(\tau) = \langle \hat{\sigma}_x(\tau)\hat{\sigma}_x(0)\rangle_h - \langle \hat{\sigma}_x\rangle_h^2$ for the Hamiltonian

$$\hat{H}_h = \frac{\Delta}{2}\hat{\sigma}_z + h\hat{\sigma}_x. \tag{3.57}$$

The latter has two eigenstates $|\pm\rangle$ with energy $E_\pm = \pm\sqrt{\Delta^2 + 4h^2}/2 \equiv \pm E_h/2$. Using the matrix elements $|v|^2 \equiv |\langle +|\sigma_x|-\rangle|^2 = \Delta^2/E_h^2$ and $|u|^2 \equiv |\langle +|\sigma_x|+\rangle|^2 = |\langle -|\sigma_x|-\rangle|^2 = 1 - |v|^2$, we obtain

$$\chi_h(\tau) = (1-|v|^2)\Big[1 - \tanh\Big(\frac{\beta E_h}{2}\Big)^2\Big] + |v|^2 \frac{\cosh((\frac{\beta}{2} - \tau)E_h)}{\cosh(\beta E_h/2)} \tag{3.58}$$

$$= \frac{4h^2}{E_h^2}\Big[1 - \tanh\Big(\frac{\beta E_h}{2}\Big)^2\Big] + \frac{\Delta^2}{E_h^2} \frac{\cosh((\frac{\beta}{2} - \tau)E_h)}{\cosh(\beta E_h/2)}. \tag{3.59}$$

In Matsubara representation, this reads as

$$\chi_h(i\nu_m) = \delta_{m,0}\beta(1-|v|^2)\Big[1 - \tanh\Big(\frac{\beta E_h}{2}\Big)^2\Big] + |v|^2 \tanh\Big(\frac{\beta E_h}{2}\Big) \frac{2E_h}{E_h^2 + \nu_m^2} \tag{3.60}$$

$$= \delta_{m,0}\beta \frac{4h^2}{E_h^2}\Big[1 - \tanh\Big(\frac{\beta E_h}{2}\Big)^2\Big] + \frac{\Delta^2}{E_h} \tanh\Big(\frac{\beta E_h}{2}\Big) \frac{2}{E_h^2 + \nu_m^2}. \tag{3.61}$$

To determine the derivative $\frac{\partial^2}{\partial h^2}\chi_h(i\nu_m)$, we use the substitution $\partial_h^2|_{h=0} = 2\partial_{h^2}|_{h=0}$.

With this we have

$$\begin{aligned}\frac{\partial^2}{\partial h^2}\chi_h(i\nu_m)|_{h=0} =& 2\partial_{h^2}\Big\{\frac{\Delta^2}{E_h}\tanh\Big(\frac{\beta E_h}{2}\Big)\frac{2}{E_h^2+\nu_m^2} \\ &+ \beta\delta_{m,0}\frac{4h^2}{E_h^2}\Big[1-\tanh^2\Big(\frac{\beta E_h}{2}\Big)\Big]\Big\}_{h=0} \\ =& \frac{4}{E_h}\frac{\partial}{\partial E_h}\Big\{\frac{\Delta^2}{E_h}\tanh\Big(\frac{\beta E_h}{2}\Big)\frac{2}{E_h^2+\nu_m^2}\Big\}_{h=0} \\ &+ \delta_{m,0}\frac{8\beta}{\Delta^2}\Big[1-\tanh^2\Big(\frac{\beta\Delta}{2}\Big)\Big] \\ =& -\frac{8}{\Delta}\tanh\Big(\frac{\beta\Delta}{2}\Big)\frac{\nu_m^2+3\Delta^2}{(\Delta^2+\nu_m^2)^2} + 2\beta\cosh^{-2}\Big(\frac{\beta\Delta}{2}\Big)\frac{2}{\Delta^2+\nu_m^2} \\ &+ \delta_{m,0}\frac{8\beta}{\Delta^2}\Big[1-\tanh^2\Big(\frac{\beta\Delta}{2}\Big)\Big].\end{aligned} \tag{3.62}$$

The Matsubara sum in (3.56) can now be evaluated numerically. Since $|\chi_h(i\nu_m)| \sim \nu_m^{-2}$ for large m, it is expected to converge.

3.2.4. Dielectric constant

Before we turn to the results, we briefly derive the relation between the static susceptibility $\chi(0)$ and the dielectric constant ε. In classical electrodynamics, the latter quantifies the response of the macroscopic polarization density $\vec{P}(\vec{r})$ of a material to an external classical electric field $\vec{E}_{\text{ext}}(\vec{r})$. For a homogeneous and isotropic medium, it is defined by the relation

$$\vec{P} = (\varepsilon - 1)\varepsilon_0 \vec{E}_{\text{ext}}. \tag{3.63}$$

Similarly, for our microscopic model, the static susceptibility $\chi(0)$ describes the response of $\langle\hat{P}\rangle/N$ to an external field h that couples to the dipole operator $\hat{P}$, i.e.,

$$\frac{\langle\hat{P}\rangle}{N} = \chi(0)h. \tag{3.64}$$

For a material of volume V, we can determine the polarization density from the microscopic dipole moments using the equation

$$|\vec{P}| = \frac{\sum_r \langle\hat{p}_r\rangle ed}{V}, \tag{3.65}$$

and, hence,

$$|\vec{P}| = \frac{\langle\hat{P}\rangle}{V} ed. \tag{3.66}$$

With Eq. (3.63) and (3.64) this yields

$$(\varepsilon - 1)\varepsilon_0 |\vec{E}_{\text{ext}}| = \chi(0) h e d \frac{N}{V}. \tag{3.67}$$

Assuming that the polarization density and the external electric field are uniform over the entire system, the interaction energy in the macroscopic (classical) description is given by $-|\vec{P}||\vec{E}_{\text{ext}}|V$. For the microscopic model, the expectation value of the interaction energy is given by $-h\langle\hat{P}\rangle$. Equating these two expressions results in the relation $|\vec{E}_{\text{ext}}|ed = h$, and, thus

$$\varepsilon = 1 + g_n^2\chi(0), \tag{3.68}$$

where the light-matter interaction strength is defined as $g_n^2 = \frac{(ed)^2}{V\varepsilon_0}N$.

3.2.5. Results and discussion

We now analyze how the static response of the interacting model is modified when it couples to the cavity mode. For that purpose, we consider the leading order $1/N$-correction in the paraelectric and quantum-paraelectric regime. As discussed in Sec. 3.1.4, we do not expect any light-induced effects in the thermodynamic limit; therefore, we focus on finite systems, where the Hartree diagram gives a non-vanishing contribution to the static susceptibility. This also allows us to compare the analytic results from the $1/N$-theory to data from exact diagonalization. In the following, we set the unit of energy to the level-splitting Δ, and the cavity frequency is given by $\Omega = 1$ unless stated otherwise.

The main panel of Fig. 3.2 illustrates the inverse static susceptibility for a system of five emitters at $\alpha = 0.2$. In mean-field approximation, this value corresponds to the quantum-paraelectric regime. The blue and the red curve show the results for a collective light-matter coupling of $g_n^2 = 0$ and $g_n^2 = 1$, respectively. Moreover, the black dashed line indicates the mean-field solution χ_∞, which becomes exact in the thermodynamic limit ($N \to \infty$). As discussed previously, the latter does not depend on the light-matter coupling strength, as the cavity corrections vanish in this limit. The solid lines correspond to the analytic solution obtained from the evaluation of the Hartree diagram, while the dots represent numerical data determined from exact diagonalization. As can be seen from the graphic, the coupling to the cavity mode does have an effect on the static response of the finite system. Without light-matter coupling (blue curve for $g_n^2 = 0$), finite-size fluctuations lead to a reduction of the static susceptibility (an increase in the inverse susceptibility) as compared to the thermodynamic limit. If the material is coupled to the cavity mode, however, the static response is enhanced (see red curve for $g_n^2 = 1$) and can even exceed the solution for $N \to \infty$. Furthermore, it should be mentioned that the analytical and exact diagonalization results are in good agreement even for this small number of dipoles. The inset in Fig. 3.2 shows how the deviation of the static susceptibility from χ_∞ depends on the system size N at $T = 0.01$ (vertical grey line in the main panel). As expected, it converges to the mean-field result as $1/N$.

To further analyze the effect of the light-matter interaction, we fix the temperature to $T = 0.01$ and consider the static susceptibility as a function of g_n^2. This is displayed in Fig. 3.3(a) for $N = 1$, $N = 5$ and $N = 16$ at $\alpha = 0.2$. Again, the $N = \infty$ result is indicated by the black dashed line and does not depend on the coupling strength g_n^2. For finite N, however, the static response grows with increasing g_n^2, and, at some point,

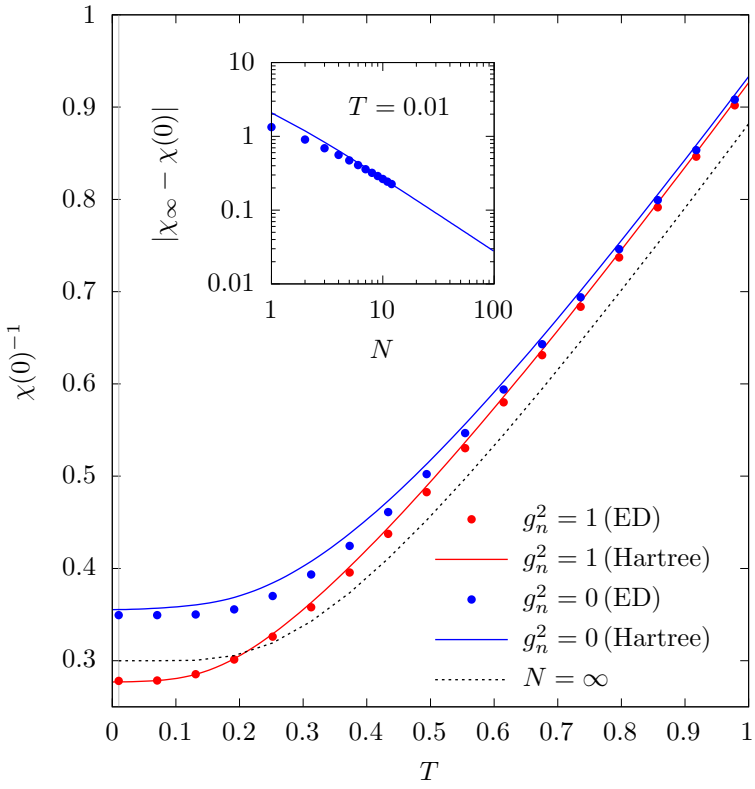

Figure 3.2.: *Static susceptibility for the interacting model with $\Delta = 1$ and $\Omega = 1$ in the (quantum-)paraelectric regime ($\alpha = 0.2$). Main panel: Inverse static susceptibility $\chi(0)$ as a function of temperature for $N = 5$ atoms with ($g_n^2 = 1$) and without ($g_n^2 = 0$) light-matter coupling. The black dashed line corresponds to the mean-field solution ($N \to \infty$). Inset: Difference between the mean-field susceptibility χ_∞ and the static susceptibility $\chi(0)$ as a function of N at $g_n^2 = 0$. The temperature is fixed at $T = 0.01$ (see vertical gray line in the main panel). In both panels, symbols correspond to results obtained from exact diagonalization (ED), whereas solid lines have been calculated from the leading $1/N$-theory (Hartree). [Graphic adapted from Ref. [60].]*

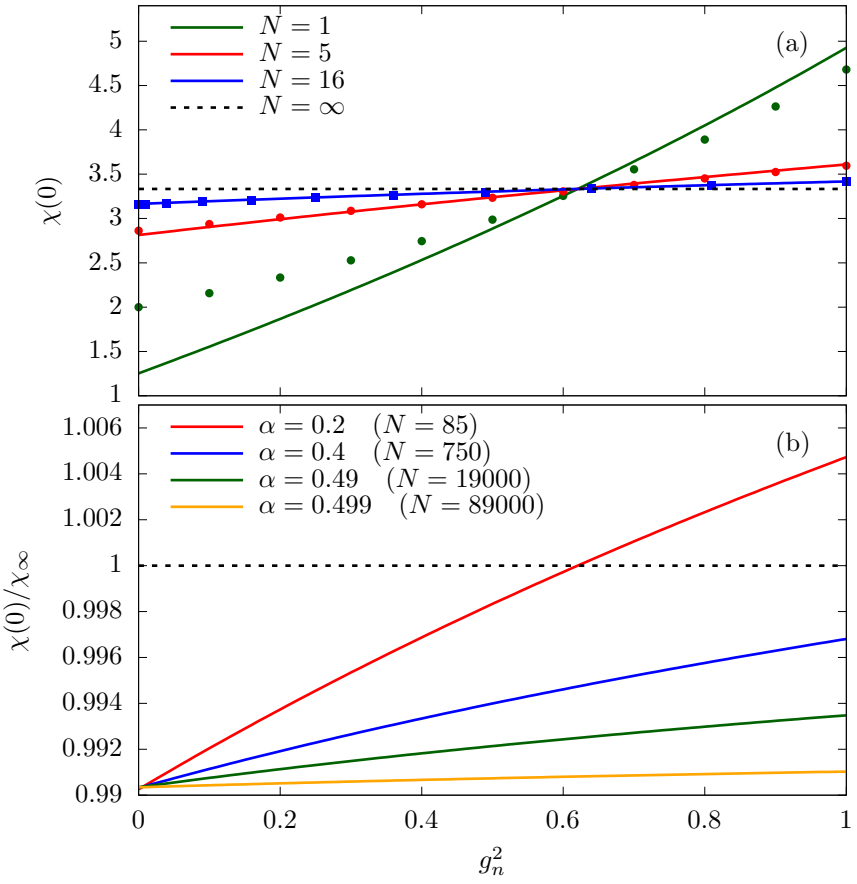

Figure 3.3.: *(a) Low-temperature results for the static susceptibility of the interacting model as a function of the collective light-matter coupling g_n^2 in the quantum-paraelectric regime ($\alpha = 0.2$, $\Delta = 1$, $\Omega = 1$). The horizontal black dashed line shows the mean-field result ($N \to \infty$). Dots indicate numerical results obtained from exact diagonalization (ED) for a system with $N = 1$ (green) and $N = 5$ (red) emitters. Calculations for $N = 16$ represented by the blue squares have been carried out using the Lanczos method. The solid curves result from a direct evaluation of the Hartree diagram for the self-energy. (b) $\chi(0)/\chi_\infty$ as a function of g_n^2 at low temperature for various values of α. All results have been obtained from the Hartree approximation for the self-energy. For each curve, N has been chosen such that the relative deviation of $\chi(0)$ from the mean-field result at $g_n^2 = 0$ is around 1%. [Graphic adapted from Ref. [60].]*

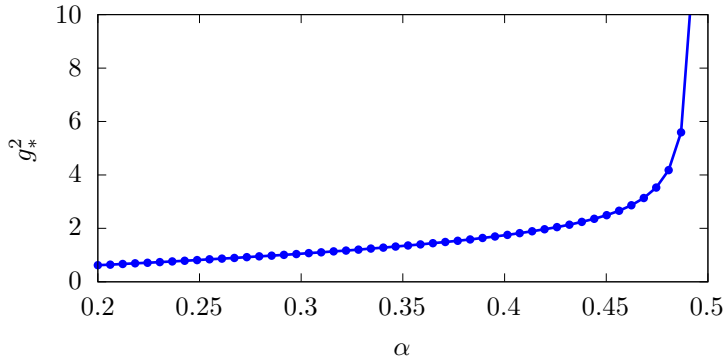

Figure 3.4.: *g_*^2 as a function of α at low temperature ($T = 0.01$). This quantity represents the value of the collective light-matter coupling that is required to compensate for the finite-size reduction of the static susceptibility (i.e., it is given by the crossing point of the static susceptibility $\chi(0)$ and the mean-field solution χ_∞). [Graphic adapted from Ref. [60].]*

even surpasses the mean-field result. Moreover, comparing the individual curves shows that the correction to χ_∞ becomes larger as N is decreased.

Thus far, all results have been obtained for a fixed value of the all-to-all interaction strength $\alpha = 0.2$. In the next step, we investigate how the cavity effect is influenced if the system approaches the transition to the ferroelectric state at $\alpha_c = 0.5$. As mentioned previously, the susceptibility χ_∞ diverges at this value; therefore, we also expect an effect on the static response of the finite system if it is close to the critical point. In Fig. 3.3(b), we plot the ratio $\chi(0)/\chi_\infty$ as a function of g_n^2 for $\alpha = 0.2, 0.4, 0.49, 0.499$; the corresponding absolute values of χ_∞ are 3.33, 10.0, 100.0, and 1000.0. Therefore, approaching the critical value α_c, requires an increasingly large number of emitters N. Otherwise, the leading $1/N$-correction becomes inaccurate. For this reason, we choose the value for each α such that the relative $1/N$-correction $|\frac{\chi_\infty - \chi(0)}{\chi_\infty}|$ is already small ($\approx 1\%$) at $g_n^2 = 0$. Again, it can be seen from the figure that the static response for the finite system is enhanced by the light-matter coupling. At fixed g_n^2, the effect is most significant for $\alpha = 0.2$ and becomes weaker as α approaches the critical value.

The results depicted in Fig. 3.4 confirm this finding. Here, we plot the value $g_n^2 = g_*^2$, at which the cavity-induced enhancement exactly cancels the finite-size reduction of the susceptibility, as a function of alpha. For instance, the value for $\alpha = 0.2$ can be extracted from Fig. 3.3(b) and corresponds to the crossing point of the red curve for the finite system and the black dashed line for the thermodynamic limit ($g_*^2 \approx 0.6$). It is interesting to note that g_*^2 does not depend on the system size N within the $1/N$-theory. It is clearly visible, that the value g_*^2 increases as α approaches its critical value. Consequently, a larger light-matter interaction is required to compensate the finite-size effect if the system is brought closer to the critical regime . This might be due to the fact that, close to criticality, finite-size fluctuations become more and more significant.

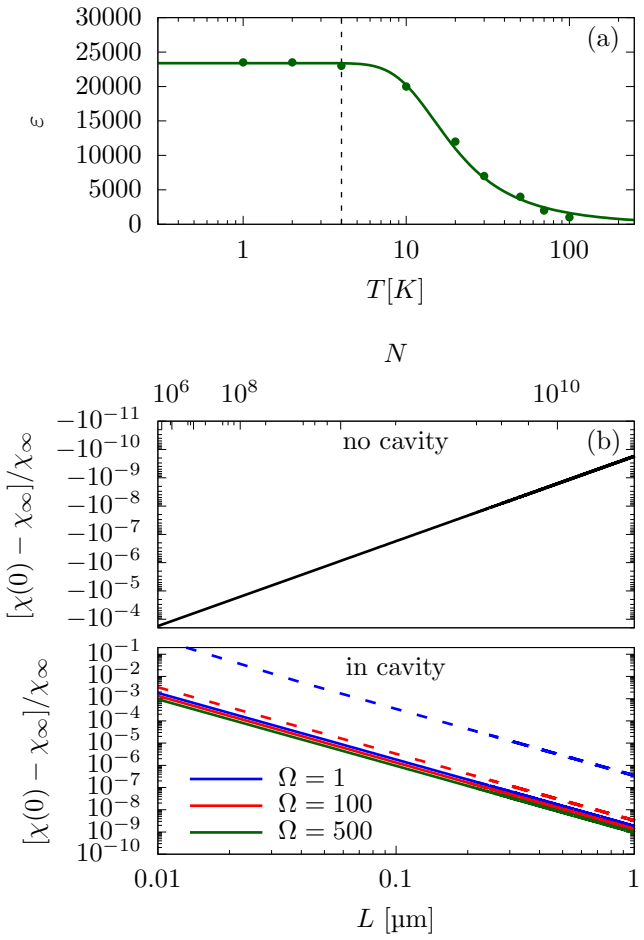

Figure 3.5.: *(a) Dielectric constant for the interacting model with $\alpha = 0.328$ and $g_n^2 = 4024$ as a function of T. The curve has been obtained from a mean-field calculation. If the transition frequency is set to 5 THz ($\Delta = 3.3$ meV), the results match experimental data for STO taken from [69], which are indicated by the dots. The vertical black dashed line marks the onset of the quantum-paraelectric regime of STO at approximately 4 K.(b) Relative deviation of the static susceptibility from the mean-field limit for the parameters estimated for STO. The upper panel shows the solution without cavity coupling, and the lower panel illustrates the results for various cavity frequencies Ω. For a three-dimensional block of material, the volume of the system is given by $L^3 = Na^3$, where $a = 3.9$ Å denotes the lattice constant of STO. The lower (upper) horizontal axis shows the system size using the length scale L (the number of atoms N). The blue (red) dashed line corresponds to the polaronic approximation for $\Omega = 1$ ($\Omega = 100$). [Graphic adapted from Ref. [60].]*

Comparison to STO

Thus far, we have freely chosen the parameters of the Hamiltonian. Therefore, all considerations have been on a purely qualitative level. In the next step, we try to relate our model to a real quantum-paraelectric material. An interesting candidate is the perovskite $SrTiO_3$ (STO) [69], which has already been mentioned in Sec. 2.4. While classical calculations for STO predict the existence of a ferroelectric state at low temperatures, the material remains paraelectric even at $T \to 0$. This is due to nuclear quantum fluctuations, which suppress the phase transition. However, it is possible to induce ferroelectricity for instance, through strain, isotope substitution or strong laser pumping [71, 64]. This is analogous to the parameter α in the present model, which drives the phase transition and even makes it possible to overcome the effect of quantum fluctuations in the quantum-paraelectric regime.

Needless to say, our simplistic Hamiltonian cannot be considered as a microscopic model for STO. But on a macroscopic level, it shows the same phenomenology. This allows us to determine the model parameters in such a way that the temperature-dependent bulk dielectric constant $\varepsilon(T)$ of STO is reproduced. For the model Hamiltonian, the latter is given by

$$\varepsilon(T) = 1 + g_n^2 \chi_\infty(i\nu_m = 0, T). \tag{3.69}$$

(see Sec. 3.2.4). Here, we use the mean-field susceptibility χ_∞ because it corresponds to the macroscopic solid. Consequently, the result is the same inside and outside the cavity. Performing a least-square fit of Eq. (3.69) to experimental data for STO taken from Ref. [69], yields the following parameters: $\Delta = 3.3$ meV (5 THz), $\alpha = 0.328\Delta$ and $g_n^2 = 4024\Delta$. The corresponding curve as well as the experimental data are displayed in Fig. 3.5(a). This approach is analogous to the mean-field fit used in Ref. [69] and [8], even though it is based on a different atomic model (anharmonic oscillator).

Using the parameters determined above, we calculate the relative deviation of the static susceptibility for a finite system from the thermodynamic limit in the low-temperature regime. The volume of the system is given by $L^3 = Na^3$, where $a = 3.9$Å denotes the lattice constant of STO [82]. Fig. 3.5(b) shows the result. Here, the lower and upper horizontal axis indicate the length scale L in µm, and the number of dipoles N, respectively. The upper panel corresponds to the system without coupling to the cavity ($g_n^2 = 0$) and, thus, only shows the finite-size reduction of the static response. In the lower panel, the collective light-matter coupling is set to $g_n^2 = 4024$, which leads to an enhancement of the susceptibility. This effect is significantly stronger than the finite-size reduction at $g_n^2 = 0$. Moreover, it can be seen that both with and without the cavity, the correction of the susceptibility for the finite system to the thermodynamic limit decays as $1/N$ (note that the N-axis is scaled logarithmically). It is expected that the leading-order correction constitutes a reasonable approximation as long as it takes a small value itself. For the given parameters, this condition is fulfilled down to very small system sizes of 10nm. This implies that the cavity-induced effect on the static susceptibility becomes experimentally observable only for very small cavities.

Polaronic interpretation

A possible explanation for the cavity-induced enhancement of the susceptibility is a mechanism similar to the phenomenon of dynamical localization [81]. Due to the light-matter interaction, the cavity mode and the matter degrees of freedom form hybrid light-matter objects, which are also referred to as polarons. This can lead to an effective reduction of the parameter Δ, and hence, suppress the quantum fluctuations that stabilize the paraelectric state. As a result, the tendency to order is enhanced and the system is pushed closer to the ferroelectric phase transition. This is indicated by an increase in the static susceptibility.

To analyze this effect for the present model, we perform the standard Lang-Firsov transformation

$$\hat{W} = e^{\frac{g_1}{\sqrt{2\Omega}}\hat{P}(\hat{a}^\dagger - \hat{a})}. \tag{3.70}$$

Under this transformation, the photon operators are shifted as $\hat{W}\hat{a}\hat{W}^\dagger = \hat{a} - g_1/\sqrt{2\Omega}\hat{P}$, such that the previous light-matter Hamiltonian $\Omega\hat{a}^\dagger\hat{a} + \hat{H}_{Ed} + \hat{H}_{dd}$ now takes the free field form $\Omega\hat{a}^\dagger\hat{a}$. The light-matter coupling enters the transformed matter Hamiltonian $\hat{W}\hat{H}_{\mathrm{mat}}\hat{W}^\dagger$. In summary, the new Hamiltonian reads as

$$\hat{H}' = \hat{W}\hat{H}\hat{W}^\dagger = \Omega\hat{a}^\dagger\hat{a} - \frac{\alpha}{2N}\sum_{r,r'}\hat{\sigma}_{x,r}\hat{\sigma}_{x,r'} + \sum_r \hat{h}'_r, \tag{3.71}$$

where

$$\hat{h}'_r = \frac{\Delta}{2}e^{\frac{g_1}{\sqrt{2\Omega}}\hat{\sigma}_{x,r}(\hat{a}^\dagger - \hat{a})}\hat{\sigma}_{z,r}e^{-\frac{g_1}{\sqrt{2\Omega}}\hat{\sigma}_{x,r}(\hat{a}^\dagger - \hat{a})}, \tag{3.72}$$

i.e., the light-matter interaction gives rise to photon emission and absorption in the tunneling. Projecting this Hamiltonian to the zero-photon sector then yields the polaronic picture, in which $\hat{h}'_r$ is approximated as

$$\hat{h}'_r \approx \frac{\tilde{\Delta}}{2}\hat{\sigma}_{z,r} \tag{3.73}$$

with the renormalized tunneling

$$\tilde{\Delta} = \Delta e^{-g_1^2/2\Omega} = \Delta e^{-\frac{1}{N}g_1^2/2\Omega}. \tag{3.74}$$

Thus, the "polaronic" susceptibility χ_{pol} can be calculated from the expression for a system without cavity, where the parameter Δ is replaced by $\tilde{\Delta}$. Similar to the $1/N$-theory, the cavity effect decreases as $1/N$ in this simple polaronic picture. However, the effect of the cavity is strongly overestimated. This can be seen in Fig. 3.5, where the results for χ_{pol} at $\Omega = 1$ and $\Omega = 100$ are indicated by the dashed lines. There are two possible reasons for this deviation. Firstly, the projection to the polaronic Hamiltonian is only expected to be accurate in the limit of large cavity frequencies $\Omega \gg \Delta$, and secondly, we have only projected the single-atom Hamiltonian $\hat{h}_r$ to the zero-photon subspace, and therefore do not take into account light-induced interactions between the polarons at different sites. Hence, our results imply that it is essential to include collective effects in order to understand the cavity-induced localization mechanism. An explanation on the level of individual atoms does not suffice.

3.3. Conclusion

Let us close this chapter with a brief summary of the most important results. First of all, it should be mentioned that our analysis is based on a model, where the coupling between light and matter is linear, and that we have focused on a regime, where the collective light-matter coupling g_n^2 can be large but the single-particle coupling g_1^2 is relatively small. Moreover, we have restricted our considerations to a single electromagnetic mode.

This allowed us to derive a collective theory, in which the response of the combined light-matter system is expressed in terms of the response functions for the isolated material. The cavity correction has been expanded in $1/N$ using standard diagrammatic techniques. From this general formalism, it can be seen that all light-induced effects on the static susceptibility vanish in the thermodynamic limit. For finite systems, however, even the static properties can be modified by the cavity mode. In this case, nonlinearities, which enter the theory via the nonlinear response functions of the bare material, are crucial for the cavity-induced effect. This observation has already been made for other coupled light-matter systems, where the interaction with the electromagnetic field affects the equilibrium state of a solid in a non-trivial way [6, 58].

In Sec. 3.2, we have applied the collective theory to a specific model of interacting dipoles. More precisely, we have calculated the leading $1/N$-correction to the static response of a small cluster of emitters. Our analysis has shown that the interaction with the cavity mode enhances the static susceptibility of the system. This finding is in accordance with data from exact diagonalization. However, it is not possible to reproduce the results from a simple polaronic interpretation, where the increase in susceptibility is explained by an effective modification of the model parameters. This implies that collective effects, which are not included in the polaronic picture, are important to fully describe the behavior of the system. As mentioned previously, the results presented in this chapter are qualitative and should not be understood as quantitative predictions for any real material. Nevertheless, a phenomenological comparison to the perovskite STO is possible and suggests that measurable effects are only obtained for small clusters of matter and small cavity volumes.

4. Dynamical mean-field study of a photon-mediated ferroelectric phase transition

In the previous chapter, we have developed a collective theory in order to investigate, how a single cavity mode influences the equilibrium state of a coupled light-matter system. The diagrammatic approach allowed us to include fluctuations beyond the mean-field approximation. This is crucial, because standard mean-field theory does not capture any photon-induced effects on the static properties of a collection of localized dipoles (see Sec. 2.3.3). In the course of this analysis, we have already encountered some important aspects that are required to engineer a system in equilibrium with quantum light. In particular, we have seen that for the single-mode setting, all contributions beyond the mean-field approximation vanish in the thermodynamic limit. Consequently, it is not possible to manipulate the equilibrium state of a macroscopic solid with just one electromagnetic mode if the single-particle coupling is finite. However, it has been shown previously that this statement is not necessarily true if the material couples to a continuum of modes, where the effect of all modes adds up [6]. In this case, the outcome depends on the specific setting. In free space or in an extended coplanar cavity, for instance, only a small range of modes efficiently couples to the matter degrees of freedom, such that the overall effect is negligible. This constraint can be overcome if the electromagnetic field is strongly confined to a small volume, which leads to an enhancement of the coupling even to degrees of freedom in the solid that would not be affected otherwise. Therefore, we now consider a setting where a macroscopic material couples to a surface plasmon polariton (SPP) mode in the proximity of a dielectric-metal interface. The SPPs may propagate freely along the metal surface but are strongly localized near the interface.

As in Sec. 3.2, we study a solid that consists of a collection of interacting dipoles. However, we now consider a two-dimensional layer inside a hetero-structure. Similar to the real material $SrTiO_3$ [69], this minimal model may undergo a paraelectric-to-ferroelectric phase transition and features a quantum-paraelectric phase at zero temperature (also see Sec. 2.4). Our goal is to investigate how this phase transition is influenced by the SPP mode. The interplay of a continuum of electromagnetic modes and ferroelectricity has already been studied in Ref. [6]. But in contrast to our approach, the authors do not start from a microscopic description of the material; instead, they express the Hamiltonian in terms of collective degrees of freedom.

The system under consideration constitutes a complex quantum many-body problem that cannot be solved exactly. Therefore, we apply dynamical mean-field theory (DMFT)

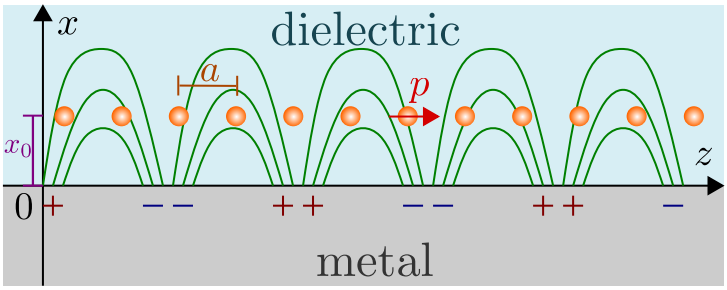

Figure 4.1.: *Schematic sketch of the setting. The graphic shows a two-dimensional slice in the x-z plane. We consider a two-dimensional material consisting of a collection of dipoles (orange dots) with dipole moment p arranged on a square lattice. The material is embedded in a dielectric medium and is located near a metal surface. The latter supports an SPP mode propagating in z-direction. The green lines represent the corresponding electric field lines. [Graphic reprinted from Ref. [61].]*

to obtain an approximate solution. The central idea of this approach is to reduce a lattice model to a self-consistent impurity model (see Sec. 2.1 and 2.2). For the light-matter system, we follow similar steps as in extended DMFT [7] and first map the model to an auxiliary problem with bosonic degrees of freedom. The corresponding impurity model then represents a generalized spin-boson model that can be solved using bosonic DMFT [3].

The remainder of this chapter is structured as follows: In Sec. 4.1 we introduce the model Hamiltonian as well as the corresponding imaginary-time action. Sec. 4.2 contains a description of the DMFT formalism and its numerical implementation. The results are discussed in Sec. 4.3, and in Sec. 4.4 we conclude with a summary of the most important findings. The content of this chapter has been published previously in Ref. [61].

4.1. Model

We consider a hetero-structure consisting of a dielectric-metal interface and a two-dimensional material that is embedded in the dielectric region. A schematic sketch of the setting is displayed in Fig. 4.1. As shown in the graphic, the two-dimensional material (orange dots) is placed at a distance x_0 parallel to the metal surface. It consists of N dipoles, which are arranged on a square lattice with lattice parameter a. The dipolar moments are parallel to the z-axis. If they align, the material acquires a non-vanishing electric polarization and becomes ferroelectric. The metal surface is located in the y-z plane. It supports a propagating surface plasmon mode that hybridizes with the bare electromagnetic field in the surrounding medium and forms a so-called surface plasmon polariton (SPP) mode. The corresponding evanescent electromagnetic field leaks into the dielectric region, and may interact with the two-dimensional material. Since the field is strongly confined to the dielectric-metal interface, the light-matter interaction is enhanced as compared to free space. This is in stark contrast to the modes traveling

along a coplanar cavity, which are extended over the full cavity volume, and therefore, would have a negligible effect on the material.

4.1.1. Hamiltonian description

The goal of this project is to investigate the effect of the SPP mode on the two-dimensional material. Therefore, we do not start from a full microscopic description of the entire hetero-structure. Instead, we focus on the material of interest and the quantized SPP mode. The dielectric-metal interface is treated classically. It does not directly enter the Hamiltonian. However, it shapes the electromagnetic environment of the system and therefore determines the structure of the SPP mode. With this, the Hamiltonian can be split into four terms

$$\hat{H} = \hat{H}_{\text{mat}} + \hat{H}_{\text{field}} + \hat{H}_{EP} + \hat{H}_{PP}. \tag{4.1}$$

The individual contributions will be discussed in greater detail in the following.

Material

The matter Hamiltonian $\hat{H}_{\text{mat}}$ describes a collection of N interacting dipoles on a square lattice with lattice constant a, and is given by

$$\hat{H}_{\text{mat}} = \hat{H}_0 + \hat{H}_{\text{nn}}, \tag{4.2}$$

where $\hat{H}_0$ corresponds to the isolated dipoles and $\hat{H}_{\text{nn}}$ is a static nearest-neighbor interaction. As in Sec. 2.4 and 3.2, the dipoles are approximated as simple two-level systems (TLS), which can be represented by pseudo-spin operators. Here, we slightly change the notation and replace the subscripts x, y, z for the Pauli matrices by the superscripts $1, 2, 3$ in order to avoid confusion with the spatial coordinates of the system. (Note that the dipole moments point in z-direction, but the dipolar transitions correspond to the Pauli operator $\hat{\sigma}_{x,r}$ in the old notation.) With this, each TLS is associated with an in-plane dipole moment $\hat{\boldsymbol{p}}_r = ed\hat{\sigma}_r^1 \boldsymbol{e}_z$, where e denotes the elementary charge, and the transition matrix element d enters the light-matter coupling below. Again, we denote the level splitting by Δ, such that the noninteracting Hamiltonian reads as

$$\hat{H}_0 = \frac{\Delta}{2} \sum_r \hat{\sigma}_r^3. \tag{4.3}$$

The dipole-dipole interaction is given by

$$\hat{H}_{\text{nn}} = -\frac{\alpha}{4} \sum_{\langle r,r' \rangle} \hat{\sigma}_r^1 \hat{\sigma}_{r'}^1, \tag{4.4}$$

where $\langle ... \rangle$ denotes the sum over nearest neighbor pairs, and the parameter α determines the strength of the direct interaction.

This Hamiltonian can, for instance, be considered as a two-level approximation for a crystal, where each unit cell is occupied by an ion that moves in an effective double-well potential. In this picture, the two levels correspond to the lowest symmetric and antisymmetric energy eigenstates for the isolated site. If the associated electronic wave functions hybridize, they form an asymmetric orbital, which gives rise to a non-vanishing average electric dipole moment. The dipole-dipole interaction then originates from the electrostatic Coulomb interaction, which can be partially screened, as well as the potential energy of the lattice distortion.

In Sec. 2.4, we have discussed the mean-field phase diagram for a material of this type. As shown in Fig. 2.8(b), it exhibits a paraelectric-to-ferroelectric phase transition that is driven by the dipole-dipole interaction α. At zero temperature, there is a quantum-paraelectric state due to the finite level splitting Δ, which gives rise to quantum fluctuations that destabilize the ferroelectric ordering. For the nearest-neighbor interaction, the approximation does not reproduce the exact behavior of the system. But nevertheless, it provides a qualitatively correct description of the overall structure of the phase diagram.

Below, we set the model parameters, such that the static dielectric response of $SrTiO_3$ (STO) is reproduced. For that purpose, we follow the same approach as in Sec. 3.2.5. However, it should be stressed again that the present Hamiltonian cannot be considered as a microscopic model for the real material. The comparison to STO is on a purely phenomenological level, and there is no direct relation between the parameters of our model and any microscopic quantities of the STO crystal. Here, we do not aim to present an ab-initio calculation for any real material. Instead, we want to (i) exemplify how DMFT can be applied to systems with quantum light-matter interactions and (ii) demonstrate that the present setting constitutes a promising platform to manipulate the ferroelectric phase transition.

SPP mode

The structure of the SPP mode is determined by the dielectric-metal interface. As mentioned previously, the metal and the dielectric are treated classically. We follow the same approach as in Ref. [21], and start from a macroscopic description, where the material is characterized by its dielectric function $\varepsilon(\omega)$. Based on this classical model, we solve Maxwell's equations, expand the transverse electromagnetic field in normal modes and quantize the theory. A detailed derivation can be found in App. A.1.

Since the dipolar moments are always parallel to the z-axis, they can only couple to the transverse magnetic (TM) SPP mode. The corresponding quantized electric radiation field may again be expanded in multiple modes and can be written as

$$\hat{\boldsymbol{E}}(\boldsymbol{r}) = \sum_{\boldsymbol{q}} \sqrt{\frac{\omega_{\boldsymbol{q}}}{2\varepsilon_0 \varepsilon(x,\omega_{\boldsymbol{q}}) N a^3}} \left[\boldsymbol{u}_{\boldsymbol{q}}(x) e^{i\boldsymbol{q}\cdot\boldsymbol{\rho}} \hat{a}_{\boldsymbol{q}} + \text{H.c.}\right], \tag{4.5}$$

where $\boldsymbol{q} = (q_y, q_z)^T$ is a two-dimensional wave vector, $\boldsymbol{\rho} = (y, z)^T$ represents the spatial coordinate in the y-z-plane, $\hat{a}_{\boldsymbol{q}}$ ($\hat{a}^\dagger_{\boldsymbol{q}}$) is the annihilation (creation) operator for a photon in

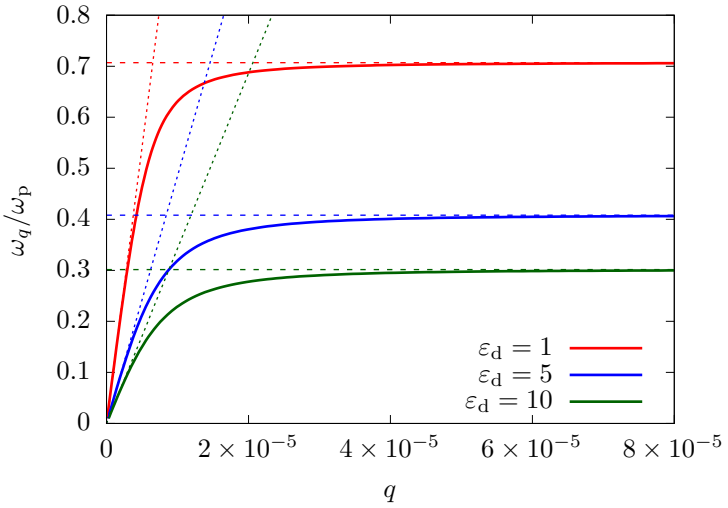

Figure 4.2.: *Dispersion relation of the SPP mode for various values of the electric permittivity ε_d in the dielectric region. The permittivity of the metal is given by a Drude response. For $q \to 0$, the dispersion relation can be approximated by a linear function with slope $c/\sqrt{\varepsilon_d}$ (dotted lines). For $q \to \infty$, it converges to a constant value of $\omega_\mathrm{p}/\sqrt{1+\varepsilon_d}$ (dashed lines). The unit of length has been set to the lattice constant $a = 3.9\text{Å}$. [Graphic adapted from Ref. [61].]*

mode $\boldsymbol{q}$, and $\omega_{\boldsymbol{q}}$ denotes the dispersion relation of the SPP mode. The spatial structure of the modes is determined by the mode functions $\boldsymbol{u}_{\boldsymbol{q}}(x)e^{i\boldsymbol{q}\cdot\boldsymbol{\rho}}$. They form an orthogonal basis and satisfy the transversality condition $\nabla \cdot \boldsymbol{u}_{\boldsymbol{q}}(\boldsymbol{r})e^{i\boldsymbol{q}\cdot\boldsymbol{\rho}} = 0$. The expressions for $\boldsymbol{u}_{\boldsymbol{q}}(x)$ can be found in App. A.1. They decay exponentially as $e^{Q_\mathrm{m}x}$ and $e^{-Q_\mathrm{d}x}$ in the metallic and dielectric regions, respectively. Both decay constants approach the value $Q_\mathrm{m}, Q_\mathrm{d} \sim |\boldsymbol{q}|$ for large wave vectors $|\boldsymbol{q}|$. As a result, the distance x_0 between the two-dimensional material and the metal surface controls the range of SPP momenta that couple to the dipoles.

The corresponding free field Hamiltonian reads as

$$\hat{H}_\mathrm{field} = \sum_{\boldsymbol{q}} \omega_{\boldsymbol{q}} \hat{a}^\dagger_{\boldsymbol{q}} \hat{a}_{\boldsymbol{q}}. \tag{4.6}$$

Henceforth, we assume that the dielectric function in the metallic region is given by a simple Drude response

$$\varepsilon_\mathrm{m}(\omega) = 1 - \left(\frac{\omega_\mathrm{p}}{\omega}\right)^2, \tag{4.7}$$

where ω_p denotes the plasma frequency of the metal. If the permittivity in the dielectric region ε_d is independent of frequency, the dispersion relation $\omega_{\boldsymbol{q}}$ increases linearly at small q with a slope of $c/\sqrt{\varepsilon_\mathrm{d}}$, and converges to a constant value of $\omega_\mathrm{p}/\sqrt{1+\varepsilon_\mathrm{d}}$ in the limit $q \to \infty$. This is illustrated in Fig. 4.2 for three different values of ε_d.

In the following, we set $\varepsilon_\mathrm{d} = 1$, such that the dispersion relation of the SPP mode can be solved analytically for $\omega_{\boldsymbol{q}}$, which yields

$$\omega_{\boldsymbol{q}} = \sqrt{\frac{\omega_\mathrm{p}^2}{2} + \boldsymbol{q}^2 c^2 - \sqrt{\frac{\omega_\mathrm{p}^4}{4} + \boldsymbol{q}^4 c^4}}. \tag{4.8}$$

Light-matter coupling

The light-matter interaction is formulated in dipole gauge (see Sec. 2.3.2) and consists of two terms. The first one describes a linear coupling between the electric field of the SPP mode and the dipole moments $\hat{\boldsymbol{p}}_r = ed\hat{\sigma}_r^1 \boldsymbol{e}_z$ of the emitters and is given by

$$\hat{H}_{EP} = \sum_{r,\boldsymbol{q}} \sqrt{\frac{\omega_{\boldsymbol{q}}}{2N}} \left[g_{\boldsymbol{q}} e^{i\boldsymbol{q}\cdot\boldsymbol{R}_r} \hat{a}_{\boldsymbol{q}} + \mathrm{H.c.} \right] \hat{\sigma}_r^1 \tag{4.9}$$

with the coupling constants

$$g_{\boldsymbol{q}} = \frac{1}{\sqrt{\varepsilon_0 \varepsilon_\mathrm{d} a^3}} \boldsymbol{u}_{\boldsymbol{q}}(x_0) \cdot ed\boldsymbol{e}_z. \tag{4.10}$$

The two-dimensional vectors $\boldsymbol{R}_r$ represent the lattice vectors for the respective sites r, and thus correspond to the positions $\boldsymbol{\rho}$ at which the electric field (4.5) is evaluated. The second term is a dipole-dipole interaction of the form

$$\hat{H}_{PP} = \sum_{r,r'} \sum_{\boldsymbol{q}} \frac{|g_{\boldsymbol{q}}|^2}{2N} e^{-i\boldsymbol{q}\cdot(\boldsymbol{R}_r - \boldsymbol{R}_{r'})} \hat{\sigma}_r^1 \hat{\sigma}_{r'}^1, \tag{4.11}$$

Although it does not directly depend on the photon operators, this contribution vanishes if the light-matter coupling is set to zero. Moreover, it ensures that the total Hamiltonian is positive definite. This can be verified by rewriting the field dependent terms $\hat{H}_\mathrm{field} + \hat{H}_{EP} + \hat{H}_{PP}$ in a diagonal form $\sum_{\boldsymbol{q}} \omega_{\boldsymbol{q}} \hat{b}_q^\dagger \hat{b}_q$ using the shifted field operators $\hat{b}_{\boldsymbol{q}} = \hat{a}_{\boldsymbol{q}} + \pi_{\boldsymbol{q}}$ with $\pi_{\boldsymbol{q}} = \sum_r \frac{g_q}{\sqrt{\omega_{\boldsymbol{q}} 2N}} e^{i\boldsymbol{q}\cdot\boldsymbol{R}_r} \hat{\sigma}_r^1$.

4.1.2. Imaginary-time action

Above, we have described the combined light-matter system by a Hamiltonian that contains photon and matter operators. Now we want to find an effective representation in which the photon degrees of freedom do not enter explicitly. We follow the same steps as for the single mode model discussed in the previous chapter (see Sec. 3.1.2). Here, we only sketch the procedure and leave a detailed derivation to App. A.2. We start from the imaginary time action

$$S = S_\mathrm{mat} + S_{PP} + S_{EP} + S_\mathrm{field}. \tag{4.12}$$

Analogous to the Hamiltonian (4.1) it has been split into four parts, corresponding to the isolated matter, the two light-matter coupling terms, and the free electromagnetic

field, respectively. We trace out the photon degrees of freedom, which yields the effective action

$$S_{\text{eff}} = S_{\text{mat}} + S_{\text{ind}}, \tag{4.13}$$

where the effect of the SPP mode is fully contained in S_{ind}. The latter is obtained from the path integral

$$e^{-S_{\text{ind}}} = e^{-S_{PP}} \int \mathcal{D}[\bar{a}, a] e^{-(S_{EP}+S_{\text{field}})}, \tag{4.14}$$

which yields a photon-induced retarded dipole-dipole interaction of the form

$$S_{\text{ind}} = -\frac{1}{2} \int_0^\beta d\tau \, d\tau' \sum_{r,r'} \sigma_r^1(\tau) W_{r,r'}^{\text{ind}}(\tau - \tau') \sigma_{r'}^1(\tau'). \tag{4.15}$$

In $\boldsymbol{k}$-space and Matsubara representation, the interaction vertex reads as

$$W_{\boldsymbol{k}}^{\text{ind}}(i\nu_n) = -|g_{\boldsymbol{k}}|^2 + |g_{\boldsymbol{k}}|^2 \frac{\omega_{\boldsymbol{k}}^2}{\nu_n^2 + \omega_{\boldsymbol{k}}^2}, \tag{4.16}$$

where the first part originates from the direct interaction S_{PP}, and the second term arises from integrating out the SPP mode.

An analytic continuation to real frequencies using the substitution $i\nu_n \to \omega + i0$ shows that $W_{\boldsymbol{k}}^{\text{ind}}$ vanishes at $\omega = 0$. Consequently, the effect of the light-matter interaction cannot be captured within the static mean-field approximation, which has already been discussed in Sec. 2.3.3. However, this perfect cancellation at zero frequency only appears if $\hat{H}_{PP}$ and $\hat{H}_{EP}$ are consistent, i.e., if the light-matter Hamiltonian is positive-definite.

4.2. Dynamical mean-field formalism

In Sec. 2.1 and 2.2, we have already introduced the basic ideas of dynamical mean-field theory (DMFT) for fermions and bosons. The central principle of this technique is to replace a lattice model by an impurity that is embedded in an effective environment. In this picture, the interplay between the impurity and all other lattice sites is incorporated in the parameters of the impurity model. Moreover, it is assumed that the self-energy of the system is purely local. With this approximation, the parameters of the effective impurity problem can be related to the corresponding lattice quantities by a set of self-consistent equations. In the following, we apply the bosonic DMFT (B-DMFT) formalism to the system under consideration. For that purpose, we first introduce an equivalent representation with bosonic degrees of freedom.

4.2.1. Bosonic representation of the model

As shown in Sec. 4.1.2 and App. A.2, the SPP mode induces an effective coupling between the individual dipoles. We combine it with the static nearest-neighbor interaction that is already contained in S_{mat}. With this, the effective action (4.13) can be rewritten

as $S_{\text{eff}} = S_0 + S_{\text{int}}$, where S_0 corresponds to the isolated emitters, and the combined interaction S_{int} is given by

$$S_{\text{int}} = -\frac{1}{2}\int_0^\beta d\tau\, d\tau' \sum_{r,r'} \sigma_r^1(\tau) W_{r,r'}(\tau-\tau')\sigma_{r'}^1(\tau') \tag{4.17}$$

with

$$W_{\boldsymbol{k}}(i\nu_n) = \frac{\alpha}{2}\left[\cos(k_y)+\cos(k_z)\right] - |g_{\boldsymbol{k}}|^2 \frac{\nu_n^2}{\nu_n^2+\omega_{\boldsymbol{k}}^2}. \tag{4.18}$$

In this expression, the first part originates from the direct interaction Hamiltonian (4.4), and the second contribution corresponds to the retarded photon-mediated interaction (4.15).

This combined dipole-dipole term can be decoupled using a Hubbard-Stratonovich transformation. For that purpose, we introduce a bosonic auxiliary field $\varphi_r(\tau)$ for each lattice site r, and define a new action S_{HS} such that

$$e^{-S_{\text{eff}}} = \int \mathcal{D}[\varphi] e^{-S_{\text{HS}}}, \tag{4.19}$$

i.e., the original action is reproduced if the auxiliary fields are integrated out. Apart from an irrelevant constant, which will be omitted in the following, the Hubbard-Stratonovich action is given by

$$S_{\text{HS}} = S_0 + S_{\varphi\varphi} + S_{\varphi\sigma}, \tag{4.20}$$

with a quadratic contribution

$$S_{\varphi\varphi} = \frac{1}{2}\int_0^\beta d\tau\, d\tau' \sum_{r,r'} \varphi_r(\tau)[W^{-1}]_{r,r'}(\tau-\tau')\varphi_{r'}(\tau'), \tag{4.21}$$

and a local linear coupling between the dipole moments and the auxiliary fields

$$S_{\varphi\sigma} = -\sum_r \int_0^\beta d\tau \varphi_r(\tau)\sigma_r^1(\tau). \tag{4.22}$$

Essentially, this model can be considered as a bosonic field theory on a lattice with an anharmonic self-interaction. The latter arises from the coupling of the fields φ_r and the pseudo-spin variables σ_r^1. In contrast to the dipole-dipole interaction in the original action S_{eff}, this anharmonicity is purely local; therefore, we can directly map the Hubbard-Stratonovich action to a local impurity problem.

4.2.2. Impurity action and self-consistent equations

We use the so-called cavity method [29, 7] to map the bosonic lattice model defined by (4.20) to a local impurity problem. In this approach, one particular lattice site $r = c$

(the "cavity site") is singled out, and all degrees of freedom corresponding to other sites are integrated out. Then a cumulant expansion up to second order is performed. A detailed derivation can be found in App. A.3.1. The resulting impurity action contains a quadratic and a linear term in $\varphi_c(\tau)$, and reads as

$$S_{\mathrm{HS}}^{\mathrm{imp}} = S_0^c + S_{\varphi\varphi}^{\mathrm{imp}} + S_{\varphi\sigma}^{\mathrm{imp}}, \tag{4.23}$$

$$S_{\varphi\sigma}^{\mathrm{imp}} = -\int_0^\beta d\tau \varphi_c(\tau)[\sigma_c^1(\tau) - h(\tau)], \tag{4.24}$$

$$S_{\varphi\varphi}^{\mathrm{imp}} = \frac{1}{2}\int_0^\beta d\tau\, d\tau' \varphi_c(\tau)\mathcal{W}^{-1}(\tau-\tau')\varphi_c(\tau'), \tag{4.25}$$

where S_0^c denotes the action of a single isolated dipole. The theory contains two effective quantities that incorporate the interaction with the surrounding lattice. Firstly, we have the retarded Weiss field $\mathcal{W}$, which is also encountered in fermionic DMFT, and secondly, there is the static field h, which couples linearly to the Hubbard-Stratonovich field $\varphi_c(\tau)$. The inclusion of h is required because the field $\varphi_c(\tau)$ may take a non-vanishing value owing to its bosonic nature [3].

For a given $\mathcal{W}$ and h, we can calculate the local expectation value $\langle\varphi_c(\tau)\rangle_{S_{\mathrm{HS}}^{\mathrm{imp}}}$ and the local connected correlation function

$$U_{c,c}(\tau) = \langle\varphi_c(\tau)\varphi_c(0)\rangle_{S_{\mathrm{HS}}^{\mathrm{imp}}}^{\mathrm{con}} \tag{4.26}$$

from the impurity action. Subsequently, the self-energy of the impurity can be computed from the Dyson equation

$$\Pi_{\mathrm{loc}} = \mathcal{W}^{-1} - U_{c,c}^{-1}. \tag{4.27}$$

Moreover, the lattice Green's function

$$U_{r,r'}(\tau) = \langle\varphi_r(\tau)\varphi_{r'}(0)\rangle_{S_{\mathrm{HS}}}^{\mathrm{con}} \tag{4.28}$$

is obtained from the Dyson equation in momentum space

$$U_{\boldsymbol{k}} = W_{\boldsymbol{k}}[1 - \Pi_{\boldsymbol{k}} W_{\boldsymbol{k}}]^{-1}, \tag{4.29}$$

where $\Pi_{\boldsymbol{k}}$ denotes the $\boldsymbol{k}$-dependent self-energy. The local lattice Green's function is given by the momentum sum $U_{r,r} = \frac{1}{N}\sum_{\boldsymbol{k}} U_{\boldsymbol{k}}$. In DMFT, we neglect the $\boldsymbol{k}$-dependence of $\Pi_{\boldsymbol{k}}$, and replace it with the local impurity self-energy Π_{loc}. Thus, the local correlation function is given by

$$U_{c,c} = \frac{1}{N}\sum_{\boldsymbol{k}} W_{\boldsymbol{k}}[1 - \Pi_{\mathrm{loc}} W_{\boldsymbol{k}}]^{-1}. \tag{4.30}$$

The resulting $U_{c,c}$ and the self-energy Π_{loc} can be used to calculate the Weiss field $\mathcal{W}$ from Eq. (4.27). The solution must be consistent with the Weiss field introduced in the impurity model. Furthermore, we assume that $\langle\varphi_r(\tau)\rangle_{S_{\mathrm{HS}}} = \phi$ for all sites r, and that it

is identical to the expectation value $\langle\varphi_c(\tau)\rangle_{S_{\mathrm{HS}}^{\mathrm{imp}}}$ obtained from the impurity action. The static field h is then given by

$$h = \left[W_{\mathrm{mf}}^{-1} - \mathcal{W}_0^{-1}\right]\phi \tag{4.31}$$

with

$$\mathcal{W}_0^{-1} = \mathcal{W}^{-1}(i\nu_{n=0}). \tag{4.32}$$

The formulas above form a closed set of self-consistent equations. Further details on the derivation are provided in App. A.3.2.

4.2.3. Impurity model

The impurity problem (4.23) describes a two-level system that couples to a continuum of modes with propagator $\mathcal{W}$, and hence, represents a generalized spin-boson model. For practical reasons, we integrate out the bosonic auxiliary fields from the impurity model, which yields the action of a single spin variable with a retarded interaction. In this way, we reduce the number of degrees of freedom the impurity solver must handle. The new impurity action reads as

$$S^{\mathrm{imp}} = S_0^c + S_{\mathrm{int},1}^{\mathrm{imp}} + S_{\mathrm{int},2}^{\mathrm{imp}} \tag{4.33}$$

with the linear contribution

$$S_{\mathrm{int},1}^{\mathrm{imp}} = b\int_0^\beta d\tau\sigma_c^1(\tau), \tag{4.34}$$

and the retarded interaction term

$$S_{\mathrm{int},2}^{\mathrm{imp}} = -\frac{1}{2}\int_0^\beta d\tau\int_0^\beta d\tau'\,\sigma_c^1(\tau)\mathcal{W}(\tau-\tau')\sigma_c^1(\tau') \tag{4.35}$$

(see App. A.3.3). We solve this model using the strong-coupling expansion described in Ref. [48, 49]. It is based on a skeleton expansion of the partition function in terms of the retarded propagator. Alternatively, we could also perform a standard hybridization expansion and apply the continuous-time quantum Monte-Carlo method [87, 31]. But even the diagrammatic approach allows us to obtain converged results by increasing the perturbation order.

The local propagator $U_{c,c}$ for the auxiliary field cannot be determined directly from the new impurity model defined by (4.33). Instead, we calculate the connected correlation function

$$\chi_{c,c}(\tau) = \langle\mathcal{T}\sigma_c^1(\tau)\sigma_c^1(0)\rangle_{S^{\mathrm{imp}}}^{\mathrm{con}}, \tag{4.36}$$

which is related to the Green's function by the equation

$$U_{c,c} = \mathcal{W} + \mathcal{W}\chi_{c,c}\mathcal{W}. \tag{4.37}$$

Inserting this into Eq. (4.27), we obtain

$$\Pi_{\mathrm{loc}} = \left[1 + \chi_{c,c}\mathcal{W}\right]^{-1} \chi_{c,c}. \tag{4.38}$$

Moreover, the static field $b = \mathcal{W}_0 h$ can be calculated from the expectation value $\langle \sigma_r^1(\tau) \rangle = \langle \sigma^1 \rangle$ and reads as

$$b = \left[\mathcal{W}_0 - W_{\mathrm{mf}}\right] \langle \sigma^1 \rangle. \tag{4.39}$$

With this, we again have a closed set of self-consistent equations.

4.2.4. Numerical implementation

To solve the self-consistent DMFT equations, we employ an iterative approach. The basic steps of the algorithm are illustrated in Fig. 4.3. It comprises two major components: the impurity solver and the set of self-consistent equations.

The impurity solver determines the local expectation values $\langle \sigma^1 \rangle$ and $\langle \sigma^3 \rangle$ as well as the local correlation function $\chi_{c,c}(\tau)$ from the impurity action. It operates in the imaginary-time domain and is based on a strong-coupling expansion similar to the one introduced in Ref. [48, 49]. The parameters of the impurity action are provided as an input, with one notable particularity regarding the Weiss field. In general, it can be written as $\mathcal{W}(\tau) = \mathcal{W}'(\tau) + w_0\delta(\tau)$, where $\mathcal{W}'(\tau)$ represents the regular part, and $w_0\delta(\tau)$ is an instantaneous contribution, corresponding to a frequency-independent part in Matsubara representation. However, for the present impurity model, the instantaneous term can be omitted due to $(\sigma_c^1)^2 = \mathbb{I}$, which merely results in a constant energy shift. Therefore, the impurity solver only takes the regular part $\mathcal{W}'(\tau)$ as an input.

The self-consistent equations allow us tp compute the Weiss field $\mathcal{W}$ and the static field b from the local correlation function $\chi_{c,c}$ and the expectation value $\langle \sigma^1 \rangle$. We perform these calculations in Matsubara space since all quantities are diagonal in this representation. Consequently, a Fourier transform is necessary when transitioning from the impurity solver to the self-consistent equations, and vice versa. However, the inverse transform from Matsubara space to the imaginary-time domain requires additional attention. This is due to the numerical cutoff in the frequency summations, which may truncate the Weiss field even before its regular part converges to zero. To address this issue, we employ the analytical approximation

$$\mathcal{W}(i\nu_n) \sim w_0 + \frac{w_2}{(i\nu_n)^2} \tag{4.40}$$

for the high-frequency tail of $\mathcal{W}(i\nu_n)$, where w_0 and w_2 are constants, which depend on the light-matter coupling strength, the parameters of the material, and the expectation value $\langle \sigma^3 \rangle$. The corresponding expressions and a detailed derivation can be found in App. A.4. At large Matsubara frequencies, the function

$$f(i\nu_n) = w_0 + \frac{w_2}{(i\nu_n)^2 - \delta^2} \tag{4.41}$$

with the regulator $\delta \ll 1$ exhibits the same behavior as the Weiss field. More precisely, the difference $\mathcal{W}(i\nu_n) - f(i\nu_n)$ decays at least as fast as $1/\nu_n^4$ for large ν_n, which ensures

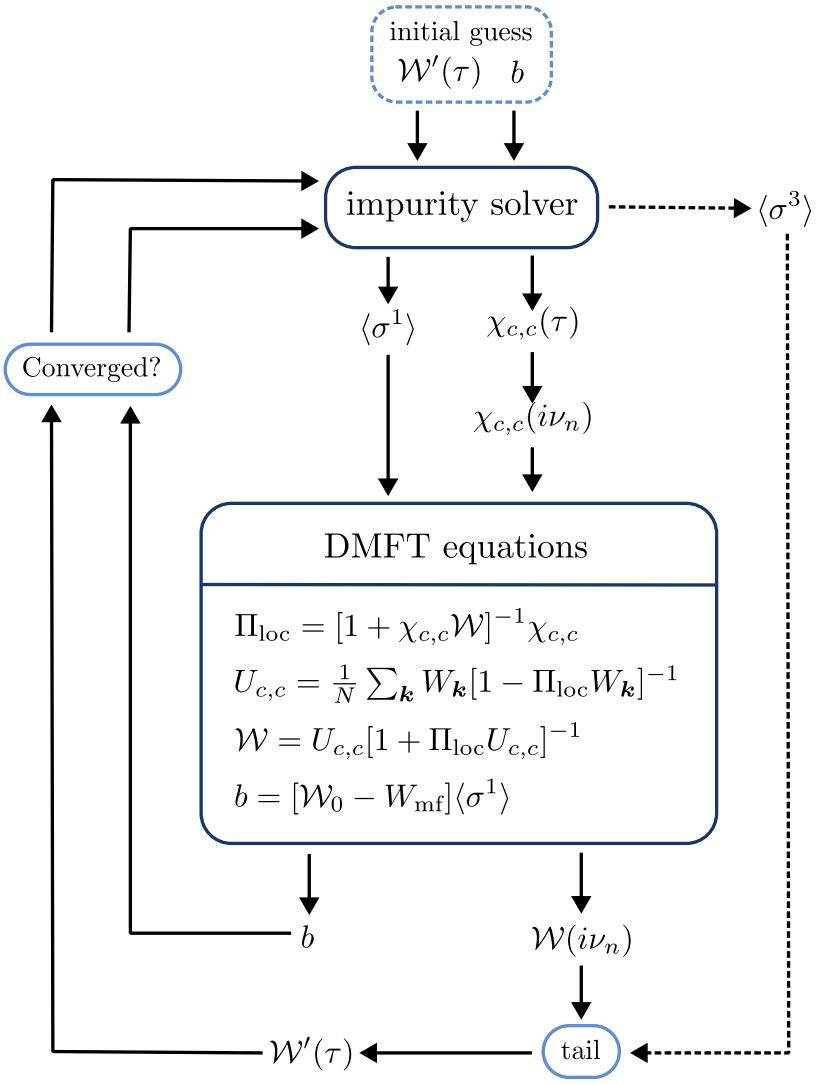

Figure 4.3.: *Illustration of the DMFT loop. [Graphic adapted from [61].]*

a smooth result when computing the numerical inverse Fourier transform. To obtain the full solution for $\mathcal{W}(\tau)$, we can then add the imaginary-time representation of f, which is known analytically. However, as discussed previously, we are only concerned with determining the regular part $\mathcal{W}'(\tau)$. Therefore, we exclude the instantaneous contribution from $f(\tau)$, and calculate

$$\mathcal{W}'(\tau) = \mathcal{F}^{-1}\left\{\mathcal{W}(i\nu_n) - f(i\nu_n)\right\} + f'(\tau), \tag{4.42}$$

with

$$f'(\tau) = \mathcal{F}^{-1}\left\{f(i\nu_n) - w_0\right\} = \frac{w_2}{2\delta}\frac{\cosh[\delta(\tau-\beta/2)]}{\sinh[\delta\beta/2]}. \tag{4.43}$$

In summary, the DMFT loop consists of the following steps:

1. Start from an initial guess for $\mathcal{W}'(\tau)$ and b.
2. Solve the impurity problem for the given input parameters to obtain $\chi_{c,c}(\tau)$, $\langle\sigma^1\rangle$ and $\langle\sigma^3\rangle$.
3. Fourier transform $\chi_{c,c}(\tau)$ to Matsubara representation.
4. Insert $\chi_{c,c}(i\nu_n)$ and $\langle\sigma^1\rangle$ into the self-consistent DMFT equations and determine the new Weiss field $\mathcal{W}(i\nu_n)$ and the new static field b.
5. Calculate the inverse Fourier transform $\mathcal{W}'(\tau)$ from $\mathcal{W}(i\nu_n)$ and $\langle\sigma^3\rangle$ using the tail correction as described above.
6. Test whether $\mathcal{W}'(\tau)$ has converged. If this is not the case, pass the new $\mathcal{W}'(\tau)$ and b to the impurity solver and restart the procedure from step 2.

4.3. Results and discussion

In the following, we analyze the results of the DMFT calculation, and investigate how the equilibrium state of the material is influenced by the SPP mode. For that purpose, we first discuss the choice of parameters for the system, and explain how the strength of the light-matter coupling is controlled (see Sec. 4.3.1). Then we consider the effect in the paraelectric and ferroelectric regime in Sec. 4.3.2 and 4.3.3, and finally, we discuss the DMFT phase diagram in Sec. 4.3.4.

4.3.1. Model parameters and light-induced interaction

To set the model parameters, we follow the same approach as in Sec. 3.2.5 and Ref. [60] and relate the macroscopic electric response of the system to the dielectric function of the real material $SrTiO_3$ (STO). As mentioned previously, STO is paraelectric at high temperatures and becomes a quantum paraelectric in the low-temperature regime [69]. However, ferroelectricity can be induced through various mechanisms, such as external strain or strong laser pumping [71, 64]. Analogously, in the current model, the phase transition is driven by the direct interaction α.

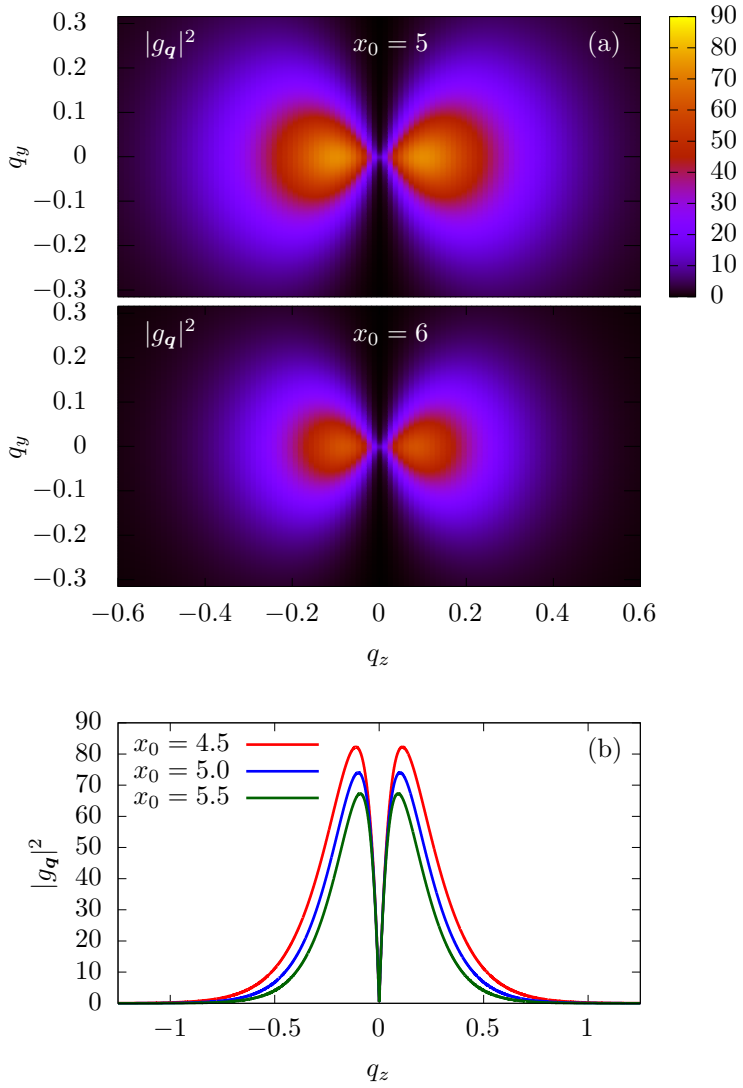

Figure 4.4.: *Light-matter coupling as a function of the mode vector* $\boldsymbol{q}$. *(a) Color plot of* $|g_{\boldsymbol{q}}|^2$ *for* $x_0 = 5$ *and* $x_0 = 6$. *(b)* $|g_{\boldsymbol{q}}|^2$ *at various values of* x_0 *for the modes propagating in the z-direction. For both figures,* $g^2 = 4024$, *where the unit of energy has been set to* Δ. *The unit of length is given by the lattice parameter* a. *[Graphic adapted from Ref. [61].]*

In mean-field approximation the matter Hamiltonian discussed in this chapter and the one considered in Ch. 3 are equivalent, and therefore exhibit the same RPA response $\chi_{\mathrm{mf}} = \frac{\chi_{\mathrm{at}}}{1-\alpha\chi_{\mathrm{at}}}$ with the atomic static susceptibility $2\tanh(\Delta/2T)/\Delta$. To quantify the strength of the light-matter coupling in the present model, we introduce the parameter

$$g^2 = \frac{e^2 d^2}{\varepsilon_{\mathrm{d}}\varepsilon_0 a^3}, \tag{4.44}$$

where d denotes the matrix element for the dipolar transitions, and a represents the lattice constant. This is analogous to the collective coupling g_n^2 for the single-mode model studied in Ch. 3. Therefore, the dielectric function for the system can again be calculated from $\varepsilon(T) = 1 + g^2\chi_{\mathrm{mf}}$, and thus, the parameters of the present model can be extracted from the same fit as in Sec. 3.2.5 (see Fig. 3.5(a)), which yields $\Delta = 3.3\mathrm{meV}$, $g^2 = 4024\Delta$, and $\alpha = 0.328\Delta$. In the following, we fix the light-matter coupling strength g^2 but vary the parameter α in order to control the phase transition. Moreover, we set the unit of energy to Δ and use the lattice parameter $a = 3.9$ Å of STO as a length scale. The dispersion relation of the SPP mode is mostly determined by the plasma frequency, which we set to $\omega_{\mathrm{p}} = \sqrt{2}$.

The $\boldsymbol{q}$-dependent coupling constants can be rewritten in terms of g^2, which yields $|g_{\boldsymbol{q}}|^2 = g^2[\boldsymbol{u}_{\boldsymbol{q}}(x_0)\cdot\boldsymbol{e}_z]^2$. Fig. 4.4(a) shows the strength of the coupling as a function of the two-dimensional wave vector $\boldsymbol{q}$ for $x_0 = 5$ and $x_0 = 6$. Generally, only a small range of momenta gives a significant contribution to the interaction. Moreover, it is clearly visible that this range decreases by increasing the distance x_0 from 5 to 6, and that the magnitude of the interaction strength becomes smaller. This is also illustrated in Fig. 4.4(b), where the coupling strength $|g_{\boldsymbol{q}}|^2$ for modes traveling along the z-axis is plotted as a function of q_z for three different values of x_0. The reason for this behavior is the exponential decay of the mode functions (see paragraph on the SPP mode in Sec. 4.1.1). In the following, we use this property to tune the strength of the coupling between the SPP mode and the material.

4.3.2. Paraelectric regime

In the normal phase, the order parameter $\langle\sigma^1\rangle$ vanishes. Therefore, we examine its static linear response to an external electric field. To determine the static susceptibility $\chi(0)$, we add the term $\hat{H}_{\mathrm{ext}} = -B_{\mathrm{ext}}\sum_r \hat{\sigma}_r^1$ to the matter Hamiltonian and include it in the self-consistent DMFT iteration. This amounts to an extra term $S_{\mathrm{ext}} = -B_{\mathrm{ext}}\int_0^\beta d\tau\sigma_c^1(\tau)$ in the impurity action. If the external field is sufficiently small, such that the system is still in the linear response regime, the linear susceptibility is approximately given by $\chi(0) \approx \langle\sigma^1\rangle/B_{\mathrm{ext}}$.

Fig. 4.5 displays the results for $\alpha = 0.2$. According to mean-field theory, the material remains paraelectric down to zero temperature in this regime. (See mean-field phase diagram in Fig. 2.8(b).) Fig. 4.5(a) shows the inverse static susceptibility as a function of temperature for three values of the distance x_0. The symbols correspond to outcomes from two different diagrammatic impurity solvers: data points marked by empty circles

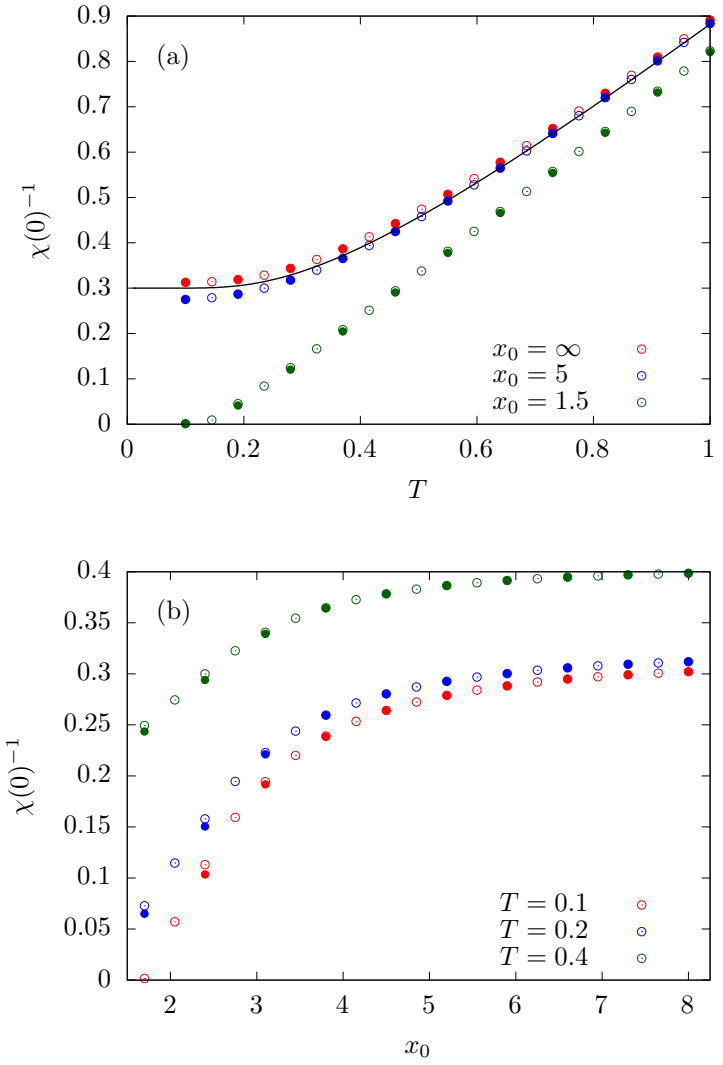

Figure 4.5.: *Inverse static susceptibility $\chi(0)^{-1}$ in the paraelectric regime. (a) $\chi(0)^{-1}$ as a function of temperature for $\alpha = 0.2$. The black line corresponds to the mean-field result, which is not affected by the distance x_0 between the paraelectric material and the dielectric-metal interface. The dots indicate the DMFT results for three different values of x_0. (b) $\chi(0)^{-1}$ for $\alpha = 0.2$ and three different temperatures as a function of the distance x_0. In both panels, empty dots correspond to the OCA solution of the impurity model, while filled symbols represent the outcome of a TCA calculation. [Graphic adapted from Ref. [61].]*

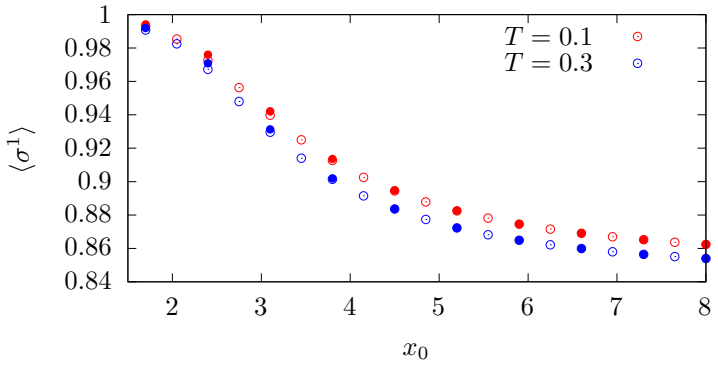

Figure 4.6.: *Order parameter in the ferroelectric regime for $\alpha = 1.0$ as a function of the distance x_0 at $T = 0.1$ and $T = 0.3$. Empty and filled symbols indicate the OCA or the TCA solution of the impurity model, respectively. [Graphic adapted from Ref. [61].]*

are results obtained from a one-crossing approximation (OCA), while filled circles represent outcomes from a two-crossing approximation (TCA). The close agreement between the solutions of the two orders of approximation indicates convergence. Due to the exponential decay of the light-matter interaction with the distance x_0 from the metal surface, the coupling to the SPP mode vanishes at $x_0 = \infty$ (red dots). Hence, the corresponding data show the response of the bare material. Even in this case, the static susceptibility deviates from the corresponding mean-field result represented by the black curve. Fluctuations beyond mean-field reduce the tendency to order, leading to a decrease in the static response. If the material approaches the metal surface, the coupling to the SPP mode increases, giving rise to a non-vanishing effect on the system's equilibrium properties. Notably, the static susceptibility is enhanced.

This behavior can also be seen in Fig. 4.5, where the inverse susceptibility $\chi(0)^{-1}$ is shown as a function of the distance x_0 at various temperatures. The increase in susceptibility with growing x_0 is most pronounced at low temperatures. Moreover, it is interesting to note that the deviation between TCA and OCA results becomes more and more significant as the distance x_0 is decreased (i.e., as the interaction with the SPP mode is enhanced). This implies that the impurity model approaches the strong-coupling regime, where higher orders in the diagrammatic expansion become more important.

4.3.3. Ferroelectric regime

In the ferroelectric phase, the solid acquires a non-vanishing average electric polarization, which is proportional to the order parameter $\langle\sigma^1\rangle$. In our model, the transition to the ferroelectric state is only possible if the parameter α exceeds a certain critical value. To investigate the effect of the SPP mode in the ferroelectric state, we therefore set $\alpha = 1$. In Fig. 4.6, we show the order parameter as a function of the distance x_0 at $T = 0.1$ and $T = 0.3$. As can be seen in the graphic, $\langle\sigma^1\rangle$ increases if the distance is decreased, which implies that the ferroelectric ordering is enhanced as the coupling to the SPP mode

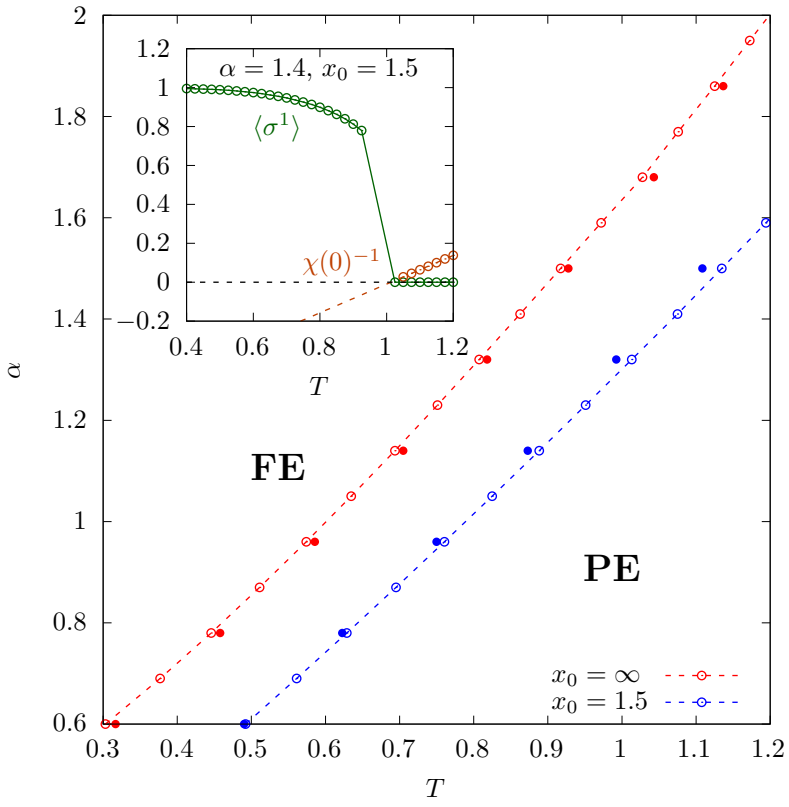

Figure 4.7.: *Main panel: Phase diagram in the α-T plane for $x_0 = \infty$ (no coupling to the SPP mode) and $x_0 = 1.5$. Empty circles correspond to OCA, and filled dots to TCA results. Inset: Order parameter (green) and inverse susceptibility (orange) for $\alpha = 1.4$ and $x_0 = 1.5$. The critical temperature T_c for the ferroelectric phase transition can be extracted from the linear fit to the inverse susceptibility data, which is indicated by the orange dashed line. [Graphic adapted from Ref. [61].]*

becomes stronger. This is consistent with the observations for the paraelectric regime. At lower temperature ($T = 0.1$), the overall effect is stronger, i.e., the enhancement is more pronounced if the system is closer to the phase transition.

4.3.4. Phase diagram

The analysis of the paraelectric and ferroelectric regimes has revealed that the surface plasmon polariton (SPP) mode significantly influences the equilibrium properties of the solid. We now investigate how this affects the phase diagram of the material. In order to obtain the boundary between the normal and disordered phase, we determine the critical temperature at various values of α for each distance x_0. For a second-order phase transition, this value can be extracted from the order parameter, which continuously drops to zero at the critical point. However, in contrast to mean-field theory, DMFT

predicts a first-order phase transition. This can be seen in the inset of Fig. 4.7, where the order parameter (green data points) is plotted as a function of temperature for $\alpha = 1.4$ and $x_0 = 1.5$. It exhibits a discontinuous jump around $T \approx 1$, which indicates a first-order transition. Consequently, there is a small region of coexistence, where both the ferroelectric and the paraelectric phase can be stabilized. A similar observation has been made previously for the DMFT solution of the standard lattice φ^4 theory. For this model, DMFT also predicts a first-order instead of a second-order transition. But nevertheless, it has been demonstrated that the DMFT results inside the ordered and disordered phase, as well as the estimated critical temperature are in excellent agreement with lattice quantum Monte-Carlo calculations [1, 2].

Due to the first-order nature of the phase transition in DMFT, it is not possible to extract a definite critical temperature from the order parameter. Therefore, we consider the divergence of the static susceptibility and use it as an estimate for the lower bound of the coexistence region and the critical temperature. This is illustrated in the inset of Fig. 4.7, where the inverse static susceptibility $\chi(0)^{-1}$ is plotted as a function of temperature (orange) for $\alpha = 1.4$ and x_0=1.5. The orange circles represent the DMFT results in the paraelectric regime. The zero crossing of the inverse susceptibility, which indicates the divergence, is extracted from a linear fit to the data (dashed orange line). As can be seen from the graphic, it is indeed close to the point where the order parameter (green symbols) jumps to zero.

The results are shown in the main panel of Fig. 4.7. Here, we plot the critical points in the α-T plane. The red curve corresponds to a distance of $x_0 = \infty$, where the material is not coupled to the SPP mode, whereas the blue curve indicates the phase boundary for a distance of $x_0 = 1.5$, where the interaction with the SPP mode has a sizable effect. Again, the filled symbols correspond to a TCA solution of the impurity model, while the empty symbols represent results obtained from an OCA calculation. It is clearly visible that the phase transition is shifted to higher temperatures due to the interaction with the SPP mode. This is in agreement with the enhancement of the order parameter in the symmetry-broken phase and the increase in susceptibility in the normal phase, which both imply that the ferroelectric state is stabilized by the photon-mediated interaction.

4.4. Conclusion

From our results, we can draw two general conclusions: first, they prove that DMFT is an appropriate technique to study macroscopic systems with quantum light-matter interactions. In particular, this formalism captures effects that remain elusive within a static mean-field approximation. And second, the results suggest that multi-layered structures constitute a promising platform to engineer material properties through the vacuum fluctuations of polaritonic degrees of freedom.

As an example, we have considered a minimal model of a two-dimensional solid that exhibits a paraelectric-to-ferroelectric phase transition. The solid couples to an SPP mode that is supported by a dielectric-metal interface. In this setting, the strength of the coupling can be tuned by changing the distance between the two-dimensional material

and the metal surface. We have seen that the light-matter interaction gives rise to an enhancement of the static electric susceptibility in the paraelectric regime. Moreover, in the ferroelectric phase, the order parameter grows if the coupling to the SPP mode increases. Both effects are most significant in the proximity of the phase transition, which leads to a stabilization of ferroelectricity over a larger range of parameters.

On a phenomenological level, this behavior can be explained as follows: the SPP mode mediates a retarded all-to-all interaction in the solid. This interaction vanishes at zero frequency, so that a simple static mean-field approximation does not predict any photon-induced effects on the equilibrium properties of the system. However, the SPP mode may influence electromagnetically active modes at $\omega \neq 0$. These components renormalize the static response of the material due to an anharmonic mixing of different modes, and thus give rise to a non-vanishing effect even at $\omega = 0$. The importance of these nonlinear interactions has already been highlighted in Ref. [6]. In addition, they are relevant to the cavity correction for the single-mode model discussed in Ch. 3 (see Sec. 3.1.5).

In the future, it would be interesting to compare the results obtained from DMFT to other approaches. However, it is challenging to find suitable techniques even for the minimal model studied in this chapter. In contrast to many methods commonly used in quantum optics, the DMFT formalism does not make use of a Markov approximation but includes the full frequency-dependent photon-mediated interaction. Moreover, it takes into account both rotating and counter-rotating terms of the light-matter interaction, which is particularly relevant in the strong coupling regime. A possible alternative to DMFT would be a lattice quantum Monte Carlo simulation. Efficient algorithms to solve spin-boson models exist [86]. However, a sign problem may arise if the light-induced interaction $W_{r,r'}(\tau)$ changes sign in the imaginary-time domain. This is expected for the present model because the zero-frequency component of $W_{r,r'}$ vanishes, and therefore $\int d\tau\, W_{r,r'}(\tau) = 0$. Moreover, for one-dimensional systems, it would be conceivable to use a matrix product state (MPS) algorithm. In general, DMFT performs best at higher dimensions, i.e., for systems with large coordination numbers. But a comparison of the results might still be interesting because the long-range nature of the photon-mediated interaction might partly compensate for the low dimension of the system. When using an MPS algorithm, it may be challenging to deal with a continuum of electromagnetic modes. To tackle this problem, one might follow a similar route as it has been done for systems with electron-phonon interactions [44, 41]

In summary, DMFT appears to be a suitable and useful approximate method for macroscopic solids with photon-induced interactions. The formalism could be extended to more complex models, ultimately enabling a realistic description of strongly correlated electron systems with quantum light-matter interactions. In the next chapter, we discuss a possible diagrammatic extension of DMFT that allows us to deal with itinerant electrons coupled to the electromagnetic field via Peierls phases.

5. Dynamical mean-field study of the Mott metal-insulator transition in a system with electron-photon interactions

Up to this point, we have focused on solids consisting of localized dipoles, where the interaction between light and matter is described by a linear coupling between the polarization density and the electric field. In this case, it is possible to map the model to an auxiliary problem with bosonic degrees of freedom that only contains on-site interactions. Consequently, the light-matter coupling can be directly included in the DMFT formalism. However, this approach is not applicable to materials with itinerant electrons, where the interaction with the electromagnetic field is introduced via the Peierls substitution. The latter describes a highly non-linear coupling between light and matter. But even if the electron-photon interaction is truncated beyond the linear order, the field couples to the current operator. As a result, all interaction terms involve two different sites, such that the light-matter coupling cannot be easily mapped to a local interaction. In this chapter, we therefore introduce a diagrammatic extension of DMFT that enables us to include non-local self-energy contributions originating from the Peierls phase factors. As in Ch. 4, we examine a two-dimensional solid coupled to an SPP mode of a dielectric-metal interface. However, our focus shifts to a quantum material described by a single-band Hubbard Hamiltonian.

In general, quantum materials are particularly sensitive to small external perturbations and thus provide an interesting platform for the optical control of matter with quantum light. The Hubbard model has been studied previously in this context. For instance, theoretical calculations for a one-dimensional Hubbard chain revealed that the coupling to a single cavity mode leads to a renormalization of the effective spin exchange interactions [46, 81]. Moreover, it has been shown that a large electron-electron interaction may create electronic transitions that couple strongly to the cavity mode. This leads to the formation of Mott polaritons, which modifies the optical conductivity of the coupled light-matter system [47]. Therefore, it seems reasonable to expect that, also for the setting studied in this chapter, light-induced effects may alter the equilibrium properties of the solid.

Apart from these theoretical findings, recent experiments have shown that it is possible to manipulate the metal-to-insulator transition in the correlated solid-state material 1T-TaS_2 using a cryogenic tunable terahertz cavity [42]. As mentioned in Sec. 2.1.1, the Hubbard model may also undergo a metal-to-insulator transition driven by the local electron-electron interaction. The metallic and the insulating state of 1T-TaS_2 correspond to a nearly commensurate and a commensurate charge density wave and thus are

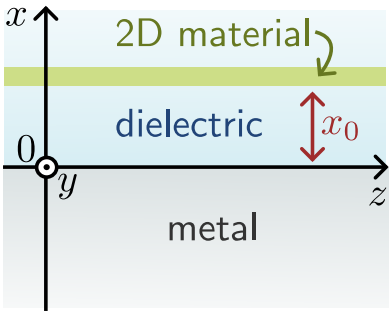

Figure 5.1.: *Cross-section of the system. The material of interest is marked in green. It is positioned in close proximity to a dielectric-metal interface supporting an SPP mode.*

different from the phases in the Hubbard model. Nevertheless, the phase transitions in both systems are of first order, and the mechanisms leading to a shift of the critical regime in 1T-TaS_2 might also apply to the Mott metal-insulator transition of the Hubbard model. In Ref [42], two possible scenarios are suggested to explain this observation: (i) the cavity-induced effect on the free energy is stronger in the metallic phase than in the insulating phase. Depending on the sign of the renormalization, this may lead to a stabilization or destabilization of the metallic phase. (ii) The electromagnetic environment created by the cavity alters the heat flow between the thermal reservoir of photons and the sample through a thermal Purcell effect [22]. This may effectively change the temperature of the material and, in turn, modify the phase transition. It is conceivable, that similar effects also occur for the two-dimensional Hubbard model that couples to an SPP mode. We take this as a further motivation to extend the DMFT formalism to the present system. Our investigation suggests that the electron-photon interaction leads to a stabilization of the metallic phase and a decrease of the Mott-insulating regime.

This chapter is organized as follows: At first, we introduce the model Hamiltonian in Sec. 5.1. Then, we explain in Sec. 5.2 how the light-matter interaction is included in the standard DMFT formalism. Sec. 5.3 contains a brief discussion of the current results, and in Sec. 5.4, we close the chapter with a conclusion and an outlook on possible future research related to the project.

5.1. Model

We consider a setting similar to the one discussed in Ch. 4. Fig. 5.1 shows a schematic sketch of the present model. Again, we study a two-dimensional material (2D) that couples to a surface plasmon polariton (SPP) mode of a dielectric-metal interface. However, while the solid discussed in Ch. 4 exhibits a ferroelectric phase transition, we now examine a material with strongly correlated electrons that may undergo a Mott metal-insulator transition. The 2D material is embedded in the dielectric region at a uniform distance x_0 from the metal surface. The latter defines the y-z-plane of our coordinate

system. The metal supports a surface plasmon mode, which hybridizes with the electromagnetic field in the surrounding medium. This gives rise to an SPP mode that propagates along the interface and decays exponentially with the distance x. Due to the spatial confinement of the corresponding field, the light-matter interaction close to the dielectric-metal interface is enhanced as compared to free space. If the spacing x_0 is small enough, this may lead to a strong coupling between the 2D solid and the radiation field of the SPP mode.

5.1.1. Full Hamiltonian

We follow the same route as in Ch. 4 and do not start from a microscopic description of all the system's components. Instead, we focus on the 2D material and the quantized SPP mode. The dielectric-metal interface is only considered as the electromagnetic environment that determines the spatial structure and the dispersion relation of the SPP mode. It is described by the electric permittivity ε_d and ε_m of the dielectric and the metal and imposes additional interface conditions on the electromagnetic field. Hence, the SPP mode is nothing but the quantized version of the electromagnetic radiation in the presence of a dielectric-metal interface. (See App. A.1 for more details.)

We describe the bare material by the single-band Hubbard Hamiltonian (2.1) introduced in Sec. 2.1.1. Moreover, we set $\mu = U/2$ to fix the average electron density to $n_\sigma = \frac{1}{2}$, such that the system may undergo a transition to a Mott-insulating phase at large electron-electron interactions U. We introduce the coupling to the SPP mode using a representation in dipole gauge (see Sec. 2.3.2). With this, the Hamiltonian for the system can be written as

$$\hat{H} = \hat{H}_\mathrm{lm} + \hat{H}_U + \hat{H}_\mathrm{field}, \tag{5.1}$$

where

$$\hat{H}_U = U \sum_j \hat{n}_{j\uparrow}\hat{n}_{j\downarrow} \tag{5.2}$$

denotes the local electron-electron interaction and

$$\hat{H}_\mathrm{field} = \sum_{\boldsymbol{q}} \omega_{\boldsymbol{q}} \hat{a}^\dagger_{\boldsymbol{q}} \hat{a}_{\boldsymbol{q}} \tag{5.3}$$

corresponds to the free radiation field of the SPP. As in Ch. 4, we set $\varepsilon_\mathrm{d} = 1$ and assume a simple Drude response for the metal, so that the dispersion relation is given by

$$\omega_{\boldsymbol{q}} = \sqrt{\frac{\omega_\mathrm{p}^2}{2} + \boldsymbol{q}^2 c^2 - \sqrt{\frac{\omega_\mathrm{p}^4}{4} + \boldsymbol{q}^4 c^4}} \tag{5.4}$$

with the plasma frequency ω_p.

The present matter Hamiltonian does not contain any dipolar transitions. Therefore, all light-matter coupling terms related to the polarization density vanish. However, the Hubbard model allows for hopping between neighboring lattice sites. Thus, the

corresponding matrix elements have to be dressed with Peierls phase factors, and the kinetic contribution in the presence of the SPP mode reads as

$$\hat{H}_{\mathrm{lm}} = -\sum_{i,j,\sigma} t_{ij} e^{ie\chi_{ij}} \hat{c}^{\dagger}_{i\sigma} \hat{c}_{j\sigma}. \tag{5.5}$$

We consider a square lattice with lattice parameter a and nearest-neighbor hopping; hence, the hopping matrix elements are given by

$$t_{ij} = \begin{cases} t & , |\boldsymbol{R}_i - \boldsymbol{R}_j| = a \\ 0 & , \text{ otherwise,} \end{cases} \tag{5.6}$$

where $\boldsymbol{R}_m$ denotes the position vector of lattice site m.

Moreover, we assume that the electromagnetic field only varies slowly within the range of one lattice spacing a. Therefore, the Peierls phases can be approximated as

$$\chi_{ij} = \int_{\boldsymbol{R}_i}^{\boldsymbol{R}_j} d\boldsymbol{r}\, \hat{\boldsymbol{A}}(\boldsymbol{r}) \approx \boldsymbol{R}_{ji} \cdot \hat{\boldsymbol{A}}_{ij} \tag{5.7}$$

with the distance vector $\boldsymbol{R}_{ji} = \boldsymbol{R}_j - \boldsymbol{R}_i$ and the vector potential $\hat{\boldsymbol{A}}_{ij} = \hat{\boldsymbol{A}}(\frac{\boldsymbol{R}_i + \boldsymbol{R}_j}{2})$ at the center of the bond between site i and j. For the SPP mode, the quantized vector potential can be written as

$$\hat{\boldsymbol{A}}(\boldsymbol{r}) = \sum_{\boldsymbol{q}} \boldsymbol{e}_{\boldsymbol{q}} \mathcal{A}_{\boldsymbol{q}} (\hat{a}^{\dagger}_{-\boldsymbol{q}} + \hat{a}_{\boldsymbol{q}}) e^{i\boldsymbol{q}\cdot\boldsymbol{\rho}}, \tag{5.8}$$

where $\boldsymbol{q} = (q_y, q_z)^T$ is a two-dimensional mode vector, the operator $\hat{a}^{\dagger}_{\boldsymbol{q}}$ ($\hat{a}_{\boldsymbol{q}}$) creates (annihilates) a photon in mode $\boldsymbol{q}$, $\boldsymbol{e}_{\boldsymbol{q}} = \bar{\boldsymbol{e}}_{-\boldsymbol{q}}$ denotes the polarization vector of the mode, and $\mathcal{A}_{\boldsymbol{q}} = \mathcal{A}_{-\boldsymbol{q}} \in \mathbb{R}$ represents the corresponding amplitude. The two-dimensional vector $\rho = (y, z)^T$ only contains the y- and z-coordinates of position $\boldsymbol{r}$. In addition, it should be mentioned that the amplitude $\mathcal{A}_{\boldsymbol{q}}$ decays exponentially with x. More details on the derivation of Eq. (5.8) and explicit expressions for the parameters can be taken from App. B.1.

5.1.2. Expansion and truncation of the light-matter interaction

The Hamiltonian (5.5) describes a highly non-linear coupling between light and matter. Expanding the Peierls phase factors in a Taylor series, the equation can be rewritten as

$$\hat{H}_{\mathrm{lm}} = \hat{H}_{\mathrm{hop}} + \sum_{n=1}^{\infty} \hat{H}^{(n)}_{\mathrm{lm}}, \tag{5.9}$$

where $\hat{H}^{(n)}_{\mathrm{lm}}$ denotes the contribution of nth order in the photon operators. The zeroth-order term $\hat{H}_{\mathrm{hop}}$ corresponds to the kinetic part of the Hubbard model. In $\boldsymbol{k}$-space it is diagonal and reads as

$$\hat{H}_{\mathrm{hop}} = \sum_{\boldsymbol{k}\sigma} \epsilon_{\boldsymbol{k}} \hat{c}^{\dagger}_{\boldsymbol{k}\sigma} \hat{c}_{\boldsymbol{k}\sigma} \tag{5.10}$$

with the electron dispersion

$$\epsilon_{\boldsymbol{k}} = -2t[\cos(k_y a) + \cos(k_z a)] \tag{5.11}$$

for the square lattice. With this, the full Hamiltonian of the system is given by

$$\hat{H} = \hat{H}_{\text{mat}} + \sum_{n=1}^{\infty} \hat{H}_{\text{lm}}^{(n)} + \hat{H}_{\text{field}}, \tag{5.12}$$

where $\hat{H}_{\text{mat}} = \hat{H}_{\text{hop}} + \hat{H}_U$ corresponds to the bare matter Hamiltonian, which is described by the Hubbard model (2.1). Henceforth, we neglect all light-matter interaction terms beyond the second order and only take into account $\hat{H}_{\text{lm}}^{(1)}$ and $\hat{H}_{\text{lm}}^{(2)}$.

The linear contribution to the interaction reads as

$$\begin{aligned} \hat{H}_{\text{lm}}^{(1)} =& -\sum_{i,j,\sigma}\sum_{\boldsymbol{q}} iet_{ij}\boldsymbol{R}_{ji}\cdot\hat{\boldsymbol{A}}_{ij}\hat{c}_{i\sigma}^{\dagger}\hat{c}_{j\sigma} \\ =& \sum_{i,j,\sigma}\sum_{\boldsymbol{q}} v_{ij}^{\boldsymbol{q}}\hat{c}_{i\sigma}^{\dagger}\hat{c}_{j\sigma}(\hat{a}_{-\boldsymbol{q}}^{\dagger}+\hat{a}_{\boldsymbol{q}}) \end{aligned} \tag{5.13}$$

with the coupling constants

$$v_{ij}^{\boldsymbol{q}} = \gamma_{\boldsymbol{q}}(\boldsymbol{R}_{ij})e^{i\boldsymbol{q}\cdot(\boldsymbol{R}_i+\boldsymbol{R}_j)/2}. \tag{5.14}$$

The factor

$$\gamma_{\boldsymbol{q}}(\boldsymbol{R}_{ij}) = iet_{ij}\mathcal{A}_{\boldsymbol{q}}\boldsymbol{R}_{ij}\cdot\boldsymbol{e}_{\boldsymbol{q}} \tag{5.15}$$

only depends on the difference $\boldsymbol{R}_{ij} = \boldsymbol{R}_i - \boldsymbol{R}_j$ and thus can be Fourier transformed, which yields

$$\begin{aligned} \gamma_{\boldsymbol{q},\boldsymbol{k}} =& \sum_{\boldsymbol{R}} e^{-i\boldsymbol{k}\cdot\boldsymbol{R}}\gamma_{\boldsymbol{q}}(\boldsymbol{R}) \\ =& -e\mathcal{A}_{\boldsymbol{q}}\boldsymbol{e}_{\boldsymbol{q}}\cdot\boldsymbol{v}_{\boldsymbol{k}} \end{aligned} \tag{5.16}$$

with the group velocity $\boldsymbol{v}_{\boldsymbol{k}} = \nabla_{\boldsymbol{k}}\epsilon_{\boldsymbol{k}}$. Using this definition, the linear coupling term can be rewritten as

$$\hat{H}_{\text{lm}}^{(1)} = \sum_{\boldsymbol{k},\boldsymbol{q},\sigma} \gamma_{\boldsymbol{q},\boldsymbol{k}+\boldsymbol{q}/2}\hat{c}_{\boldsymbol{k}+\boldsymbol{q}\sigma}^{\dagger}\hat{c}_{\boldsymbol{k}\sigma}(\hat{a}_{-\boldsymbol{q}}^{\dagger}+\hat{a}_{\boldsymbol{q}}). \tag{5.17}$$

The second-order light-matter interaction is given by

$$\begin{aligned} \hat{H}_{\text{lm}}^{(2)} =& \frac{1}{2}\sum_{i,j,\sigma} t_{ij}e^2(\boldsymbol{R}_{ji}\cdot\hat{\boldsymbol{A}}_{ij})^2\hat{c}_{i\sigma}^{\dagger}\hat{c}_{j\sigma} \\ =& \frac{1}{2}\sum_{i,j,\sigma}\sum_{\boldsymbol{q}_1,\boldsymbol{q}_2} \tilde{v}_{ij}^{\boldsymbol{q}_1\boldsymbol{q}_2}\hat{c}_{i\sigma}^{\dagger}\hat{c}_{j\sigma}(\hat{a}_{-\boldsymbol{q}_1}^{\dagger}+\hat{a}_{\boldsymbol{q}_1})(\hat{a}_{-\boldsymbol{q}_2}^{\dagger}+\hat{a}_{\boldsymbol{q}_2}), \end{aligned} \tag{5.18}$$

where

$$\tilde{v}_{ij}^{\boldsymbol{q}_1\boldsymbol{q}_2} = \tilde{\gamma}_{\boldsymbol{q}_1\boldsymbol{q}_2}(\boldsymbol{R}_{ij})e^{i(\boldsymbol{q}_1+\boldsymbol{q}_2)\cdot(\boldsymbol{R}_i+\boldsymbol{R}_j)/2}. \tag{5.19}$$

Again, the coupling constant contains a factor that only depends on the distance $\boldsymbol{R}_{ij}$. It reads as

$$\tilde{\gamma}_{\boldsymbol{q}_1\boldsymbol{q}_2}(\boldsymbol{R}_{ij}) = e^2 t_{ij} \mathcal{A}_{\boldsymbol{q}_1} \mathcal{A}_{\boldsymbol{q}_2} (\boldsymbol{e}_{\boldsymbol{q}_1} \cdot \boldsymbol{R}_{ij})(\boldsymbol{e}_{\boldsymbol{q}_2} \cdot \boldsymbol{R}_{ij}) \tag{5.20}$$

and can be transformed to $\boldsymbol{k}$-space, which gives

$$\begin{aligned} \tilde{\gamma}_{\boldsymbol{q}_1,\boldsymbol{q}_2,\boldsymbol{k}} &= \sum_{\boldsymbol{R}} e^{-i\boldsymbol{k}\cdot\boldsymbol{R}} \tilde{\gamma}_{\boldsymbol{q}_1\boldsymbol{q}_2}(\boldsymbol{R}) \\ &= -e^2 (\mathcal{A}_{\boldsymbol{q}_1} \boldsymbol{e}_{\boldsymbol{q}_1} \cdot \nabla_{\boldsymbol{k}})(\mathcal{A}_{\boldsymbol{q}_2} \boldsymbol{e}_{\boldsymbol{q}_2} \cdot \nabla_{\boldsymbol{k}}) \epsilon_{\boldsymbol{k}}. \end{aligned} \tag{5.21}$$

With this, the second-order light-matter Hamiltonian can be recast into the form

$$\hat{H}^{(2)}_{\mathrm{lm}} = \frac{1}{2} \sum_{\boldsymbol{q}_1,\boldsymbol{q}_2,\boldsymbol{k}} \sum_{\sigma} \tilde{\gamma}_{\boldsymbol{q}_1,\boldsymbol{q}_2,\boldsymbol{k}+(\boldsymbol{q}_1+\boldsymbol{q}_2)/2} \hat{c}^\dagger_{\boldsymbol{k}+\boldsymbol{q}_1+\boldsymbol{q}_2\sigma} \hat{c}_{\boldsymbol{k}\sigma} (\hat{a}^\dagger_{-\boldsymbol{q}_1} + \hat{a}_{\boldsymbol{q}_1})(\hat{a}^\dagger_{-\boldsymbol{q}_2} + \hat{a}_{\boldsymbol{q}_2}). \tag{5.22}$$

A detailed calculation of the Fourier transforms is given in App. B.2.

5.2. DMFT formalism

We aim to integrate the interaction with the SPP mode into the DMFT formalism using diagrammatic perturbation theory. For that purpose, we supplement the local self-energy of the impurity model by a number of $\boldsymbol{k}$-dependent terms from a diagrammatic series. Incorporating the light-matter interaction does not change the structure of the single-site impurity problem. This is due to the fact that DMFT only includes diagrams with the same site index at all internal and external vertices. The light-matter coupling constants $v^{\boldsymbol{q}}_{ij}$ and $\tilde{v}^{\boldsymbol{q}_1\boldsymbol{q}_2}_{ij}$, however, vanish for $i \neq j$, such that any diagram involving the SPP mode depends on at least two different lattice sites. Therefore, we separate the self-energy into a part Σ^{mat} that only contains U interaction lines and a contribution Σ^{SPP} that accounts for the additional electron-photon coupling.

With this definition, DMFT provides a local approximation for Σ^{mat}, while Σ^{SPP} can be estimated from the leading order diagrams of the perturbation series. Fig. 5.2 illustrates the two self-energy contributions. Note that we have boldified the electronic Green's function lines, i.e., they correspond to the fully interacting system. The basic idea of this approach is similar to the GW+DMFT approximation described in [7], where the local and non-local contributions of the Coulomb interaction are separated in a similar manner. We implement the DMFT algorithm using the NESSi library [80], which is designed for non-equilibrium Green's functions. Therefore, the equations below are expressed in the Keldysh formalism.

5.2.1. Self-energy contribution of the SPP mode

As a first approximation, we only take into account the leading-order diagrams contributing to the skeleton expansion of Σ^{SPP}, which are highlighted by the green box in Fig. 5.2. In general, the lowest-order terms resulting from the linear light-matter interaction are given by a Hartree-like and a Fock-like diagram (upper two diagrams in

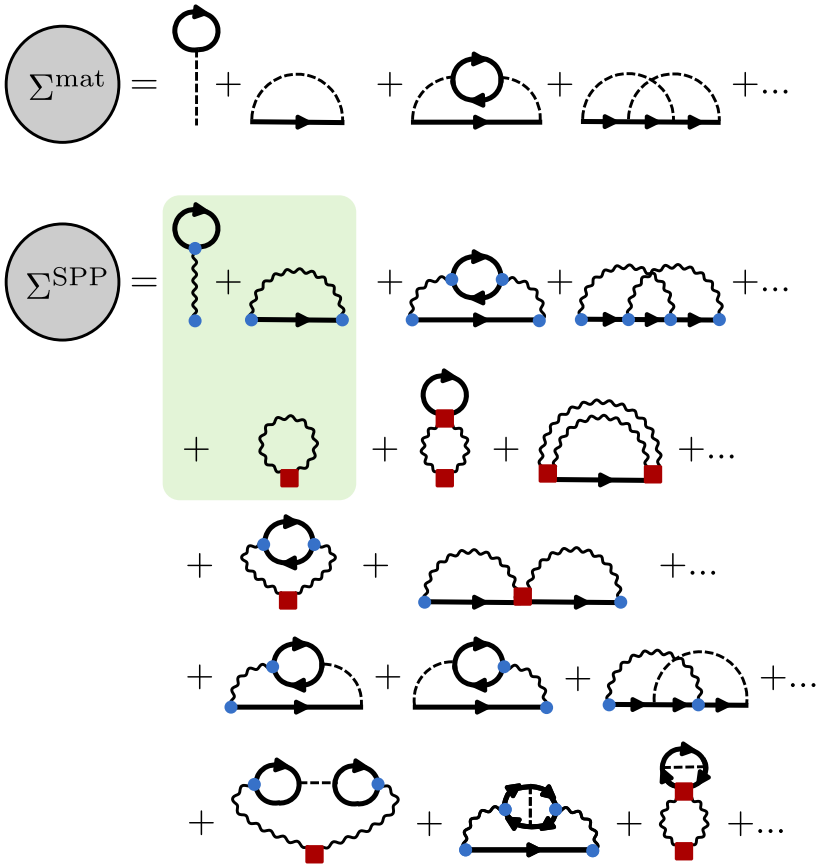

Figure 5.2.: *Separation of the electron self-energy. While Σ^{mat} only contains U-interaction lines (dashed lines), Σ^{SPP} also includes photon propagators (wavy lines). The bold solid lines correspond to the fully interacting Green's function. Blue dots represent interaction vertices for the linear light-matter coupling ($v_{ij}^{\boldsymbol{q}}$ or $\gamma_{\boldsymbol{q},\boldsymbol{k}+\boldsymbol{q}/2}$ and c.c.), and red squares indicate interaction vertices for the second-order term of the light-matter Hamiltonian ($\tilde{v}_{ij}^{\boldsymbol{q}_1\boldsymbol{q}_2}$ or $\tilde{\gamma}_{\boldsymbol{q}_1,\boldsymbol{q}_2,\boldsymbol{k}+(\boldsymbol{q}_1+\boldsymbol{q}_2)}$).*

the green box). In position representation, the Hartree-term is given by the following expression

$$\Sigma^{\mathrm{H}}_{ij\sigma}(t,t') = \delta_{\mathcal{C}}(t,t')i\int_{\mathcal{C}} d\bar{t}\sum_{lm\boldsymbol{q}} v^{\boldsymbol{q}}_{ij} D^0_{\boldsymbol{q}}(t,\bar{t}) v^{-\boldsymbol{q}}_{lm} G_{lm\sigma}(\bar{t},\bar{t}), \tag{5.23}$$

where

$$G_{ij\sigma}(t,t') = -i\langle T_{\mathcal{C}}\hat{c}_{i\sigma}(t)\hat{c}^\dagger_{j\sigma}(t')\rangle \tag{5.24}$$

denotes the fully interacting electron Green's function and

$$D^0(t,t') = -i\langle T_{\mathcal{C}}\hat{a}_{\boldsymbol{q}}(t)\hat{a}^\dagger_{\boldsymbol{q}}(t')\rangle - i\langle T_{\mathcal{C}}\hat{a}_{-\boldsymbol{q}}(t')\hat{a}^\dagger_{-\boldsymbol{q}}(t)\rangle \tag{5.25}$$

represents the free photon propagator. However, due to the geometry of the lattice, the Green's function is invariant under an exchange of the position indices, i.e., $G_{lm\sigma}(\bar{t},\bar{t}) = G_{ml\sigma}(\bar{t},\bar{t})$. Moreover, the light-matter coupling constants satisfy the relation $v^{-\boldsymbol{q}}_{lm} = -v^{-\boldsymbol{q}}_{ml}$. Consequently, the Hartree-like contribution to the self-energy can be rewritten as

$$\Sigma^{\mathrm{H}}_{ij\sigma}(t,t') = -\delta_{\mathcal{C}}(t,t')i\int_{\mathcal{C}} d\bar{t}\sum_{lm\boldsymbol{q}} v^{\boldsymbol{q}}_{ij} D^0_{\boldsymbol{q}}(t,\bar{t}) v^{-\boldsymbol{q}}_{ml} G_{ml\sigma}(\bar{t},\bar{t}) = -\Sigma^{\mathrm{H}}_{ij\sigma}(t,t') \tag{5.26}$$

and therefore equals zero. The Fock-like term gives rise to a non-vanishing contribution and reads as

$$\Sigma^{(1)}_{\boldsymbol{k}\sigma}(t,t') = i\sum_{\boldsymbol{q}} |\gamma_{\boldsymbol{q},\boldsymbol{k}-\boldsymbol{q}/2}|^2 G_{\boldsymbol{k}-\boldsymbol{q}\sigma}(t,t') D^0_{\boldsymbol{q}}(t,t'). \tag{5.27}$$

Now, we turn to the lowest-order diagram originating from the second-order light-matter interaction (lower diagram in the green box). The corresponding self-energy is proportional to a delta-function in time and thus can be written as $\Sigma^{(2)}_{\boldsymbol{k}}(t,t') = \delta_{\mathcal{C}}(t,t')s_{\boldsymbol{k}}(t)$, where

$$s_{\boldsymbol{k}}(t) = i\frac{1}{2}\sum_{\boldsymbol{q}} \tilde{\gamma}_{\boldsymbol{q},-\boldsymbol{q},\boldsymbol{k}} D^0_{\boldsymbol{q}}(t,t). \tag{5.28}$$

This contribution can be interpreted as a photon-induced correction to the electron dispersion $\epsilon_{\boldsymbol{k}}$.

5.2.2. Impurity problem

As mentioned previously, the electron-photon interaction does not alter the structure of the single-site impurity action, which is given by

$$S_{\mathrm{imp}} = \int_{\mathcal{C}} dt dt' \sum_{\sigma} \bar{c}_\sigma(t)\mathcal{G}^{-1}(t,t')c_\sigma(t') - U\int_{\mathcal{C}} dt\, n_\uparrow(t)n_\downarrow(t), \tag{5.29}$$

where the Weiss field can be expressed in terms of the hybridization function Δ as

$$\mathcal{G}^{-1}(t,t') = (i\partial_t + \mu)\delta_{\mathcal{C}}(t,t') - \Delta(t,t'). \tag{5.30}$$

The Green's function of the impurity is defined as

$$G_\sigma^{\mathrm{imp}} = -i\langle c_\sigma(t)\bar{c}_\sigma(t')\rangle_{S_{\mathrm{imp}}} \tag{5.31}$$

with $\langle ...\rangle_{S_{\mathrm{imp}}} = \mathcal{Z}^{-1}\int \mathcal{D}[\bar{c},c](e^{iS_{\mathrm{imp}}}...)$ and the partition function $\mathcal{Z} = \int \mathcal{D}[\bar{c},c]e^{iS_{\mathrm{imp}}}$. It is related to the Weiss field and the self-energy Σ_{imp} by the Dyson equation

$$G_\sigma^{\mathrm{imp}} = \mathcal{G} + G_\sigma^{\mathrm{imp}} * \Sigma_{\mathrm{imp}} * \mathcal{G}, \tag{5.32}$$

where the operator $*$ indicates a convolution in time. (See Sec. 2.1.4 for a brief introduction to DMFT on the Keldysh contour.)

We solve the impurity problem using iterative perturbation theory (IPT). In this approach, the self-energy is approximated by the two lowest-order terms of a diagrammatic expansion in the interaction U and reads as

$$\Sigma_{\mathrm{imp}}(t,t') \approx s_U\delta_{\mathcal{C}}(t,t') + \Sigma_U(t,t'), \tag{5.33}$$

where, at half-filing,

$$s_U = U\langle n_\sigma\rangle = U/2, \tag{5.34}$$

and

$$\Sigma_U(t,t') = U^2\mathcal{G}(t,t')\mathcal{G}(t,t')\mathcal{G}(t',t). \tag{5.35}$$

At first view, this may seem like a crude approximation, and indeed, the calculation should rather be understood as a first qualitative analysis of the system. However, it should be mentioned that, at half-filling, the IPT method does not only give reasonable results for small U, but also becomes exact if U is large compared to the bandwidth of the non-interacting system. Hence, the IPT method can be considered as an interpolation between the weak-coupling and strong-coupling limit [29]. Since the first term in Eq. (5.33) is diagonal in time, it can be absorbed in the chemical potential $\tilde{\mu} = \mu - s_U$, which vanishes for a half-filled system. Thus, the impurity Dyson equation can be rewritten as

$$[(i\partial_t + \tilde{\mu})\mathbb{I} - \Delta - \Sigma_U] * G_\sigma^{\mathrm{imp}} = \mathbb{I}. \tag{5.36}$$

5.2.3. Self-consistency

Following the DMFT method, we assume that

$$G_\sigma^{\mathrm{imp}} = G_\sigma^{\mathrm{loc}} = \frac{1}{N}\sum_{\boldsymbol{k}} G_{\boldsymbol{k}\sigma}, \tag{5.37}$$

where G_σ^{loc} denotes the local lattice Green's function. Moreover, we approximate the matter part of the self-energy with the local impurity self-energy, i.e.,

$$\Sigma_{\boldsymbol{k}\sigma}^{\mathrm{mat}}(t,t') \approx \Sigma_{\mathrm{imp}}(t,t'). \tag{5.38}$$

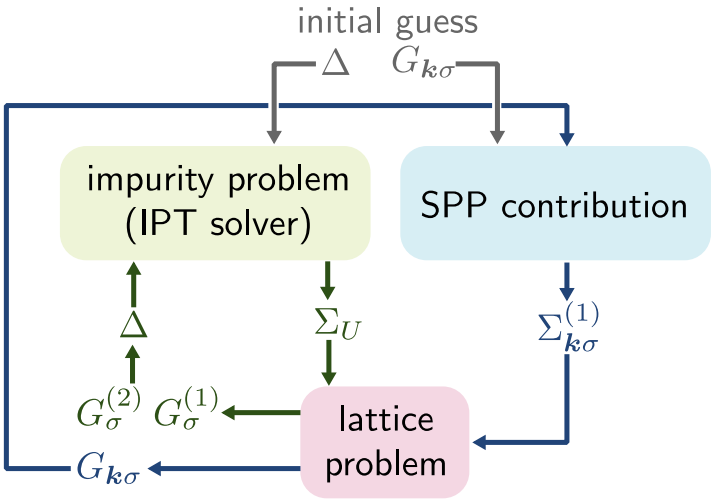

Figure 5.3.: *Algorithm flowchart of the DMFT loop for the Hubbard model with coupling to the SPP mode.*

With this approximation, we take into account all local diagrams of Σ^{mat} up to arbitrary order in U. The self-energy contribution due to the SPP mode is estimated from the lowest order diagrams introduced in Sec. 5.2.1 and thus reads as

$$\Sigma^{\text{SPP}}_{\boldsymbol{k}\sigma}(t,t') \approx \delta_{\mathcal{C}}(t,t')s_{\boldsymbol{k}}(t) + \Sigma^{(1)}_{\boldsymbol{k}\sigma}(t,t'). \tag{5.39}$$

Therefore, the lattice Dyson equation can be written as

$$\left[(i\partial_t + \tilde{\mu} - \eta_{\boldsymbol{k}})\mathbb{I} - \Sigma_U - \Sigma^{(1)}_{\boldsymbol{k}\sigma}\right] * G_{\boldsymbol{k}\sigma} = \mathbb{I} \tag{5.40}$$

with the renormalized electron dispersion $\eta_{\boldsymbol{k}} = \epsilon_{\boldsymbol{k}} + s_{\boldsymbol{k}}$.

For the system under consideration, we encountered numerical issues when solving the impurity Dyson equation (5.32) for the Weiss field $\mathcal{G}$ if the material is in the Mott-insulating phase. To avoid this problem, we express the self-consistency in terms of the hybridization function Δ. In this formulation, the impurity Dyson equation is replaced by the relation

$$\Delta + G^{(1)}_\sigma * \Delta = G^{(2)}_\sigma \tag{5.41}$$

with

$$G^{(1)}_\sigma = \frac{1}{N}\sum_{\boldsymbol{k}} (\eta_{\boldsymbol{k}}\mathbb{I} + \Sigma^{GW}_{\boldsymbol{k}}) * G_{\boldsymbol{k}\sigma} \tag{5.42}$$

$$G^{(2)}_\sigma = \frac{1}{N}\sum_{\boldsymbol{k}} [\Sigma^{GW}_{\boldsymbol{k}} + (\eta_{\boldsymbol{k}}\mathbb{I} + \Sigma^{GW}_{\boldsymbol{k}}) * G_{\boldsymbol{k}\sigma} * (\eta_{\boldsymbol{k}}\mathbb{I} + \Sigma^{GW}_{\boldsymbol{k}})] \tag{5.43}$$

Even for the square lattice, Eq. (5.41) can be solved numerically and yields convergent results in the metallic and Mott-insulating regime. A derivation of the expression is given in App. B.3.

The algorithm to solve the self-consistent DMFT equations is illustrated by the flowchart in Fig. 5.3. It consists of the following steps:

1. Start from an initial guess for the hybridization function Δ and pass it to the IPT impurity solver. Initialize the lattice Green's function $G_{\boldsymbol{k}\sigma}$.
2. IPT impurity solver: Determine $\mathcal{G}$ using Eq. (5.30) and calculate the IPT self-energy Σ_U from Eq. (5.35).
3. Contribution of the SPP mode: Calculate the self-energy $\Sigma^{(1)}_{\boldsymbol{k}\sigma}$ defined in Eq. (5.27).
4. Lattice problem: Solve the Dyson equation (5.40) for $G_{\boldsymbol{k}\sigma}$ and determine $G^{(1)}_{\sigma}$ and $G^{(2)}_{\sigma}$ using Eq. (5.42) and (5.43).
5. Update the hybridization function Δ by solving Eq. (5.41).
6. If the result has not converged yet, repeat the procedure starting from step 2.

5.3. Results and discussion

This section provides a brief overview of the current findings. We first discuss in Sec. 5.3.1 how the strength of the electron-photon coupling can be influenced and specify the choice of parameters. In Sec. 5.3.2, we consider the DMFT results and analyze how the Mott metal-insulator transition is affected by the self-energy contribution from the SPP mode.

5.3.1. Coupling strength and parameters

The strength of the electron-photon interaction is determined by the vertices $\gamma_{\boldsymbol{q},\boldsymbol{k}-\boldsymbol{q}/2}$ and $\tilde{\gamma}_{\boldsymbol{q},-\boldsymbol{q},\boldsymbol{k}}$ defined in Eq. (5.16) and (5.21). These vertices control how much each mode $\boldsymbol{q}$ of the electromagnetic field contributes to the self-energy at a given lattice vector $\boldsymbol{k}$. Evaluating the corresponding expression for the linear coupling to the SPP mode yields

$$\begin{aligned}|\gamma_{\boldsymbol{q},\boldsymbol{k}-\boldsymbol{q}/2}|^2 =& \frac{2}{N}\frac{g^2}{\omega_{\boldsymbol{q}}} t^2 e^{-2Q_{\mathrm{d}}x_0}\mathcal{N}_{\boldsymbol{q}}^2\left(\frac{Q_{\mathrm{d}}}{q^2}\right)^2 \times \\ & \times \left\{q_y \sin[(k_y - q_y/2)a] + q_z \sin[(k_z - q_z/2)a]\right\}^2,\end{aligned} \tag{5.44}$$

where the normalization factor $\mathcal{N}_{\boldsymbol{q}}$ and the $\boldsymbol{q}$-dependent decay constant Q_{d} are defined in App. A.1, $q = |\boldsymbol{q}|$, and the dispersion relation $\omega_{\boldsymbol{q}}$ is given by Eq. (5.4). Moreover, we have introduced the energy scale

$$g^2 = \frac{e^2 a^2}{\varepsilon_0 \varepsilon_{\mathrm{d}} a^3}, \tag{5.45}$$

which determines the overall coupling strength. Note that this parameter exhibits a similar structure as the collective coupling defined in Sec. 3.2 and Ch. 4. Again, the

numerator has the dimension of a dipole moment squared, while the denominator scales as the size of a single unit cell a^3. However, the dipole moment in the numerator depends on the lattice constant a, such that g^2 is not proportional to the density $N/V = 1/a^3$ but only scales as $1/a$. The coupling constant for the second-order light-matter interaction reads as

$$\begin{aligned}\tilde{\gamma}_{\boldsymbol{q},-\boldsymbol{q},\boldsymbol{k}} = &-\frac{1}{N}\frac{g^2}{\omega_{\boldsymbol{q}}} t e^{-2Q_{\mathrm{d}}x_0} \mathcal{N}_{\boldsymbol{q}}^2 \left(\frac{Q_{\mathrm{d}}}{q^2}\right)^2 \times \\ &\times \left[q_y^2 \cos(k_y a) + q_z^2 \cos(k_z a)\right].\end{aligned} \tag{5.46}$$

Below, we fix the hopping matrix element to $t = 0.03$ eV, which serves as our unit of energy. This value is comparable to the nearest-neighbor hopping amplitudes calculated for real quasi-two-dimensional organic molecular crystals [67]. Moreover, we define the unit of length as the lattice parameter $a = 10^{-9}$ m, consistent with typical values observed in real organic materials (see, e.g., footnote 32 in [18]). As a result, the speed of light is calculated as $c = 6577.6 \times 10^3$ (noting that we have set $\hbar = 1$) and $g^2 \approx 600$.

Both $|\gamma_{\boldsymbol{q},\boldsymbol{k}-\boldsymbol{q}/2}|^2$ and $\tilde{\gamma}_{\boldsymbol{q},-\boldsymbol{q},\boldsymbol{k}}$ vanish as $q \to \infty$; consequently, only a finite range of $\boldsymbol{q}$-vectors contributes to the interaction. The coupling decays exponentially as the distance x_0 between the two-dimensional material and the metal surface is increased. Furthermore, the interaction strength can be modified by changing the plasma frequency ω_{p}. This is illustrated in Fig. 5.4 and 5.5, where $N|\gamma_{\boldsymbol{q},\boldsymbol{k}-\boldsymbol{q}/2}|^2$ and $N\tilde{\gamma}_{\boldsymbol{q},-\boldsymbol{q},\boldsymbol{k}}$ are plotted as a function of $\boldsymbol{q}$ at three different $\boldsymbol{k}$-points for $\omega_{\mathrm{p}} = 2$ and $\omega_{\mathrm{p}} = 1$. It is clearly visible that a decrease in the plasma frequency leads to an enhancement of the linear light-matter interaction constant $|\gamma_{\boldsymbol{q},\boldsymbol{k}-\boldsymbol{q}/2}|^2$. The same applies to the magnitude of the second-order coupling strength $\tilde{\gamma}_{\boldsymbol{q},-\boldsymbol{q},\boldsymbol{k}}$.

This behavior can be explained as follows: for $c \gg \omega_{\boldsymbol{q}}$, $Q_{\mathrm{d}} \approx Q_{\mathrm{m}} \sim q$ and $\mathcal{N}_{\boldsymbol{q}}^2 \sim aq/2$. As a result, the decay constants and the normalization factor are independent of the SPP dispersion $\omega_{\boldsymbol{q}}$, and the light-matter coupling strengths are proportional to $1/\omega_{\boldsymbol{q}}$. In addition, $\omega_{\boldsymbol{q}}$ is approximately given by $\omega_{\mathrm{p}}/\sqrt{2}$ except for $q \ll 1$, where it takes a smaller value (see App. A.1 for more details). Hence, $|\gamma_{\boldsymbol{q},\boldsymbol{k}-\boldsymbol{q}/2}|^2$ and $\tilde{\gamma}_{\boldsymbol{q},-\boldsymbol{q},\boldsymbol{k}}$ are almost inversely proportional to the plasma frequency for most modes $\boldsymbol{q}$. In the following, we use this behavior to control the interaction between the SPP mode and the material. The distance x_0 is set to 2.5.

5.3.2. Mott metal-insulator transition

To investigate the effect of the SPP mode on the Mott metal-insulator transition, we consider two quantities. On the one hand, we determine the local Matsubara Green's function $G_\sigma^{\mathrm{loc}}(\tau) = -iG_\sigma^{\mathrm{loc}}(-i\tau, 0)$ at $\tau = \beta/2$, which provides an estimate for the local density of states at the Fermi level. (See App. B.4.1 for further explanations.) In the metallic regime, $G_\sigma^{\mathrm{loc}}(\beta/2)$ takes a finite value due to the quasiparticle peak appearing in the density of states at $\omega = 0$ (i.e., at the Fermi energy). Conversely, the Mott-insulating state is characterized by an energy gap. Consequently, there is no spectral weight at zero frequency, and $G_\sigma^{\mathrm{loc}}(\beta/2)$ vanishes.

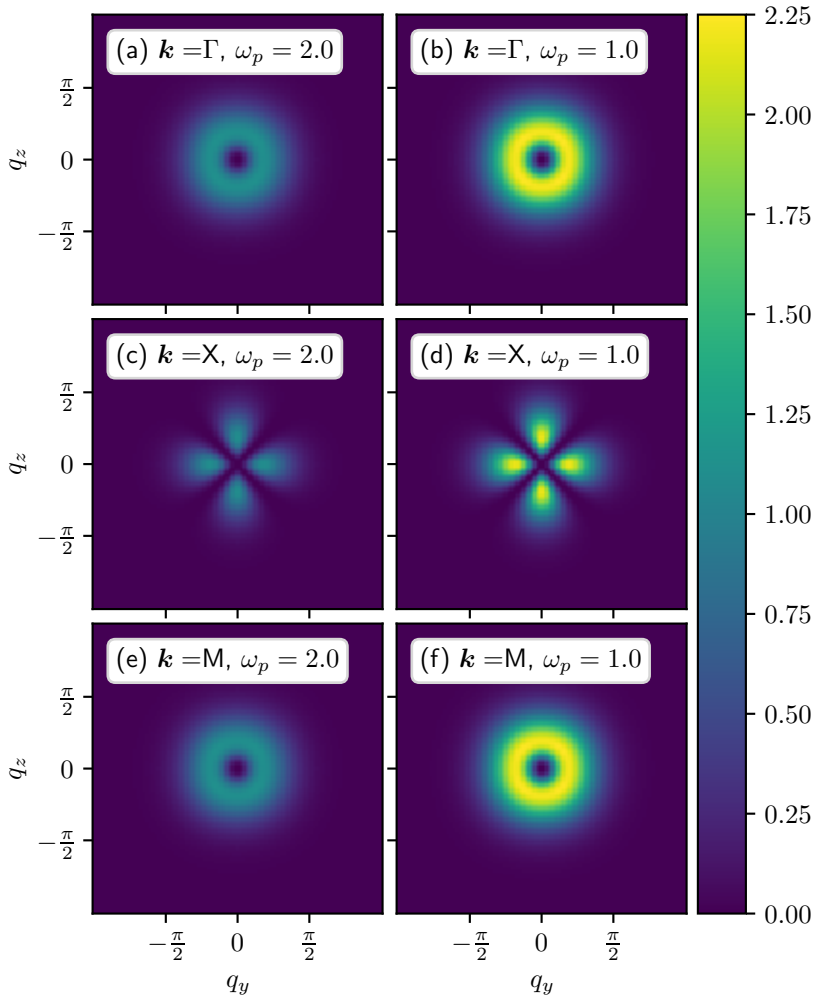

Figure 5.4.: *Coupling constant* $N|\gamma_{\boldsymbol{q},\boldsymbol{k}-\boldsymbol{q}/2}|^2$ *for the linear light-matter interaction as a function of the mode vector* $\boldsymbol{q}$ *at a given crystal momentum* $\boldsymbol{k}$*. For panels (a), (c), and (e), the plasma frequency has been set to* $\omega_p = 2.0$*, while (b), (d), and (f) show the results for* $\omega_p = 1.0$*. The* $\boldsymbol{k}$*-values correspond to the high symmetry points* $\Gamma = (0,0)^T$ *(panel (a) and (b)),* $X = (\pi,0)^T$ *(panel (c) and (d)), and* $M = (\pi,\pi)^T$ *(panel (e) and (f)). The unit of energy is equal to the hopping matrix element* t*, whereas the unit of length is given by the lattice parameter* a*. The distance* x_0 *has been set to* 2.5*.*

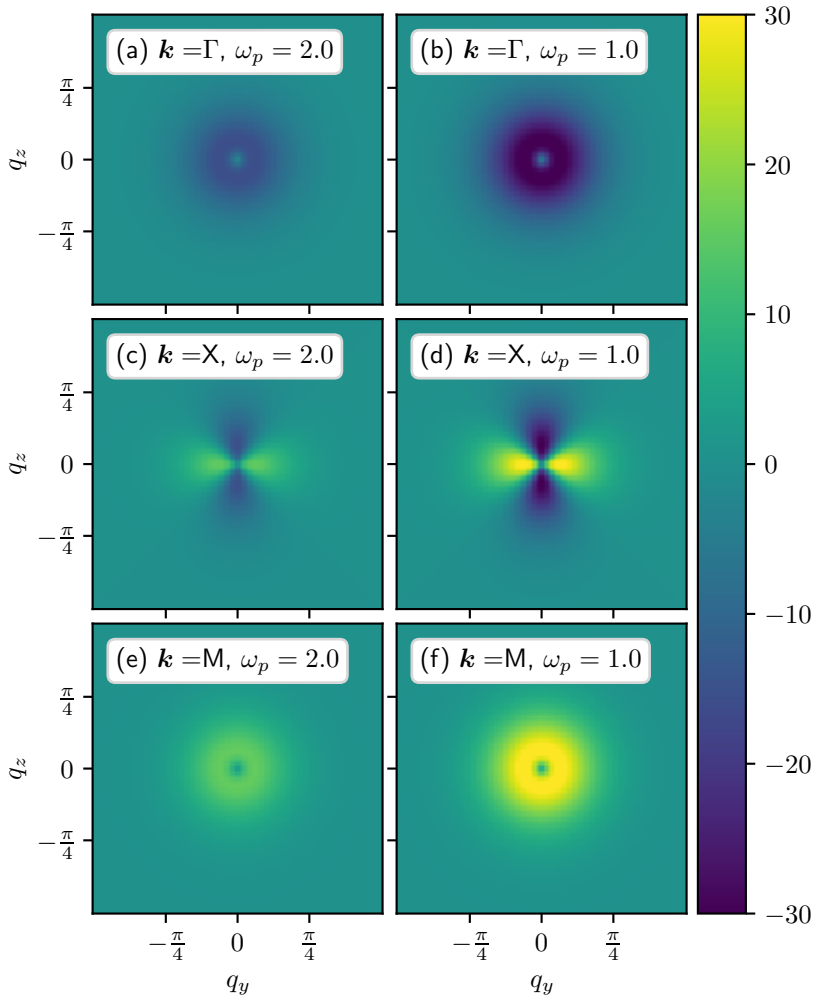

Figure 5.5.: *Coupling constant $N\tilde{\gamma}_{\boldsymbol{q},-\boldsymbol{q},\boldsymbol{k}}$ for the second-order light-matter interaction as a function of the mode vector $\boldsymbol{q}$ at a given crystal momentum $\boldsymbol{k}$. For panels (a), (c), and (e), the plasma frequency has been set to $\omega_p = 2.0$, while (b), (d), and (f) show the results for $\omega_p = 1.0$. The $\boldsymbol{k}$-values correspond to the high-symmetry points $\Gamma = (0,0)^T$ (panel (a) and (b)), $X = (\pi,0)^T$ (panel (c) and (d)), and $M = (\pi,\pi)^T$ (panel (e) and (f)). The unit of energy is equal to the hopping matrix element t, whereas the unit of length is given by the lattice parameter a. The distance x_0 has been set to 2.5.*

On the other hand, we calculate the double occupancy

$$D = \langle \hat{n}_{j\uparrow} \hat{n}_{j\downarrow} \rangle = \frac{1}{4} - \frac{i}{U} \left[\int_{\mathcal{C}} d\bar{t}\, \Sigma_U(t, \bar{t}) G_\sigma^{\mathrm{loc}}(\bar{t}, t) \right]^{<} . \tag{5.47}$$

(A derivation of this formula is given in App. B.4.2.) In the non-interacting limit, D takes a value of $1/4$ owing to the fact that at half filling, each site may take one of the four possible states $|\uparrow\rangle$ (one electron with spin up), $|\downarrow\rangle$ (one electron with spin down), $|\uparrow\downarrow\rangle$ (doubly occupied site), or $|0\rangle$ (empty site) with equal probability. As U is increased, however, the cost in energy for doubly occupied sites becomes larger, which leads to a reduction of D.

Fig. 5.6 displays the DMFT results at three different inverse temperatures β for $N = 10 \times 10$. The data illustrated by the green triangles correspond to a system without coupling to the SPP mode ($g^2 = 0$). Panels (a), (c), and (e) clearly show a phase transition from a metal with $G_\sigma^{\mathrm{loc}}(\beta/2) < 0$ to a Mott insulator with $G_\sigma^{\mathrm{loc}}(\beta/2) = 0$. At $\beta = 10$ and $\beta = 20$, there is a region where both phases coexist, which indicates a first-order phase transition. The two solutions have been obtained by increasing or decreasing U and using the result from the previous U value as an initial guess for the DMFT iteration. Similarly, the double occupancy in panel (d) and (f) exhibits a discontinuous jump and a coexistence region near the phase transition. The curves for $\beta = 5$ (panel (a) and (b)) are almost continuous. This is in agreement with previous DMFT calculations, which predict that the region of coexistence becomes smaller as the temperature is increased (β is decreased) until it shrinks to a single critical point, where the transition is of second order. Above this temperature, there is no insulating state due to thermal activations across the Mott-Hubbard gap [29].

Moreover, it can be seen that the critical interaction U decreases with increasing temperature. This behavior can be attributed to the higher entropy of the insulating DMFT solution compared to the metallic regime, which leads to a stronger reduction of the free energy with rising T. However, DMFT does not take into account spin fluctuations, which may counteract this effect. In fact, it has been shown for the two-dimensional square lattice that anti-ferromagnetic correlations reverse the slope of the critical line $U_{\mathrm{c}}(T)$ and might even inhibit a transition to the metallic phase at $T = 0$ [77]. Nevertheless, the DMFT calculation provides a reasonable estimate for the behavior of the system and thus offers a qualitative understanding of the photon-induced effect on the Mott metal-insulator transition.

The red crosses and the blue dots in Fig. 5.6 represent results for a non-vanishing light-matter interaction ($g^2 = 600$) and a plasma frequency of $\omega_{\mathrm{p}} = 2$ and $\omega_{\mathrm{p}} = 1$, respectively. For all $\beta = 1/T$, the phase transition shifts to higher values of U as ω_{p} is reduced. This indicates that the metallic state is stabilized as the coupling to the SPP mode is enhanced. The nature of the phase transition is not affected. There is still a coexistence region near the critical interaction U_{c}, which becomes smaller as β is decreased (T is increased). In addition, DMFT still predicts that the Mott-insulating phase will be entropically stabilized if the temperature is increased.

A possible explanation for this behavior is the effective renormalization of the hopping matrix elements due to the second-order light-matter interaction. As mentioned

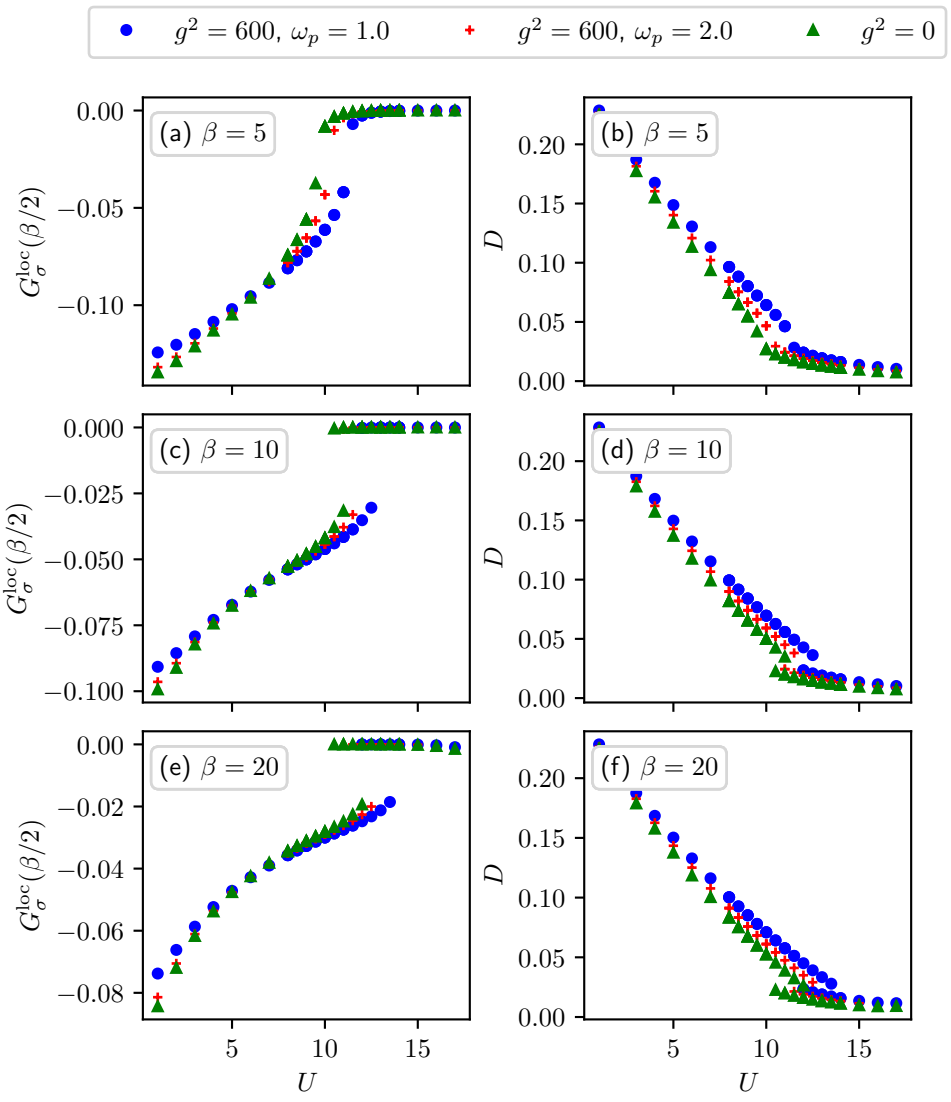

Figure 5.6.: *DMFT results for the local Matsubara Green's function at $\tau = \beta/2$ (panels (a), (c), and (e)), and the double occupancy D (panels (b), (d), and (f)) as a function of U at various inverse temperatures β. All calculations have been performed for a lattice of $N = 10 \times 10$ sites. The green triangles correspond to the bare material with vanishing light-matter coupling, while the blue dots and the red crosses correspond to an interacting system, where the plasma frequency of the metal region has been set to $\omega_p = 1$ and $\omega_p = 2$, respectively. In both cases, the distance x_0 is fixed to 2.5 and $g^2 = 600$. The unit of energy is given by the hopping parameter t, and the unit of length has been set to the lattice constant a.*

previously, the corresponding self-energy contribution $s_{\boldsymbol{k}}$ can be absorbed in the effective electron dispersion $\eta_{\boldsymbol{k}} = \epsilon_{\boldsymbol{k}} + s_{\boldsymbol{k}}$. For the model under consideration, $s_{\boldsymbol{k}}$ can be written as $s_{\boldsymbol{k}} = -2\Delta t[\cos(k_y a) + \cos(k_x a)]$, so that $\eta_{\boldsymbol{k}} = -2(t + \Delta t)[\cos(k_y a) + \cos(k_x a)]$ and thus takes the same form as the non-interacting electron dispersion with a renormalized hopping amplitude $t_{\text{eff}} = t + \Delta t$. The change Δt in the hopping amplitude is given by

$$\begin{aligned}\Delta t &= -\frac{1}{4}\frac{1}{N}\sum_{\boldsymbol{q}} D^0_{\boldsymbol{q}}(\beta)\frac{g^2}{\omega_{\boldsymbol{q}}} t e^{-2Q_{\text{d}}x_0}\mathcal{N}^2_{\boldsymbol{q}}\left(\frac{Q_{\text{d}}}{q^2}\right)^2 q_y^2 \\ &= -\frac{1}{4}\frac{1}{N}\sum_{\boldsymbol{q}} D^0_{\boldsymbol{q}}(\beta)\frac{g^2}{\omega_{\boldsymbol{q}}} t e^{-2Q_{\text{d}}x_0}\mathcal{N}^2_{\boldsymbol{q}}\left(\frac{Q_{\text{d}}}{q^2}\right)^2 q_z^2,\end{aligned} \tag{5.48}$$

where $D^0_{\boldsymbol{q}}(\beta) = -\cosh(\beta\omega_{\boldsymbol{q}}/2)/\sinh(\beta\omega_{\boldsymbol{q}}/2)$ denotes the Matsubara component of the bare photon propagator at $\tau = \beta$.

The upper panel of Fig. 5.7 displays the effective electron dispersion $\eta_{\boldsymbol{k}}$ at $\beta = 10$ for $\omega_{\text{p}} = 1$ and $\omega_{\text{p}} = 2$. Moreover, the dashed gray line indicates the non-interacting electron dispersion $\epsilon_{\boldsymbol{k}}$. As can be seen in the graphic, the interaction with the SPP mode gives rise to a positive renormalization of the hopping amplitude, which becomes larger as the plasma frequency is decreased. This is also shown in the lower left panel of Fig. 5.7, where Δt is plotted as a function of ω_{p} for three different inverse temperatures β. The effective change in t is largest at low plasma frequencies, where the coupling to the SPP mode is strongest, and decreases as ω_{p} is increased, such that the light-matter interaction becomes weaker.

The lower right panel in Fig. 5.7 illustrates the temperature dependence of Δt. In general, the effect is more significant at smaller values of ω_{p}, i.e., if the electron-photon coupling is strong. The blue curve for $\omega_{\text{p}} = 1$ indicates that the light-induced renormalization of the hopping matrix elements is most pronounced at high temperatures (small β), which can be attributed to an increase in the thermal photon fluctuations. These results imply that the second-order contribution of the coupling to the SPP mode effectively increases the hopping amplitude, giving rise to a stronger delocalization of the electrons. As a result, the transition to the Mott-insulating state is suppressed, and the material remains metallic up to larger values of the Hubbard interaction U.

This effect can also be translated into an effective change in U. We define a modified electron-electron interaction $U_{\text{eff}} = Ut/(t + \Delta t)$ to account for the change Δt of the hopping matrix elements due to the second-order light-matter interaction. Fig. 5.8 shows the DMFT results for the double occupancy as a function of U_{eff}. In this representation, the data for a system without light-matter interaction (green triangles) and the outcomes for the coupled light-matter system (blue dots and red crosses) are very close. However, they do not collapse into a single curve. The remaining deviation can be attributed to the first-order term of the electron-photon interaction. As can be seen in the graphic, this contribution also leads to a slight stabilization of the metallic phase.

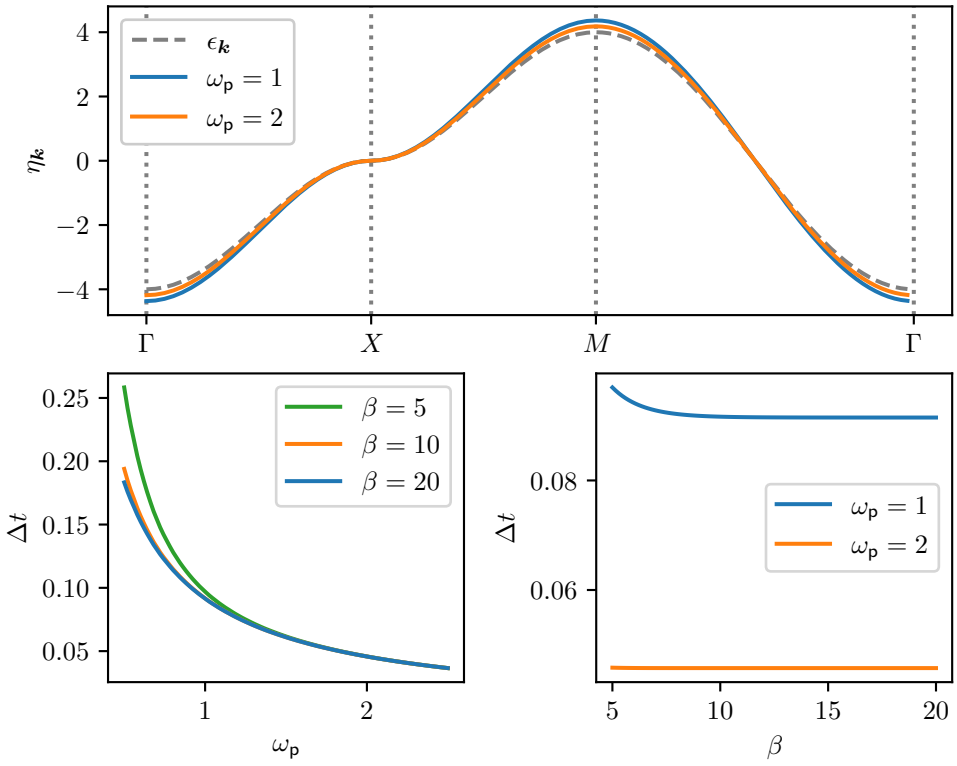

Figure 5.7.: *Renormalization of the hopping amplitude due to the self-energy contribution $s_{\boldsymbol{k}}$ of the second-order light-matter interaction term. Upper panel: renormalized electron dispersion $\eta_{\boldsymbol{k}} = \epsilon_{\boldsymbol{k}} + s_{\boldsymbol{k}}$ at $\beta = 10$ for $\omega_p = 1, 2$. The gray dashed line indicates the bare non-interacting electron dispersion. Lower left panel: photon-induced change Δt of the hopping matrix elements as a function of the plasma frequency ω_p for $\beta = 1, 10, 20$. Lower right panel: Δt as a function of the inverse temperature $\beta = 1/T$ for $\omega_p = 1, 2$.*

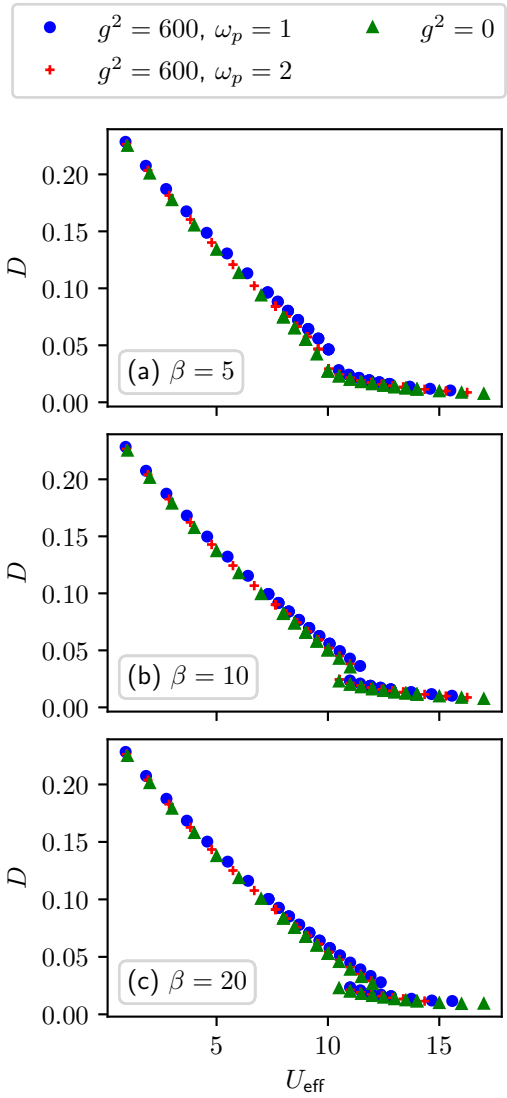

Figure 5.8.: *Double occupancy as a function of the effective Hubbard interaction* $U_{\text{eff}} = Ut/(t + \Delta t)$*, where* Δt *denotes the effective change in the electron dispersion due to the self-energy contribution* $s_{\boldsymbol{k}}$ *of the second-order light-matter coupling term. The calculation has been performed for a lattice of* $N = 10 \times 10$ *sites, and the distance has been fixed to* $x_0 = 2.5$*, where the unit of length is given by the lattice parameter* a*. The unit of energy has been set to the hopping amplitude* t*.*

5.4. Conclusion and outlook

Our results suggest that the Mott metal-insulator transition of the half-filled 2D Hubbard model can be affected by the vacuum fluctuations of the electromagnetic field near a dielectric-metal interface. The current setting allows us to control the intensity of the light-matter interaction through various parameters and thereby tune the strength of the photon-induced effect. Specifically, we have altered the plasma frequency of the metallic region, which leads to a nearly homogeneous scaling of the light-matter coupling across most mode vectors $\boldsymbol{q}$. Our calculations indicate that the interaction with the SPP mode stabilizes the metallic phase, shifting the transition to the Mott-insulating state to higher values of the Hubbard interaction U.

The underlying physical mechanism is yet to be understood and requires further analysis. An important aspect could be the effective enhancement of the hopping amplitude due to the second-order light-matter interaction, which leads to a stronger delocalization of electrons and thus favors the metallic over the Mott-insulating phase. Moreover, it is conceivable that the free energy F_m of the metallic phase is influenced more strongly by the electromagnetic field than the free energy F_i of the Mott insulator. This has been discussed as a possible scenario for the cavity-induced shift of the metal-to-insulator transition in 1T-TeS_2 [42]. In particular, a reduction of F_m relative to F_i would cause a stabilization of the metallic state over a larger range of parameters.

To verify whether this mechanism is also relevant to the present model, it might be insightful to compute the free energy of the system. In addition, this analysis would allow us to identify the true critical point of the phase transition, where the free energy contributions of the two phases intersect. Furthermore, it might be interesting to calculate and analyze the spectral function of the material. Given that the DMFT algorithm is already implemented in the complex time domain, this would only require an additional time evolution on the real-time axis and a Fourier transform of the resulting retarded electron Green's function.

The aforementioned steps are all based on the current approximation scheme. Once this formalism has been fully leveraged, more refined techniques might provide further insights into the physical behavior of the system and help validate previous findings. For instance, the impurity problem could be solved with a method that goes beyond IPT. Possible approaches include the one-crossing or two-crossing approximation [20] or the CT-QMC method [87, 31], which is, however, limited to the imaginary-time domain.

Moreover, it might be worthwhile to extend the number of diagrams incorporated in the self-energy contribution of the SPP mode. One possible approach is to substitute the free photon propagators $D^0_{\boldsymbol{q}}$ in $s_{\boldsymbol{k}}$ and $\Sigma^{(1)}_{\boldsymbol{k}\sigma}$ with a renormalized propagator $D_{\boldsymbol{q}}$ that includes polarization diagrams consisting of matter operators. This approach would account for the feedback of the material on the SPP mode. Even if the polarization diagrams were treated approximately, e.g., by neglecting vertex corrections, this would allow incorporating self-energy diagrams up to infinite order in $D^0_{\boldsymbol{q}}$. However, it should be noted that the approximation scheme requires a slight modification of the DMFT loop, as the photon propagator $D_{\boldsymbol{q}}$ has to be determined self-consistently. This is analogous to the GW+DMFT formalism, where the screened Coulomb interaction is determined

in a similar manner [7].

Once a comprehensive framework for the system under consideration has been developed, the formalism can be applied to more realistic models. In terms of the material, it might be interesting to consider quasi-two-dimensional organic charge-transfer salts of the κ-(BEDT-TTF)$_2$X family. These compounds may undergo a Mott metal-insulator transition driven by chemical substitution, pressure, or temperature [18, 11] and are effectively described by a frustrated half-filled Hubbard model on a square lattice with next-nearest-neighbor hopping along one diagonal of the square plaquettes [67]. Thus, the DMFT formalism would only need slight adaption to account for the broken particle-hole symmetry.

Furthermore, it is important to note that we deliberately selected unrealistically low values for the plasma frequency of the metal supporting the surface plasmon mode. This choice was made for demonstrative purposes, as it enables us to push the strength of the light-matter coupling into a regime where the effect of the SPP mode becomes significant. In typical metals, ω_p ranges between 5 eV and 15 eV [56], corresponding to 167 to 500 in units of the hopping amplitude t for the present model. Therefore, the parameter regime studied in this chapter may not be accessible in experiments. To address this challenge, the SPP mode could be substituted with a surface phonon polariton (SPhP) mode. SPhPs can exhibit frequencies on the order of 10^{-2} eV [57, 91], which would permit exploring the parameter regime where photon-induced effects are measurable.

In summary, our results suggest that multilayered structures offer a promising platform for engineering the equilibrium properties of 2D quantum materials through the vacuum fluctuations of the electromagnetic field. The approximation scheme presented in this chapter can be readily extended and might even prove relevant to future experiments.

6. Conclusion

In the course of this thesis, we have analyzed several models with quantum light-matter interactions and investigated how the vacuum fluctuations of the electromagnetic field affect the equilibrium properties of the system. For that purpose, we introduced a collective theory for single-mode models and adapted the standard dynamical mean-field approach to systems with dipolar or Peierls phase coupling. Our theoretical considerations predict that the coupling between light and matter may give rise to non-trivial effects that go beyond a simple static mean-field picture. We have shown that it is possible to modify the response of a microscopic system with a single cavity mode and to influence phase transitions in macroscopic solids by coupling them to a continuum of electromagnetic modes. This was demonstrated for a paraelectric-to-ferroelectric phase transition in Ch. 4 and a Mott metal-insulator transition in Ch. 5.

For macroscopic materials with linear light-matter interaction, the combined effect of multiple modes can be crucial. As discussed in Ch. 3, this is due to the fact that the radiative corrections of a single mode to the mean-field matter response vanish in the thermodynamic limit if the single-particle coupling strength is finite. To achieve a significant effect, it is therefore essential that a sufficiently large fraction of the photon modes contributes to the interaction. We thus considered a setting where the electromagnetic field near a dielectric-metal interface hybridizes with matter excitations of the metal and forms surface plasmon polaritons (SPPs).

The SPPs are strongly confined to the interface, leading not only to an enhancement of the light-matter interaction, but also enabling control of the coupling strength by changing the distance between the material of interest and the metal surface. Moreover, in solids with Peierls phase coupling, the strength of the light-matter interaction heavily depends on the plasma frequency of the metal region. Therefore, similar multi-layered structures might be of interest for experimental studies, as they provide means to control the interplay of light and matter through various parameters.

The collective theory presented in Ch. 3 is quite general and only relies on a linear interaction between the cavity mode and the matter degrees of freedom. Thus, the formalism should also be applicable to other order parameters, such as incommensurate charge density waves or exciton condensates, which couple linearly to the electromagnetic radiation field. In addition, it might be interesting to analyze the dynamic response of systems out of equilibrium within this theoretical framework.

Furthermore, we have seen in Ch. 4 and 5 that dynamical mean-field theory (DMFT) is a versatile method that can be readily adapted to coupled light-matter systems. In particular, DMFT offers the capability to treat a continuum of electromagnetic modes with arbitrary spatial structure and dispersion, without requiring further simplifications such as a Markov or rotating wave approximation. Hence, the formalism could be applied

to more complex geometries than the translationally invariant hetero-structure studied in this thesis. Moreover, it should be mentioned that the electromagnetic environment can affect the longitudinal part of the electromagnetic field and thereby alter the electrostatic Coulomb interaction. Up to this point, we have not considered this factor. However, within the DMFT framework for dipolar coupling, this effect could be readily incorporated into the effective dipole-dipole interaction.

In the future, it might be interesting to combine the mapping procedure presented in Ch. 4 with the diagrammatic treatment of the Peierls phase factors discussed in Ch. 5. This would permit the study of more general systems with dipolar transitions and itinerant electrons that couple to the electromagnetic field, potentially allowing for predictions on the behavior of real materials. Moreover, it might be illuminating to benchmark the DMFT formalism for coupled light-matter systems against other theoretical techniques and to test it in real experiments to further assess its strengths and limitations. If DMFT proves to provide reliable physical predictions, it could become a valuable theoretical tool in the emergent field of "cavity quantum materials" and ultimately help to engineer the properties of real solids with quantum light.

A. Appendix to Ch. 4

A.1. Quantization of the SPP mode

As mentioned in the main text, we start from a classical treatment of the dielectric-metal interface, which defines the electromagnetic environment for the SPP mode. To derive a classical description for the SPP mode in terms of its electric and magnetic field, we solve the macroscopic Maxwell's equations closely following Ref. [21]. In the end, we quantize the resulting electromagnetic field to obtain a non-classical description for the SPP mode.

Assuming that the relative permeability $\mu = 1$ in both the metallic and the dielectric region, the materials are fully characterized by their electric permittivity ε. In the absence of free charges and currents, Maxwell's equations read as

$$\boldsymbol{\nabla} \cdot \boldsymbol{D} = 0, \tag{A.1}$$

$$\boldsymbol{\nabla} \cdot \boldsymbol{H} = 0, \tag{A.2}$$

$$\boldsymbol{\nabla} \times \boldsymbol{E} = -\mu_0 \frac{\partial \boldsymbol{H}}{\partial t}, \tag{A.3}$$

$$\boldsymbol{\nabla} \times \boldsymbol{H} = \varepsilon_0 \varepsilon \frac{\partial \boldsymbol{E}}{\partial t}. \tag{A.4}$$

We first solve the equations using an ansatz of the form $\boldsymbol{F} = \boldsymbol{\mathcal{F}}(x) e^{i(qz-\omega t)}$ for all fields, which corresponds to a mode traveling along the z-axis. Later, we obtain the full solution by summing up all possible directions of propagation. Apart from that, we focus on the transverse magnetic (TM) mode with $E_y = H_x = H_z = 0$. This yields

$$iq\mathcal{H}_y(x) = i\omega\varepsilon_0\varepsilon(x,\omega)\mathcal{E}_x(x) \tag{A.5}$$

$$\partial_x \mathcal{H}_y(x) = -i\omega\varepsilon_0\varepsilon(x,\omega)\mathcal{E}_z(x) \tag{A.6}$$

for the x and z component of Eq. (A.4) and

$$iq\mathcal{E}_x(x) - \partial_x \mathcal{E}_z(x) = \mu_0 i\omega \mathcal{H}_y(x) \tag{A.7}$$

for the y component of Eq. (A.3).

Eliminating $\mathcal{H}_y(x)$ from Eq. (A.5) and (A.6), we obtain

$$\mathcal{E}_z(x) = -\frac{i}{q}\partial_x \mathcal{E}_x(x). \tag{A.8}$$

With this result, we can substitute $\mathcal{E}_z(x)$ in Eq. (A.7). Moreover, we replace $\mathcal{H}_y(x)$ using Eq. (A.5), which gives

$$0 = \partial_x^2 \mathcal{E}_x(x) - Q^2 \mathcal{E}_x(x), \tag{A.9}$$

with

$$Q(x) = \sqrt{q^2 - \left(\frac{\omega}{c}\right)^2 \varepsilon(x,\omega)}. \tag{A.10}$$

The solution of Eq. (A.9) reads as

$$\mathcal{E}_x(x) = \begin{cases} A_\mathrm{m} e^{Q_\mathrm{m} x} & , x < 0 \\ A_\mathrm{d} e^{-Q_\mathrm{d} x} & , x > 0 \end{cases} \tag{A.11}$$

where Q_m and Q_d refer to $Q(x)$ evaluated for the dielectric function ε_m or ε_d in the metal ($x < 0$) or the dielectric ($x > 0$), respectively.

The tangential components of $\boldsymbol{H}$ and $\boldsymbol{E}$ are continuous at the interface; therefore, using (A.5) and the solution (A.11) to obtain $\mathcal{H}_y$, we get

$$A_\mathrm{m} = \frac{\varepsilon_\mathrm{d}}{\varepsilon_\mathrm{m}} A_\mathrm{d}. \tag{A.12}$$

Moreover, calculating $\mathcal{E}_z$ from (A.8) and (A.11), the continuity condition for $\boldsymbol{E}$ yields

$$Q_\mathrm{m} A_\mathrm{m} = -Q_\mathrm{d} A_\mathrm{d}. \tag{A.13}$$

Combining these two expressions gives the dispersion relation

$$\frac{Q_\mathrm{m}}{\varepsilon_\mathrm{m}} = -\frac{Q_\mathrm{d}}{\varepsilon_\mathrm{d}}, \tag{A.14}$$

which can be solved for

$$q = \frac{\omega}{c} \sqrt{\frac{\varepsilon_\mathrm{m} \varepsilon_\mathrm{d}}{\varepsilon_\mathrm{m} + \varepsilon_\mathrm{d}}}. \tag{A.15}$$

Let us briefly analyze the result for a constant permittivity ε_d in the dielectric region and a Drude response

$$\varepsilon_\mathrm{m}(\omega) = 1 - \left(\frac{\omega_\mathrm{p}}{\omega}\right)^2 \tag{A.16}$$

in the metallic part of the system. In this case, Eq. (A.15) cannot be solved analytically for the frequency; therefore, we consider the asymptotic behavior of $\omega(q)$. In the limit of small ω, we can Taylor expand $1/\varepsilon_\mathrm{m}$ in powers of ω. Since it vanishes up to second order, we can neglect this contribution for $\omega \ll 0$, which yields $\omega \approx qc/\sqrt{\varepsilon_\mathrm{d}}$. Moreover, for propagating modes, the wave number q has to be real; thus, the argument of the square root has to be positive, which yields the condition $\omega < \omega_\mathrm{p}/\sqrt{\varepsilon_\mathrm{d} + 1}$. At this point, Eq. (A.15) diverges, i.e., the frequency ω approaches this value as $q \to \infty$. In Fig. 4.2 in the main text, we plot the dispersion relation at three different permittivities ε_d. The asymptotic results for $\omega \ll 1$ and $q \to \infty$ are indicated by the dotted and dashed lines, respectively.

For all DMFT calculations, we set $\varepsilon_\mathrm{d} = 1$. In this case, the dispersion relation can be solved analytically for the frequency. There is only one physical solution, which is given by

$$\omega_q = \sqrt{\frac{\omega_\mathrm{p}^2}{2} + q^2 c^2 - \sqrt{\frac{\omega_\mathrm{p}^4}{4} + q^4 c^4}}. \tag{A.17}$$

To quantize the electromagnetic field, we introduce the bosonic operators $\hat{a}_{\boldsymbol{q}}^{\dagger}$ ($\hat{a}_{\boldsymbol{q}}$), which create (annihilate) a photon with wave vector $\boldsymbol{q} = (q_y, q_z)^T = q(\sin(\varphi), \cos(\varphi))^T$, where $\varphi \in [0, 2\pi)$ denotes the angle to the z-axis. With this definition, we include all possible directions of propagation for the TM SPP mode, and the electric field operator can be expanded as follows

$$\hat{\boldsymbol{E}}(\boldsymbol{r}) = \sum_{\boldsymbol{q}} \sqrt{\frac{\omega_{\boldsymbol{q}}}{2\varepsilon_0 \varepsilon(x, \omega_{\boldsymbol{q}}) N a^3}} [\boldsymbol{u}_{\boldsymbol{q}}(x) e^{i\boldsymbol{q}\cdot\boldsymbol{\rho}} \hat{a}_{\boldsymbol{q}} + \text{H.c.}], \tag{A.18}$$

where a denotes the lattice constant, such that the total volume of the system is given by $V = Na^3$. Moreover, we have defined the two-dimensional position vector $\boldsymbol{\rho} = (y, z)^T$, and the mode functions

$$\boldsymbol{u}_{\boldsymbol{q}}(x) = \mathcal{N}_{\boldsymbol{q}} \begin{cases} e^{Q_{\mathrm{m}} x} \begin{pmatrix} 1 \\ i(Q_{\mathrm{m}}/q)\sin(\varphi) \\ i(Q_{\mathrm{m}}/q)\cos(\varphi) \end{pmatrix}, & x < 0 \\ e^{-Q_{\mathrm{d}} x} \begin{pmatrix} 1 \\ -i(Q_{\mathrm{d}}/q)\sin(\varphi) \\ -i(Q_{\mathrm{d}}/q)\cos(\varphi) \end{pmatrix}, & x > 0 \end{cases}. \tag{A.19}$$

The normalization factors $\mathcal{N}_{\boldsymbol{q}}$ are calculated from the condition $\int_V d^3r |\boldsymbol{u}_{\boldsymbol{q}}(x)|^2 = Na^3$, which yields

$$\mathcal{N}_{\boldsymbol{q}} = \sqrt{a} \left\{ \frac{1}{2Q_{\mathrm{m}}} \left[1 + \left(\frac{Q_{\mathrm{m}}}{q} \right)^2 \right] + \frac{1}{2Q_{\mathrm{d}}} \left[1 + \left(\frac{Q_{\mathrm{d}}}{q} \right)^2 \right] \right\}^{-\frac{1}{2}}. \tag{A.20}$$

In free space, where the electromagnetic field can be expanded in simple plane waves, i.e., $\boldsymbol{u}_{\boldsymbol{q}}(x) \sim e^{iq_x x}$, this factor would be proportional to $\frac{1}{\sqrt{Na^3}}$ and thus would vanish in the thermodynamic limit. This proves that the spatial confinement of the SPP mode to the dielectric-metal interface due to the exponential decay of the mode functions gives rise to an enhancement of the light-matter interaction as compared to the vacuum case.

A.2. Photon-induced interaction

In the following, we derive an expression for the photon-induced interaction. We start from the full imaginary-time action

$$S = S_{\mathrm{mat}} + S_{PP} + S_{EP} + S_{\mathrm{field}}, \tag{A.21}$$

where the free SPP mode is described by

$$S_{\mathrm{field}} = \int_0^{\beta} d\tau \bar{a}_{\boldsymbol{q}}(\tau) \left[\partial_\tau + \omega_{\boldsymbol{q}} \right] a_{\boldsymbol{q}}(\tau) \tag{A.22}$$

and the linear coupling between light and matter is given by

$$S_{EP} = \int_0^\beta d\tau \sum_{r,\boldsymbol{q}} \sqrt{\frac{\omega_{\boldsymbol{q}}}{2N}} \left[g_{\boldsymbol{q}} e^{i\boldsymbol{q}\cdot\boldsymbol{R}_r} a_{\boldsymbol{q}}(\tau) + \text{c.c.} \right] \sigma_r^1(\tau). \tag{A.23}$$

Integrating out the bosonic fields $a_q(\tau)$ and $\bar{a}_{\boldsymbol{q}}(\tau)$ yields an induced interaction S_{ind}, which is defined by the relation

$$e^{-S_{\text{ind}}} = e^{-S_{PP}} \int \mathcal{D}[\bar{a}, a] e^{-(S_{EP}+S_{\text{field}})}. \tag{A.24}$$

Note that we have also included the dipolar self-interaction in the definition because it originates from the light-matter coupling as well.

The Gaussian path integral in Eq. (A.24) can be solved analytically and evaluates to

$$S_{\text{ind}} = -\frac{1}{2} \int_0^\beta d\tau \int_0^\beta d\tau' \sum_{r,r'} \sigma_r^1(\tau) W_{r,r'}^{\text{ind}}(\tau - \tau') \sigma_{r'}^1(\tau'), \tag{A.25}$$

where

$$W_{r,r'}^{\text{ind}}(\tau) = -\sum_{\boldsymbol{q}} \frac{|g_{\boldsymbol{q}}|^2}{N} e^{-i\boldsymbol{q}\cdot(\boldsymbol{R}_r - \boldsymbol{R}_{r'})} \left[1 + \omega_{\boldsymbol{q}} D_{\boldsymbol{q}}^0(\tau) \right]. \tag{A.26}$$

Here $D_{\boldsymbol{q}}^0(\tau)$ represents the photon propagator in free space and is given by

$$D_{\boldsymbol{q}}^0(\tau) = -\langle a_{\boldsymbol{q}}(\tau) \bar{a}_{\boldsymbol{q}}(0) \rangle_{S_{\text{field}}} = -\frac{e^{-\tau\omega_{\boldsymbol{q}}}}{1 - e^{-\beta\omega_{\boldsymbol{q}}}}. \tag{A.27}$$

In Matsubara representation it reads as

$$D_{\boldsymbol{q}}^0(i\nu_m) = \frac{1}{i\nu_m - \omega_{\boldsymbol{q}}}. \tag{A.28}$$

The induced interaction $W_{r,r'}^{\text{ind}}$ only depends on the distance $\boldsymbol{R}_r - \boldsymbol{R}_{r'}$; therefore, we can perform a lattice Fourier transform of the form

$$f_{\boldsymbol{k}} = \sum_r f_r e^{i\boldsymbol{k}\cdot\boldsymbol{R}_r}. \tag{A.29}$$

This yields

$$W_{\boldsymbol{k}}(i\nu_n) = -\sum_{\boldsymbol{G}\in\mathcal{L}_{\text{R}}} |g_{\boldsymbol{k}+\boldsymbol{G}}|^2 \frac{\nu_n^2}{\nu_n^2 + \omega_{\boldsymbol{k}+\boldsymbol{G}}^2}, \tag{A.30}$$

where $\mathcal{L}_{\text{R}}$ denotes the set of reciprocal lattice vectors. However, as can be seen in Fig. 4.4 in the main text, the coupling constants $|g_{\boldsymbol{q}}|^2$ strongly decay at large q; thus, we assume that they vanish outside the first Brillouin zone, i.e., $|g_{\boldsymbol{k}+\boldsymbol{G}}|^2 \to 0$ for $\boldsymbol{G} \neq \boldsymbol{0}$, such that the induced interaction can be simplified as

$$W_{\boldsymbol{k}}(i\nu_n) = -|g_{\boldsymbol{k}}|^2 \frac{\nu_n^2}{\nu_n^2 + \omega_{\boldsymbol{k}}^2}. \tag{A.31}$$

This is the expression we use in the main text.

A.3. Derivation of the DMFT equations

A.3.1. Mapping the lattice action to an impurity problem

We derive the impurity problem from the full Hubbard-Stratonovich action

$$S_{\mathrm{HS}} = S_0 + S_{\varphi\varphi} + S_{\varphi\sigma} \tag{A.32}$$

with the quadratic term

$$S_{\varphi\varphi} = \frac{1}{2}\int_0^\beta d\tau \int_0^\beta d\tau' \sum_{r,r'} \varphi_r(\tau)[W^{-1}]_{r,r'}(\tau-\tau')\varphi_{r'}(\tau') \tag{A.33}$$

and the local linear interaction

$$S_{\varphi\sigma} = -\sum_r \int_0^\beta d\tau \varphi_r(\tau)\sigma_r^1(\tau) \tag{A.34}$$

(see Sec. 4.2.1 in the main text). The action for the isolated emitters can be written as the sum

$$S_0 = \sum_r S_0^r, \tag{A.35}$$

where S_0^r describes a single dipole at site r.

We aim to reduce this lattice problem to a model that describes a single impurity in an effective environment. For that purpose, we use the so-called cavity method [29, 7] and single out one site c, which is referred to as "the cavity site". Then we split the action into three parts: The first one includes all onsite terms and reads as

$$S^c = S_0^c + S_{\varphi\varphi}^c + S_{\varphi\sigma}^c \tag{A.36}$$

with

$$S_{\varphi\varphi}^c = \frac{1}{2}\int_0^\beta d\tau \int_0^\beta d\tau' \varphi_c(\tau)[W^{-1}]_{c,c}(\tau-\tau')\varphi_c(\tau') \tag{A.37}$$

and

$$S_{\varphi\sigma}^c = -\int_0^\beta d\tau \varphi_c(\tau)\sigma_c^1(\tau). \tag{A.38}$$

The second one describes a lattice, where site c is missing, i.e., there is a cavity at site c. It is given by

$$S^{(c)} = \sum_{r\neq c} S_0^r + S_{\varphi\varphi}^{(c)} + S_{\varphi\sigma}^{(c)} \tag{A.39}$$

with

$$S^{(c)}_{\varphi\varphi} = \frac{1}{2}\int_0^\beta d\tau \int_0^\beta d\tau' \sum_{r\neq c}\sum_{r'\neq c} \varphi_r(\tau)[W^{-1}]_{r,r'}(\tau-\tau')\varphi_{r'}(\tau') \tag{A.40}$$

and

$$S^{(c)}_{\varphi\sigma} = -\sum_{r\neq c}\int_0^\beta d\tau \varphi_r(\tau)\sigma^1_r(\tau). \tag{A.41}$$

And finally, there is the contribution

$$\Delta S = \sum_{r\neq c}\int_0^\beta d\tau \varphi_r(\tau)t_r(\tau) \tag{A.42}$$

with

$$t_r(\tau) = \int_0^\beta d\tau' [W^{-1}]_{r,c}(\tau-\tau')\varphi_c(\tau'), \tag{A.43}$$

describing the interaction of the cavity site with the rest of the lattice.

Based on this description, we formally integrate out all degrees of freedom that do not correspond to the cavity site. This yields an effective action S_{hyb} that incorporates the interaction of the impurity at site c with the surrounding lattice. We denote the matter fields by ξ_r and $\bar{\xi}_r$, such that the corresponding path integral is given by

$$\begin{aligned}\int \mathcal{D}[\varphi_{r\neq c}] \int \mathcal{D}[\xi_{r\neq c}\bar{\xi}_{r\neq c}] e^{-S_{HS}} \\ = e^{-S^c}\int \mathcal{D}[\varphi_{r\neq c}] \int \mathcal{D}[\xi_{r\neq c}\bar{\xi}_{r\neq c}] e^{-(S^{(c)}+\Delta S)} = e^{-(S^c+S^{\mathrm{hyb}})}.\end{aligned} \tag{A.44}$$

The effective action S_{hyb} can be expressed in terms of a cumulant expansion

$$S^{\mathrm{hyb}} = -\sum_{n=1}^{\infty}\frac{(-1)^n}{n!}\sum_{r_1\ldots r_n\neq 0}\int_0^\beta d\tau_1 \ldots \int_0^\beta d\tau_n t_{r_n}(\tau_1)\ldots t_{r_n}(\tau_n) K_{r_1\ldots r_n}(\tau_1\ldots\tau_n) \tag{A.45}$$

with the connected correlation functions

$$K_{r_1\ldots r_n}(\tau_1\ldots\tau_n) = \langle \varphi_{r_1}(\tau_1)\ldots\varphi_{r_n}(\tau_n)\rangle^{\mathrm{con}}_{S^{(c)}}. \tag{A.46}$$

As indicated by the subscript $S^{(c)}$, the time-ordered expectation values are evaluated for the action (A.39).

In DMFT, all terms beyond second order are truncated, such that

$$S^{\mathrm{hyb}} = S^{\mathrm{hyb}}_1 + S^{\mathrm{hyb}}_2, \tag{A.47}$$

where the first-order contribution reads as

$$S_1^{\mathrm{hyb}} = \int_0^\beta d\tau \varphi_c(\tau) h(\tau) \tag{A.48}$$

with

$$h(\tau) = \sum_{r\neq c} \int_0^\beta d\tau' [W^{-1}]_{c,r}(\tau-\tau') \langle \mathcal{T}\varphi_r(\tau')\rangle_{S^{(c)}}, \tag{A.49}$$

and the second-order term is given by

$$S_2^{\mathrm{hyb}} = -\int_0^\beta d\tau \int_0^\beta d\tau' \varphi_c(\tau)\Delta_{\mathrm{hyb}}(\tau-\tau')\varphi_c(\tau') \tag{A.50}$$

with the hybridization function

$$\Delta_{\mathrm{hyb}}(\tau) = \sum_{r\neq c}\sum_{r'\neq c} \int_0^\beta d\tau_1 \int_0^\beta d\tau_2 [W^{-1}]_{c,r}(\tau-\tau_1) U^{(c)}_{r,r'}(\tau_1-\tau_2)[W^{-1}]_{r',c}(\tau_2) \tag{A.51}$$

and the propagator

$$U^{(c)}_{r,r'}(\tau) = \langle \mathcal{T}\varphi_r(\tau)\varphi_{r'}(0)\rangle^{\mathrm{con}}_{S^{(c)}}. \tag{A.52}$$

In summary, we obtain the approximate impurity action

$$S^{\mathrm{imp}}_{HS} = S^c_0 + S^{\mathrm{imp}}_{\varphi\varphi} + S^{\mathrm{imp}}_{\varphi\sigma} \tag{A.53}$$

with a linear term

$$S^{\mathrm{imp}}_{\varphi\sigma} = S^c_{\varphi\sigma} + S_1^{\mathrm{hyb}} = -\int_0^\beta d\tau \varphi_c(\tau)[\sigma^1_c(\tau) - h(\tau)] \tag{A.54}$$

and a quadratic contribution

$$S^{\mathrm{imp}}_{\varphi\varphi} = S^c_{\varphi\varphi} + S_2^{\mathrm{hyb}} = \frac{1}{2}\int_0^\beta d\tau \int_0^\beta d\tau' \varphi_c(\tau)\mathcal{W}^{-1}(\tau-\tau')\varphi_c(\tau'), \tag{A.55}$$

where the Weiss field

$$\mathcal{W}^{-1}(\tau) = [W^{-1}]_{c,c}(\tau) - \Delta_{\mathrm{hyb}}(\tau) \tag{A.56}$$

incorporates the onsite interaction $[W^{-1}]_{c,c}(\tau)$ as well as the hybridization function.

A.3.2. Derivation of the self-consistency conditions

The impurity problem derived in the previous section contains two effective fields $h(\tau)$ and $\mathcal{W}(\tau)$, which cannot be calculated analytically. However, assuming a local self-energy, we can express these fields in terms of the corresponding lattice quantities.

Let us first consider the Weiss field $\mathcal{W}(\tau)$ defined in Eq. (A.56). It depends on the hybridization function (A.51), which is calculated from the propagator $U^{(c)}_{r,r'}$ for the lattice with a cavity at site c. The latter can be written in terms of the propagator

$$U_{r,r'}(\tau - \tau') = \langle \varphi_r(\tau)\varphi_{r'}(\tau')\rangle^{\mathrm{con}}_{S_{HS}} \tag{A.57}$$

for the full lattice by removing the connection between site c and all other points r, which yields

$$U^{(c)}_{r,r'}(i\nu_n) = U_{r,r'}(i\nu_n) - \frac{U_{rc}(i\nu_n)U_{cr'}(i\nu_n)}{U_{cc}(i\nu_n)}. \tag{A.58}$$

Note that the second term is divided by $U_{c,c}(i\nu_n)$ in order to avoid double counting. Inserting this expression into Eq. (A.51) and performing a lattice Fourier transform, we obtain

$$\Delta_{\mathrm{hyb}} = \frac{1}{N}\sum_{\boldsymbol{k}} E_{\boldsymbol{k}}^2 U_{\boldsymbol{k}} - \frac{\left(\frac{1}{N}\sum_{\boldsymbol{k}} E_{\boldsymbol{k}}U_{\boldsymbol{k}}\right)^2}{\frac{1}{N}\sum_{\boldsymbol{k}} U_{\boldsymbol{k}}} \tag{A.59}$$

with

$$E_{\boldsymbol{k}} = W^{-1}_{\boldsymbol{k}} - [W^{-1}]_{c,c}. \tag{A.60}$$

Introducing the self-energy $\Pi_{\boldsymbol{k}}$, the propagator for the full lattice is given by the Dyson equation

$$U^{-1}_{\boldsymbol{k}} = W^{-1}_{\boldsymbol{k}} - \Pi_{\boldsymbol{k}}. \tag{A.61}$$

In DMFT, the self-energy is assumed to be purely local, i.e., independent of $\boldsymbol{k}$. Thus, we can define the local quantity

$$F^{-1} = [W^{-1}]_{c,c} - \Pi_{\mathrm{loc}}, \tag{A.62}$$

where Π_{loc} denotes the self-energy, and rewrite the Dyson equation as

$$U^{-1}_{\boldsymbol{k}} = F^{-1} + E_{\boldsymbol{k}}. \tag{A.63}$$

Therefore,

$$\begin{aligned}\frac{1}{N}\sum_{\boldsymbol{k}} E_{\boldsymbol{k}}U_{\boldsymbol{k}} &= \frac{1}{N}\sum_{\boldsymbol{k}} \frac{E_{\boldsymbol{k}}}{F^{-1}+E_{\boldsymbol{k}}} = \frac{1}{N}\sum_{\boldsymbol{k}}\left(\frac{E_{\boldsymbol{k}}+F^{-1}}{F^{-1}+E_{\boldsymbol{k}}} - \frac{F^{-1}}{F^{-1}+E_{\boldsymbol{k}}}\right)\\ &= 1 - F^{-1}\frac{1}{N}\sum_{\boldsymbol{k}} U_{\boldsymbol{k}}\end{aligned} \tag{A.64}$$

and

$$\begin{aligned}\frac{1}{N}\sum_{\boldsymbol{k}} E_{\boldsymbol{k}}^2 U_{\boldsymbol{k}} &= \frac{1}{N}\sum_{\boldsymbol{k}} E_{\boldsymbol{k}} \frac{E_{\boldsymbol{k}}}{F^{-1}+E_{\boldsymbol{k}}} = \frac{1}{N}\sum_{\boldsymbol{k}} E_{\boldsymbol{k}}\left(1-\frac{F^{-1}}{F^{-1}+E_{\boldsymbol{k}}}\right) \\ &= \underbrace{\frac{1}{N}\sum_{\boldsymbol{k}} E_{\boldsymbol{k}}}_{=0} - F^{-1}\frac{1}{N}\sum_{\boldsymbol{k}} E_{\boldsymbol{k}} U_{\boldsymbol{k}} = -F^{-1} + \left(F^{-1}\right)^2 \frac{1}{N}\sum_{\boldsymbol{k}} U_{\boldsymbol{k}},\end{aligned} \tag{A.65}$$

such that

$$\Delta_{\mathrm{hyb}} = F^{-1} - \left[\frac{1}{N}\sum_{\boldsymbol{k}} U_{\boldsymbol{k}}\right]^{-1} = F^{-1} - [U_{c,c}]^{-1}. \tag{A.66}$$

Inserting this expression into Eq. (A.56), we finally obtain

$$\begin{aligned}\mathcal{W}^{-1}(i\nu_n) &= [W^{-1}]_{c,c}(i\nu_n) - \Delta(i\nu_n) \\ &= [W^{-1}]_{c,c}(i\nu_n) - F^{-1}(i\nu_n) + [U_{c,c}]^{-1}(i\nu_n) \\ &= [U_{c,c}]^{-1}(i\nu_n) + \Pi_{\mathrm{loc}}(i\nu_n).\end{aligned} \tag{A.67}$$

With this, we have rewritten the Weiss field only in terms of quantities that correspond to the full lattice without a cavity at site c.

Now we turn to the field $h(\tau)$ and relate it to the Weiss field $\mathcal{W}(\tau)$. For that purpose, we calculate the derivative $\frac{\delta \ln \mathcal{Z}}{\delta \varphi_c(\tau)}$ in two different ways: First, we evaluate the partition function $\mathcal{Z}$ for the full lattice action S_{HS}, which yields

$$\frac{\delta \ln \mathcal{Z}}{\delta \varphi_c(\tau)} = \langle \sigma_c^1(\tau)\rangle - \sum_r \int_0^\beta d\tau' [W^{-1}]_{cr}(\tau-\tau')\langle \varphi_r(\tau')\rangle. \tag{A.68}$$

Second, we express $\mathcal{Z}$ in terms of the impurity action $S_{\mathrm{HS}}^{\mathrm{imp}}$ and obtain

$$\frac{\delta \ln \mathcal{Z}}{\delta \varphi_c(\tau)} = \langle \sigma_c^1(\tau)\rangle - h(\tau) - \int_0^\beta d\tau'\, \mathcal{W}^{-1}(\tau-\tau')\langle \varphi_c(\tau')\rangle. \tag{A.69}$$

We assume that the expectation value $\langle \varphi_r(\tau)\rangle$ is uniform over the entire lattice and does not depend on τ, i.e. $\langle \varphi_r(\tau)\rangle = \phi \;\forall\, r, \tau$. Moreover, we introduce the shorthand notation

$$\mathcal{W}_0^{-1} = \mathcal{W}^{-1}(i\nu_n = 0), \tag{A.70}$$

and

$$W_{\mathrm{mf}}^{-1} = W_{\boldsymbol{k}=\boldsymbol{0}}^{-1}(i\nu_n = 0). \tag{A.71}$$

Then, equating (A.68) and (A.69) and solving for h, finally yields

$$h = \left[W_{\mathrm{mf}}^{-1} - \mathcal{W}_0^{-1}\right]\phi. \tag{A.72}$$

A.3.3. Eliminating the auxiliary field from the impurity problem

In the following, we re-express the impurity problem only in terms of the pseudo-spin variable σ_c^1. This is the type of action the impurity solver is designed for. To obtain a suitable representation, we trace out the auxiliary field φ_c from $S_{\mathrm{HS}}^{\mathrm{imp}}$. The resulting Gaussian path integral

$$\int \mathcal{D}[\varphi_c] e^{-S_{HS}^{\mathrm{imp}}} = e^{-S^{\mathrm{imp}}} \tag{A.73}$$

can be evaluated analytically and yields

$$S^{\mathrm{imp}} = S_0^c - \frac{1}{2} \int_0^\beta d\tau \int_0^\beta d\tau' [\sigma_c^1(\tau) - h] \mathcal{W}(\tau - \tau') [\sigma_c^1(\tau') - h]. \tag{A.74}$$

This can be rewritten as

$$S^{\mathrm{imp}} = S_0^c + S_{\mathrm{int},1}^{\mathrm{imp}} + S_{\mathrm{int},2}^{\mathrm{imp}} + \mathrm{const.} \tag{A.75}$$

with the linear term

$$S_{\mathrm{int},1}^{\mathrm{imp}} = b \int_0^\beta d\tau \sigma_c^1(\tau) \tag{A.76}$$

and the quadratic contribution

$$S_{\mathrm{int},2}^{\mathrm{imp}} = -\frac{1}{2} \int_0^\beta d\tau \int_0^\beta d\tau' \, \sigma_c^1(\tau) \mathcal{W}(\tau - \tau') \sigma_c^1(\tau'), \tag{A.77}$$

where the field b is given by

$$b = \mathcal{W}_0 \left[W_{mf}^{-1} - \mathcal{W}_0^{-1} \right] \phi. \tag{A.78}$$

It is not possible to directly calculate expectation values and correlation functions of φ_c from the new action (A.75); therefore, we relate these quantities to the pseudo-spin variable σ_c^1. To eliminate ϕ, we use the condition

$$\left\langle \frac{\delta S_{HS}}{\delta \varphi_r(\tau)} \right\rangle_{S_{HS}} \Bigg|_{\varphi_r(\tau)=\phi} = \sum_{r'} \int_0^\beta d\tau' [W^{-1}]_{r,r'}(\tau - \tau') \phi - \langle \sigma_r^1(\tau) \rangle_{S_{HS}} \Bigg|_{\varphi_r(\tau)=\phi} = 0, \tag{A.79}$$

which must be satisfied because ϕ is a stationary path. We can read from this equation that the expectation value

$$\langle \sigma_r^1(\tau) \rangle_{S_{HS}} \Big|_{\varphi_r(\tau)=\phi} = \langle \sigma^1 \rangle \tag{A.80}$$

must also be independent of r and τ, and thus

$$\phi = W_{mf}\langle\sigma^1\rangle. \tag{A.81}$$

With this identity and Eq. (A.78), the field b is given by

$$b = [\mathcal{W}_0 - W_{mf}]\,\langle\sigma^1\rangle. \tag{A.82}$$

In the next step, we aim to find a relation between the local correlation function

$$\chi_{c,c} = \langle T\sigma_c^1(\tau)\sigma_c^1(\tau')\rangle^{\mathrm{con}} \tag{A.83}$$

and the propagator $U_{c,c}$. The latter can be calculated from the generating functional

$$\mathcal{G}[J] = \ln\left\langle \exp\left[\int_0^\beta d\tau\, J(\tau)\varphi_c(\tau)\right]\right\rangle_{S_{\mathrm{HS}}^{\mathrm{imp}}} \tag{A.84}$$

by taking the derivative

$$\left.\frac{\delta^2\mathcal{G}[J]}{\delta J(\tau)\delta J(\tau')}\right|_{J=0} = U_{c,c}(\tau-\tau'). \tag{A.85}$$

Moreover, integrating out φ_c from the expression for $\mathcal{G}[J]$, we obtain

$$\left.\frac{\delta^2\mathcal{G}[J]}{\delta J(\tau)\delta J(\tau')}\right|_{J=0} = \mathcal{W}(\tau-\tau') + \int_0^\beta d\tau_1 \int_0^\beta d\tau_2 \mathcal{W}(\tau-\tau_1)\chi_{c,c}(\tau_1-\tau_2)\mathcal{W}(\tau_2-\tau'), \tag{A.86}$$

and hence

$$U_{c,c}(i\nu_n) = \mathcal{W}(i\nu_n) + \mathcal{W}(i\nu_n)\chi_{c,c}(i\nu_n)\mathcal{W}(i\nu_n). \tag{A.87}$$

Inserting this into Eq. (A.67), yields

$$\Pi_{\mathrm{loc}} = (1+\chi_{c,c}\mathcal{W})^{-1}\,\chi_{c,c}, \tag{A.88}$$

so that finally all relevant quantities on the impurity can be directly calculated from the new action (A.75).

A.4. Tail correction

A.4.1. High-frequency behavior of the Weiss field

In the following, we analyze the high-frequency behavior of the Weiss field. For that purpose, we consider an expansion in the inverse Matsubara frequency and neglect all terms beyond second order, i.e., we assume that for $i\nu_n \to \infty$ the Weiss field can be written as

$$\mathcal{W} \sim w_0 + \frac{w_2}{(i\nu_n)^2}. \tag{A.89}$$

Moreover, we use the ansatzes

$$\chi_{c,c} \sim \frac{c_2}{(i\nu_n)^2} \tag{A.90}$$

for the local dipole-dipole correlation function and

$$W_{\boldsymbol{k}} \sim w_0^{\boldsymbol{k}} + \frac{w_2^{\boldsymbol{k}}}{(i\nu_n)^2} \tag{A.91}$$

for the interaction matrix. The coefficients c_2, $w_0^{\boldsymbol{k}}$, and $w_2^{\boldsymbol{k}}$ are derived in App. A.4.2 and A.4.3. Here we focus on the Weiss field and express w_0 and w_2 in terms of these parameters.

We start from the self-energy Π_{loc}, which is given by Eq. (4.38). Inserting (A.89) and (A.90), yields the asymptotic behavior

$$\Pi_{\mathrm{loc}} = \chi_{c,c} - \chi_{c,c}\mathcal{W}\chi_{c,c} + \chi_{c,c}\mathcal{W}\chi_{c,c}\mathcal{W}\chi_{c,c} - \cdots \sim \frac{c_2}{(i\nu_n)^2} + \mathcal{O}((i\nu_n)^{-4}). \tag{A.92}$$

With this result and the ansatz (A.91), we obtain

$$U_{\boldsymbol{k}} = W_{\boldsymbol{k}} + W_{\boldsymbol{k}}\Pi_{\mathrm{loc}}W_{\boldsymbol{k}} + W_{\boldsymbol{k}}\Pi_{\mathrm{loc}}W_{\boldsymbol{k}}\Pi_{\mathrm{loc}}W_{\boldsymbol{k}} + \cdots \sim w_0^{\boldsymbol{k}} + \frac{w_2^{\boldsymbol{k}} + (w_0^{\boldsymbol{k}})^2 c_2}{(i\nu_n)^2} + \mathcal{O}((i\nu_n)^{-4}) \tag{A.93}$$

from the Dyson equation (4.29), such that

$$U_{c,c} \sim \frac{1}{N}\sum_{\boldsymbol{k}} w_0^{\boldsymbol{k}} + \frac{\frac{1}{N}\sum_{\boldsymbol{k}} w_2^{\boldsymbol{k}} + \frac{1}{N}\sum_{\boldsymbol{k}} (w_0^{\boldsymbol{k}})^2 c_2}{(i\nu_n)^2} + \mathcal{O}((i\nu_n)^{-4}). \tag{A.94}$$

Therefore, we can see from Eq. (4.27) that the Weiss field decays as

$$\begin{aligned} \mathcal{W} &= U_{c,c} - U_{c,c}\Pi_{\mathrm{loc}}U_{c,c} + U_{c,c}\Pi_{\mathrm{loc}}U_{c,c}\Pi_{\mathrm{loc}}U_{c,c} - \ldots \\ &\sim m_0^{(1)} + \frac{m_2^{(1)} + \left[m_0^{(2)} - \left(m_0^{(1)}\right)^2\right] c_2}{(i\nu_n)^2} + \mathcal{O}((i\nu_n)^{-4}), \end{aligned} \tag{A.95}$$

where we have defined the parameters

$$m_0^{(1)} = \frac{1}{N}\sum_{\boldsymbol{k}} w_0^{\boldsymbol{k}} \tag{A.96}$$

$$m_0^{(2)} = \frac{1}{N}\sum_{\boldsymbol{k}} \left(w_0^{\boldsymbol{k}}\right)^2 \tag{A.97}$$

$$m_2^{(1)} = \frac{1}{N}\sum_{\boldsymbol{k}} w_2^{\boldsymbol{k}}. \tag{A.98}$$

Hence, the coefficients for the high-frequency tail of the Weiss field are given by

$$w_0 = m_0^{(1)} \tag{A.99}$$

and

$$w_2 = m_2^{(1)} + \left[m_0^{(2)} - \left(m_0^{(1)}\right)^2\right] c_2. \tag{A.100}$$

A.4.2. High-frequency behavior of the local dipole-dipole correlation function

In the previous section, we have used Eq. (A.90) as an ansatz for the asymptotic behavior of the local dipole-dipole correlation function $\chi_{c,c}$ at large Matsubara frequencies. We now derive an expression for the coefficient c_2 using the spectral representation of $\chi_{c,c}$. The spectral function is defined by the relation

$$A(\omega) = -\frac{1}{\pi}\mathrm{Im}\left\{\chi_{c,c}(\omega)\right\}. \tag{A.101}$$

In Matsubara space, the local dipole-dipole correlation function can be expressed in terms of $A(\omega)$, which yields

$$\begin{aligned}\chi_{c,c}(i\nu_n) &= \int_0^\beta d\omega A(\omega)\left[\frac{1}{i\nu_n-\omega}-\frac{1}{i\nu_n+\omega}\right]\\ &= \int_0^\beta d\omega A(\omega)\frac{2\omega}{(i\nu_n)^2}\frac{1}{1-(\omega/i\nu_n)^2}\\ &= \frac{1}{(i\nu_n)^2}\int_0^\beta 2\omega A(\omega)+\mathcal{O}((i\nu_n)^{-4}).\end{aligned} \tag{A.102}$$

To get from the second to the third line, we have performed a Taylor expansion in $1/(i\nu_n)$. For $i\nu_n \to \infty$, the leading contribution is given by the term $\sim (i\nu_n)^{-2}$; thus, the ansatz (A.90) is justified and the coefficient c_2 is given by

$$c_2 = \int_0^\beta d\omega 2\omega A(\omega). \tag{A.103}$$

We can also write the imaginary-time representation of $\chi_{c,c}$ in terms of the spectral function. It reads as

$$\chi_{c,c}(\tau) = \int_0^\beta d\omega A(\omega)\frac{\cosh[\omega(\tau-\beta/2)]}{\sinh[\omega\beta/2]}. \tag{A.104}$$

Taking the derivative with respect to τ, we obtain

$$\partial_\tau\chi_{c,c}(\tau) = \int_0^\beta d\omega A(\omega)\omega\frac{\sinh[\omega(\tau-\beta/2)]}{\sinh[\omega\beta/2]}, \tag{A.105}$$

and hence

$$\partial_\tau\chi_{c,c}(\tau)\Big|_{\tau=0} = -\int_0^\beta d\omega\omega A(\omega). \tag{A.106}$$

Combining this result with Eq. (A.103), allows us to eliminate the spectral function, which yields

$$c_2 = -2\partial_\tau \chi_{c,c}(\tau)\Big|_{\tau=0}. \tag{A.107}$$

Next, we derive an explicit expression for the derivative $\partial_\tau \chi_{c,c}(\tau)$. For that purpose, we recall that

$$\partial_\tau \chi_{c,c}(\tau) = \partial_\tau \langle T\hat{\sigma}_c^1(\tau)\hat{\sigma}_c^1(0)\rangle. \tag{A.108}$$

For $\tau > 0$, this can be rewritten as

$$\partial_\tau \chi_{c,c}(\tau) = \langle [\partial_\tau \hat{\sigma}_c^1(\tau)]\hat{\sigma}_c^1(0)\rangle, \tag{A.109}$$

where $\partial_\tau \hat{\sigma}_c^1(\tau)$ is given by the Heisenberg equation of motion

$$\partial_\tau \hat{\sigma}_c^1(\tau) = \left[\hat{H}, \hat{\sigma}_c^1(\tau)\right] = \sum_r \frac{\Delta}{2}[\hat{\sigma}_r^3(\tau), \hat{\sigma}_c^1(\tau)] = \Delta i \hat{\sigma}_c^2(\tau). \tag{A.110}$$

Hence, we finally obtain

$$\partial_\tau \chi_{c,c}(\tau)\Big|_{\tau=0} = \Delta i \langle \hat{\sigma}_c^2 \hat{\sigma}_c^1\rangle = \Delta \langle \hat{\sigma}_c^3\rangle = \Delta \langle \sigma^3\rangle, \tag{A.111}$$

and thus

$$c_2 = -2\Delta \langle \sigma^3\rangle. \tag{A.112}$$

A.4.3. High-frequency behavior of the dipole-dipole interaction matrix

The high-frequency behavior of the dipole-dipole interaction matrix is approximately given by Eq. (A.91). To determine the coefficients $w_0^{\boldsymbol{k}}$ and $w_2^{\boldsymbol{k}}$, we perform a Taylor expansion of $W_{\boldsymbol{k}}(i\nu_n)$ in the inverse Matsubara frequency, which yields

$$\begin{aligned} W_{\boldsymbol{k}}(i\nu_n) =& \frac{\alpha}{2}\left[\cos(k_y) + \cos(k_z)\right] - |g_{\boldsymbol{k}}|^2 \frac{\nu_n^2}{\nu_n^2 + \omega_{\boldsymbol{k}}^2} \\ =& \frac{\alpha}{2}\left[\cos(k_y) + \cos(k_z)\right] - |g_{\boldsymbol{k}}|^2 \frac{1}{1 + (\omega_{\boldsymbol{k}}/\nu_n)^2} \\ =& \frac{\alpha}{2}\left[\cos(k_y) + \cos(k_z)\right] - |g_{\boldsymbol{k}}|^2 - \frac{|g_{\boldsymbol{k}}|^2 \omega_{\boldsymbol{k}}^2}{(i\nu_n)^2} + \mathcal{O}((i\nu_n)^{-4}), \end{aligned} \tag{A.113}$$

and therefore

$$w_0^{\boldsymbol{k}} = \frac{\alpha}{2}\left[\cos(k_y) + \cos(k_z)\right] - |g_{\boldsymbol{k}}|^2, \tag{A.114}$$

$$w_2^{\boldsymbol{k}} = -|g_{\boldsymbol{k}}|^2 \omega_{\boldsymbol{k}}^2. \tag{A.115}$$

B. Appendix to Ch. 5

B.1. Vector potential for the quantized SPP mode

In general, the electromagnetic vector potential depends on the gauge of the electromagnetic field. Here, we assume a generalized Coulomb gauge, i.e., we set $\nabla \cdot [\varepsilon(\boldsymbol{r})\boldsymbol{A}] = 0$. With this choice of gauge, the vector potential is directly related to the transverse electric displacement field $\boldsymbol{D}_\perp = -\varepsilon_0 \varepsilon \partial_t \boldsymbol{A}$. In App. A.1, we have calculated the electric field $\boldsymbol{E}$ corresponding to the transverse electric displacement field in the presence of a dielectric-metal interface, representing a surface plasmon polariton (SPP) mode. Using the same mode expansion and photon operators, the quantized vector potential in the dielectric region reads as

$$\hat{\boldsymbol{A}}(\boldsymbol{r}) = \sum_{\boldsymbol{q}} \frac{i}{\sqrt{2\varepsilon_0 \varepsilon_\mathrm{d} \omega_{\boldsymbol{q}} N a^3}} [\boldsymbol{u}_{\boldsymbol{q}}(x) e^{i\boldsymbol{q}\cdot\boldsymbol{\rho}} \hat{a}_{\boldsymbol{q}} - \mathrm{H.c.}], \tag{B.1}$$

where the mode functions $\boldsymbol{u}_{\boldsymbol{q}}(x)$ are defined in (A.19), and the SPP dispersion $\omega_{\boldsymbol{q}}$ is given by (A.17).

In Ch. 5, we slightly change the notation. Due to the relations $\omega_{\boldsymbol{q}} = \omega_{-\boldsymbol{q}}$ and $\boldsymbol{u}_{\boldsymbol{q}} = \bar{\boldsymbol{u}}_{-\boldsymbol{q}}$, the above expression can be rewritten as

$$\hat{\boldsymbol{A}}(\boldsymbol{r}) = \sum_{\boldsymbol{q}} \frac{\boldsymbol{u}_{\boldsymbol{q}}(x)}{\sqrt{2\varepsilon_0 \varepsilon_\mathrm{d} \omega_{\boldsymbol{q}} N a^3}} i(\hat{a}_{\boldsymbol{q}} - \hat{a}^\dagger_{-\boldsymbol{q}}) e^{i\boldsymbol{q}\cdot\boldsymbol{\rho}}. \tag{B.2}$$

Moreover, we redefine the photon creation and annihilation operators as $\hat{a}^\dagger_{\boldsymbol{q}} \to i\hat{a}^\dagger_{\boldsymbol{q}}$ and $\hat{a}_{\boldsymbol{q}} \to -i\hat{a}_{\boldsymbol{q}}$, such that

$$\hat{\boldsymbol{A}}(\boldsymbol{r}) = \sum_{\boldsymbol{q}} \frac{\boldsymbol{u}_{\boldsymbol{q}}(x)}{\sqrt{2\varepsilon_0 \varepsilon_\mathrm{d} \omega_{\boldsymbol{q}} N a^3}} (\hat{a}_{\boldsymbol{q}} + \hat{a}^\dagger_{-\boldsymbol{q}}) e^{i\boldsymbol{q}\cdot\boldsymbol{\rho}}. \tag{B.3}$$

Note that this substitution only adds a complex phase to the operators and does not alter the canonical commutation relations; thus, the physics remains unaffected.

Apart from these modifications, we separate the mode functions into a polarization vector $\boldsymbol{e}_{\boldsymbol{q}}$ and a scalar function $u_{\boldsymbol{q}}(x)$, i.e.,

$$\boldsymbol{u}_{\boldsymbol{q}}(x) = \boldsymbol{e}_{\boldsymbol{q}} u_{\boldsymbol{q}}(x) \tag{B.4}$$

with the complex unit vector

$$\boldsymbol{e}_{\boldsymbol{q}} = \left[1 + \left(\frac{Q_\mathrm{d}}{q}\right)^2\right]^{-\frac{1}{2}} \begin{pmatrix} 1 \\ -i(Q_\mathrm{d}/q) q_y/q \\ -i(Q_\mathrm{d}/q) q_z/q \end{pmatrix}, \tag{B.5}$$

which satisfies the symmetry $\boldsymbol{e_q} = \bar{\boldsymbol{e}}_{-\boldsymbol{q}}$, and

$$u_{\boldsymbol{q}}(x) = \mathcal{N}_{\boldsymbol{q}} e^{-Q_{\mathrm{d}} x} \left[1 + \left(\frac{Q_{\mathrm{d}}}{q}\right)^2\right]^{+\frac{1}{2}}, \tag{B.6}$$

where $\mathcal{N}_{\boldsymbol{q}}$ and Q_{d} are given by Eq. (A.20) and (A.10), respectively. Introducing the x-dependent amplitude

$$\mathcal{A}_{\boldsymbol{q}} = \frac{u_{\boldsymbol{q}}(x)}{\sqrt{2\varepsilon_0 \varepsilon_{\mathrm{d}} \omega_{\boldsymbol{q}} N a^3}} \tag{B.7}$$

with $\mathcal{A}_{\boldsymbol{q}} = \mathcal{A}_{-\boldsymbol{q}} \in \mathbb{R}$, the vector potential finally takes the simple form

$$\hat{\boldsymbol{A}}(\boldsymbol{r}) = \sum_{\boldsymbol{q}} \boldsymbol{e_q} \mathcal{A}_{\boldsymbol{q}} (\hat{a}^\dagger_{-\boldsymbol{q}} + \hat{a}_{\boldsymbol{q}}) e^{i\boldsymbol{q}\cdot\boldsymbol{\rho}}. \tag{B.8}$$

B.2. Lattice Fourier transform of the light-matter Hamiltonian

B.2.1. Linear light-matter interaction

The linear term of the light-matter interaction is given by

$$\hat{H}^{(1)}_{\mathrm{lm}} = \sum_{i,j,\sigma} \sum_{\boldsymbol{q}} v^{\boldsymbol{q}}_{ij} \hat{c}^\dagger_{i\sigma} \hat{c}_{j\sigma} (\hat{a}^\dagger_{-\boldsymbol{q}} + \hat{a}_{\boldsymbol{q}}) \tag{B.9}$$

with the coupling constants

$$v^{\boldsymbol{q}}_{ij} = \gamma_{\boldsymbol{q}}(\boldsymbol{R}_{ij}) e^{i\boldsymbol{q}\cdot(\boldsymbol{R}_i + \boldsymbol{R}_j)/2}, \tag{B.10}$$

where

$$\gamma_{\boldsymbol{q}}(\boldsymbol{R}_{ij}) = iet_{ij} \mathcal{A}_{\boldsymbol{q}} \boldsymbol{R}_{ij} \cdot \boldsymbol{e_q} \tag{B.11}$$

only depends on the difference $\boldsymbol{R}_{ij} = \boldsymbol{R}_i - \boldsymbol{R}_j$. The two quantities satisfy the symmetry relations

$$\gamma_{\boldsymbol{q}}(\boldsymbol{R}_{ij}) = -\gamma_{\boldsymbol{q}}(\boldsymbol{R}_{ji}) = -\bar{\gamma}_{-\boldsymbol{q}}(\boldsymbol{R}_{ij}) = \bar{\gamma}_{-\boldsymbol{q}}(\boldsymbol{R}_{ji}) \tag{B.12}$$

and

$$v^{\boldsymbol{q}}_{ij} = -v^{\boldsymbol{q}}_{ji} = -\bar{v}^{-\boldsymbol{q}}_{ij} = \bar{v}^{-\boldsymbol{q}}_{ji}. \tag{B.13}$$

We first calculate the lattice Fourier transform of $\gamma_{\boldsymbol{q}}(\boldsymbol{R}_{ij})$, which yields

$$\begin{aligned} \gamma_{\boldsymbol{q},\boldsymbol{k}} &= \sum_{\boldsymbol{R}} e^{-i\boldsymbol{k}\cdot\boldsymbol{R}} \gamma_{\boldsymbol{q}}(\boldsymbol{R}) \\ &= -e\mathcal{A}_{\boldsymbol{q}} (\boldsymbol{e_q} \cdot \nabla_{\boldsymbol{k}}) \sum_{\boldsymbol{R}} t_{\boldsymbol{R}} e^{-i\boldsymbol{k}\cdot\boldsymbol{R}} \\ &= -e\mathcal{A}_{\boldsymbol{q}} (\boldsymbol{e_q} \cdot \nabla_{\boldsymbol{k}}) \epsilon_{\boldsymbol{k}} \\ &= -e\mathcal{A}_{\boldsymbol{q}} \boldsymbol{e_q} \cdot \boldsymbol{v_k}. \end{aligned} \tag{B.14}$$

In the second line, we have introduced the notation $t_{\boldsymbol{R}_{ij}} = t_{ij}$. Moreover, we have used the fact that the lattice Fourier transform of the hopping matrix elements t_{ij} is nothing but the non-interacting electronic dispersion relation to obtain the third line. The vector $\boldsymbol{v}_{\boldsymbol{k}}$ in the last line denotes the group velocity of the non-interacting electrons and is defined as $\boldsymbol{v}_{\boldsymbol{k}} = \nabla_{\boldsymbol{k}} \epsilon_{\boldsymbol{k}}$.

In the next step, we transform the linear light-matter Hamiltonian to $\boldsymbol{k}$-space. We start with inserting (B.10) into (B.9) and perform a lattice Fourier transform of the electron creation and annihilation operators, which gives

$$\begin{aligned}\hat{H}_{\mathrm{lm}}^{(1)} =& \sum_{i,j,\sigma} \sum_{\boldsymbol{q}} \gamma_{\boldsymbol{q}}(\boldsymbol{R}_{ij}) e^{i\boldsymbol{q}\cdot(\boldsymbol{R}_i+\boldsymbol{R}_j)/2} \hat{c}_{i\sigma}^\dagger \hat{c}_{j\sigma} (\hat{a}_{-\boldsymbol{q}}^\dagger + \hat{a}_{\boldsymbol{q}}) \\ =& \sum_{i,j,\sigma} \sum_{\boldsymbol{q}} \gamma_{\boldsymbol{q}}(\boldsymbol{R}_{ij}) e^{i\boldsymbol{q}\cdot(\boldsymbol{R}_i+\boldsymbol{R}_j)/2} \frac{1}{\sqrt{N}} \sum_{\boldsymbol{k}_1} \hat{c}_{\boldsymbol{k}_1\sigma}^\dagger e^{-i\boldsymbol{k}_1\cdot\boldsymbol{R}_i} \times \\ & \times \frac{1}{\sqrt{N}} \sum_{\boldsymbol{k}_2} \hat{c}_{\boldsymbol{k}_2\sigma} e^{i\boldsymbol{k}_2\cdot\boldsymbol{R}_j} (\hat{a}_{-\boldsymbol{q}}^\dagger + \hat{a}_{\boldsymbol{q}}).\end{aligned} \tag{B.15}$$

Then, we use the substitution $\boldsymbol{R}_i = \boldsymbol{R}_j + \boldsymbol{S}$ and obtain

$$\begin{aligned}\hat{H}_{\mathrm{lm}}^{(1)} =& \sum_{\boldsymbol{R}_j,\boldsymbol{S},\sigma} \frac{1}{N} \sum_{\boldsymbol{q},\boldsymbol{k}_1,\boldsymbol{k}_2} \gamma_{\boldsymbol{q}}(\boldsymbol{S}) e^{i\boldsymbol{q}\cdot(2\boldsymbol{R}_j+\boldsymbol{S})/2} \hat{c}_{\boldsymbol{k}_1\sigma}^\dagger e^{-i\boldsymbol{k}_1\cdot(\boldsymbol{R}_j+\boldsymbol{S})} \hat{c}_{\boldsymbol{k}_2\sigma} e^{i\boldsymbol{k}_2\cdot\boldsymbol{R}_j} (\hat{a}_{-\boldsymbol{q}}^\dagger + \hat{a}_{\boldsymbol{q}}) \\ =& \sum_{\boldsymbol{S},\sigma} \sum_{\boldsymbol{q},\boldsymbol{k}_1,\boldsymbol{k}_2} \gamma_{\boldsymbol{q}}(\boldsymbol{S}) e^{i\boldsymbol{q}\cdot\boldsymbol{S}/2} e^{-i\boldsymbol{k}_1\cdot\boldsymbol{S}} \hat{c}_{\boldsymbol{k}_1\sigma}^\dagger \hat{c}_{\boldsymbol{k}_2\sigma} (\hat{a}_{-\boldsymbol{q}}^\dagger + \hat{a}_{\boldsymbol{q}}) \delta_{\boldsymbol{k}_1,\boldsymbol{q}+\boldsymbol{k}_2} \\ =& \sum_{\boldsymbol{S},\sigma} \sum_{\boldsymbol{q},\boldsymbol{k}} \gamma_{\boldsymbol{q}}(\boldsymbol{S}) e^{-i(\boldsymbol{k}+\boldsymbol{q}/2)\cdot\boldsymbol{S}} \hat{c}_{\boldsymbol{k}+\boldsymbol{q}\sigma}^\dagger \hat{c}_{\boldsymbol{k}\sigma} (\hat{a}_{-\boldsymbol{q}}^\dagger + \hat{a}_{\boldsymbol{q}}).\end{aligned} \tag{B.16}$$

Note that we have assumed here that only $\boldsymbol{q}$-vectors within the first Brillouin zone of the material contribute. Otherwise, the δ-function in the second line would have to be replaced by a sum $\sum_{\boldsymbol{G}\in\mathcal{L}_{\mathrm{R}}} \delta_{\boldsymbol{k}_1,\boldsymbol{q}+\boldsymbol{G}+\boldsymbol{k}_2}$, where $\mathcal{L}_{\mathrm{R}}$ denotes the reciprocal lattice of the solid. However, a truncation of the $\boldsymbol{q}$-modes is justified for the present model since the coupling strength is exponentially suppressed for large $\boldsymbol{q}$ (see Sec. 5.3.1). With this simplification and the definition of the lattice Fourier transform of $\gamma_{\boldsymbol{q}}(\boldsymbol{R})$, we finally get

$$\hat{H}_{\mathrm{lm}}^{(1)} = \sum_{\boldsymbol{k},\boldsymbol{q},\sigma} \gamma_{\boldsymbol{q},\boldsymbol{k}+\boldsymbol{q}/2} \hat{c}_{\boldsymbol{k}+\boldsymbol{q}\sigma}^\dagger \hat{c}_{\boldsymbol{k}\sigma} (\hat{a}_{-\boldsymbol{q}}^\dagger + \hat{a}_{\boldsymbol{q}}). \tag{B.17}$$

B.2.2. Second-order light-matter interaction

The second-order term of the light-matter Hamiltonian reads as

$$\hat{H}_{\mathrm{lm}}^{(2)} = \frac{1}{2} \sum_{i,j,\sigma} \sum_{\boldsymbol{q}_1,\boldsymbol{q}_2} \tilde{v}_{ij}^{\boldsymbol{q}_1\boldsymbol{q}_2} \hat{c}_{i\sigma}^\dagger \hat{c}_{j\sigma} (\hat{a}_{-\boldsymbol{q}_1}^\dagger + \hat{a}_{\boldsymbol{q}_1}) (\hat{a}_{-\boldsymbol{q}_2}^\dagger + \hat{a}_{\boldsymbol{q}_2}), \tag{B.18}$$

where

$$\tilde{v}_{ij}^{\boldsymbol{q}_1\boldsymbol{q}_2} = \tilde{\gamma}_{\boldsymbol{q}_1\boldsymbol{q}_2}(\boldsymbol{R}_{ij}) e^{i(\boldsymbol{q}_1+\boldsymbol{q}_2)\cdot(\boldsymbol{R}_i+\boldsymbol{R}_j)/2} \tag{B.19}$$

with

$$\tilde{\gamma}_{\boldsymbol{q}_1\boldsymbol{q}_2}(\boldsymbol{R}_{ij}) = e^2 t_{ij} \mathcal{A}_{\boldsymbol{q}_1} \mathcal{A}_{\boldsymbol{q}_2} (\boldsymbol{e}_{\boldsymbol{q}_1} \cdot \boldsymbol{R}_{ij})(\boldsymbol{e}_{\boldsymbol{q}_2} \cdot \boldsymbol{R}_{ij}). \tag{B.20}$$

The factor $\tilde{\gamma}_{\boldsymbol{q}_1\boldsymbol{q}_2}(\boldsymbol{R}_{ij})$ only depends on the difference $\boldsymbol{R}_{ij} = \boldsymbol{R}_i - \boldsymbol{R}_j$. Thus, we can perform a lattice Fourier transform, which yields

$$\begin{aligned}
\tilde{\gamma}_{\boldsymbol{q}_1,\boldsymbol{q}_2,\boldsymbol{k}} &= \sum_{\boldsymbol{R}} e^{-i\boldsymbol{k}\cdot\boldsymbol{R}} \tilde{\gamma}_{\boldsymbol{q}_1\boldsymbol{q}_2}(\boldsymbol{R}) \\
&= \sum_{\boldsymbol{R}} e^{-i\boldsymbol{k}\cdot\boldsymbol{R}} e^2 t_{\boldsymbol{R}} \mathcal{A}_{\boldsymbol{q}_1} \mathcal{A}_{\boldsymbol{q}_2} (\boldsymbol{e}_{\boldsymbol{q}_1} \cdot \boldsymbol{R})(\boldsymbol{e}_{\boldsymbol{q}_2} \cdot \boldsymbol{R}) \\
&= -e^2 (\mathcal{A}_{\boldsymbol{q}_1} \boldsymbol{e}_{\boldsymbol{q}_1} \cdot \nabla_{\boldsymbol{k}})(\mathcal{A}_{\boldsymbol{q}_2} \boldsymbol{e}_{\boldsymbol{q}_2} \cdot \nabla_{\boldsymbol{k}}) \sum_{\boldsymbol{R}} e^{-i\boldsymbol{k}\cdot\boldsymbol{R}} t_{\boldsymbol{R}} \\
&= -e^2 (\mathcal{A}_{\boldsymbol{q}_1} \boldsymbol{e}_{\boldsymbol{q}_1} \cdot \nabla_{\boldsymbol{k}})(\mathcal{A}_{\boldsymbol{q}_2} \boldsymbol{e}_{\boldsymbol{q}_2} \cdot \nabla_{\boldsymbol{k}}) \epsilon_{\boldsymbol{k}}.
\end{aligned} \tag{B.21}$$

As in the previous subsection, we have used the definition $t_{\boldsymbol{R}_{ij}} = t_{ij}$ and the fact that the non-interacting electron dispersion $\epsilon_{\boldsymbol{k}}$ can be identified with the Fourier transform of the hopping amplitudes.

To determine the $\boldsymbol{k}$-space representation of the second-order light-matter interaction, we substitute Eq. (B.19) into the Hamiltonian (B.18). Moreover, we perform a lattice Fourier transform of the electron operators. From this, we obtain

$$\begin{aligned}
\hat{H}^{(2)}_{\mathrm{lm}} =& \frac{1}{2} \sum_{i,j,\sigma} \sum_{\boldsymbol{q}_1,\boldsymbol{q}_2} \tilde{\gamma}_{\boldsymbol{q}_1\boldsymbol{q}_2}(\boldsymbol{R}_{ij}) e^{i(\boldsymbol{q}_1+\boldsymbol{q}_2)\cdot(\boldsymbol{R}_i+\boldsymbol{R}_j)/2} \hat{c}^\dagger_{i\sigma} \hat{c}_{j\sigma} (\hat{a}^\dagger_{-\boldsymbol{q}_1} + \hat{a}_{\boldsymbol{q}_1})(\hat{a}^\dagger_{-\boldsymbol{q}_2} + \hat{a}_{\boldsymbol{q}_2}) \\
=& \frac{1}{2} \sum_{i,j,\sigma} \sum_{\boldsymbol{q}_1,\boldsymbol{q}_2} \tilde{\gamma}_{\boldsymbol{q}_1\boldsymbol{q}_2}(\boldsymbol{R}_{ij}) e^{i(\boldsymbol{q}_1+\boldsymbol{q}_2)\cdot(\boldsymbol{R}_i+\boldsymbol{R}_j)/2} \frac{1}{\sqrt{N}} \sum_{\boldsymbol{k}_1} e^{-i\boldsymbol{k}_1\cdot\boldsymbol{R}_i} \hat{c}^\dagger_{\boldsymbol{k}_1\sigma} \times \\
& \times \frac{1}{\sqrt{N}} \sum_{\boldsymbol{k}_2} e^{i\boldsymbol{k}_2\cdot\boldsymbol{R}_j} \hat{c}_{\boldsymbol{k}_2\sigma} (\hat{a}^\dagger_{-\boldsymbol{q}_1} + \hat{a}_{\boldsymbol{q}_1})(\hat{a}^\dagger_{-\boldsymbol{q}_2} + \hat{a}_{\boldsymbol{q}_2}).
\end{aligned} \tag{B.22}$$

Then, we introduce a lattice vector $\boldsymbol{S}$ with $\boldsymbol{R}_i = \boldsymbol{R}_j + \boldsymbol{S}$ and substitute the sum over $\boldsymbol{R}_i$ with a sum over $\boldsymbol{S}$, which yields

$$\begin{aligned}
\hat{H}^{(2)}_{\mathrm{lm}} =& \frac{1}{2} \sum_{\boldsymbol{S},\boldsymbol{R}_j,\sigma} \sum_{\boldsymbol{q}_1,\boldsymbol{q}_2} \frac{1}{N} \sum_{\boldsymbol{k}_1,\boldsymbol{k}_2} \tilde{\gamma}_{\boldsymbol{q}_1\boldsymbol{q}_2}(\boldsymbol{S}) e^{i(\boldsymbol{q}_1+\boldsymbol{q}_2)\cdot(2\boldsymbol{R}_j+\boldsymbol{S})/2} e^{-i\boldsymbol{k}_1\cdot(\boldsymbol{R}_j+\boldsymbol{S})} \hat{c}^\dagger_{\boldsymbol{k}_1\sigma} \times \\
& \times e^{i\boldsymbol{k}_2\cdot\boldsymbol{R}_j} \hat{c}_{\boldsymbol{k}_2\sigma} (\hat{a}^\dagger_{-\boldsymbol{q}_1} + \hat{a}_{\boldsymbol{q}_1})(\hat{a}^\dagger_{-\boldsymbol{q}_2} + \hat{a}_{\boldsymbol{q}_2}) \\
=& \frac{1}{2} \sum_{\boldsymbol{S},\sigma} \sum_{\boldsymbol{q}_1,\boldsymbol{q}_2} \sum_{\boldsymbol{k}_1,\boldsymbol{k}_2} \tilde{\gamma}_{\boldsymbol{q}_1\boldsymbol{q}_2}(\boldsymbol{S}) e^{i(\boldsymbol{q}_1+\boldsymbol{q}_2)\cdot\boldsymbol{S}/2} e^{-i\boldsymbol{k}_1\cdot\boldsymbol{S}} \hat{c}^\dagger_{\boldsymbol{k}_1\sigma} e^{i\boldsymbol{k}_2\cdot\boldsymbol{R}_j} \hat{c}_{\boldsymbol{k}_2\sigma} \times \\
& \times (\hat{a}^\dagger_{-\boldsymbol{q}_1} + \hat{a}_{\boldsymbol{q}_1})(\hat{a}^\dagger_{-\boldsymbol{q}_2} + \hat{a}_{\boldsymbol{q}_2}) \delta_{\boldsymbol{k}_1,\boldsymbol{k}_2+\boldsymbol{q}_1+\boldsymbol{q}_2} \\
=& \frac{1}{2} \sum_{\boldsymbol{S},\sigma} \sum_{\boldsymbol{q}_1,\boldsymbol{q}_2,\boldsymbol{k}} \tilde{\gamma}_{\boldsymbol{q}_1\boldsymbol{q}_2}(\boldsymbol{S}) e^{-i(\boldsymbol{k}+(\boldsymbol{q}_1+\boldsymbol{q}_2)/2)\cdot\boldsymbol{S}} \hat{c}^\dagger_{\boldsymbol{k}+\boldsymbol{q}_1+\boldsymbol{q}_2\sigma} \hat{c}_{\boldsymbol{k}\sigma} \times \\
& \times (\hat{a}^\dagger_{-\boldsymbol{q}_1} + \hat{a}_{\boldsymbol{q}_1})(\hat{a}^\dagger_{-\boldsymbol{q}_2} + \hat{a}_{\boldsymbol{q}_2}).
\end{aligned} \tag{B.23}$$

Again, we assume that the coupling to $\boldsymbol{q}$-modes beyond the first Brillouin zone of the solid is strongly suppressed, such that the sums over $\boldsymbol{q}_1$ and $\boldsymbol{q}_2$ can be considered to

run over vectors within the same range as the sums over $\boldsymbol{k}_1$ and $\boldsymbol{k}_2$. (Otherwise, the δ-function in the second step would have to be replaced by a δ-comb.) To get the final result, we use the definition of $\tilde{\gamma}_{\boldsymbol{q}_1,\boldsymbol{q}_2,\boldsymbol{k}}$ and obtain

$$\hat{H}^{(2)}_{\mathrm{lm}} = \frac{1}{2}\sum_{\boldsymbol{q}_1,\boldsymbol{q}_2,\boldsymbol{k}}\sum_{\sigma}\tilde{\gamma}_{\boldsymbol{q}_1,\boldsymbol{q}_2,\boldsymbol{k}+(\boldsymbol{q}_1+\boldsymbol{q}_2)/2}\hat{c}^{\dagger}_{\boldsymbol{k}+\boldsymbol{q}_1+\boldsymbol{q}_2\sigma}\hat{c}_{\boldsymbol{k}\sigma}(\hat{a}^{\dagger}_{-\boldsymbol{q}_1}+\hat{a}_{\boldsymbol{q}_1})(\hat{a}^{\dagger}_{-\boldsymbol{q}_2}+\hat{a}_{\boldsymbol{q}_2}). \tag{B.24}$$

B.3. Self-consistent equation for the hybridization function

In the following, we derive the self-consistent equation (5.41) that describes the relation between the lattice Green's function and the hybridization function of the impurity model. We start from the impurity Dyson equation

$$[(i\partial_t+\tilde{\mu})\mathbb{I}-\Delta-\Sigma_U]*G^{\mathrm{imp}}_{\sigma}=\mathbb{I} \tag{B.25}$$

and the lattice Dyson equation

$$\left[(i\partial_t+\tilde{\mu}-\eta_{\boldsymbol{k}})\mathbb{I}-\Sigma_U-\Sigma^{(1)}_{\boldsymbol{k}\sigma}\right]*G_{\boldsymbol{k}\sigma}=\mathbb{I}. \tag{B.26}$$

Moreover, we define the quantities

$$Z^{-1}=(i\partial_t+\tilde{\mu})\mathbb{I}-\Sigma_U \tag{B.27}$$

and

$$Y_{\boldsymbol{k}}=\eta_{\boldsymbol{k}}\mathbb{I}+\Sigma^{(1)}_{\boldsymbol{k}}. \tag{B.28}$$

With this, (B.25) can be rewritten as

$$\begin{aligned}
&[Z^{-1}-\Delta]*G^{\mathrm{imp}}_{\sigma}=\mathbb{I} && \text{(B.29)}\\
\Leftrightarrow\ &[\mathbb{I}-Z*\Delta]*G^{\mathrm{imp}}_{\sigma}=Z && \text{(B.30)}\\
\Leftrightarrow\ &G^{\mathrm{imp}}_{\sigma}=Z+Z*\Delta*G^{\mathrm{imp}}_{\sigma} && \text{(B.31)}\\
\Leftrightarrow\ &G^{\mathrm{imp}}_{\sigma}=Z+G^{\mathrm{imp}}_{\sigma}*\Delta*Z, && \text{(B.32)}
\end{aligned}$$

where the last equality is obtained by multiplying both sides of the equation with $G^{\mathrm{imp}}_{\sigma}*Z^{-1}$ from the left and ${G^{\mathrm{imp}}_{\sigma}}^{-1}*Z$ from the right. Similarly, (B.26) becomes

$$\begin{aligned}
&[Z^{-1}-Y_{\boldsymbol{k}}]*G_{\boldsymbol{k}\sigma}=\mathbb{I} && \text{(B.33)}\\
\Leftrightarrow\ &[\mathbb{I}-Z*Y_{\boldsymbol{k}}]*G_{\boldsymbol{k}\sigma}=Z && \text{(B.34)}\\
\Leftrightarrow\ &G_{\boldsymbol{k}\sigma}=Z+Z*Y_{\boldsymbol{k}}*G_{\boldsymbol{k}\sigma} && \text{(B.35)}\\
\Leftrightarrow\ &G_{\boldsymbol{k}\sigma}=Z+G_{\boldsymbol{k}\sigma}*Y_{\boldsymbol{k}}*Z, && \text{(B.36)}
\end{aligned}$$

where we have multiplied both sides of (B.35) with $G_{\boldsymbol{k}}*Z^{-1}$ from the left and $G^{-1}_{\boldsymbol{k}}*Z$ from the right to obtain the last line.

The local lattice Green's function is given by

$$G_\sigma^{\mathrm{loc}} = \frac{1}{N}\sum_{\boldsymbol{k}} G_{\boldsymbol{k}\sigma}. \tag{B.37}$$

Furthermore, we introduce the quantities

$$G_\sigma^{(1)} = \frac{1}{N}\sum_{\boldsymbol{k}} Y_{\boldsymbol{k}} * G_{\boldsymbol{k}\sigma} \tag{B.38}$$

$$G_\sigma^{(2)} = \frac{1}{N}\sum_{\boldsymbol{k}} [Y_{\boldsymbol{k}} + Y_{\boldsymbol{k}} * G_{\boldsymbol{k}\sigma} * Y_{\boldsymbol{k}}]. \tag{B.39}$$

Due to the particle-hole symmetry of the system, $\sum_{\boldsymbol{k}} \epsilon_{\boldsymbol{k}} = 0$ and $\sum_{\boldsymbol{k}} s_{\boldsymbol{k}} = 0$. With $\eta_{\boldsymbol{k}} = \epsilon_{\boldsymbol{k}} + s_{\boldsymbol{k}}$ we thus obtain $\sum_{\boldsymbol{k}} \eta_{\boldsymbol{k}} = 0$, i.e., the definition of $G_\sigma^{(2)}$ is identical with Eq. (5.43) in the main text. We sum both sides of Eq. (B.35) over $\boldsymbol{k}$ and normalize the result by N, which yields

$$G_\sigma^{\mathrm{loc}} = Z + Z * G_\sigma^{(1)}. \tag{B.40}$$

Moreover, we multiply both sides of Eq. (B.36) from the left by $Y_{\boldsymbol{k}}$, sum over $\boldsymbol{k}$, and divide by N. The resulting expression reads as

$$G_\sigma^{(1)} = G_\sigma^{(2)} * Z. \tag{B.41}$$

The self-consistency condition $G_\sigma^{\mathrm{imp}} = G_\sigma^{\mathrm{loc}}$ allows us to eliminate G_σ^{imp} in (B.32) using (B.40). From this, we obtain

$$Z * G_\sigma^{(1)} = Z * \Delta * Z + Z * G_\sigma^{(1)} * \Delta * Z. \tag{B.42}$$

Then we substitute $G_\sigma^{(1)}$ on the left-hand side of the above expression using Eq. (B.41), which yields

$$Z * G_\sigma^{(2)} * Z = Z * \Delta * Z + Z * G_\sigma^{(1)} * \Delta * Z. \tag{B.43}$$

Finally, we multiply both sides of the equation from the left and the right with Z^{-1} and get the self-consistent equation

$$G_\sigma^{(2)} = \Delta + G_\sigma^{(1)} * \Delta. \tag{B.44}$$

B.4. Physical quantities indicating the Mott metal-insulator transition

B.4.1. Interpretation of $G(\beta/2)$

In Sec. 5.3, we use the local Matsubara Green's function at $\tau = \beta/2$ to detect the Mott metal-insulator transition. Below, we briefly discuss how this quantity can be interpreted. For that purpose, we consider a general fermionic Matsubara Green's function

$$G(\tau) = \frac{1}{\beta}\sum_{i\omega_n} G(i\omega_n) e^{-i\omega_n \tau}. \tag{B.45}$$

The corresponding imaginary-frequency representation can be written in terms of the spectral function $A(\omega) = -\operatorname{Im}\{G^{\mathrm{ret}}(\omega)\}/\pi$ with the retarded Greens function G^{ret} and reads as

$$G(i\omega_n) = \int_{-\infty}^{+\infty} d\omega \, \frac{A(\omega)}{i\omega_n - \omega}. \tag{B.46}$$

Substituting this into Eq. (B.45) yields

$$G(\tau) = \int_{-\infty}^{+\infty} d\omega \, A(\omega) F(\omega, \tau), \tag{B.47}$$

where we have defined the function

$$F(\omega, \tau) = \frac{1}{\beta} \sum_{i\omega_n} e^{-i\omega_n \tau} \frac{1}{i\omega_n - \omega}. \tag{B.48}$$

The Matsubara sum can be replaced by the complex contour integral

$$F(\omega, \tau) = \frac{1}{2\pi i \beta} \oint f(z, \omega, \tau) h(z) dz, \tag{B.49}$$

with

$$f(z, \omega, \tau) = e^{-i\omega_n \tau} \frac{1}{i\omega_n - \omega} \tag{B.50}$$

and

$$h(z) = \beta(1 - n_F(z)), \tag{B.51}$$

where

$$n_F(z) = \frac{1}{e^{\beta z} + 1} \tag{B.52}$$

denotes the Fermi distribution. The function $h(z)$ exhibits poles at the fermionic Matsubara frequencies, which must be encircled by the contour. Moreover, $h(z)$ controls the convergence in the left half-plane, such that the integrand of (B.49) vanishes for $|z| \to \infty$. In addition, $f(z, \omega, \tau)$ has a single pole at $z = \omega$. Therefore, the contour integral evaluates to

$$F(\omega, \tau) = -\frac{1}{\beta} \operatorname{Res}\left[f(z = \omega, \omega, \tau) h(z = \omega)\right] = -e^{\omega(\beta - \tau)} n_F(\omega), \tag{B.53}$$

where $\operatorname{Res}\left[f(z = \omega, \omega, \tau) h(z = \omega)\right]$ denotes the residue of the integrand at $z = \omega$.

We now turn to the case, where $\tau = \beta/2$. At this imaginary time,

$$-F(\omega, \tau = \beta/2) = [2\cosh(\beta\omega/2)]^{-1}. \tag{B.54}$$

As illustrated in Fig. B.1, this function features a single peak at $\omega = 0$. The width of the peak depends on the inverse temperature β. However, it is relatively narrow for all values shown in the graphic. Therefore, the quantity

$$-G(\beta/2) = \int_{-\infty}^{+\infty} d\omega \, A(\omega)[-F(\omega, \beta/2)] \tag{B.55}$$

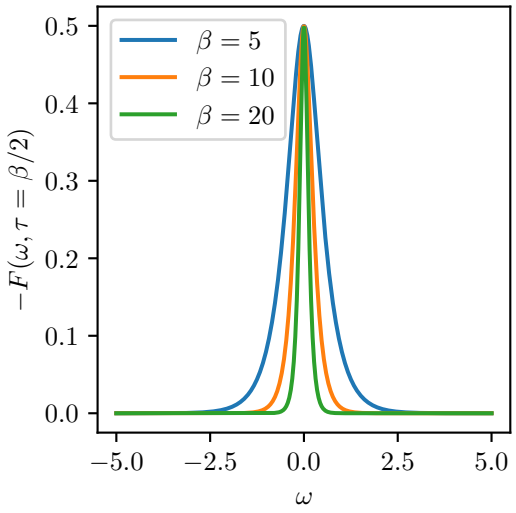

Figure B.1.: $-F(\omega, \tau)$ *at* $\tau = \beta/2$ *for three different inverse temperatures* $\beta = 1/T$.

provides an estimate for the magnitude of the spectral function at $\omega = 0$. This general relation also applies to the local Green's function $G_\sigma^{\mathrm{loc}}(\beta/2)$ and thus helps to detect the Mott metal-insulator transition. For the Mott-insulating phase, the local spectral function has no spectral weight at zero frequency (i.e., the local density of states vanishes at the Fermi level) due to a finite energy gap. As a result, $G_\sigma^{\mathrm{loc}}(\beta/2)$ vanishes. Conversely, the metallic regime is characterized by a quasiparticle peak at zero frequency, such that $G_\sigma^{\mathrm{loc}}(\beta/2) \neq 0$.

B.4.2. Calculation of the double occupancy from the impurity self-energy

In this section, we derive an expression for the double occupancy $D = \langle \hat{n}_{i\uparrow} \hat{n}_{i\downarrow} \rangle$. For that purpose, we first describe how to find a general relation between the self-energy and the interaction Hamiltonian of a system. We consider an arbitrary fermionic lattice Green's function

$$G_{ij\sigma}(t, t') = -i\Theta_{\mathcal{C}}(t, t') \langle \hat{c}_{i\sigma}(t) \hat{c}_{j\sigma}^\dagger(t') \rangle + i\Theta_{\mathcal{C}}(t, t') \langle \hat{c}_{j\sigma}^\dagger(t') \hat{c}_{i\sigma}(t) \rangle, \tag{B.56}$$

where $\Theta_{\mathcal{C}}(t, t')$ denotes the Heaviside function on the Keldysh contour. We calculate the time derivative of $G_{ij\sigma}(t, t')$, which yields

$$i\partial_t G_{ij\sigma}(t, t') = \delta_{\mathcal{C}}(t, t') \underbrace{\langle \hat{c}_{i\sigma}(t) \hat{c}_{j\sigma}^\dagger(t) + \hat{c}_{j\sigma}^\dagger(t) \hat{c}_{i\sigma}(t) \rangle}_{\delta_{ij}} - i \langle T_{\mathcal{C}} \underbrace{[i\partial_t \hat{c}_{i\sigma}(t)]}_{-[\hat{H}(t), \hat{c}_{i\sigma}(t)]} \hat{c}_{j\sigma}^\dagger(t') \rangle. \tag{B.57}$$

The Kronecker delta in the first term is obtained due to the fermionic anti-commutation relation, and the derivative of the operator in the second term can be rewritten in terms of the Hamiltonian of the system using the Heisenberg equation of motion. We assume that the Hamiltonian can be split into two parts

$$\hat{H} = \hat{H}_0 + \hat{H}_{\mathrm{int}}, \tag{B.58}$$

where

$$\hat{H}_0 = \sum_{a,b,\sigma} h_{ab} \hat{c}^\dagger_{a\sigma} \hat{c}_{b\sigma} \tag{B.59}$$

denotes the (non-interacting) quadratic contribution, and $\hat{H}_{\text{int}}$ accounts for the interactions. Using the relation

$$[\hat{c}^\dagger_\alpha \hat{c}_\beta, \hat{c}_\gamma] = -\delta_{\gamma\alpha} \hat{c}_\beta, \tag{B.60}$$

the commutator between $\hat{H}_0$ and $\hat{c}_{i\sigma}(t)$ evaluates to

$$[\hat{H}_0(t), \hat{c}_{i\sigma}(t)] = -\sum_{b,\sigma} h_{ib} \hat{c}_{b\sigma}(t), \tag{B.61}$$

and thus

$$\begin{aligned} i\langle T_\mathcal{C}[\hat{H}_0(t), \hat{c}_{i\sigma}(t)] \hat{c}^\dagger_{j\sigma}(t')\rangle &= \sum_{b,\sigma} h_{ib}(-i)\langle T_\mathcal{C} \hat{c}_{b\sigma}(t) \hat{c}^\dagger_{j\sigma}(t')\rangle \\ &= \sum_{b,\sigma} h_{ib} G_{bj\sigma}(t,t'). \end{aligned} \tag{B.62}$$

With this, Eq. (B.57) can be rewritten as

$$i\partial_t G_{ij\sigma}(t,t') = \delta_\mathcal{C}(t,t')\delta_{ij} + \sum_{b,\sigma} h_{ib} G_{bj\sigma}(t,t') + i\langle T_\mathcal{C}[\hat{H}_{\text{int}}(t), \hat{c}_{i\sigma}(t)] \hat{c}^\dagger_{j\sigma}(t')\rangle. \tag{B.63}$$

Comparing the expression above to the Dyson equation

$$i\partial_t G_{ij\sigma}(t,t') = \delta_\mathcal{C}(t,t')\delta_{ij} + \sum_{b,\sigma} h_{ib} G_{bj\sigma}(t,t') + \int_\mathcal{C} d\bar{t} \sum_{b\sigma} \Sigma_{ib}(t,\bar{t}) G_{bj\sigma}(\bar{t},t'), \tag{B.64}$$

we obtain the general formula

$$\langle T_\mathcal{C}[\hat{H}_{\text{int}}(t), \hat{c}_{i\sigma}(t)] \hat{c}^\dagger_{j\sigma}(t')\rangle = -i \int_\mathcal{C} d\bar{t} \sum_{b\sigma} \Sigma_{ib}(t,\bar{t}) G_{bj\sigma}(\bar{t},t'). \tag{B.65}$$

For the Hubbard interaction

$$\hat{H}_U = U \sum_j \hat{n}_{j\uparrow} \hat{n}_{j\downarrow}, \tag{B.66}$$

the lesser component of the right-hand side of Eq. (B.65) at $t = t'$ yields

$$-\langle \hat{c}^\dagger_{i\uparrow}(t)[\hat{H}_U(t), \hat{c}_{i\sigma}(t)]\rangle = U\langle \hat{n}_{i\uparrow}\hat{n}_{i\downarrow}\rangle. \tag{B.67}$$

On the other hand, this is equal to

$$-\langle \hat{c}^\dagger_{i\uparrow}(t)[\hat{H}_U(t), \hat{c}_{i\sigma}(t)]\rangle = -i\left[\int_\mathcal{C} d\bar{t} \sum_{b\sigma} \Sigma^{\text{mat}}_{ib}(t,\bar{t}) G_{bj\sigma}(\bar{t},t)\right]^<, \tag{B.68}$$

where the self-energy contribution due to the Hubbard interaction is approximately given by

$$\Sigma_{ij}^{\mathrm{mat}}(t,t') \approx \delta_{ij}[\delta_{\mathcal{C}}(t,t')s_U + \Sigma_U(t,t')] \tag{B.69}$$

within our DMFT formalism. Thus, we find

$$\begin{aligned} U\langle \hat{n}_{i\uparrow}\hat{n}_{i\downarrow}\rangle =& -i\left[\int_{\mathcal{C}} d\bar{t} \sum_{b\sigma} \delta_{ib}[\delta_{\mathcal{C}}(t,\bar{t})s_U + \Sigma_U(t,\bar{t})]G_{bj\sigma}(\bar{t},t)\right]^{<} \\ =& s_U(t)\langle \hat{n}_\sigma\rangle - i\left[\int_{\mathcal{C}} d\bar{t}\, \Sigma_U(t,\bar{t})G_\sigma^{\mathrm{loc}}(\bar{t},t)\right] \\ =& \frac{U}{4} - i\left[\int_{\mathcal{C}} d\bar{t}\, \Sigma_U(t,\bar{t})G_\sigma^{\mathrm{loc}}(\bar{t},t)\right]^{<}, \end{aligned} \tag{B.70}$$

where we have used that $\langle \hat{n}_\sigma\rangle = 1/2$ for a half-filled system. Therefore, the double occupancy is given by

$$D = \langle \hat{n}_{i\uparrow}\hat{n}_{i\downarrow}\rangle = \frac{1}{4} - \frac{i}{U}\left[\int_{\mathcal{C}} d\bar{t}\, \Sigma_U(t,\bar{t})G_\sigma^{\mathrm{loc}}(\bar{t},t)\right]^{<}. \tag{B.71}$$

Bibliography

[1] Oscar Akerlund et al. "Dynamical mean field approximation applied to quantum field theory". In: *Phys. Rev. D* 88 (12 Dec. 2013), p. 125006. DOI: 10.1103/PhysRevD.88.125006. URL: https://link.aps.org/doi/10.1103/PhysRevD.88.125006.

[2] Oscar Akerlund et al. "Extended mean field study of complex φ^4-theory at finite density and temperature". In: *Phys. Rev. D* 90 (6 Sept. 2014), p. 065008. DOI: 10.1103/PhysRevD.90.065008. URL: https://link.aps.org/doi/10.1103/PhysRevD.90.065008.

[3] Peter Anders et al. "Dynamical mean-field theory for bosons". In: *New Journal of Physics* 13.7 (July 2011), p. 075013. DOI: 10.1088/1367-2630/13/7/075013. URL: https://dx.doi.org/10.1088/1367-2630/13/7/075013.

[4] Peter Christian Anders. "Dynamical mean-field theory for bosons and bose-fermi mixtures". Doctoral thesis. ETH Zürich, 2011. DOI: 10.3929/ethz-a-007146448. URL: https://www.research-collection.ethz.ch/handle/20.500.11850/104009.

[5] Hideo Aoki et al. "Nonequilibrium dynamical mean-field theory and its applications". In: *Rev. Mod. Phys.* 86 (2 June 2014), pp. 779–837. DOI: 10.1103/RevModPhys.86.779. URL: https://link.aps.org/doi/10.1103/RevModPhys.86.779.

[6] Yuto Ashida et al. "Quantum Electrodynamic Control of Matter: Cavity-Enhanced Ferroelectric Phase Transition". In: *Phys. Rev. X* 10 (4 Nov. 2020), p. 041027. DOI: 10.1103/PhysRevX.10.041027. URL: https://link.aps.org/doi/10.1103/PhysRevX.10.041027.

[7] Thomas Ayral, Silke Biermann, and Philipp Werner. "Screening and nonlocal correlations in the extended Hubbard model from self-consistent combined GW and dynamical mean field theory". In: *Phys. Rev. B* 87 (12 Mar. 2013), p. 125149. DOI: 10.1103/PhysRevB.87.125149. URL: https://link.aps.org/doi/10.1103/PhysRevB.87.125149.

[8] John H. Barrett. "Dielectric Constant in Perovskite Type Crystals". In: *Phys. Rev.* 86 (1 Apr. 1952), pp. 118–120. DOI: 10.1103/PhysRev.86.118. URL: https://link.aps.org/doi/10.1103/PhysRev.86.118.

[9] D. N. Basov, R. D. Averitt, and D. Hsieh. "Towards properties on demand in quantum materials". In: *Nature Materials* 16.11 (Nov. 2017), pp. 1077–1088. ISSN: 1476-4660. DOI: 10.1038/nmat5017. URL: https://doi.org/10.1038/nmat5017.

[10] K. S. D. Beach, R. J. Gooding, and F. Marsiglio. "Reliable Padé analytical continuation method based on a high-accuracy symbolic computation algorithm". In: *Phys. Rev. B* 61 (8 Feb. 2000), pp. 5147–5157. DOI: 10.1103/PhysRevB.61.5147. URL: https://link.aps.org/doi/10.1103/PhysRevB.61.5147.

[11] M. Buzzi et al. "Phase Diagram for Light-Induced Superconductivity in $\kappa-(ET)_2-X$". In: *Phys. Rev. Lett.* 127 (19 Nov. 2021), p. 197002. DOI: 10.1103/PhysRevLett.127.197002. URL: https://link.aps.org/doi/10.1103/PhysRevLett.127.197002.

[12] Krzysztof Byczuk and Dieter Vollhardt. "Correlated bosons on a lattice: Dynamical mean-field theory for Bose-Einstein condensed and normal phases". In: *Phys. Rev. B* 77 (23 June 2008), p. 235106. DOI: 10.1103/PhysRevB.77.235106. URL: https://link.aps.org/doi/10.1103/PhysRevB.77.235106.

[13] Changfeng Chen, Ariel Reich, and L. M. Falicov. "Surface properties of a heavy-fermion system: An exact many-body solution to a periodic-cluster Hubbard model". In: *Phys. Rev. B* 38 (18 Dec. 1988), pp. 12823–12833. DOI: 10.1103/PhysRevB.38.12823. URL: https://link.aps.org/doi/10.1103/PhysRevB.38.12823.

[14] Claude Cohen-Tannoudji, Jacques Dupont-Roc, and Gilbert Grynberg. "Classical Electrodynamics: The Fundamental Equations and the Dynamical Variables". In: *Photons and Atoms*. John Wiley & Sons, Ltd, 1997. Chap. 1, pp. 5–77. DOI: https://doi.org/10.1002/9783527618422.ch1. eprint: https://onlinelibrary.wiley.com/doi/pdf/10.1002/9783527618422.ch1. URL: https://onlinelibrary.wiley.com/doi/abs/10.1002/9783527618422.ch1.

[15] Daniele De Bernardis, Tuomas Jaako, and Peter Rabl. "Cavity quantum electrodynamics in the nonperturbative regime". In: *Phys. Rev. A* 97 (4 Apr. 2018), p. 043820. DOI: 10.1103/PhysRevA.97.043820. URL: https://link.aps.org/doi/10.1103/PhysRevA.97.043820.

[16] Daniele De Bernardis et al. "Breakdown of gauge invariance in ultrastrong-coupling cavity QED". In: *Phys. Rev. A* 98 (5 Nov. 2018), p. 053819. DOI: 10.1103/PhysRevA.98.053819. URL: https://link.aps.org/doi/10.1103/PhysRevA.98.053819.

[17] P.G. de Gennes. "Collective motions of hydrogen bonds". In: *Solid State Communications* 1.6 (1963), pp. 132–137. ISSN: 0038-1098. DOI: https://doi.org/10.1016/0038-1098(63)90212-6. URL: https://www.sciencedirect.com/science/article/pii/0038109863902126.

[18] Michael Dumm et al. "Bandwidth-controlled Mott transition in $\kappa-(BEDT-TTF)_2Cu[N(CN)_2]Br_xCl_{1-x}$: Optical studies of correlated carriers". In: *Phys. Rev. B* 79 (19 May 2009), p. 195106. DOI: 10.1103/PhysRevB.79.195106. URL: https://link.aps.org/doi/10.1103/PhysRevB.79.195106.

[19] N. Dupius and S. Pairault. "A strong-coupling expansion for the Hubbard model". In: *International Journal of Modern Physics B* 14.24 (2000), pp. 2529–2560. DOI: 10.1142/S0217979200002430. URL: https://doi.org/10.1142/S0217979200002430.

[20] Martin Eckstein and Philipp Werner. "Nonequilibrium dynamical mean-field calculations based on the noncrossing approximation and its generalizations". In: *Phys. Rev. B* 82 (11 Sept. 2010), p. 115115. DOI: 10.1103/PhysRevB.82.115115. URL: https://link.aps.org/doi/10.1103/PhysRevB.82.115115.

[21] E. N. Economou. "Surface Plasmons in Thin Films". In: *Phys. Rev.* 182 (2 June 1969), pp. 539–554. DOI: 10.1103/PhysRev.182.539. URL: https://link.aps.org/doi/10.1103/PhysRev.182.539.

[22] Francesca Fassioli et al. *Controlling radiative heat flow through cavity electrodynamics*. 2024. arXiv: 2403.00851 [physics.optics].

[23] Johannes Flick et al. "Atoms and molecules in cavities, from weak to strong coupling in quantum-electrodynamics (QED) chemistry". In: *Proceedings of the National Academy of Sciences* 114.12 (2017), pp. 3026–3034. DOI: 10.1073/pnas.1615509114. eprint: https://www.pnas.org/doi/pdf/10.1073/pnas.1615509114. URL: https://www.pnas.org/doi/abs/10.1073/pnas.1615509114.

[24] J. K. Freericks. "Strong-coupling expansions for the attractive Holstein and Hubbard models". In: *Phys. Rev. B* 48 (6 Aug. 1993), pp. 3881–3891. DOI: 10.1103/PhysRevB.48.3881. URL: https://link.aps.org/doi/10.1103/PhysRevB.48.3881.

[25] Jacopo Fregoni, Francisco J. Garcia-Vidal, and Johannes Feist. "Theoretical Challenges in Polaritonic Chemistry". In: *ACS Photonics* 9.4 (2022), pp. 1096–1107. DOI: 10.1021/acsphotonics.1c01749. eprint: https://doi.org/10.1021/acsphotonics.1c01749. URL: https://doi.org/10.1021/acsphotonics.1c01749.

[26] Hongmin Gao et al. "Photoinduced Electron Pairing in a Driven Cavity". In: *Phys. Rev. Lett.* 125 (5 July 2020), p. 053602. DOI: 10.1103/PhysRevLett.125.053602. URL: https://link.aps.org/doi/10.1103/PhysRevLett.125.053602.

[27] Antoine Georges and Gabriel Kotliar. "Hubbard model in infinite dimensions". In: *Phys. Rev. B* 45 (12 Mar. 1992), pp. 6479–6483. DOI: 10.1103/PhysRevB.45.6479. URL: https://link.aps.org/doi/10.1103/PhysRevB.45.6479.

[28] Antoine Georges and Werner Krauth. "Numerical solution of the d=∞ Hubbard model: Evidence for a Mott transition". In: *Phys. Rev. Lett.* 69 (8 Aug. 1992), pp. 1240–1243. DOI: 10.1103/PhysRevLett.69.1240. URL: https://link.aps.org/doi/10.1103/PhysRevLett.69.1240.

[29] Antoine Georges et al. "Dynamical mean-field theory of strongly correlated fermion systems and the limit of infinite dimensions". In: *Rev. Mod. Phys.* 68 (1 Jan. 1996), pp. 13–125. DOI: 10.1103/RevModPhys.68.13. URL: https://link.aps.org/doi/10.1103/RevModPhys.68.13.

[30] Roy J. Glauber and M. Lewenstein. "Quantum optics of dielectric media". In: *Phys. Rev. A* 43 (1 Jan. 1991), pp. 467–491. DOI: 10.1103/PhysRevA.43.467. URL: https://link.aps.org/doi/10.1103/PhysRevA.43.467.

[31] Emanuel Gull et al. "Continuous-time Monte Carlo methods for quantum impurity models". In: *Rev. Mod. Phys.* 83 (2 May 2011), pp. 349–404. DOI: 10.1103/RevModPhys.83.349. URL: https://link.aps.org/doi/10.1103/RevModPhys.83.349.

[32] Martin C. Gutzwiller. "Effect of Correlation on the Ferromagnetism of Transition Metals". In: *Phys. Rev. Lett.* 10 (5 Mar. 1963), pp. 159–162. DOI: 10.1103/PhysRevLett.10.159. URL: https://link.aps.org/doi/10.1103/PhysRevLett.10.159.

[33] A. Hemmerich and T. W. Hänsch. "Two-dimesional atomic crystal bound by light". In: *Phys. Rev. Lett.* 70 (4 Jan. 1993), pp. 410–413. DOI: 10.1103/PhysRevLett.70.410. URL: https://link.aps.org/doi/10.1103/PhysRevLett.70.410.

[34] A. Hemmerich et al. "Trapping Atoms in a Dark Optical Lattice". In: *Phys. Rev. Lett.* 75 (1 July 1995), pp. 37–40. DOI: 10.1103/PhysRevLett.75.37. URL: https://link.aps.org/doi/10.1103/PhysRevLett.75.37.

[35] Wen-Jun Hu and Ning-Hua Tong. "Dynamical mean-field theory for the Bose-Hubbard model". In: *Phys. Rev. B* 80 (24 Dec. 2009), p. 245110. DOI: 10.1103/PhysRevB.80.245110. URL: https://link.aps.org/doi/10.1103/PhysRevB.80.245110.

[36] J. Hubbard. "Electron correlations in narrow energy bands". In: *Proc. R. Soc. A* 276 (1963), pp. 238–257. DOI: 10.1098/rspa.1963.0204. URL: https://doi.org/10.1098/rspa.1963.0204.

[37] J. Hubbard. "Electron correlations in narrow energy bands III. An improved solution". In: *Proc. R. Soc. A* 281 (1964), pp. 401–419. DOI: 10.1098/rspa.1964.0190. URL: https://doi.org/10.1098/rspa.1964.0190.

[38] Dario Frank Hügel. "Self-consistent methods for interacting lattice bosons with U(1)-symmetry-breaking". Doctoral thesis. LMU München, 2018. DOI: 10.5282/edoc.21897. URL: https://edoc.ub.uni-muenchen.de/21897/.

[39] D. Jaksch and P. Zoller. "The cold atom Hubbard toolbox". In: *Annals of Physics* 315.1 (2005). Special Issue, pp. 52–79. ISSN: 0003-4916. DOI: https://doi.org/10.1016/j.aop.2004.09.010. URL: https://www.sciencedirect.com/science/article/pii/S0003491604001782.

[40] D. Jaksch et al. "Cold Bosonic Atoms in Optical Lattices". In: *Phys. Rev. Lett.* 81 (15 Oct. 1998), pp. 3108–3111. DOI: 10.1103/PhysRevLett.81.3108. URL: https://link.aps.org/doi/10.1103/PhysRevLett.81.3108.

[41] David Jansen, Christian Jooss, and Fabian Heidrich-Meisner. "Charge density wave breakdown in a heterostructure with electron-phonon coupling". In: *Phys. Rev. B* 104 (19 Nov. 2021), p. 195116. DOI: 10.1103/PhysRevB.104.195116. URL: https://link.aps.org/doi/10.1103/PhysRevB.104.195116.

[42] Giacomo Jarc et al. “Cavity-mediated thermal control of metal-to-insulator transition in 1T-TaS2”. In: *Nature* 622.7983 (Oct. 2023), pp. 487–492. ISSN: 1476-4687. DOI: 10.1038/s41586-023-06596-2. URL: https://doi.org/10.1038/s41586-023-06596-2.

[43] M. Jarrell. “Hubbard model in infinite dimensions: A quantum Monte Carlo study”. In: *Phys. Rev. Lett.* 69 (1 July 1992), pp. 168–171. DOI: 10.1103/PhysRevLett.69.168. URL: https://link.aps.org/doi/10.1103/PhysRevLett.69.168.

[44] Eric Jeckelmann, Chunli Zhang, and Steven R. White. “Metal-insulator transition in the one-dimensional Holstein model at half filling”. In: *Phys. Rev. B* 60 (11 Sept. 1999), pp. 7950–7955. DOI: 10.1103/PhysRevB.60.7950. URL: https://link.aps.org/doi/10.1103/PhysRevB.60.7950.

[45] Junjiro Kanamori. “Electron Correlation and Ferromagnetism of Transition Metals”. In: *Progress of Theoretical Physics* 30.3 (Sept. 1963), pp. 275–289. ISSN: 0033-068X. DOI: 10.1143/PTP.30.275. eprint: https://academic.oup.com/ptp/article-pdf/30/3/275/5278869/30-3-275.pdf. URL: https://doi.org/10.1143/PTP.30.275.

[46] Martin Kiffner et al. “Manipulating quantum materials with quantum light”. In: *Phys. Rev. B* 99 (8 Feb. 2019), p. 085116. DOI: 10.1103/PhysRevB.99.085116. URL: https://link.aps.org/doi/10.1103/PhysRevB.99.085116.

[47] Martin Kiffner et al. “Mott polaritons in cavity-coupled quantum materials”. In: *New Journal of Physics* 21.7 (July 2019), p. 073066. DOI: 10.1088/1367-2630/ab31c7. URL: https://dx.doi.org/10.1088/1367-2630/ab31c7.

[48] Aaram J. Kim et al. “Pseudoparticle vertex solver for quantum impurity models”. In: *Phys. Rev. B* 106 (8 Aug. 2022), p. 085124. DOI: 10.1103/PhysRevB.106.085124. URL: https://link.aps.org/doi/10.1103/PhysRevB.106.085124.

[49] Aaram J. Kim et al. “Vertex-Based Diagrammatic Treatment of Light-Matter-Coupled Systems”. In: *Phys. Rev. Lett.* 130 (3 Jan. 2023), p. 036901. DOI: 10.1103/PhysRevLett.130.036901. URL: https://link.aps.org/doi/10.1103/PhysRevLett.130.036901.

[50] Anton Frisk Kockum et al. “Ultrastrong coupling between light and matter”. In: *Nat. Rev. Phys.* 1 (Jan. 2019), pp. 19–40. DOI: 10.1038/s42254-018-0006-2. URL: https://www.nature.com/articles/s42254-018-0006-2.

[51] A. Femius Koenderink, Andrea Alù, and Albert Polman. “Nanophotonics: Shrinking light-based technology”. In: *Science* 348.6234 (2015), pp. 516–521. DOI: 10.1126/science.1261243. eprint: https://www.science.org/doi/pdf/10.1126/science.1261243. URL: https://www.science.org/doi/abs/10.1126/science.1261243.

[52] Ling B. Kong, Haitao Huang, and Sean Li. “Fundamentals of Ferroelectric Materials”. In: *Ferroelectric Materials for Energy Applications*. Ed. by Haitao Huang and James F. Scott. Hoboken, New Jersey: Wiley-VCH, 2018, pp. 1–30.

[53] Willis E. Lamb and Robert C. Retherford. "Fine Structure of the Hydrogen Atom by a Microwave Method". In: *Phys. Rev.* 72 (3 Aug. 1947), pp. 241–243. DOI: 10.1103/PhysRev.72.241. URL: https://link.aps.org/doi/10.1103/PhysRev.72.241.

[54] S. K. Lamoreaux. "Demonstration of the Casimir Force in the 0.6 to $6\mu m$ Range". In: *Phys. Rev. Lett.* 78 (1 Jan. 1997), pp. 5–8. DOI: 10.1103/PhysRevLett.78.5. URL: https://link.aps.org/doi/10.1103/PhysRevLett.78.5.

[55] Steven K Lamoreaux. "The Casimir force: background, experiments, and applications". In: *Reports on Progress in Physics* 68.1 (Nov. 2004), p. 201. DOI: 10.1088/0034-4885/68/1/R04. URL: https://dx.doi.org/10.1088/0034-4885/68/1/R04.

[56] Derrick Langley et al. "Optical metamaterials for photonics applications". In: *Adaptive Coded Aperture Imaging, Non-Imaging, and Unconventional Imaging Sensor Systems*. Ed. by David P. Casasent et al. Vol. 7468. International Society for Optics and Photonics. SPIE, 2009, 74680H. DOI: 10.1117/12.828509. URL: https://doi.org/10.1117/12.828509.

[57] Maria Cristina Larciprete et al. "Tuning and hybridization of surface phonon polaritons in α-MoO3 based metamaterials". In: *Opt. Express* 30.8 (Apr. 2022), pp. 12788–12796. DOI: 10.1364/OE.453726. URL: https://opg.optica.org/oe/abstract.cfm?URI=oe-30-8-12788.

[58] S. Latini et al. "The ferroelectric photo ground state of $SrTiO_3$: Cavity materials engineering". In: *PNAS* 118 (31 Aug. 2021), e2105618118. DOI: 10.1073/pnas.2105618118. URL: https://pubmed.ncbi.nlm.nih.gov/34315818/.

[59] Katharina Lenk and Martin Eckstein. "Collective excitations of the $U(1)$-symmetric exciton insulator in a cavity". In: *Phys. Rev. B* 102 (20 Nov. 2020), p. 205129. DOI: 10.1103/PhysRevB.102.205129. URL: https://link.aps.org/doi/10.1103/PhysRevB.102.205129.

[60] Katharina Lenk et al. *Collective theory for an interacting solid in a single-mode cavity*. 2022. arXiv: 2205.05559 [cond-mat.str-el].

[61] Katharina Lenk et al. "Dynamical mean-field study of a photon-mediated ferroelectric phase transition". In: *Phys. Rev. B* 106 (24 Dec. 2022), p. 245124. DOI: 10.1103/PhysRevB.106.245124. URL: https://link.aps.org/doi/10.1103/PhysRevB.106.245124.

[62] Jiajun Li and Martin Eckstein. "Manipulating Intertwined Orders in Solids with Quantum Light". In: *Phys. Rev. Lett.* 125 (21 Nov. 2020), p. 217402. DOI: 10.1103/PhysRevLett.125.217402. URL: https://link.aps.org/doi/10.1103/PhysRevLett.125.217402.

[63] Jiajun Li et al. "Electromagnetic coupling in tight-binding models for strongly correlated light and matter". In: *Phys. Rev. B* 101 (20 May 2020), p. 205140. DOI: 10.1103/PhysRevB.101.205140. URL: https://link.aps.org/doi/10.1103/PhysRevB.101.205140.

[64] Xian Li et al. “Terahertz field-induced ferroelectricity in quantum paraelectric $SrTiO_3$”. In: *Science* 364.6445 (2019), pp. 1079–1082. DOI: 10.1126/science.aaw4913. eprint: https://www.science.org/doi/pdf/10.1126/science.aaw4913. URL: https://www.science.org/doi/abs/10.1126/science.aaw4913.

[65] Curdin Maissen et al. “Ultrastrong coupling in the near field of complementary split-ring resonators”. In: *Phys. Rev. B* 90 (20 Nov. 2014), p. 205309. DOI: 10.1103/PhysRevB.90.205309. URL: https://link.aps.org/doi/10.1103/PhysRevB.90.205309.

[66] Giacomo Mazza and Antoine Georges. “Superradiant Quantum Materials”. In: *Phys. Rev. Lett.* 122 (1 Jan. 2019), p. 017401. DOI: 10.1103/PhysRevLett.122.017401. URL: https://link.aps.org/doi/10.1103/PhysRevLett.122.017401.

[67] J. Merino et al. “Quasiparticles at the Verge of Localization near the Mott Metal-Insulator Transition in a Two-Dimensional Material”. In: *Phys. Rev. Lett.* 100 (8 Feb. 2008), p. 086404. DOI: 10.1103/PhysRevLett.100.086404. URL: https://link.aps.org/doi/10.1103/PhysRevLett.100.086404.

[68] Walter Metzner and Dieter Vollhardt. “Correlated Lattice Fermions in $d = \infty$ Dimensions”. In: *Phys. Rev. Lett.* 62 (3 Jan. 1989), pp. 324–327. DOI: 10.1103/PhysRevLett.62.324. URL: https://link.aps.org/doi/10.1103/PhysRevLett.62.324.

[69] K. A. Müller and H. Burkard. “$SrTiO_3$: An intrinsic quantum paraelectric below 4 K”. In: *Phys. Rev. B* 19 (7 Apr. 1979), pp. 3593–3602. DOI: 10.1103/PhysRevB.19.3593. URL: https://link.aps.org/doi/10.1103/PhysRevB.19.3593.

[70] E. Müller-Hartmann. “Correlated fermions on a lattice in high dimensions”. In: *Z. Physik B* 74 (Dec. 1989), pp. 507–512. DOI: 10.1007/BF01311397. URL: https://link.springer.com/article/10.1007/BF01311397.

[71] T. F. Nova et al. “Metastable ferroelectricity in optically strained $SrTiO_3$”. In: *Science* 364.6445 (2019), pp. 1075–1079. DOI: 10.1126/science.aaw4911. eprint: https://www.science.org/doi/pdf/10.1126/science.aaw4911. URL: https://www.science.org/doi/abs/10.1126/science.aaw4911.

[72] R. Peierls. “Zur Theorie des Diamagnetismus von Leitungselektronen”. In: *Z. Physik* 80 (Nov. 1933), pp. 763–791. DOI: 10.1007/BF01342591. URL: https://link.springer.com/article/10.1007/BF01342591.

[73] E. M. Purcell. “Spontaneous Emission Probabilities at Radio Frequencies”. In: *Proceedings of the American Physical Society*. Vol. 69. American Physical Society, June 1946, pp. 674–674. DOI: 10.1103/PhysRev.69.674. URL: https://link.aps.org/doi/10.1103/PhysRev.69.674.

[74] Ariel Reich and L. M. Falicov. “Heavy-fermion system: An exact many-body solution to a periodic-cluster Hubbard model”. In: *Phys. Rev. B* 37 (10 Apr. 1988), pp. 5560–5570. DOI: 10.1103/PhysRevB.37.5560. URL: https://link.aps.org/doi/10.1103/PhysRevB.37.5560.

[75] Juan Román-Roche, Fernando Luis, and David Zueco. "Photon Condensation and Enhanced Magnetism in Cavity QED". In: *Phys. Rev. Lett.* 127 (16 Oct. 2021), p. 167201. DOI: 10.1103/PhysRevLett.127.167201. URL: https://link.aps.org/doi/10.1103/PhysRevLett.127.167201.

[76] Christian Schäfer et al. "Modification of excitation and charge transfer in cavity quantum-electrodynamical chemistry". In: *Proceedings of the National Academy of Sciences* 116.11 (2019), pp. 4883–4892. DOI: 10.1073/pnas.1814178116. eprint: https://www.pnas.org/doi/pdf/10.1073/pnas.1814178116. URL: https://www.pnas.org/doi/abs/10.1073/pnas.1814178116.

[77] T. Schäfer et al. "Fate of the false Mott-Hubbard transition in two dimensions". In: *Phys. Rev. B* 91 (12 Mar. 2015), p. 125109. DOI: 10.1103/PhysRevB.91.125109. URL: https://link.aps.org/doi/10.1103/PhysRevB.91.125109.

[78] F. Schlawin, D. M. Kennes, and M. A. Sentef. "Cavity quantum materials". In: *Applied Physics Reviews* 9.1 (Feb. 2022), p. 011312. ISSN: 1931-9401. DOI: 10.1063/5.0083825. eprint: https://pubs.aip.org/aip/apr/article-pdf/doi/10.1063/5.0083825/19819541/011312_1_online.pdf. URL: https://doi.org/10.1063/5.0083825.

[79] Frank Schlawin, Andrea Cavalleri, and Dieter Jaksch. "Cavity-Mediated Electron-Photon Superconductivity". In: *Phys. Rev. Lett.* 122 (13 Apr. 2019), p. 133602. DOI: 10.1103/PhysRevLett.122.133602. URL: https://link.aps.org/doi/10.1103/PhysRevLett.122.133602.

[80] Michael Schüler et al. "NESSi: The Non-Equilibrium Systems Simulation package". In: *Computer Physics Communications* 257 (2020), p. 107484. ISSN: 0010-4655. DOI: https://doi.org/10.1016/j.cpc.2020.107484. URL: https://www.sciencedirect.com/science/article/pii/S0010465520302277.

[81] Michael A. Sentef et al. "Quantum to classical crossover of Floquet engineering in correlated quantum systems". In: *Phys. Rev. Res.* 2 (3 July 2020), p. 033033. DOI: 10.1103/PhysRevResearch.2.033033. URL: https://link.aps.org/doi/10.1103/PhysRevResearch.2.033033.

[82] Dongbin Shin et al. "Quantum paraelectric phase of $SrTiO_3$ from first principles". In: *Phys. Rev. B* 104 (6 Aug. 2021), p. L060103. DOI: 10.1103/PhysRevB.104.L060103. URL: https://link.aps.org/doi/10.1103/PhysRevB.104.L060103.

[83] Dominik Sidler et al. "A perspective on ab initio modeling of polaritonic chemistry: The role of non-equilibrium effects and quantum collectivity". In: *The Journal of Chemical Physics* 156.23 (June 2022), p. 230901. ISSN: 0021-9606. DOI: 10.1063/5.0094956. eprint: https://pubs.aip.org/aip/jcp/article-pdf/doi/10.1063/5.0094956/19820362/230901_1_online.pdf. URL: https://doi.org/10.1063/5.0094956.

[84] R. N. Silver, D. S. Sivia, and J. E. Gubernatis. "Maximum-entropy method for analytic continuation of quantum Monte Carlo data". In: *Phys. Rev. B* 41 (4 Feb. 1990), pp. 2380–2389. DOI: 10.1103/PhysRevB.41.2380. URL: https://link.aps.org/doi/10.1103/PhysRevB.41.2380.

[85] Herbert Walther et al. "Cavity quantum electrodynamics". In: *Reports on Progress in Physics* 69.5 (Apr. 2006), p. 1325. DOI: 10.1088/0034-4885/69/5/R02. URL: https://dx.doi.org/10.1088/0034-4885/69/5/R02.

[86] Manuel Weber. "Quantum Monte Carlo simulation of spin-boson models using wormhole updates". In: *Phys. Rev. B* 105 (16 Apr. 2022), p. 165129. DOI: 10.1103/PhysRevB.105.165129. URL: https://link.aps.org/doi/10.1103/PhysRevB.105.165129.

[87] Philipp Werner et al. "Continuous-Time Solver for Quantum Impurity Models". In: *Phys. Rev. Lett.* 97 (7 Aug. 2006), p. 076405. DOI: 10.1103/PhysRevLett.97.076405. URL: https://link.aps.org/doi/10.1103/PhysRevLett.97.076405.

[88] Roger Whatmore. "Ferroelectric Materials". In: *Springer Handbook of Electronic and Photonic Materials*. Ed. by Safa Kasap and Peter Capper. Boston, MA: Springer US, 2007, pp. 597–623.

[89] T Yanagisawa. "Physics of the Hubbard model and high temperature superconductivity". In: *Journal of Physics: Conference Series* 108.1 (Mar. 2008), p. 012010. DOI: 10.1088/1742-6596/108/1/012010. URL: https://dx.doi.org/10.1088/1742-6596/108/1/012010.

[90] Zhidong Zhang. "Exact solution of two-dimensional (2D) Ising model with a transverse field: A low-dimensional quantum spin system". In: *Physica E: Low-dimensional Systems and Nanostructures* 128 (2021), p. 114632. ISSN: 1386-9477. DOI: https://doi.org/10.1016/j.physe.2021.114632. URL: https://www.sciencedirect.com/science/article/pii/S138694772100014X.

[91] Yixi Zhou et al. "Thermal and electrostatic tuning of surface phonon-polaritons in LaAlO3/SrTiO3 heterostructures". In: *Nature Communications* 14.1 (Nov. 2023), p. 7686. ISSN: 2041-1723. DOI: 10.1038/s41467-023-43464-z. URL: https://doi.org/10.1038/s41467-023-43464-z.

Acknowledgments

I am deeply grateful to many individuals whose support and guidance made this thesis possible.

First and foremost, I extend my sincere appreciation to my supervisor, Prof. Dr. Martin Eckstein, for his consistent guidance and encouragement and for giving me the opportunity to delve into this fascinating field of research in the first place. His dedication and expertise profoundly shaped this work, and I am extremely thankful for all the invaluable insights he shared with me.

I am also indebted to Prof. Dr. Silvia Viola Kusminskiy for co-supervising this thesis during my time in the QuCoLiMa Research Training Group at the Friedrich-Alexander University Erlangen-Nuremberg and for engaging discussions on my project.

Likewise, my heartfelt thanks go to the examination commission for their time and effort in evaluating this thesis.

Furthermore, I had the pleasure of collaborating with Prof. Dr. Philipp Werner, whose excellent expertise and advice greatly enriched our projects. I am especially thankful for the opportunity to visit his research group in Fribourg and gain insights into the CT-QMC method.

Additionally, I extend my gratitude to Dr. Jiajun Li for many stimulating discussions, particularly in the early stages of my PhD, when he was a postdoc in our group. His insights significantly contributed to our research outcomes.

I also wish to acknowledge my former colleagues at the Friedrich-Alexander University in Erlangen, where I spent the first years of my doctorate. Special thanks to Dr. Christopher Stahl and Paul Fadler. Alongside their PhD studies, they did a great job at maintaining the Thoss cluster and managing everything IT-related in our group. Furthermore, I must mention Ursula Maerker, the secretary of our chair, whose excellent administrative skills ensured the smooth functioning of the Chair of Theoretical Solid State Physics.

Moreover, I am thankful to my colleagues at the University of Hamburg, where I completed my PhD studies. The support of PHYSnet's excellent IT service and Anna Zharinova's administrative efficiency greatly facilitated my transition from Erlangen to Hamburg and my daily research. Furthermore, I would like to thank my fellow PhD students Eva Paprotzki, Francesco Valiera, and Fabian Künzel for many pleasant conversations during lunch and the friendly working atmosphere in the office.

Apart from that, I am extremely grateful to my brother and my dad for their meticulous proofreading of this thesis. And last but not least, heartfelt thanks to my parents for their unwavering support and encouragement throughout my academic journey.